Control and generalised synchronisation in a chaotic laser

By

Greg Kociuba

A thesis submitted to the University of Queensland
for the degree of Doctor of Philosophy
Department of Physics
April 2003

Typeset in LaTeX 2_ε.

Except where acknowledged in the customary manner, the material presented in this thesis is, to the best of my knowledge, original and has not been submitted in whole or part for a degree in any university.

Greg Kociuba

Acknowlegements

I would like to thank my supervisors Norman Heckenberg, Dingyuan Tang, and Andrew White. Norm has always been there when I have needed him. His guidance has been immeasurable over the course of my PhD. I have learnt to be independent, and to back myself, since Norm has let me go off on a tangent on occasions where it wasn't obvious to him where I was going. It didn't always produce results, but its all part of the process. He has taught to step back and see the overall picture, as I have tended to dive into the details to quickly. He has helped me develop my problem skills my showing me different points of view, and how you can view a problem on different scales. Norm has this dry, penetrating wit, which only he can deliver the punch line that well. Dingyuan was my second supervisor for about the first half of my PhD, and is exceptional at generating results quickly. He taught me a lot about how to used the experimental system efficiently, and just his general approach in the lab which is work, work, and work until you get the result you want. Andrew was thrust into being my associate supervisor ("against" his will :-) when Dingyuan left. He was involved in my first publication, and has shown me how to express scientific results clearly (well, relatively anyway). His louder than life and unstoppable attitude has been inspiring.

My office mates Paul Cochrane, Ben Travaglione, Greg (not me! the "other one")

Hutchinson, and other people in general. Our office must have been the craziest, most non politically correct room in the department (or any where for that matter! no subject was left untouched). This has helped all of us get by, and Paul, the New Zealander, well I've nearly managed to 'beat the Kiwi out of you' (sorry about that). Your one of the nicest guys I know Paul, thanks for all your help. Thanks to all you guys for pretending my jokes and bad humour was actually funny!

I would like to thank my flatmates Bec, Shannon, and Alisa for feeding me during the last stage of my write up. My other flatmate Nimalan for being a Sri Lankan, therefore crazy about cricket just like me ! The girls in the house are expecting me to cook for them when I finish, and are expecting my awesome curries that I can make. I learnt to make these curries from Bill Munro whom I flatted with earlier. I have to thank you as well Bill, and your two horrible cats !

The workshop staff headed by Alan Reid have produce lab equipment of extremely high quality, and have always been there when 'a small job' was required.

Most importantly, I would like to thank my Mum, Dad, Kathy, and Vicky, and other family members for their support and endless love during my life. They have always encouraged me to do what I wanted, and have accepted me for who I am. They have helped me through the tough times which is not easy over long distances. During the time of difficulties, music has been the constant that has kept me going, especially at times when you think are crossing the bifurcation of sanity. During my write up, the Beethoven symphonies were a great source of inspiration. It makes you wonder how such creativity can emerge. Just as grand are his 32 piano sonatas ("symphony for the piano") and piano concertos. I dedicate this thesis to Beethoven and his extraordinary music which transcends time.

List of Publications

- G. Kociuba, N. R. Heckenberg, and A. G. White. *Transforming chaos to periodic oscillations.*
  Phys. Rev. E **64**, 056220 (2001)
- G. Kociuba and N. R. Heckenberg. *Controlling the complex Lorenz equations by modulation.*
  Phys. Rev. E **66**, 026205 (2002)
- G. Kociuba, N. R. Heckenberg. *Controlling chaos in a Lorenz–like system using feedback.* (submitted to Phys. Rev. E.)

Abstract

This thesis describes an experimental and numerical investigation of control of an autonomous Lorenz–like chaotic laser system. Any chaotic system has an attractor which defines how the dynamics evolves, and it contains a number of unstable periodic orbits. Stabilising one of these leads to predictable periodic oscillations as it is known that if one of the unstable periodic orbits is stabilised then the system is globally stable.

Two different control methods have been studied. A parametric perturbation method is considered where a sinusoidal modulation is applied to the pump power of the laser. Control well above the threshold had never been previously observed in this laser, contrary to expectation. Careful experimental and numerical studies presented here show that not only is control possible with modulation at a frequency near the average chaotic pulsation frequency, but control to various periodic states emerged during appropriate conditions.

The second method of control investigated here is based on the delayed feedback method introduced by Pyragas. An error signal is generated from the difference between a signal and its value delayed in time, and this difference is fed back to modulate a system parameter. Control to various periodic states, and the steady state, had previously been observed in the ammonia laser, and was confirmed by the author numerically and experimentally. Detailed numerical studies support and extend the experimental results, and are used to explore the effects of varying the feedback delay over several pulse periods. An additional loop delay is introduced to allow for the fact that the difference signal takes some time to be fed back into the system in the ammonia laser. Control can be achieved for delays of several pulsation periods.

A simpler version of the Pyragas method is also investigated where only the delayed signal is used as the feedback. Control to periodic states, and to steady state, is found with a similar accessible range of dynamics as with the original Pyragas method. Both feedback versions of control can be thought of as self–synchronisation of the system variables with their previous values.

The effect of bandwidth of the feedback is modelled numerically using the complex Lorenz equations. The chaotic dynamics is still controlled even if the bandwidth is slightly less than the average pulsation frequency of the chaos.

Finally the question of difficulty of control is addressed, and synchronisation is used to help determine the location of the controlled dynamics in parameter space.

Contents

List of Figures
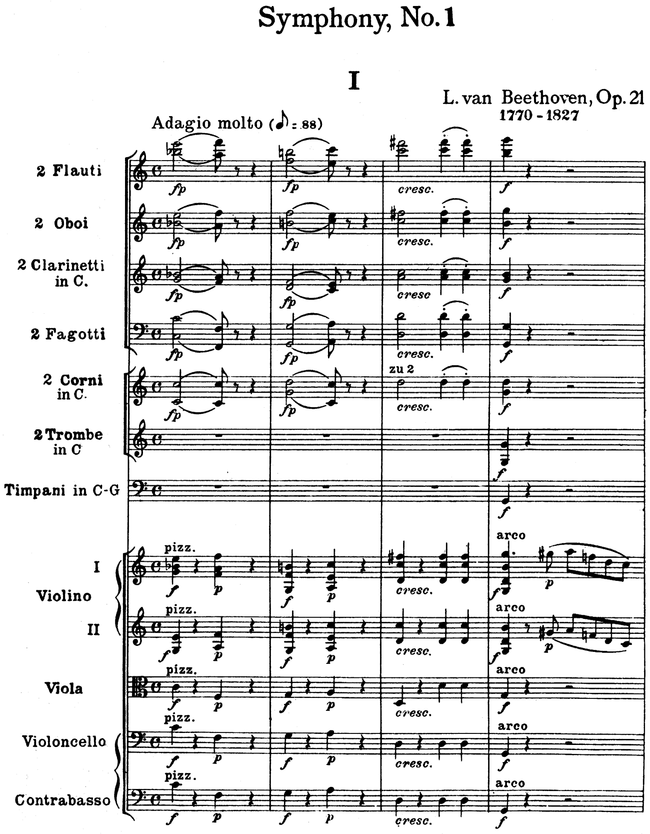
1

Introduction

A system is chaotic if its dynamics is bounded but it has sensitive dependence to initial conditions. This means that two initial points separated by an infinitessimal amount will follow each other for a time, after which they become uncorrelated. The dynamics is not repeated after a finite time, but nor is it random since the dynamics is described by a particular set of rules which are deterministic. A system can only lack repeatability if the evolution or trajectories of individual points do not cross one another. This can only happen if the system is embedded in at least three dimensions. If a system is described by at least three variables which are nonlinearly coupled to each other, as is common in many physical systems, then chaos could emerge under appropriate conditions.

There are many situations in mechanical, electrical, optical, nuclear, chemical, and biological systems where chaotic behaviour occurs, which is destructive or at least increases inefficiencies in those systems. It may not be possible or convenient to design out chaos in a system. If the chaotic dynamics could be replaced by simpler regular dynamics then a more stable, and predictable system could be created. In some cases it might be possible to improve the performance of a device by controlling the initially chaotic dynamics. Examples would include increasing the output power of an otherwise chaotic laser, or driving a mechanical device harder without destroying it or something else in the process. To do this, an understanding of how a chaotic system responds when various perturbations are applied is required. This has led to much research in this area in many fields of engineering, science including the biological sciences, and many cross–disciplinary fields. A deeper understanding of chaotic systems has led to research where chaos can be considered a feature. Many possible dynamical states can be accessed within a chaotic system if an appropriate perturbation is applied.

Controlling chaos usually implies there is deterministic relationship between the phase or amplitude of the controlled chaotic signal, and an applied perturbation as time evolves. For periodic oscillators, the phenomenon of synchronisation has been described as early as the 17th century by Huygens [2] (English translation [3]) where synchronisation was observed between pendulum clocks hanging on a wall. An understanding of how periodic oscillators synchronise has given insights to explaining how more complex dynamical systems such as chaos can be synchronised or controlled. The term *synchronisation* has taken on a variety of meanings over the years. It has ranged from complete agreement or correlation between the dynamics of two coupled systems, to the weaker definition of correlation in time. Control of chaos can be seen as a subset of synchronisation where the phase or amplitude of a chaotic variable becomes regular, and the phase difference between the two systems typically has a constant value during control. Synchronisation of a chaotic system with an external controller can lead to a correlation between the periods of the chaotic system, and the controller, but the amplitudes may not be correlated. This type of behaviour may persist for a particular range of a controller parameter [4]. Within this window there is a narrow region where the amplitude dynamics is simplified and therefore controlled [5]. Information about the location and width of the synchronisation region is useful to estimate how well a particular chaotic system can be controlled. A narrower synchronisation window will generally make control more experimentally difficult to implement. Understanding the properties of synchronisation is important so that this information can be used to estimate the location of the narrow control region within the synchronisation window.

1.1 Mechanism of synchronisation and control

In periodic oscillators there are two different mechanisms of synchronisation [6]. The first is frequency locking of the natural oscillation frequency to the external source where the phase difference becomes constant. The second mechanism involves the suppression of the natural dynamics of the system driven by an external signal. In this case the frequency of the external source does not have to lie near the natural oscillation frequency of the system to be controlled, as is typically the case with the first method. Both these mechanisms have recently been extended to chaotic systems in terms of synchronisation where the amplitudes of the periodic controller and the system are not necessarily correlated [7].

Periodic oscillators can be easily frequency locked to an appropriate weak periodic modulation, since the time scale is well defined with an extremely narrow distribution of orbit periods, which is not the case in nonlinear systems [8]. The phase difference at integers n and m for the periodic oscillator, and the periodic modulation, each with phases ϕ_1, and ϕ_2 respectively, will be $\theta = n\phi_1 - m\phi_2$. This will be a constant during perfect synchronisation or locking. The beat frequency is

$$\dot{\theta} = \Delta\omega - C \sin\theta \tag{1.1}$$

where $\Delta\omega = n\omega_1^0 - m\omega_2^0$ is the difference between the natural frequencies of the oscillator and the periodic modulator, and C is the coupling strength. Frequency locking is achieved when $|\frac{\Delta\omega}{C}| \leq 1$ and this triangular region of the C–$\Delta\omega$ plane is known as the Arnold tongue [4]. Perfect synchronisation is destroyed if noise is present [8]. The above approach can be modified for the situation of synchronising, or controlling a chaotic oscillator. The phase of a periodic oscillator is simple to define because of the presence of well-defined regular motion. Each of the variables of a chaotic oscillator has different irregular behaviour so it is not obvious which variable should be used to determine the phase of the system, and in fact there is no unique method to determine the phase of a chaotic variable [8] although the long term behaviour is the same qualitatively for a sensible choice of phase. Three common methods used to calculate phase are discussed in detail in section 3.3, and the phase is calculated here using the times of the amplitude peaks of the time varying intensity pulsations. The dynamics of the phase is important as it contains information about the state of synchronisation when compared to the phase of the external perturbation, and is relevant for any chaos control method.

1.2 Stages of synchronisation

Perfect frequency locking or control corresponds to *perfect synchronisation* between the dynamics of the system and an applied modulation, and is the first stage of synchronisation. The second stage is commonly referred to as *phase synchronisation* where the average frequency of a system, and the applied modulation are identical. There are no phase slips, however the amplitudes of the system variable and the modulation are generally uncorrelated. In the third stage of synchronisation, only the average frequencies are identical, but positive and negative phase slips occur so there is usually no phase, or amplitude correlation between the system dynamics, and the applied modulation. This stage is known as *weak synchronisation*.

The transition route to the weak synchronisation state, from an unsynchronised state was recently discovered by Boccaletti [9]. There is perfect synchronisation for a particular modulation frequency ν_c. As the frequency is shifted away from ν_c and hence synchronisation, control is lost momentarily as phase slips develop. The average time between successive phase slips is

$$\ln \frac{1}{\tau} \approx |\nu - \nu_c|^{-1/2} \tag{1.2}$$

and is initially large, slips becoming more frequent as $|\nu - \nu_c|$ increases. This is known as super long laminar behaviour [9]. The phase slips become more regular as ν increases to the point where the times between successive phase slips are almost equal [9], and the associated dynamics is called periodic phase synchronisation. As the frequency increases further a transition is reached where the time between successive phase slips follows a type 1 intermittency scaling law [10]

$$\tau \approx |\nu - \nu_c|^{-1/2} \tag{1.3}$$

which corresponds to the same scaling law describing time between phase slips in forced periodic oscillators. Phase synchronisation was first observed in mutually coupled [11] or periodically forced chaotic oscillators [12], which were extensively studied in theoretical models [13, 14], and experiments [15–17]. Phase synchronisation is important in many physiological systems. One example is the synchronisation which can occur between the human heartbeat and the respiratory system. This was shown for the first time by Schafer *et al.* [18], and is also seen in magnetoencephalography and electromyography of Parkinsonian patients where the time evolution of the peripheral tremor rhythms indicates synchronisation between cortical motor areas [19], and electroencephalograms during visual stimulation. Synchronisation occurs, followed by desynchronisation which is necessary to proceed from one cognitive state to another [20]. Information about the different stages of synchronisation for a particular system can be useful to determine how well a system can be controlled. For applications where the chaotic dynamics must be eliminated to give regular dynamics, phase synchronisation will only partially control the phase of the chaotic system to the applied perturbation in the sense that there are no phase slips, and the amplitude of the resultant signal will generally be uncorrelated with that of the applied perturbation. In this thesis the aim is to control not only the phase of the intensity pulsations, but also the amplitude of a chaotic ammonia laser experimentally, and to model this process numerically. The following discussion about different ways of controlling chaos is summarised in a flow diagram in figure 1.1. Methods to control chaos fall into two broad categories. Firstly there is state independent control where one or more of the system parameters (or variables) is varied externally independently of the state of the system. Secondly, there is control by delayed feedback where the system parameter/s (or variable/s) is/are modulated by a signal which depends on the state of the system. The state independent and delayed feedback control methods could either require a detailed knowledge of a particular dynamical system and therefore require a set of differential equations describing the system, or only basic knowledge of the system such as the characteristic time of the system which does not require knowledge of the equations. Both the state independent and feedback control methods can be developed either from a model independent or a model dependent superset. For simplicity only the developments of the state independent case are shown in figure 1.1

In many applications a complete accurate set of differential equations describing a particular physical system may not be possible to generate within a reasonable time. For this reason, experimentally there has been a strong emphasis in researching control of chaotic systems without the knowledge of the equations of motion. The state independent control method can take two possible paths. The applied modulation can either be resonant or non resonant with the chaotic system.

1.3 Non-resonant control

A dynamical system $\dot{x} = F(x, \mu)$ with a bifurcation point μ_c, can be controlled if the control parameter μ is varied close to μ_c. There is a structural change in the equation once the bifurcation parameter is time dependent $\mu(t)$. The stability now depends on time and the result is that the time of instability t^* can be calculated [21]

$$\int_0^{t^*} \lambda(\tau) d\tau = 0 \tag{1.4}$$

and the associated value of the bifurcation parameter is $\mu(t^*)$. There exists a time $0 < \hat{t} < t^*$ which corresponds to the static bifurcation point $\mu(\hat{t})$, so that $\mu(t^*) > \mu(\hat{t})$. The values of the eigenvalues are positive between times $\hat{t}$ and t^*, but the global dynamics is stable, so there appears to be an accumulation of stability of the negative eigenvalues during $0 < t < \hat{t}$ which prevents the system becoming globally unstable for $\hat{t} < t < t^*$. This is known as a *delayed bifurcation.* There are several theory [22, 23] and experimental results for systems such as a loss modulated non autonomous CO_2 laser [24], and an autonomous ammonia laser [25] which make use of this phenomenon to stabilise a dynamical system. This has the obvious advantage that it is easy to do and only knowledge of the bifurcation point is required, but stabilisation cannot be achieved in this way for a control parameter significantly greater than the bifurcation point.

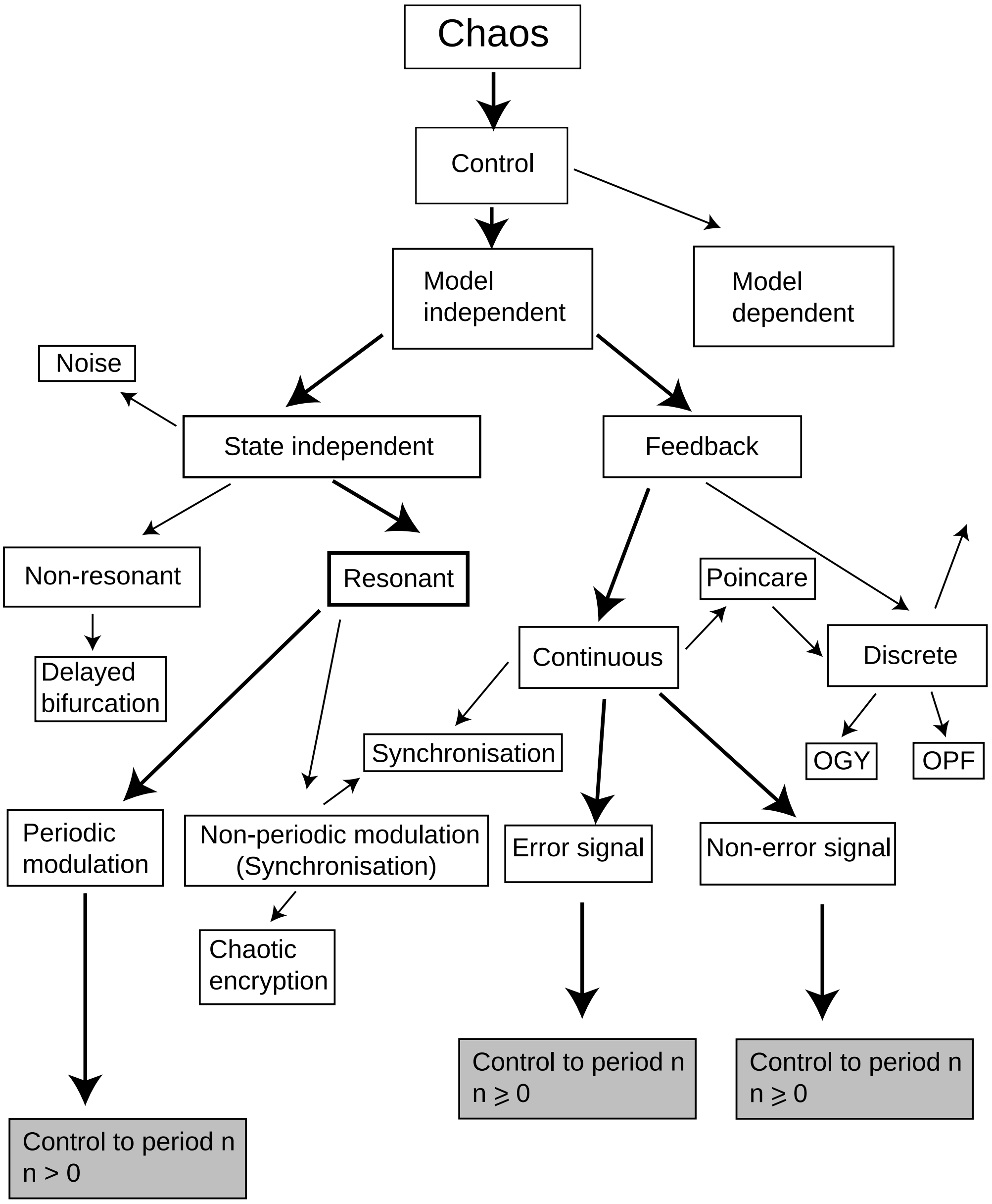

FIGURE 1.1: Schematic of general methods of controlling chaos. The thick arrows indicate the route to control used in this thesis.

1.4 Resonant control

The simplest resonant control method is to apply a periodic modulation to a system parameter (or variable). This is one of the control methods used here experimentally in an optically pumped far infrared ammonia laser, and numerically in the Lorenz–Haken laser model. This was first proposed in 1990 by Lima et al. [26] who gave a theoretical treatment of the non autonomous Duffing-Holmes oscillator. They found that a modulation amplitude of a few percent was required to control the chaotic dynamics. Experimental evidence of this phenomenon was observed in a chaotic magnetoelastic beam which can be modelled as a Duffing-Holmes oscillator, and chaos was controlled for a modulation amplitude of around 10% [27]. Numerical investigations of control in the Rössler and Lorenz systems were performed where the control signal $f(t)$ was written as $f(t) = \sin(\omega t)$. Perfect synchronisation was found in the phase coherent Rössler system [12] when the drive frequency was equal to the main resonance ω_0, $\frac{1}{2}\omega_0$, and $2\omega_0$ corresponding to locking ratios of 1:1, 2:1, and 1:2 respectively. In the Lorenz system perfect phase synchronisation was found only for very large modulation amplitudes, and for a locking ratio of 1:1 with 1:2 and 2:1 not found [12]. The Lorenz system has relatively large variations in the dynamics of the phase, resulting in a large distribution of orbit times. The parameters used in the Rössler system correspond to a very narrow distribution of orbit times of the chaotic system allowing perfect synchronisation to occur more easily. A CO_2 laser with feedback producing homoclinic spikes was controlled [17] by periodic modulation with amplitudes from 0.9% to 2% with a locking ratio of 1:1. Perfect control was achieved only when corrections were made to the applied periodic modulation frequency. The corrections were calculated using the average phase slip rate within a time interval Δt which corresponds to a shift in frequency $\Delta\nu = -a(\frac{ds}{dt})_{\Delta t}$, where s is the phase difference between the laser intensity, and the modulation, and a is a suitable positive coefficient. The slip rate is updated each time interval so the modulation frequency becomes

$$f(t) = \nu_0(t) + \sum \Delta\nu(t) \tag{1.5}$$

which tends to ν_0 as the phase slips become rarer and rarer.

More complex modulation signals can be used to control a system such as using a prerecorded time sequence of chaotic pulsations as the perturbation [28], and a prerecorded chaotic signal controlling the amplitude and phase of a chaotic ammonia laser to the prerecorded signal [29]. This in itself is a large field which includes the application of chaotic encryption [30], and the theory of synchronising non identical systems [31]. Lastly it is possible to control a chaotic system by applying noise to a system parameter or variable [32] and to induce order in lasers using quantum noise [33]. State independent control methods applied to the chaotic ammonia laser are discussed in Chapters 5 and 6.

1.5 Time delayed feedback control

The feedback control method falls into two classes, discrete, and continuous feedback. One of the first control methods proposed in 1990 was discrete feedback using the Ott, Grebogi, and Yorke method (OGY) [34]. This is discussed in detail in appendix A. A perturbation is applied to the system whenever the state of the system is near an unstable manifold whose position and properties have been calculated in some detail. This information is used to generate the perturbation. The OGY method has been experimentally implemented in a magnetoelastic ribbon [35].

There are many variations of the OGY method such as the occasional proportional feedback method (OPF) developed by Hunt in 1991 [36] where a pulse is injected into a chaotic system whenever a particular output of the system is within a window near a pre-assigned state. This is relatively efficient in highly dissipative systems where the rate of contraction in phase space is so large that the attractor dynamics can be represented as a one dimensional map in two coordinates. These types of feedback are discrete for both discrete and continuous systems. The OPF method was implemented in an autonomously chaotic solid-state laser operating in a relatively high dimension [37], and the unstable steady state was stabilised in a chaotic multimode Nd:YAG laser with an intracavity nonlinear KTP (titanyl potassium phosphate) crystal [38]. There are other similar control schemes such as recursive proportional feedback (RPF) [39].

Control by continuous delayed feedback is more widespread in nature and in self–evolving systems due to the inherent continuity of time. The delayed feedback signal may contain an error signal as developed by Pyragas [40] which tends to zero as the system approaches control. A chaotic analog circuit was controlled by feeding an error signal generated by the circuit back into the circuit [41]. Alternatively the delayed feedback signal may not go to zero, but the feedback system may effectively become part of a new dynamical system which has simpler dynamics. Both methods have been explored by the author in the ammonia laser, and in the Lorenz–Haken laser model, and are discussed in Chapter 7. There are other continuous feedback schemes such as the adaptive proportional feedback (APF) [42] which is a continuous version of OPF. The Pyragas control method has also been modified to allow for drift occurring in the positions of either the unstable steady state, or the unstable periodic orbit and is then called dissipative feedback control (DF) [43]. The Pyragas method can also be used to control to steady state if the feedback is non perturbative [43, 44], as observed in a class B laser [45], and in a frequency doubled Nd:YAG laser [46]. Time delayed feedback control can only stabilise orbits with short periods or small Lyapunov exponents [47], but this is overcome by including multiple delays [48] rather than just a single delay.

1.6 Controlling chaos in the ammonia laser and in the Lorenz–Haken model

The main aim in this thesis is to investigate methods of control in a laser system which can be described by the Lorenz–Haken equations. Most experimental results mentioned in the preceding sections have been obtained from non autonomous chaotic systems. There are relatively few control results on autonomous systems, and there are only results by Dykstra [49] on controlling a single mode autonomous laser that the author is aware of. A chaotic system can be expected to be controlled in theory, but there are many issues which may hinder the possibility of obtaining control in a real system. Each chaotic system has its own characteristic time scale, which has some spread in the time distribution. Control is more easily achieved for a narrower time distribution as discussed in section 1.1, so the first question is: is control possible, and can it be achieved easily in an autonomous single mode laser system? What type of controlled dynamics can be generated in the laser, and how does this compare with the model? Synchronisation is also a predicted phenomenon in chaotic systems, so how does this manifest itself in the laser system, and how is control related to synchronisation? These questions are addressed by the author in this thesis.

The next chapter will briefly introduce a number of concepts in the theory of chaotic dynamics which are applied in the experimental and theoretical work described in subsequent chapters. Chapter 3 deals with the Lorenz equations, and the particular form which can be used to model the dynamics of the ammonia laser system on which experiments have been performed. Chapter 4 deals with the experimental apparatus, and some data used to show the existence of chaos in the ammonia laser. The subsequent chapters describe several ways in which chaotic dynamics in the ammonia laser have successfully been controlled. In particular Chapter 5 and 6 deal with control by periodic modulation experimentally, and numerically respectively.

Chapter 7 discusses two delayed feedback methods, subtractive, and non subtractive, both experimentally, and numerically. Finally, Chapter 8 deals with chaotic synchronisation.
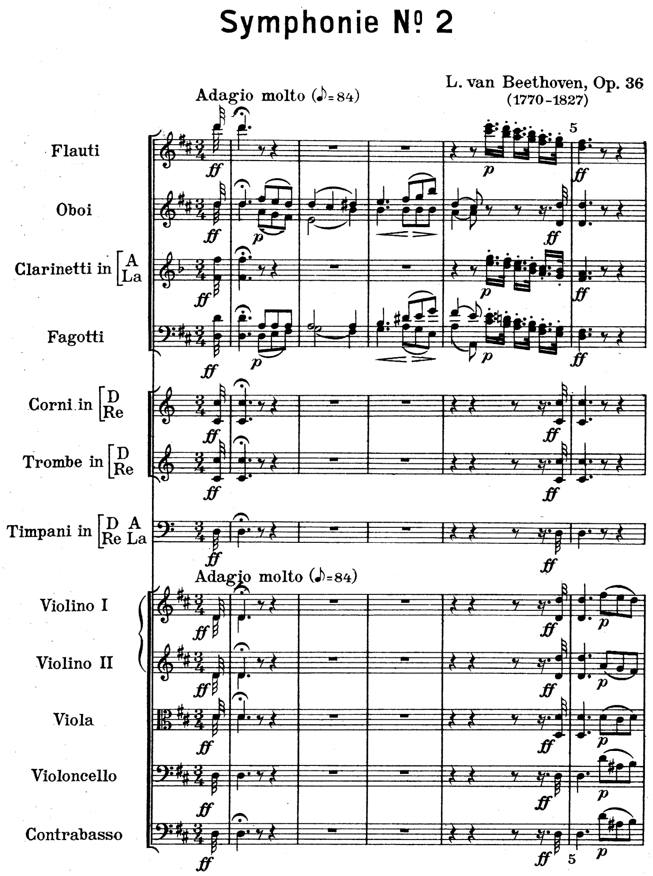
2

Invariant properties of chaos

2.1 Chaos: Irregular non-periodic dynamics

This chapter will briefly introduce a number of concepts in the theory of chaotic dynamics which are applied in the experimental, and theoretical work described in subsequent chapters.

Irregular behaviour is very common in physical systems and for centuries the philosophy used in attempting to understand such systems was based on oversimplified linear methods. This effectively assumes a system can be decomposed into a set of independent periodic harmonic oscillators, or modes. The complexity of the dynamics could be increased by adding more modes to the system. To describe turbulence or chaos by this approach would require an infinite number of modes. The dynamics can be represented by a set of differential equations

$$\dot{x} = F_\mu(x(t)) \tag{2.1}$$

where x is a vector, and μ is a parameter which can change the complexity of the dynamics from low to high as μ is increased. In particular there may be a critical value of $\mu = \mu_c$ where the dynamical behaviour asymptotes to a new regime which fills a different region of space and is known as an attractor. The attractor is embedded in phase space which is space spanned by the system variables. The point μ_c is called a bifurcation point if there is an abrupt change in dynamics as μ changes from $\mu_c - \epsilon$ to $\mu_c + \epsilon$ for small ϵ. The equations of motion may sometimes be solved analytically but if the system is in a non–equilibrium or irregular state, analytic methods fail because they tend to assume periodic oscillatory solutions. Oscillatory solutions can be used to solve the differential equation in principle, but non–periodic solutions would require an infinite Fourier sum which makes the analytic method intractable. If a system *is* actually made up of an infinite number of modes then we are stuck with the infinite Fourier series. However for a large class of non–equilibrium systems this is not the case as they tend to contain a low number of modes which interact in a nonlinear way generating complicated dynamics. It is clear from these types of systems that the number of modes has very little to do with the complexity of the dynamics. It is therefore necessary to give up the old philosophy that understanding individual trajectories leads to an understanding of the system, and correlating complexity with number of independent modes, to the newer philosophy which is more statistical in nature, where the global dynamics is more important than individual trajectories. This leads to new concepts such as the *dimension* of a system, or the number of non–negative *eigenvalues* contained in a system, as will be discussed in detail.

2.2 Characterisation of chaos

As mentioned previously, an attractor is the subspace which all trajectories follow after some initial transients (which are just the paths traced out in phase space during time evolution each with a different initial condition). The attractor is invariant under the flow $F(x)$ given $\dot{x} = F(x)$, which means the attractor doesn't change if time evolves forwards or backwards, for almost every initial condition on the attractor. That is, the remaining points can be covered by cubes of arbitrarily small volume thus have zero measure. The easiest way to distinguish between periodic and non–periodic behaviour is by applying the Fourier transform to one of the variables of the system. The spectrum of a periodic signal is a sequence of δ functions, the first being the fundamental frequency, and the remainder are the integer multiples. A quasi–periodic signal would possess the same spectrum as above with an additional set of δ functions that are linear combinations of the original frequencies. It is more difficult to distinguish between quasi–periodic with a large number of modes and a chaotic signal. Quasiperiodic systems with a large number of modes are less common as the modes would have to be very weakly coupled. If the coupling is too strong then chaotic dynamics evolves rather than quasi–periodic [50]. The chaos spectrum appears as broadened peaks with a broad background. This would appear to have an infinite number of modes and therefore an infinite dimension. Although the Fourier transform cannot distinguish between infinite dimensional and chaotic dynamics of finite dimension, it is a useful guide to the nature of the dynamics of a system. Since a chaotic system is aperiodic, the chaotic attractor cannot have any two trajectories intersecting. This is the reason why a system must have a least three degrees of freedom to allow chaos to emerge. A two dimensional system can be made chaotic if one parameter is made time dependent, where time itself effectively becomes the third degree of freedom. This is known as *non–autonomous chaos.* If no modulation is required to generate chaos, then that system possesses at least three degrees of freedom and produces *autonomous chaos.* Both types of chaos will have chaotic attractors with the property that there are an infinite number of unstable periodic orbits contained in the attractor [51]. This leads to stretching and folding of trajectories in phase space depending on whether a trajectory is near an unstable point, and a stable point respectively. Although there are unstable points, there must be enough stable points so that the chaotic attractor is attracting, otherwise trajectories would just eventually escape to some other subspace. The combination of the boundedness of the attractor, and the fact that no two trajectories can intersect results in the attractor possessing infinitely fine fractal structure.

2.2.1 Statistical analysis–Ergodic theory

To investigate the effects of different perturbations applied to a chaotic system some measures are required which can quantify the perturbed system. One way to analyse the dynamics is to examine individual trajectories. This can be very difficult to do in a chaotic system since they may not initially begin on the chaotic attractor, and hence will correspond to transient dynamics. Once the trajectories have evolved onto the attractor then there still remains the problem that a particular initial condition may evolve and be restricted to a subspace of the chaotic attractor for a long time before the remaining attractor is visited. This will lead to misleading conclusions about the nature of the dynamics. This can be minimised if "typical" conditions are chosen, but these are often not known *a priori.*

To simplify the analysis of dynamics and minimise the above problems, it is better to shift the emphasis to invariant measures which only consider long term dynamics. A given probability measure ρ is invariant under the map $x_t = f^t(x)$ if it is time independent

$$\rho[f^t(E)] = \rho(E) \tag{2.2}$$

where E is a subspace that contains x. ρ is *ergodic* if for every continuous function ϕ the time average is equal to the space average

$$\lim_{T\to\infty} \frac{1}{T} \int_0^T \phi[f^t x(0)]dt = \int \rho dx \phi(x) \tag{2.3}$$

for almost all initial conditions $x(0)$ on the attractor. If ρ cannot be decomposed into two smaller measures $\rho \neq \rho_1 + \rho_2$, then again it is ergodic. An attractor contains an uncountable number of distinct ergodic measures. Not all these measures are physical such as an unstable fixed point. (This is all summarised in Eckmann [51]). This cannot be measured in the presence of unavoidable noise which occurs in physical systems. Mathematically, a measure is physical if a system $\dot{x} = F(x)$ has the same measure as $\dot{x} = F(x) + \epsilon$ as $\epsilon \to 0$, and the *natural measure*, defined in the next section, is an example of a physical measure.

2.2.2 Natural measure

An attractor has many unstable periodic orbits which fill certain regions of phase space. The density distribution of these orbits is invariant as $t \to \infty$. but is generally far from uniform in space. To calculate this measure the attractor must be covered with a grid of cubes of length ϵ_i. A random initial condition x_0 evolving for a time T will spend a fraction of this time t_i inside the ith cube which can be written as $t_i = f(x_0, T, \epsilon_i)$. As T increases the fraction of time a trajectory spends in the ith cube approaches a constant and is equal to the *natural measure* which is given by

$$\mu_i = \lim_{T\to\infty} \frac{f(x_0, T, \epsilon_i)}{T} \tag{2.4}$$

Two intuitive examples of the natural measure for a system containing a stable fixed point, and a system containing a periodic orbit will make this clear. A system with a fixed point p has a simple ergodic probability measure $\rho = \delta_p$ since all points end up at the fixed point as $t \to \infty$. For a periodic state the periodic orbit can be considered as an extension of the fixed point, and hence defined as a continuous set of delta functions $\Gamma = \{\delta_{f^t a} : 0 \leq t < T\}$. The ergodic measure is

$$\rho = \delta_\Gamma = \frac{1}{T}\int_0^T dt\delta_{f^t a} \tag{2.5}$$

For each bifurcation parameter μ in equation 2.1 there may be α attractors A^μ_α, each one having at least one physical measure ρ^μ_α. The presence of bifurcations has broken the continuity of relationships between μ, ρ^μ_α and the stability properties (eigenvalues λ_i). However there may be continuous relations between the bifurcation parameter μ, and the associated physical measures ρ^μ_α when the parameter μ is restricted to lying only in between two bifurcation points. For example, in Chapter 5 it is shown that the period 1 pulsation in the ammonia laser increases in amplitude monotonically with pump power from the period 1 threshold to the chaos threshold. Basic structural information about a particular chaotic attractor under investigation is required, so that an estimate of an appropriate perturbation can be made. A similar invariant to the natural measure is considered here, and is known as a *recurrence plot* [52], which emphasises the unstable periodic orbits that exist in a chaotic attractor. For example, the Euclidean distance is calculated between two points separated by time τ in the five dimensional phase space for the complex Lorenz equations discussed in detail in Chapter 3. If the distance is less than a tolerance chosen to be 0.2 then a count is registered at the time separation bin τ. This condition is tested for each of the 100 million points lying on the chaotic attractor of the complex Lorenz equations, and the bin is incremented appropriately. The result is shown in figure 2.1 which shows sharp peaks approximately at multiples of the fundamental pulsation period which is calculated from the average pulsation period of the time trace to be 3.08 time units. The first peak in the histogram is at 2.666 time units which is consistent

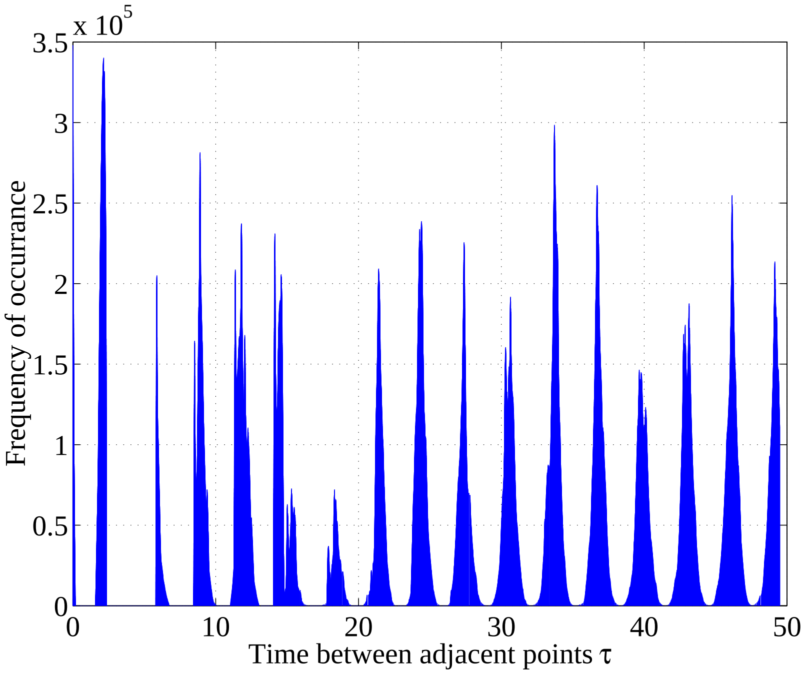

FIGURE 2.1: Frequency of occurrence for orbits of length τ where the end points of the orbits in phase space are within a distance of 0.2 (Arb. units). The first peak is at time $\tau = 2.666$. See text for details.

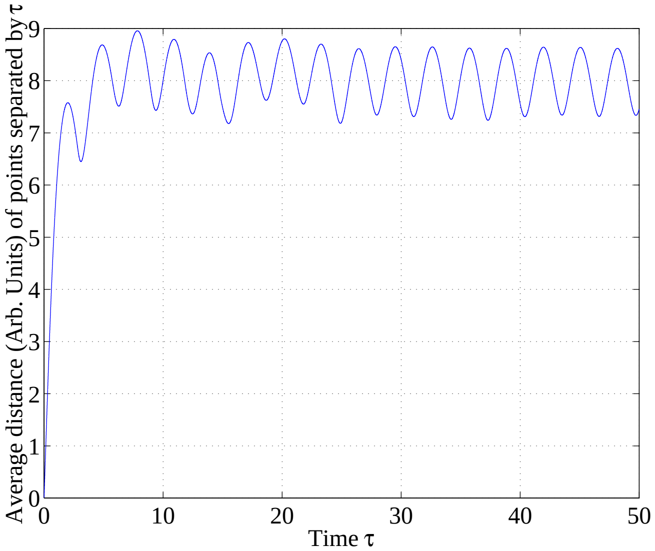

FIGURE 2.2: Distance of points separated by time τ averaged over the whole attractor. The first minimum corresponds to $\tau = 3.0955$.

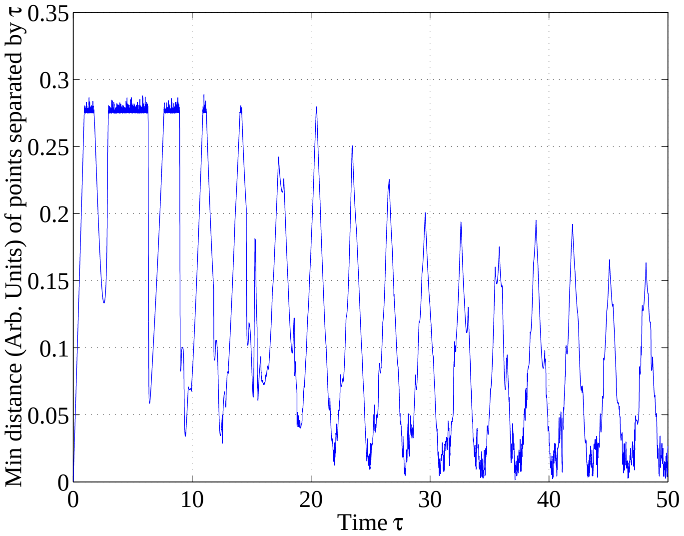

FIGURE 2.3: Distances are calculated for points separated by time τ for all points on the chaotic attractor, and the minimum distance is calculated, and plotted as a function of τ

with the results in Chapters 5, and 6 where a modulation was applied to the chaotic system at a higher frequency than the average pulsation frequency of the system. The recurrence plot is a good indication of the periods of the unstable periodic orbits in the chaotic system, and as will be seen is useful information to determine the modulation frequency required in a non-feedback control method, or the delay required for a feedback control method. The general trend of the histogram did not depend critically on the distance tolerance, although if the tolerance was set too low then a number of the peaks would vanish, and if the tolerance was set too high then the sharp peaks in figure 2.1 would be completely broadened. Two other methods of finding the periods of the unstable orbits were used. The first involved calculating the distance between two points separated by time τ, and averaged this over 100 million points of the chaotic attractor. This is shown in figure 2.2. Since the distance is averaged over the attractor the minima occur very close to multiples of the average pulsation period (the value for the first minima in figure 2.2 is 3.0955). The second method involves searching for orbits of period τ over the attractor as in the previous method except that only the minimum distance is recorded rather than the average for each time τ. The result is shown in figure 2.3. An orbit which has the smallest distance after time τ is likely to be an orbit which is almost closed suggesting that it is very close to the corresponding unstable periodic orbit. The value of the first minimum is 2.588 time units which is close to the histogram result. Hence both these numbers can be used as a starting point for a particular control experiment. These two methods of finding the periods of the unstable orbits do not rely on estimating an appropriate tolerance as was required in figure 2.1 so are easier to calculate.

2.2.3 Lyapunov exponents and dimension

Finding the invariant measures of a system is useful as it gives information about the long term dynamics. But it does not give any indication about the magnitude of stability of the long term dynamics. If searching for simple dynamics such as a controlled state is desired, then a measure of stability is required to indicate the existence of the simple dynamics, or a controlled state. A simple way to quantify stability in a system is to calculate the stability of the fixed points which are invariant measures. A point displaced by ϵ from a fixed point will be exponentially attracted or repelled to the fixed point if ϵ is small enough so that equation 2.1 can be expanded as a Taylor series where the terms higher than first order are insignificant. The expansion or contraction rate is the Lyapunov exponent.

The first order approximation restricts the use of the Lyapunov exponents of fixed points to be only an indication of how trajectories may appear in phase space. It is more useful to have a rate of expansion and contraction which is averaged over the whole attractor. This quantity is known as the global Lyapunov exponent, and there is one representing the stability along each dimension of a system. They can be calculated using the multiplicative ergodic theorem of Oseledec [53] In a dynamical system of the form $x_t = f^t(x)$, ρ is a probability measure contained in a subspace M and $f = M \rightarrow M$ preserves the measure. Then define the matrix of partial derivatives, or Jacobian as

$$T^t_{x\ i,j} = \frac{\partial f^t_i}{\partial x_j} \tag{2.6}$$

If ρ is ergodic (and compact) then for almost all x with respect to the measure ρ the limits exits

$$\lim_{t\rightarrow\infty}(T^{t*}_{x\ i,j} T^t_{x\ i,j})^{\frac{1}{2t}} = \Lambda_x \tag{2.7}$$

$$\lim_{t\rightarrow\infty}\frac{1}{t}\log||T^t u|| = \lambda^i \tag{2.8}$$

where $\lambda^{(1)} \geq \lambda^{(2)} \geq \ldots \lambda^{(n)}$ are the eigenvalues of Λ_x and u is the associated eigenvector. This is generally calculated numerically, but rounding errors can grow significantly if there are very small numbers present in the matrix Λ_x. Hence the Lyapunov exponents are calculated here using the differential equations.

Calculation of Lyapunov exponents from differential equations

The simplest way to determine the average expansion and contraction rates is to have a set of initial conditions which are infinitesimally close to each other and allow them to evolve. The problem with this method is that these points must be relatively close to each other after hundreds of orbits so that linear theory is still valid at these distances. A computer with hundreds of bits precision is required for this procedure and is currently not available. This problem can be avoided by using the phase space plus tangent space technique developed by Bennetin *et al.* [54], and is the preferred method used here. An initial condition x_0 lying on the chaotic attractor is evolved by the equations of motion creating a trajectory in phase space which is called the *fiducial trajectory*.

An infinitesimal sphere is constructed so that x_0 is at the center. Points which lie on this sphere are evolved by the action of the linearised equations of motion, while x_0 is evolved using the nonlinear equations of motion to give x. An orthonormal frame is defined at x_0 and is evolved by the linearised equations of motion. The principal axis tends to diverge, and each vector tends to align to the direction of most rapid growth so they will eventually become indistinguishable. These problems are avoided if a repeated use of the Gram–Schmidt reorthonormalisation procedure is applied to the basis vectors. Let the initial set of basis vectors be $\{e_1, \ldots, e_n\}$ which is acted upon by the linearised equations of motion to give $\{v_1, \ldots, v_n\}$. Since each of these tries to align itself along the λ_1 direction, and the Gram–Schmidt procedure is orientation preserving then the initial labeling of the vectors can be arbitrary. These vectors are

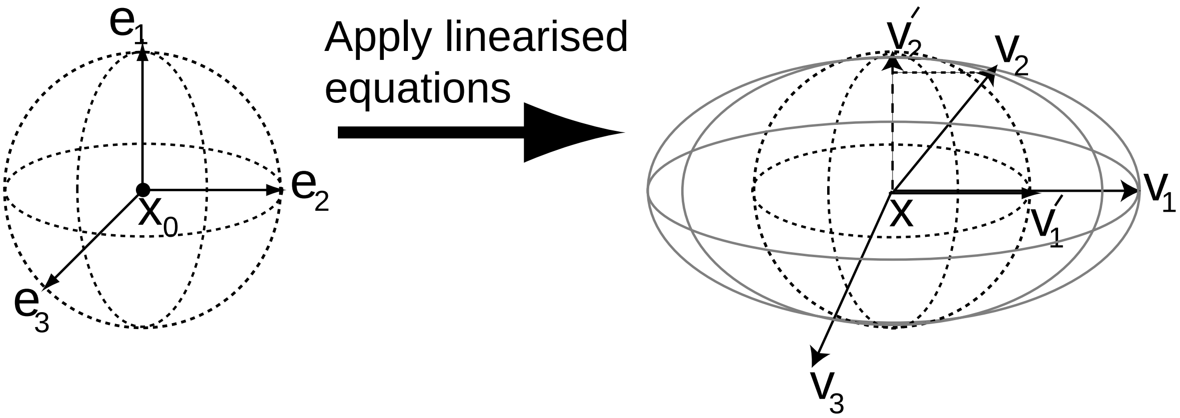

Figure 2.4: Evolution of an infinitesimal sphere around x_0 by the action of the linearised equations of motion while x_0 is evolved using the non linear equations of motion. The sphere becomes distorted into an ellipse due to the non equal Lyapunov exponents along each axis. v_1 becomes renormalised to $v\prime_1$. Only the component of v_2 orthogonal to $v\prime_1$ is taken and renormalised to give $v\prime_2$ using the Gram–Schmidt reorthonormalisation procedure.

renormalised to give $\{v\prime_1, \ldots, v\prime_n\}$

$$\begin{aligned} v\prime_1 &= \frac{v_1}{||v_1||}, \\ v\prime_2 &= \frac{v_2 - \langle v_2, v\prime_1 \rangle v\prime_1}{||v_2 - \langle v_2, v\prime_1 \rangle v\prime_1||}, \\ &\ldots \\ v\prime_n &= \frac{v_n - \langle v_n, v\prime_{n-1} \rangle v\prime_{n-1} - \cdots - \langle v_n, v\prime_1 \rangle v\prime_1}{||v_n - \langle v_n, v\prime_{n-1} \rangle v\prime_{n-1} - \cdots - \langle v_n, v\prime_1 \rangle v\prime_1||}, \end{aligned} \tag{2.9}$$

where $\langle\ ,\ \rangle$ is the inner product. The frequency of renormalisation is not critical as long as the magnitude and direction of the vectors do not exceed computer limitations, and typically is performed once per orbit of the dynamical system. The direction of the first vector remains unchanged by the renormalisation procedure and is free to align itself along the most rapidly growing direction as shown in figure 2.4. The second vector $v\prime_2$ is not free to seek the most rapidly or second most rapidly growing direction. This is because $v\prime_2$ is constructed by removing any $v\prime_1$ component present so that it is orthogonal to it. This "rotation" is due to the action of the Gram–Schmidt procedure rather than the action of the linearised equations of motion which is graphically shown in figure 2.4. The two dimensional subspace spanned by the original vectors v_1 and v_2 has its orientation preserved since the new vectors $v\prime_1$ and $v\prime_2$ span this same space. It is the two dimensional subspace that is most rapidly growing, and has area proportional to $e^{(\lambda_1+\lambda_2)t}$. λ_2 can be obtained from the mean growth rate of the projection of v_2 on $v\prime_2$. Projection of the k^{th} evolved vector to the updated one produces a correct update of the mean growth rate for the k^{th} largest Lyapunov exponent. The ergodic properties of the attractor allow a large portion of the attractor to be visited so that the Lyapunov exponents are a good representation of the "average" rates of expansion and contraction. Since averages are taken over a long time, the sensitivity of the Lyapunov exponents to initial conditions is diminished and the exponents can be considered invariant and classed as a statistical quantity. This is the procedure used to obtain Lyapunov exponents discussed in Chapter 6, and 7.

2.2.4 Fractal dimension

Another measure which is useful in characterising control is the fractal dimension of the attractor. Chaotic dynamics has a non integer dimension, and regular dynamics has an integer dimension as will become apparent shortly.

The Lyapunov exponents can not only indicate the dimension of the system, but can be used to calculate the fractal dimension of the system if the global Lyapunov exponents are used. This is known as the Kaplan-Yorke conjecture [55]. The Lyapunov dimension is

$$D_L = K + \frac{\sum_{a=1}^{K} \lambda_a}{|\lambda_{K+1}|} \tag{2.10}$$

where the eigenvalues are ordered from largest (positive) to smallest, and K is chosen such that $\sum_{a=1}^{K} \lambda_a > 0$, and $\sum_{a=1}^{K+1} \lambda_a < 0$. The eigenvalues here are the global Lyapunov exponents of the system. If all the exponents are negative then the attractor is zero dimensional. One would intuitively expect the dimension to increase as the number of positive eigenvalues increases as more phase space is allowed to be filled. More specifically, for each additional positive Lyapunov exponent λ_a which is greater than the magnitude of the smallest negative exponent, the Lyapunov dimension increases by approximately one.

There are other ways to calculate the fractal dimension which involve the distribution of "points" in phase space. The term "points" is used here since even if the system is a flow i.e. a differential equation and therefore continuous, time must be discretised in any numerical integration routine or experiment. Let the time series of variable x be $y(k)$ where $k = 1 \ldots N$. Then we can take the natural measure $\rho(x)$ to be

$$\rho(x) = \frac{1}{N} \sum_{k=1}^{N} \delta^d(x - y(k)) \tag{2.11}$$

So that the fraction of points in $\Re^d$ within a volume V in phase space is

$$\int_V d^d x \rho(x) \tag{2.12}$$

This measure is robust to noise and thus qualifies as a *physical measure* as defined in section 2.2.1, and will be used to calculate the dimension of a system.

One of the most physically intuitive ways to measure the dimension of a system is to observe how the number of points in phase space lying within a radius scales as the radius approaches zero, given that the volume of radius r in dimension d will scale as r^d. Hence at a particular location x with a small radius r, we expect the number of points $n(x, r)$ within this sphere to scale as

$$n(x, r) \approx r^{d(x)} \tag{2.13}$$

where $d(x)$ is the dimension at x. If the attractor is bounded by R_a then r should satisfy $|\frac{r}{R_a}| \ll 1$. A regular object has an integer dimension which remains unchanged at all positions in the object using equation 2.13, but this uniformity of dimension within an object is not guaranteed for complex structures such as an attractor. In the same way the Lyapunov exponents are averaged over the trajectories to create invariant global exponents, a similar method is used to create an invariant dimension. The number of points within radius r can be expressed as

$$n(x,r) = \frac{1}{N}\sum_{k=1}^{N} H(r - |y(k) - x|) \tag{2.14}$$

where $y = (x_1, x_2, \ldots, x_n)$ and x belongs to this set, and H is the Heavyside function

$$H(p) = \left\{ \begin{array}{ccc} 1 & \text{if} & p > 1 \\ 0 & \text{if} & p < 0 \end{array} \right\} \tag{2.15}$$

The density of points on the attractor $\rho(x)$ will be non-uniform in general, so more information about the system can be extracted by looking at the moments of the function $n(x,r)$.

We can generalise 2.14 so that different aspects of the distribution can be obtained, and define the correlation function [56, 57] to be

$$\begin{aligned} C(q,r) &= \int d^d\rho(x)n(x,r)^{(q-1)} && (2.16) \\ &= \frac{1}{M}\sum_{k=1}^{M}\left[\frac{1}{K}\sum_{n=1}^{K} H(r - |y(n) - y(k)|)\right]^{(q-1)} && (2.17) \end{aligned}$$

in the limit of small r (but not taking it completely to zero otherwise there would be no points inside this volume at every location due to discrete data). The fractal dimension D_q is defined in the limit that r is small to be

$$C(q,r) \approx r^{(q-1)D_q} \tag{2.18}$$

If this limit exists it is conveniently expressed as

$$D_q = \lim_{r \to small} \frac{\log[C(q,r)]}{(q-1)\log[r]} \tag{2.19}$$

This should be computed for a range of r so that a good estimate of the log–log slope can be made.

The simplest dimension to calculate is the box counting dimension where $q = 0$.

$$D_0 = \lim_{r \to small} \frac{\log N(r)}{\log \frac{1}{r}} \tag{2.20}$$

N is the number of spheres ("boxes") of radius r required to cover the data set so that

$$N(r) \approx r^{-D_0} \tag{2.21}$$

As was mentioned earlier, the dimension can be calculated by observing how the number of points within a radius r scales with r using equation 2.13. This is the $q = 2$ case in the correlation equation 2.16 and is the most widely used method for calculating the fractal dimension. The $q = 1$ case is known as the information dimension D_1 and has been associated with the Lyapunov dimension D_L [55].

The correlation equation 2.16 for $C(q,r)$ was constructed so that various moments of the distribution could be considered. The attractor has a non–uniform density in general, and it can have "hot spots" and "cold spots" where the trajectories in phase space visit much more regularly than normal, and visit rarely, respectively. These regions can be interwoven in a complex way, so that the attractor could be said to be *multifractal*. The correlation function can bring out these features depending on the value of q used. For $q > 1$ the contribution of the higher probabilities in the sum become more important even though there may be fewer boxes of these probabilities than normal. This therefore gives information about the existence of "hot spots". Similarly for $q < 1$ the contribution is skewed in favour of the boxes with low probability indicating the presence of "cold spots". The dimension of a system very close to or at the unstable fixed point can have a significantly different value to the average dimension calculated for a range of typical values. This was shown to occur in the Henon map where the dimension was calculated using the information dimension ($q = 2$) at the saddle point and at a very small distance from the saddle point. The dimensions calculated were 1.36 and 1.21 [58]. An expression was found by these authors for the dimension at a saddle point. This was constructed for a map $x_{n+1} = F(x_n)$ which has a saddle point at p having a unstable and stable eigenvalues $\lambda_{1j} > 1$, and $\lambda_{2j} > 1$ respectively. The dimension is

$$D_p(x) = 1 - \frac{\log \lambda_{1j}}{\log \lambda_{2j}} \tag{2.22}$$

The value for the dimension averaged over 20 random initial conditions was 1.27 ± 0.01 which actually agreed well with the dimension calculated from the Lyapunov exponents $D_L = 1.26$. These results show that one should know roughly where the fixed points are in phase space if a good estimate of ρ is to be made. Since an infinite time series is not attainable, we want to make sure for a given finite time series that the system is not spending too much time in the extremities, which would be the hot and cold spots, and the fixed points. We should at least be aware that the system could happen to be in these regions for a significant fraction of the finite sampled time, so a skewed probability distribution will be measured altering the true value for the dimension and other invariant quantities. If the initial conditions can be accessed, then it is desirable to choose them far from the fixed points, and not near the hot and cold spots. Locating the fixed points is relatively easy, however the hot and cold spots are more difficult to locate since they can be interwoven in a fractal way.

Using chaos to generate new initial conditions in the ammonia laser

In the experiments described in this thesis the chaotic system used was an autonomous ring laser. The initial conditions here could not be controlled so I had to rely on the random fluctuations of the system to produce a random initial condition. The fact that these initial conditions were random meant that there was no particular preference given to hot and cold spots or the fixed points. In fact it is almost certain that the initial conditions produced did not lie on the chaotic attractor, since there was always transient dynamics before it was replaced by chaos. It is possible in principle to control the initial conditions of the laser by injecting a second field of known amplitude into the laser. The problem is that there are quantum and thermal fluctuations associated with both the ring laser and the external laser giving rise to an uncertainty in the initial conditions for the electric field. The difficulty in measuring the polarisation of the gain material and the inversion meant that I did not attempt to control the initial conditions other than allowing the laser to evolve for a period of time T_0 before performing an experiment. The initial conditions at T_0 are almost certainly on the chaotic attractor (due to the extremely high dissipation in the Lorenz–like system discussed in chapter 3), and can be made to be far from the fixed points for a suitable choice of T_0.

2.2.5 Entropy

A chaotic system has sensitive dependence to initial conditions. Two nearby points in phase space which are initially unresolvable and are assumed to be the same point, will separate after some time to become distinguishable. By learning about the trajectory we can in principle obtain more information about the initial conditions even if with limited precision. The sensitive dependence of initial conditions has created information. Let W be a bounded region invariant under a map M containing the probability measure ρ, and let W be partitioned into r segments $W_1, W_2, \ldots W_r$. For the partition $\{W_i\}$ the entropy is

$$H\{W_i\} = \sum_{i=1}^{r} \rho(W_i) \ln[W_i]^{-1} \tag{2.23}$$

Each of these partitions is divided into successively smaller ones by the inverse map. The first step is

$$W_j \cup M^{-1}(W_k) \tag{2.24}$$

to give $\{W_i^{(1)}\}$ where j and k are taken from $1, \ldots, r$ and only the non–zero intersections will be used as partitions. These new partitions are subdivided further by operating the map M^{-2} on each of these to give

$$W_j \cup M^{-1}(W_k) \cup M^{-2}(W_l) \tag{2.25}$$

giving $\{W_i^{(2)}\}$ So $\{W_i^{(n)}\}$ is

$$W_{i_1} \cup M^{-1}(W_{I_2}) \cup M^{-2}(W_l) \cdots \cup M^{-n+1}(W_{i_n}) \tag{2.26}$$

Then

$$h(\rho, \{W_i\}) = lim_{n\to\infty} \frac{1}{n} H(\{W_i^{(n)}\}) \tag{2.27}$$

which still depends on the initial partition so this is maximised to give the metric entropy or the Kolmogorov and Sinai entropy which is commonly known as *entropy* [51]

$$h(\rho) = \sup_{W_i} h(\rho, \{W_i\}) \tag{2.28}$$

Consider the baker's map as an example where precision is limited to a two–state measurement "top" or "bottom". If a measurement is made at the start, and the first iterate then this determines which of the four segments the initial condition begun.

By taking two measurements each of resolution $\frac{1}{2}$, information about the position of the initial condition to a resolution of $\frac{1}{4}$ has been achieved. Therefore as the map evolves further, and measurements are taken at each stage, the precision of the initial condition is known to a greater precision hence information is gained as the map ("time") evolves.

The amount of information gained depends on how sensitive the system is to initial conditions and intuitively one would expect the entropy to be related to the positive eigenvalues. This was found to be the case [59]. In fact there is an elegant relation between entropy and the positive eigenvalues:

$$h(\rho) \leq \sum_{\lambda_i > 0} \lambda_i \tag{2.29}$$

The equality holds for Hamiltonian systems [60] but also for axiom A attractors of dissipative systems [59]. Axiom A attractors are hyperbolic and the periodic orbits are dense.

The eigenvalues calculated from the global Lyapunov exponents can be used as an estimate for entropy using equation 2.29. During a controlled state there is no new information created as time evolves so that the entropy is zero, and non zero for non periodic states. This makes entropy a good measure for control.

2.3 Conclusion

The techniques developed using statistical analysis can be used to describe a chaotic system in terms of recurrence plots, Lyapunov exponents, dimension, and entropy. These quantities have the desirable property that there is no explicit time dependence since a time average of some form has been used. This is desirable because transient dynamical behaviour can be ignored as only the long term dynamics is important in terms of controlling a chaotic system. In an experiment there is often not enough data to produce invariant measures so one must reduce themselves to analyse trajectories in phase space. Lacking the luxury of infinite time so only a portion of the attractor can be visited. This limitation can be minimised by using an experimental system with reasonably fast dynamics, and by avoiding regions of phase space which are either "hot spots", "cold spots", or the fixed points of the system. These measures can also be applied to dynamics in the non chaotic regime. In particular, when the aim is to find controlled states, the variations of these measures can point to their location.

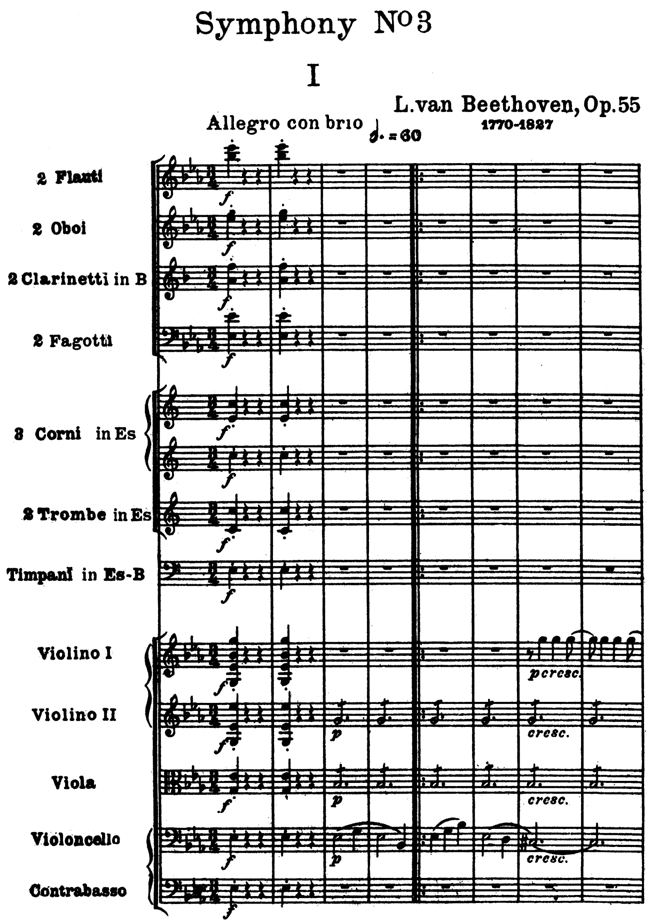

3

The Lorenz equations

In 1963 Edward Lorenz set out to provide a simple model to describe the different types of dynamics occurring in Rayleigh-Bernard convection of a fluid [61]. This system consists of a fluid in a container which has heat applied from below. If the temperature gradient is constant maintaining a constant temperature difference, then there is no motion. If this steady state becomes unstable then there is convection of the fluid. A set of partial differential equations was derived which included information about the acceleration of gravity, coefficient of thermal expansion, viscosity, and the thermal conductivity. Lorenz expanded the velocity and temperature variables into spatial Fourier series and truncated the series to reduce the infinite dimension to a finite one. The result is a set of ordinary non-linear differential equations

$$\begin{aligned}\dot{X} &= -\sigma X + \sigma Y \\ \dot{Y} &= -XZ + rX - Y \\ \dot{Z} &= XY - bZ\end{aligned} \tag{3.1}$$

Where X is proportional to the intensity of the convective motion, Y is proportional to the temperature difference between the ascending and descending currents, and Z is proportional to the distortion of the vertical temperature profile from linearity. The parameter σ is the Prandtl number, r is the ratio of the Rayleigh number R_a to the critical Rayleigh number R_c where convection occurs. The equations are symmetric in X and Y so are unchanged under the transformation $(X,\ Y,\ Z) \rightarrow (-X,\ ,-Y,\ Z)$. An analytic solution of this set of differential equations will not exist in general, so it is useful to investigate the behaviour of the solutions near the fixed points of the system. This can be easily performed by perturbation theory. Given a system $\dot{x} = F(x)$ with a fixed point x_0, the steady state solution infinitessimally close to x_0 is $x(t) = x_0 e^{\lambda t}$ where λ is the associated eigenvalue to the determinant equation

$$|J(F(x)) - \lambda| = 0, \tag{3.2}$$

and J is the Jacobian operator $J^i_{,j}F = \frac{\partial F^i}{\partial x_j}$ i.e. the matrix of partial derivative operators. For the Lorenz system, setting the linearised solutions to be x_0,y_0, and z_0 for variables X, Y, and Z respectively, the linearised equations are

$$\begin{bmatrix} \dot{x}_0 \\ \dot{y}_0 \\ \dot{z}_0 \end{bmatrix} = \begin{bmatrix} -\sigma & \sigma & 0 \\ (r-Z) & -1 & -X \\ Y & X & -b \end{bmatrix} \begin{bmatrix} x_0 \\ y_0 \\ z_0 \end{bmatrix} \tag{3.3}$$

The values (X, Y, Z) are chosen to be steady state. From this it is easy to calculate the divergence

$$\frac{\partial \dot{X}}{\partial X} + \frac{\partial \dot{Y}}{\partial Y} + \frac{\partial \dot{Z}}{\partial Z} = -(\sigma + b + 1) \tag{3.4}$$

Thus the variation of a volume element V_0 in phase space is $\dot{V}_0 = -(\sigma + b + 1)V_0$, and it shrinks to zero as $t \to \infty$. Systems with this property are dissipative. This just means that the volume of phase space tends to zero so that the attractor is flattened and approaches a two dimensional surface. An attractor is a bounded subspace where all initial conditions eventually end up as $t \to \infty$. Identifying attracting sets can give us a clear picture of how trajectories evolve in phase space.

The trivial solution $(X, Y, Z) = (0, 0, 0)$ has a characteristic equation of the matrix 3.2

$$[\lambda + b][\lambda^2 + (\sigma + 1)\lambda + \sigma(1 - r)] = 0 \tag{3.5}$$

For $0 < r < 1$ there are three negative real roots. One is positive when $r > 1$ so that $r = 1$ defines the onset of convection. For $r > 1$ two more fixed points appear at

$$X = Y = \pm\sqrt{b(r-1)}, Z = r - 1 \tag{3.6}$$

The characteristic equation is a cubic

$$\lambda^3 + (\sigma + b + 1)\lambda^2 + (r + \sigma)b\lambda + 2\sigma b(r - 1) = 0 \tag{3.7}$$

This has one real negative root and two complex conjugate roots for $r > 1$. The complex roots are imaginary if

$$r = \frac{\sigma(\sigma + b + 3)}{(\sigma - b - 1)} \tag{3.8}$$

and beyond this the real part becomes positive. If $\sigma < b + 1$ there is no positive value for r so the steady state is stable. If $\sigma > b + 1$ then the steady state becomes unstable for a sufficiently large Rayleigh number. The complex roots indicate the oscillatory nature of the solution, so that a perturbation from the fixed point will lead to oscillations in intensity. The fixed points C1 and C2 exist for $r \geq 1$ and are

$$C1 = (\sqrt{b(r-1)}, \sqrt{b(r-1)}, r - 1) \tag{3.9}$$

$$C2 = (-\sqrt{b(r-1)}, -\sqrt{b(r-1)}, r - 1) \tag{3.10}$$

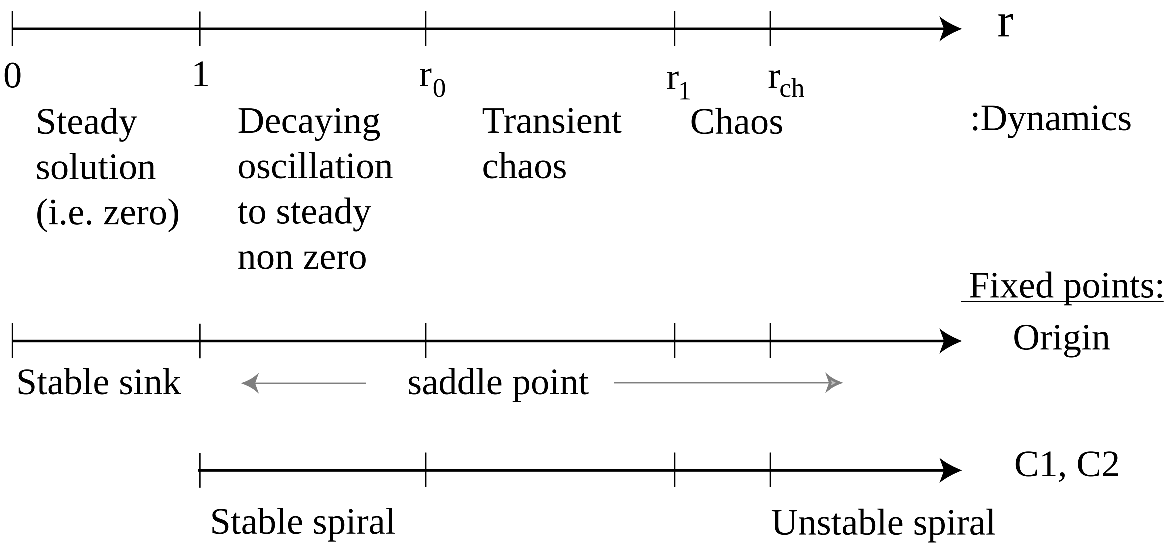

FIGURE 3.1: For the Lorenz system the type of dynamics and the stability of fixed points is shown as a function of r.

A brief summary of the dynamics and the stability of the fixed points which shows the different type of dynamics and the associated stability of the origin, C1, and C2 in between the bifurcation points is given in figure 3.1. To obtain a more intuitive picture of the dynamics that can occur for different values of r, seven schematic plots representing the phase space of the Lorenz system for various values of r are shown in figure 3.2. This now includes information about the stability along the three eigenvectors associated with each fixed point. This helps give a picture of the shape of the attractor traced out by a trajectory in phase space. At $|r| < 1$ there is only one fixed point which is a stable sink shown in figure 3.2a. The symmetry is broken for $1 < r < r_0$ since now there is a creation of two more fixed points, and the origin loses its stability along one of the three orthogonal axes associated with the three eigenvalues. The two remaining stable directions form a stable two dimensional manifold. The newly created fixed points C1 and C2 are stable as shown in 3.2b. Increasing r (3.2c) causes these two fixed points to possess a two dimensional manifold where trajectories spiral in along that plane. These oscillations grow in figure 3.2d until they meet the unstable manifold of the origin and form a closed orbit which includes the origin and encloses the fixed point $C1$. This is known as a homoclinic orbit and has an infinite period. By symmetry there will be another homoclinic orbit enclosing $C2$ as shown in figure 3.2e. Increasing r further breaks the homoclinic orbit but now allows the trajectories to cross the two dimensional stable manifold of the origin as shown in figure 3.2f. Points in phase space moving towards the origin which are within a very small distance ϵ can be expelled either in one direction or the opposite depending if the point is within $+\epsilon$ or $-\epsilon$ of the origin, hence the outcome of a trajectory depends sensitively on the previous position of the trajectory relative to the origin. This apparent chaotic behaviour cannot last since the fixed points C1 and C2 are not unstable, so the trajectory will eventually end up on C1 or C2 which are the attractors. There is a narrow region between r_1 and r_{ch} where a chaotic attractor exists, although the other two stable attractors at C1 and C2 coexist. The system becomes fully chaotic when the fixed points C1 and C2 are unstable as shown in figure 3.2g. The only attractor here is the chaotic attractor.

It is clear that the shape of any of the attractors is going to be relatively thin since there is always a stable manifold at C1 and C2 which has the effect of squashing the trajectories in phase space to a plane - hence the negative divergence calculated previously in equation 3.4. This would indicate that the dimension of the attractor would lie somewhere in between 2 and 3. The exact value depends on the system parameters. One would expect that if the stable manifolds of C1 and C2 are highly attracting then the trajectories in phase space would be rapidly contracted onto a surface thus reducing the dimension of the attractor to be much closer to a dimension of 2 rather than 3. The actual trajectories can be calculated numerically by integrating equation 3.1 for some initial conditions and the solution $X(t)$ is shown in figure

(a) Stable (b) Stable oscillations (c) Larger stable oscillations

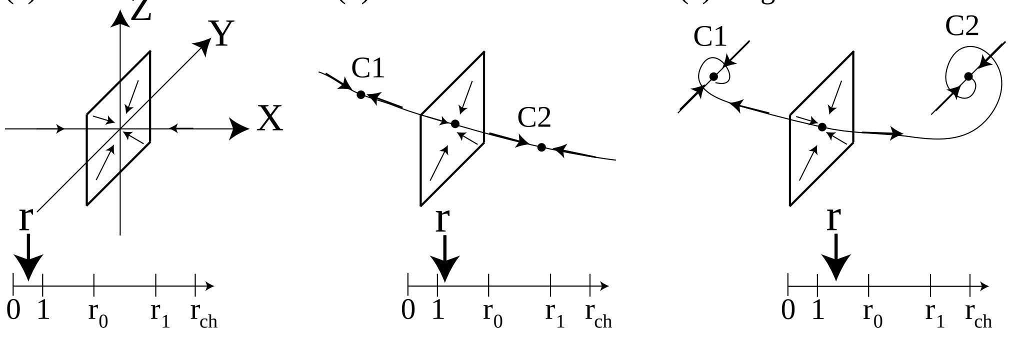

(d) Larger stable oscillations (e) Homoclinic orbit

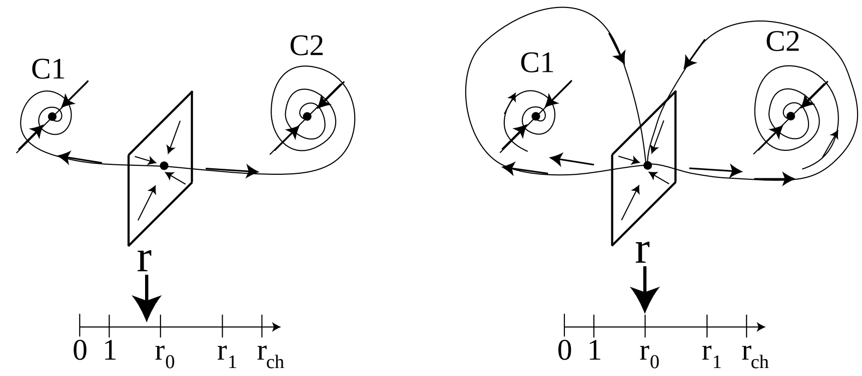

(f) Transient chaos (g) Fully chaotic

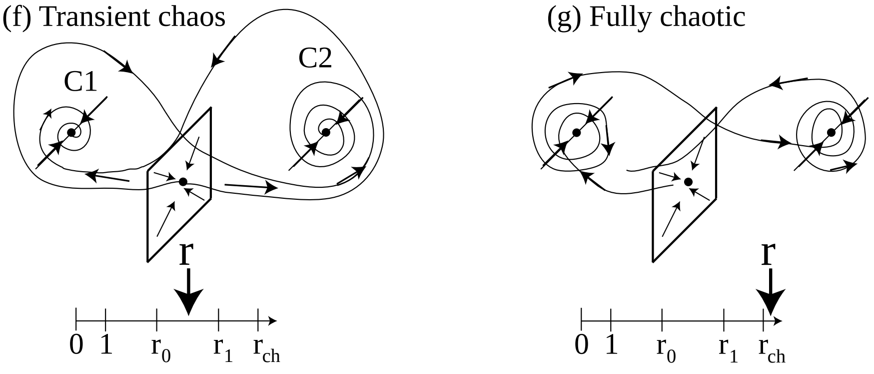

FIGURE 3.2: This shows the stability of the fixed points and an estimate of the trajectories in phase space as r is varied in the Lorenz equations.

3.4c which shows sequences of growing pulsations in the positive and negative direction. The number of pulsations before there is a change in sign of the field appears random. The phase space portrait for the system shows that a growing sequence of pulses corresponds to an outward spiral on one of the leaves in phase space.

3.1 The Lorenz–Haken Laser equations

Instabilities in laser systems have been observed at least since 1964 [62] but their origins were often obscure. Investigating laser instabilities in 1975 led Haken to find an isomorphism between the Maxwell–Bloch laser equations, and the Lorenz equations raising the possibility of explaining at least some laser instabilities in terms of chaotic dynamics. The Maxwell–Bloch laser equations representing the dynamics of a single mode homogeneously broadened two level laser in a ring cavity can be written in the slowly varying envelope approximation as:

$$\begin{aligned} \dot{E} &= \kappa(P - E) - c\frac{\partial E}{\partial x} && (3.11) \\ \dot{P} &= \gamma_{\perp}(ED - P) && (3.12) \\ \dot{D} &= \gamma_{\|}(\lambda + 1 - D - \lambda EP) && (3.13) \end{aligned}$$

where E is the electric field, P is the polarisation of the gain material, and D is the population inversion of the two level atoms. These parameters have associated decay rates κ, $\gamma_{\perp}$, and $\gamma_{\|}$ respectively. The pump $\lambda = (D_0 - D_c)/D_c$ where the unsaturated population inversion is D_0 and the critical inversion is D_c which is the value of the population inversion at the lasing threshold . For isomorphism between these laser equations and the Lorenz equations, there must be zero divergence of the electric field which appears in equation 3.11. This is easily satisfied by a slowly varying travelling plane wave electric field. The equations 3.11–3.13 will become the Lorenz equations 3.1 if the following parameters are transformed

$$\begin{gathered} t \to \frac{\tau\sigma}{\kappa}, \qquad (3.14) \\ E \to \sqrt{\beta(r-1)}X, \quad P \to \sqrt{\beta(r-1)}Y, \quad D \to \sqrt{\beta(r-1)}Z, \\ \gamma_{\perp} \to \frac{\kappa}{\sigma}, \quad \gamma_{\|} = \frac{\kappa\beta}{\sigma}, \quad \lambda \to (r-1). \end{gathered}$$

The laser equations 3.11–3.13 assume that the laser oscillation frequency, the atomic resonance, and the empty cavity resonance all have the same frequency. This is a condition which is not always easily met experimentally. The restriction can be removed by re-deriving the laser equations in a more general way so that the effect of detuning the cavity from the atomic resonance can be included, as is shown in Appendix B.

$$\begin{aligned}\dot{E} &= -\kappa((1+i\delta)E-\lambda P) && (3.15)\\ \dot{P} &= -\kappa/\sigma((1-i\delta)P-ED) && (3.16)\\ \dot{D} &= \kappa\beta/\sigma(1-D-1/2(E^{\star}P+P^{\star}E)), && (3.17)\end{aligned}$$

$$\sigma=\kappa/\gamma_{\perp} \quad \beta=\gamma_{\|}/\gamma_{\perp}$$

where E, P are now complex fields, and D is a scalar, δ is the detuning of the cavity resonance relative to the atomic line center. In steady state

$$\delta=\omega_c-\omega_a \tag{3.18}$$

where the empty cavity frequency is ω_c. The transition frequency of the lasing atoms is ω_a and has an associated line width $\Delta\omega_a$, which is inversely proportional to $\gamma_{\perp}$. The laser frequency is pulled between the empty cavity and the atomic transition frequency, so that

$$\begin{aligned}\omega_l &= \frac{\frac{\omega_c}{\kappa}+\frac{\omega_a}{\Delta\omega_a}}{\frac{\Delta\omega_a+\kappa}{\kappa\Delta\omega_a}}, \quad \text{or} && (3.19)\\ \omega_l &= \omega_c+\kappa\delta, \quad \text{or} && (3.20)\\ \omega_l &= \omega_a-\Delta\omega_a\delta. && (3.21)\end{aligned}$$

3.1.1 Dynamics of the complex laser equations

The dynamics of the Lorenz equations were analysed at the start of this chapter to show the bifurcation sequence and the phase portraits for different values of r.

This can be repeated for the laser equations by inverting the transformation 3.14 and setting the detuning δ to zero. The previous graphs 3.1 and 3.2 will now have the pump axis r replaced by λ, and the bifurcation points will be scaled according to the inverse transformation applied to the Lorenz equations so that the subcritical Hopf bifurcation occurs ($r = r_{ch}$) at

$$\lambda_{Hopf} = \frac{\kappa(\kappa + \gamma_{\|} + 3\gamma_{\perp})}{\gamma_{\perp}(\kappa - \gamma_{\|} - \gamma_{\perp})} \tag{3.22}$$

Hence the necessary condition for chaos is that $\kappa > \gamma_{\|} + \gamma_{\perp}$ which corresponds to a laser with a relatively lossy cavity. This relation is therefore known as the bad cavity condition. Many lasers require a low cavity decay rate in order that lasing can occur which makes satisfying the bad cavity condition extremely difficult. This is the reason why chaos was not unambiguously observed in a laser until 1984 [63] where Weiss, and Klische showed that the gain in the far infrared ammonia laser is so high that the bad cavity condition could easily be satisfied. This particular laser has a high gain allowing a lower cavity decay rate, and chaos could be created with a sufficiently large pumping.

Although the bad cavity condition still holds, the situation is now different when $\delta \neq 0$ as the equations become complex . The electric field and polarisation can be written as a sum of real and imaginary components.

$$E = X_1 + iX_2, \quad P = Y_1 + iY_2, \quad D = Z \tag{3.23}$$

Substituting this into the complex laser equations 3.15-3.17 results in a five dimensional system. This means there is a bifurcation at $\delta = 0$ since there is a creation of two new fixed points.

$$\dot{X}_1 = -(X_1 - \delta X_2 - \lambda Y_1 \tag{3.24}$$

$$\dot{X}_2 = -(X_2 + \delta X_1 - \lambda Y_2) \tag{3.25}$$

$$\dot{Y}_1 = -(1/\sigma)(Y_1 + \delta Y_2 - X_1 Z) \tag{3.26}$$

$$\dot{Y}_2 = -(1/\sigma)(Y_2 - \delta Y_1 - X_2 Z) \tag{3.27}$$

$$\dot{Z} = (\beta/\sigma)(1 - Z - (X_1 Y_1 + X_2 Y_2)) \tag{3.28}$$

The dynamics is now more complex since the embedding dimension of the attractor has changed from three (in the non detuned case) to five. In the limit as the detuning tends to zero, the dynamics of the system asymptotes to Lorenz chaos, and as the detuning is increased the route to chaos changes to period doubling [64]. The bifurcation diagram in the parameter regime used in this thesis is shown in figure 3.3. This was calculated by integrating the equations 3.11–3.13 and calculating the periodicity of the intensity time trace. A pattern of pulsations repeating after n cycles is called period n, and is graphically represented as n vertical parallel lines, period zero is a light grey line, and chaos as a wide dark grey line. The range of dynamics shown here is similar to the results of Zeghlache and Mandel [65] even though they used different decay rates. In both cases the period doubling route to chaos doesn't occur until the detuning δ is at least 0.2. As the detuning is increased further the threshold for period 1 at the start of the period doubling sequence also increases. Eventually there will be no chaos for large enough δ. To simplify the graphics, the phase space studied can be reduced to two variables X_1 and X_2 which is enough to gain significant information about the system [66]. Abraham et al. [66] showed that the intensity return map which is a plot of $I(n+1)$ against $I(n)$ where $I(n)$ is the nth intensity peak corresponding to the nth intensity pulsation, still retains a cusp like feature in the detuned case, except that the peak cusp is rounded rather than sharp due to phase modulation. This slightly modified cusp shape changes insignificantly as the detuning is increased. The topology of the detuned system compared to the non detuned one was found to be similar even though the detuned system has the additional feature of alternative routes to chaos. The Lyapunov dimension of the chaotic attractor D_L was found to be 3.05 for the system parameters in figure 3.3 with $\delta = 0.2$ and $\lambda = 46$. This is almost one dimension higher than the non detuned counterpart with $D_L = 2.06$. These parameters are used in all numerical simulations presented in this thesis since they correspond to similar behaviour observed in the laser, and are not varied unless otherwise specified.

3.2 Comparing the Lorenz–Haken model with the ammonia laser

In this thesis the chaotic dynamics in the ammonia laser is explored in terms of examining its behaviour under various external perturbations, and exploring ways to simplify the dynamics. The dynamics is modified by perturbing the structure of phase space, but it is not desired to apply a very large perturbation as this is likely to create a drastically different system which may bear little resemblance to the original system. The properties of this new system may not be described using standard chaos theory such as the structure of a chaotic attractor discussed in the previous chapter. The infinite number of unstable periodic orbits may become finite, severely truncated, or have very complicated stability behaviour within each orbit cycle of the associated unstable periodic orbits as can happen with sinusoidal perturbations [67]. The experimental system can never be equated exactly with the model as there are many assumptions required to make the laser equations isomorphic to the Lorenz equations. The aim is not to make direct comparisons of the experiment with the model, but to compare general properties such as the occurrence of control, and generalised synchronisation which rely on global principles such as the structure of the attractor, and ergodic properties of chaos (see previous chapter for details). If a result in the experimental system is not observed in the Lorenz–Haken model, then it is not obvious how that particular phenomenon could be reproduced in another chaotic system of similar global properties. Why then choose the Lorenz–Haken equations? These equations have been extensively studied [68], and has been applied to fluid dynamics [61]. There has been many detailed comparisons made between the Lorenz equations, and the single mode autonomous ammonia laser [49, 69, 70]. Comparisons were also made between the ammonia laser, the Lorenz equation and more complex models describing the effects of optical pumping on the three level system by Weiss *et al.* [71]. Many qualitative comparisons agree with the general routes of bifurcations to chaos [72], statistical dynamics in the chaotic, and the metastable regime [73], and invariant constants such as the fractal dimension [74]. The parameters used in the model such as the decay rates, are not chosen to correspond exactly with the experiment, but rather an “effective parameter” is chosen such that the *dynamics* of the model correspond well to the experimental observations.

There are some issues which are not explained by the Lorenz model or more complex models, such as the existence of periodic oscillations observed experimentally before the chaos threshold, and the relative position of the first threshold (lasing threshold), and second threshold (chaos) do not quite agree (see Chapter 4). On the whole the relatively large amount of agreement between various statistical quantities, and the laser makes the complex Lorenz–Haken model an obvious choice to make qualitative comparisons between the experimental system, and the numerical simulations, and to access parameters, and variables not experimentally conveniently measurable.

Typical Intensity ($E^* \cdot E$) time traces in the chaotic regime are shown for the case $\delta = 0$ and $\delta = 0.2$ in figure 3.4a and 3.4b. The corresponding fields $X(t)$ and the real component of $X(t)$ are shown in figure 3.4c and 3.4d respectively.

The largest differences between the two systems become apparent when the variable $X(t)$ for the resonant case, and the real component of $X(t)$ for the detuned case is compared. The peaks of $X(t)$ in figure 3.4c are more evenly distributed around the values ± 10 than 3.4d which corresponds to $X_1(t)$ in the five dimensional system. This shows there is a modulation with a period of the order of tens of the average pulsation period of the time trace, which does not appear in the intensity time trace 3.4b. This is because the intensity is a combination of the real and imaginary components of $X(t)$ and is expressed as $I(t) = X_1^2(t) + X_2^2(t)$, and $X_2(t)$ has a similar slow modulation as $X_1(t)$ (not shown) such that the resultant intensity is free from the slow modulation.

The attractor for the Lorenz equations with $\delta = 0$ is shown in figure 3.5. It is similar to the sketches based on linear stability analysis in figure 3.2 indicating this analysis gives a reasonable estimate to the topology of phase space. The attractor for the complex Lorenz equations in figure 3.6 looks similar to the Lorenz attractor except for the presence of slow modulation which shows up as trajectories following a deformed torus in additions to the two spiral structures which look very similar to the non–detuned attractor.. This is also seen in figure 3.7 which shows two projections of the five dimensional system to the real field $X(t)$, imaginary $X(t)$ and $Z(t)$ (left figure), and the real $Y(t)$, imaginary $Y(t)$ and $Z(t)$ respectively (right figure).

3.3 Phase of a chaotic signal

In any control experiment the concept of the phase of a particular variable of a chaotic system needs to be developed, since this instantaneous phase will be compared to the instantaneous phase of an external perturbation, so that existence of control can be established.

The phase is closely related to the displacement $dx(t)$ along the chaotic trajectory [11] where there is a zero expansion rate between two infinitesimal adjacent trajectories at $dx(t)$ (corresponding to a zero Lyapunov exponent [11]). If a chaotic flow has a proper rotation about a reference point then a shift along the trajectory $dx(t)$ can be uniquely mapped to a shift of phase $d\phi(t)$ of the oscillator. Three common methods for calculating phase are firstly, the dynamics can be projected on an x–y plane and the phase can be defined as the angle

$$\phi(t) = \arctan \frac{y(t)}{x(t)}. \tag{3.29}$$

The second method consists of constructing a surface which is one dimension lower than the number of variables of the chaotic system. This surface is known as a Poincare section and is oriented in the variable space, known as phase space, such that the chaotic trajectory crosses this surface once for each orbit. Each successive crossing is associated with a phase increase of 2π, and the instantaneous phase can be calculated by linear interpolation

$$\phi(t) = 2\pi k + 2\pi \frac{t - \tau_k}{\tau_{k+1} - \tau_k} \quad \tau_k < t < \tau_{k+1} \tag{3.30}$$

where the time of the kth crossing of the flow with the Poincare section is τ_k. There may be many different possible orientations of a Poincare section which will all satisfy the restriction of one crossing of a chaotic trajectory for each cycle. In particular there is a Poincare section which corresponds to successive maxima or minima of a scalar chaotic time series. This eliminates the need to reconstruct the dynamics in a higher dimension then finding an appropriate Poincare section if one only has access to a scalar variable, since the peaks of the series of pulsations (or troughs) from the scalar variable is equivalent to an appropriate Poincare section [8]. The third method is the analytical approach introduced by Gabor [75]. The amplitude $A(t)$, and phase $\phi(t)$ of a chaotic signal can be decoupled so that the chaotic signal can be represented as

$$\Phi(t) = s(t) + j\tilde{s}(t) = A(t)e^{j\phi(t)}, \tag{3.31}$$

where $\tilde{s}(t)$ is the Hilbert transform of the observed time series $s(t)$

$$\tilde{s}(t) = \frac{1}{\pi} P.V. \int_{-\infty}^{\infty} \frac{s(\tau)}{t-\tau} d\tau, \tag{3.32}$$

where $P.V.$ represents the Cauchy principal value for the integral.

The three methods of calculating phase of a chaotic signal work equally well if a chaotic flow rotates about a reference point. The phase may not be defined for chaotic oscillators which are far from phase coherent. An example is the Rössler oscillator at a=0.25 [8] where the chaotic trajectory does not cycle the unstable fixed point in all rotations. Since the phase does not increase monotonically in time, no proper Poincare section can be constructed.

In the experiments in this thesis the only accessible variable is the intensity, so to minimise the errors in the Poincare section and phase, the second method of calculating phase involving the peaks of successive intensity maxima is used.

3.4 Conclusion

The similarities between the complex Lorenz model, and the ammonia laser in terms of statistical measures of chaos, and invariant measures like the dimension of the attractors have previously been shown to compare quite well. Therefore this provides enough motivation to use the complex Lorenz model to describe phenomena observed in the ammonia laser. There are experimental difficulties in repeating experiments precisely, and exploring the affects of small parameter changes is limited. This is easy to do numerically, and can give information about appropriate parameter values to explore experimentally. Conversely, the features observed in the experiments can be used to narrow the region of computation in the model, which is at least three dimensions typically, thus reducing computation time by over an order of magnitude.

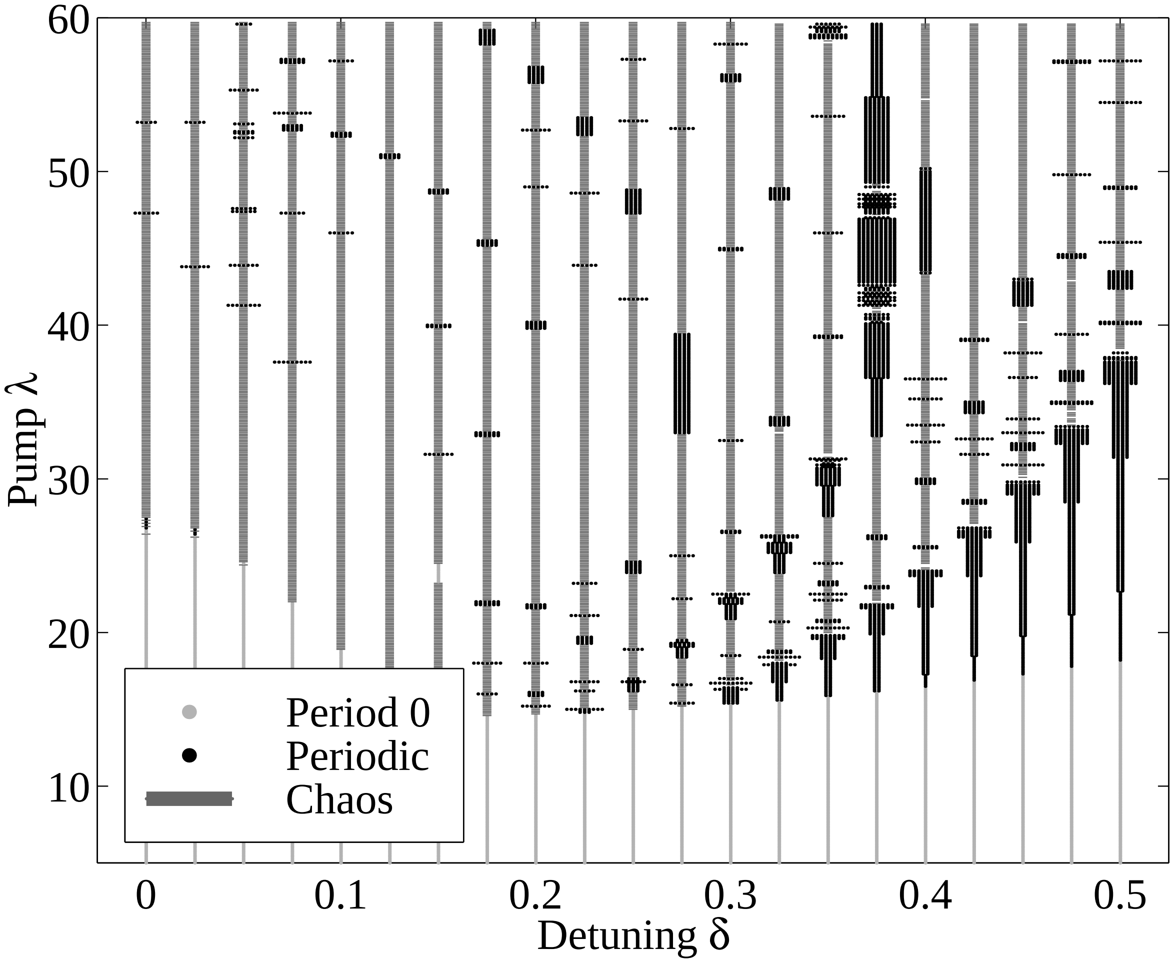

FIGURE 3.3: The bifurcation diagram for the detuned laser equations (complex Lorenz) where λ is the pump and δ is the detuning. The light grey lines represent period zero, the black lines represent periodic behaviour where the value of the period is the number of adjacent parallel black lines for each pair of bifurcation parameters λ and δ, the wide dark grey lines are chaotic behaviour. The parameters used are $\sigma = 1.5$, $\beta = 0.25$, and $\kappa = 1$.

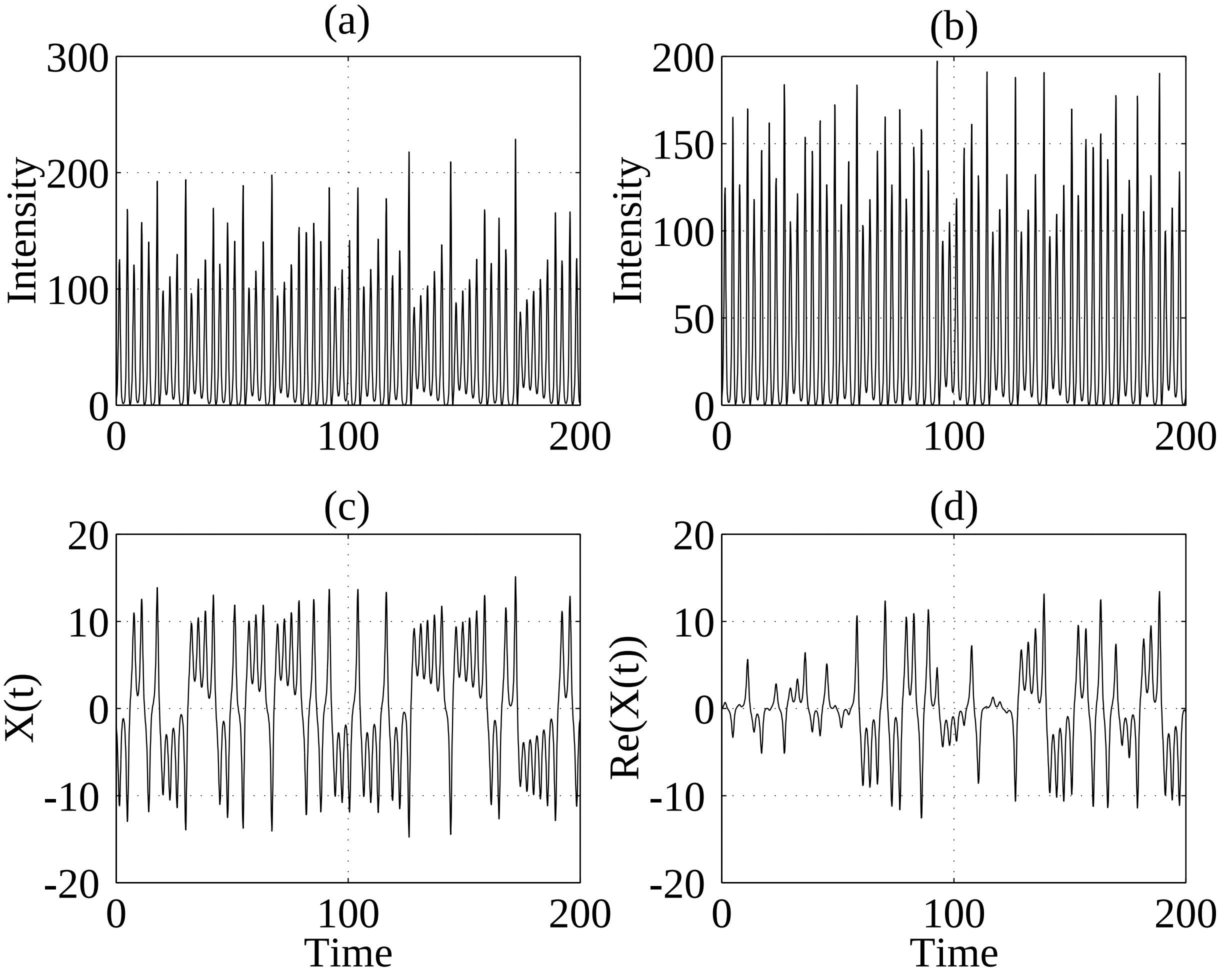

FIGURE 3.4: Two Intensity time traces $(X^*(t) \cdot X(t))$ for the Complex Lorenz system with $\delta = 0$ at (a), and $\delta = 0.2$ (b). The corresponding fields in both cases are shown at (c) and (d).

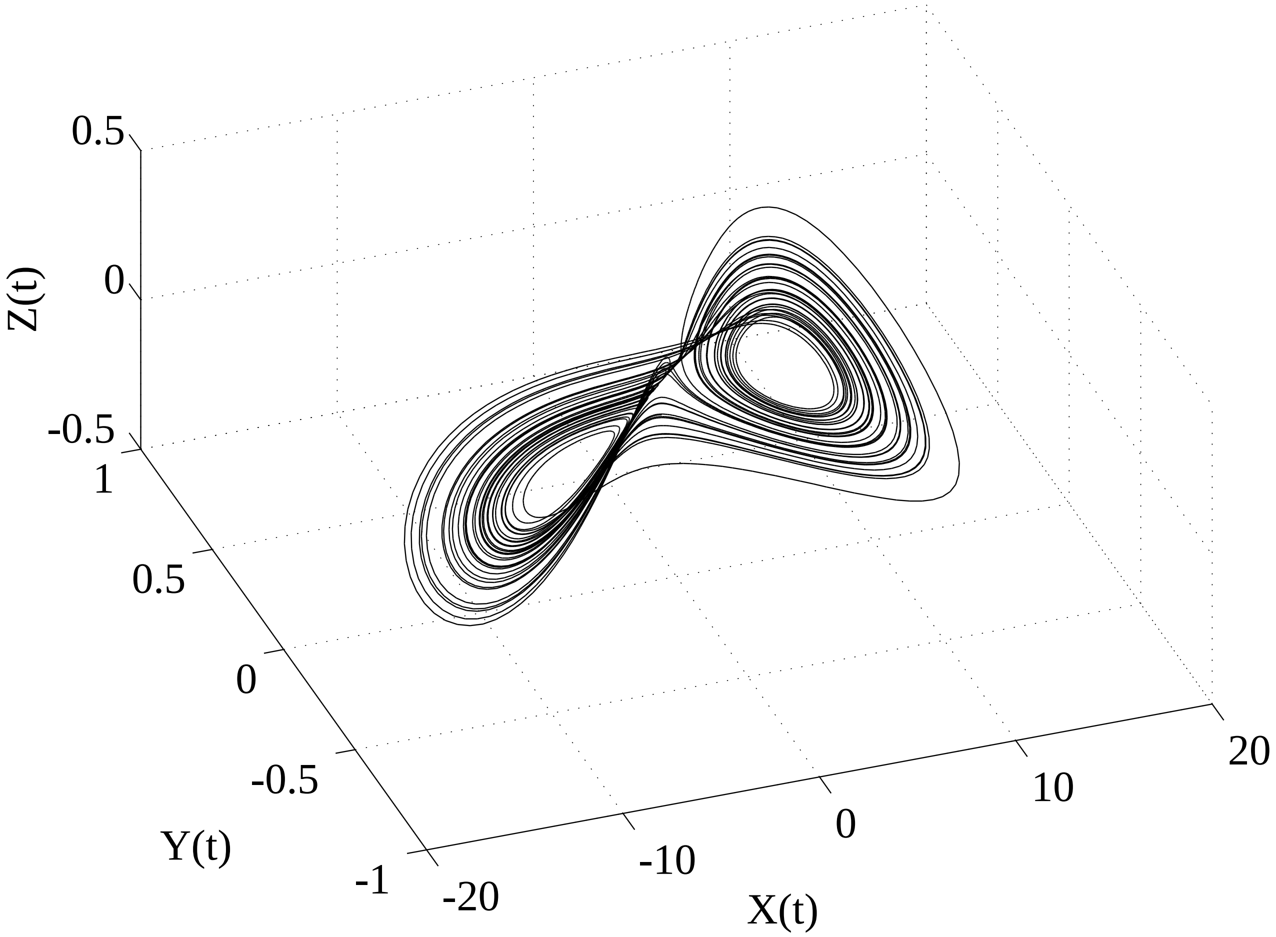

FIGURE 3.5: The attractor for the Complex Lorenz system with $\delta = 0$ corresponding to the Lorenz equations.

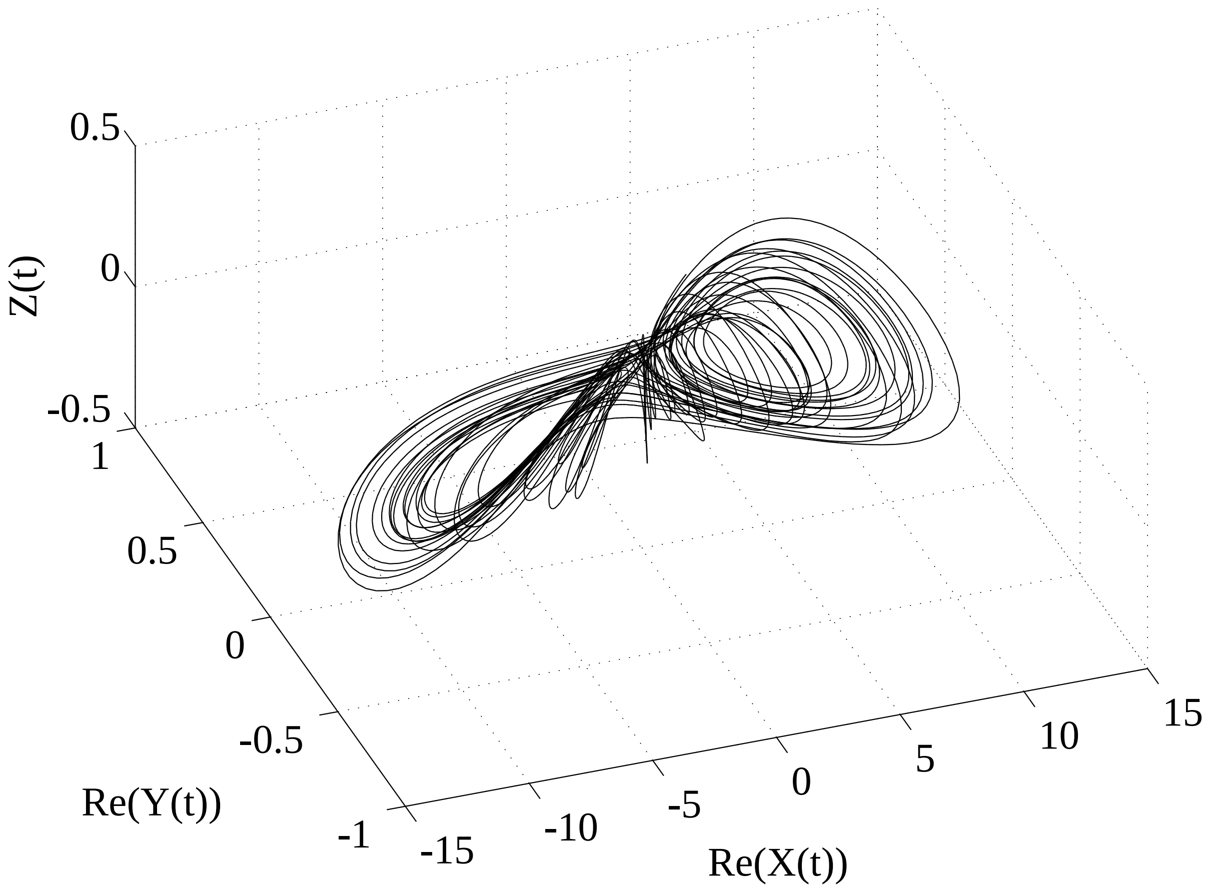

Figure 3.6: A projection of the attractor for the Complex Lorenz system showing the real component of X(t), the imaginary component of X(t), and Z(t) with $\delta = 0.2$.

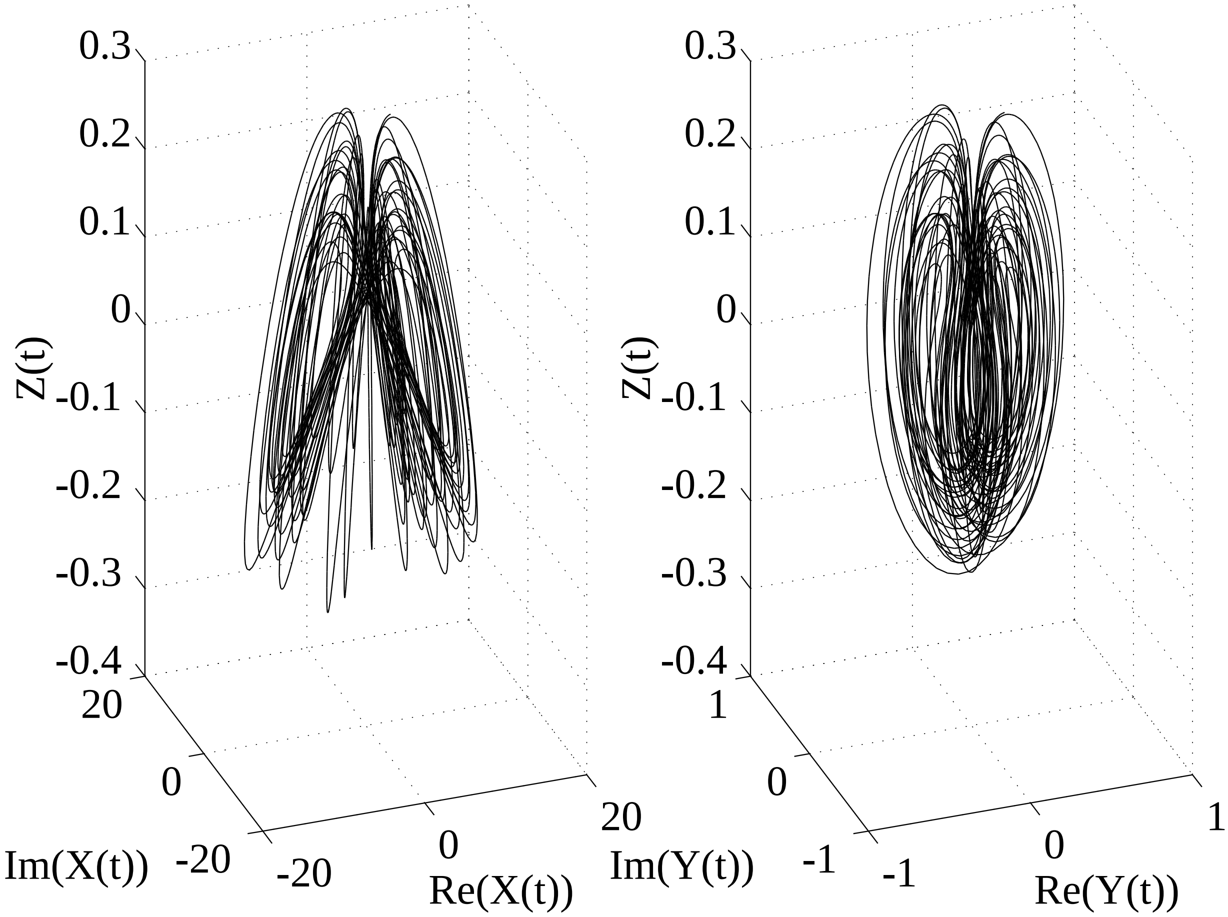

Figure 3.7: A projection of the attractor for the Complex Lorenz system showing Re(Y(t)), Im(Y(t)), and Z(t) with $\delta = 0.2$.
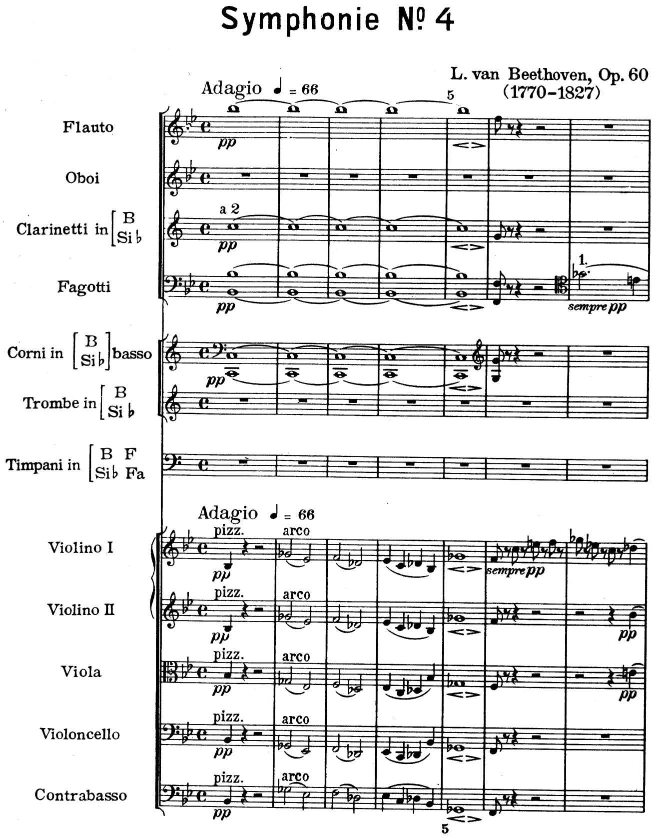
4

Chaos in the ammonia laser

4.1 Introduction

To experimentally investigate the effects of modulating an autonomous nonlinear system with a chaos threshold, a suitable system should be chosen so that measurements of dynamical variables is possible with good accuracy. Ideally accessibility to all the variables would be desirable but it is difficult to find a system which has all its variables accessible for measurement, so it is easier to find a physical system where only a subset of its variables can be measured. This does not prevent calculations such as the period of dynamics and invariant measures. These include the fractal dimension which can be derived using Takens' theorem [76].

In 1984 Weiss and Klische [63] suggested that Lorenz–like chaos could be observed in the far infrared laser as the requirement of the bad cavity condition could be satisfied. In an optically pumped FIR laser the homogeneous linewidth is determined by pressure broadening since only one velocity group of molecules is excited. Since such optically pumped lasers operate at low pressures the homogeneous linewidth is very narrow, allowing the bad cavity condition to be met for only moderate empty cavity losses.

The molecules CH_3OH and CH_2F_2 were reported to be the most efficient for a FIR laser [77], until the 81.5 μm transition in the $^{14}NH_3$ laser was discovered. This has a gain of 1.5 m^{-1} [78] which still allows lasing threshold to be reached with a relatively large empty cavity loss. There is an AC-Stark splitting in the gain line of the forward but not the backward emission, although there is an AC-Stark broadening present which can be larger than the homogeneous linewidth. This can be overcome by increasing the gas pressure of the lasing material. Subsequently if was found that the 153 μm transition of an $^{15}NH_3$ laser has a higher gain than the $^{14}NH_3$ transition. This makes it a good chaotic system to study since the pump power threshold for chaos is lower in the $^{15}NH_3$ system.

Although the only conveniently measurable variable is the square of the electric field, the intensity, it is rather easy to measure accurately. The pump power and detuning are two accessible parameters which can be modified externally. Although it is not easy to vary the detuning rapidly, the pump power can be modulated on a sub-microsecond time scale using an acousto-optic modulator.

4.2 Experimental apparatus

4.2.1 The ammonia ring laser

The ammonia laser used in this work has a ring cavity of perimeter length 2 m and the optics consist of a curved gold mirror, a gold blazed grating and a copper wire mesh (see figure 4.1). The concave mirror has a 2 m radius of curvature and reflects both the pump radiation and the lasing radiation. The grating has a grid constant of 12.4 μm which is much less than the lasing wavelength 153 μm so behaves as a totally reflective mirror at that wavelength. This grating has a second purpose which is to couple the pump radiation into the ring cavity. The pump enters the side of the box through a ZnSe window and is reflected off a gold coated mirror onto the diffraction grating. The angle of the beam to the grating is adjusted so that the first

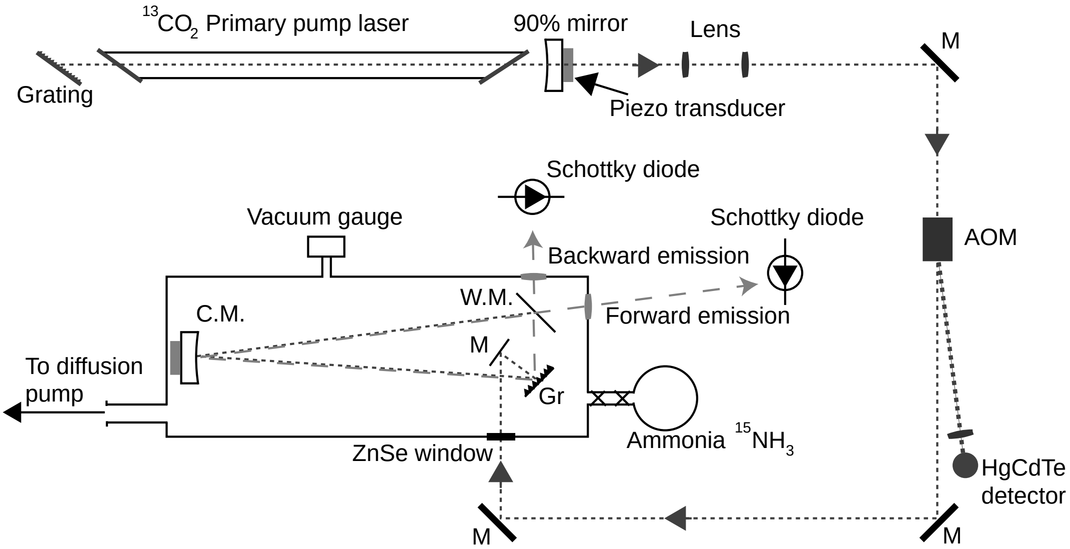

FIGURE 4.1: The experimental layout. Pump laser beam passes through mode matching lenses, the AOM, and is directed into the ring cavity via mirrors M. It then diffracts off the grating GR onto the curved mirror C.M. The pump radiation is totally absorbed before reaching the wire mesh W.M. The FIR radiation is coupled out of the ring cavity to either Schottky diode depending on the direction the radiation is travelling.

order diffraction of the pump is coupled into the ring resonator. The copper wire mesh has a grid constant of 50 μm which couples 16 % of the lasing radiation out of the ring resonator. This radiation can exit in either direction so two polyethylene lenses of focal length 5 cm are fixed to the walls of the stainless steel box allowing the two beams to be coupled out of the box. The box is covered with a perspex plate and can be evacuated with a rotary pump and diffusion pump and filled with $^{15}NH_3$ gas. To minimise expansion and contraction of the resonator length, a quartz rod is used as a mount for the optical elements. The ring cavity must be pre aligned before the box is sealed and evacuated. The gold concave mirror is mounted on a micrometer controlled translation stage so that the cavity length can be changed with minimal change in transverse alignment. The micrometer screw is coupled out of the box so that cavity length adjustments can be made while the box is closed and under a vacuum. The box contains a thermal conductivity vacuum gauge (Thermovac TM202) to monitor the pressure inside. The rotary pump and diffusion pump combination is used for pre-pumping to less than 1 μbar before filling the box with the isotopic ammonia gain material. The $^{15}NH_3$ gas comes in a 1 litre glass bottle filled at 1 atmosphere pressure (Aldridge 98 % purity $^{15}NH_3$) and has two taps in series with narrow separation which allows for a controlled fill of gas, and prevents contamination of the ammonia reservoir.

4.2.2 Experimental setup

The ammonia laser is optically pumped by an isotopic carbon dioxide laser using $^{13}CO_2$. The beam from the carbon dioxide laser passes through a telescope so that a waist is formed inside the ring cavity, then it passes though an acousto optic modulator (AOM) (Isomet 1207B-6) to allow dynamics to be imposed onto the pump power. This is fed through the ZnSe window onto mirror M and gets coupled into the ring cavity via the diffraction grating. The laser action at wavelength 153 μm can be bidirectional giving a forward emission and a backward emission, which pass through the polyethylene lenses in the box which focusses the radiation onto two Schottky diodes. All the measurements described in this thesis were made with unidirectional operation in the backward direction. The second Schottky diode was used to check that there was not forward emission.

The cavity length of both the pump laser and the ammonia laser can be adjusted both manually through a micrometer, and electronically via a piezo electric transducer. The dynamics of the pump can be monitored by measuring the intensity of the first diffraction order from the AOM onto a liquid nitrogen cooled HgCdTe detector. Intensity data from the ring laser and the pump dynamics are simultaneosly recorded and displayed using a digital storage oscilloscope (Tektronix TDS430A) with a sampling rate of 25 MHz and a maximum record length of 120000 points per channel, and a spectrum analyser (HP70000 series 100Hz-2GHz).

4.2.3 Optically pumped ammonia laser

The ammonia laser is pumped between the ground vibrational state sub-level a(5,4), and the first excited ν_2 vibrational state s(5,4). This corresponds to a wavelength of 10.78 μm which coincides with the strong 10R(18) line in the $^{13}CO_2$ laser [79]. It is therefore strongly absorbed and efficiently excites molecules to a level where a very strong population inversion can be maintained. This in turn generates the very high gain needed to exceed the lasing threshold in a laser cavity satisfying the bad cavity condition. The far infrared transition occurs between two rotational states s(5,4) and a(4,4) which are adjacent, and correspond to a wavelength of 152.9 μm as shown in figure 4.2. The bad cavity condition which is discussed in chapter 2 is easily fulfilled by lowering the gas pressure of the ring laser system. At low pressure the far infrared transition is Doppler broadened, however only one velocity group of

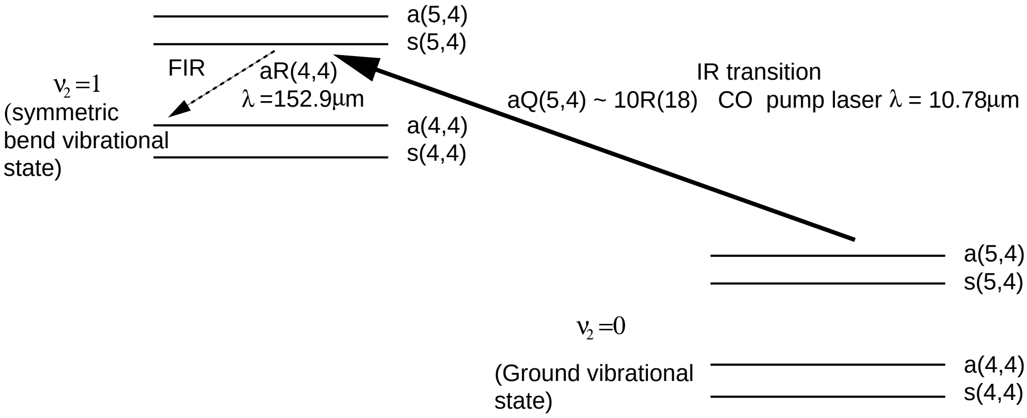

FIGURE 4.2: The energy level diagram showing the pump transition aQ(5,4) and the FIR transition aR(4,4) of $^{15}NH_3$.

lasing molecules can be selected with optical pumping. The laser therefore behaves as a homogeneously broadened laser with travelling plane waves as required for the Lorenz-Haken model. Optical pumping can also produce bi-directional radiation [80] depending on which velocity group of ammonia molecules the pump radiation is exciting, but such operation is avoided in the present work.

The first of two thresholds correspond to the onset of lasing which occurs between 40–100mW of CO_2 pump power. The second threshold corresponds to the onset of chaotic dynamics which occurs for pump powers greater than 3W depending on the ammonia gas pressure. Hence it is very easy to achieve lasing, but more difficult to reach the second threshold.

4.2.4 The $^{13}CO_2$ laser

A wavelength of 10.78 μm is used as the optical pump because it coincides closely with the aQ(5,4) vibrational transition in isotopic ammonia. The isotopic carbon dioxide laser tube (Ultra Lasertech 9123 $^{13}C^{16}O_2$) is sealed and contains $^{13}C^{16}O_2$ diluted with three parts nitrogen and seven parts helium to give a total pressure of

20-22 Torr. It has an outer water jacket for cooling and zinc selenide (ZnSe) Brewster windows at both ends. The length of the laser tube is 0.8 m and it is electrically excited by a discharge current of 6 mA providing a maximum of 10 W at the 10R(18) transition when the laser is new, degrading after about 1000 hours of use. The cavity is a Fabry-Perot with a 2 m radius of curvature ZnSe plano-concave output coupler with reflectivity of 90 % on the curved surface with the flat surface anti-reflection coated. This mirror is mounted to a piezo ceramic transducer so that the cavity length can be electrically varied, the expansion coefficient being approximately 4.9 nm/V. A change in cavity length by half a wavelength corresponds to a free spectral range of 150 MHz giving a cavity tuning rate of 0.136 MHz/V, reduced somewhat by frequency pulling [81]. The other reflector is a blazed diffraction grating which is used to select the 10.78μm transition. A grating is required since the 10.78μm transition does not have the highest gain in the carbon dioxide laser.

4.2.5 Detectors

The HgCdTe detector

The pump radiation is detected using a Societe Anonyme de Telecommunications (SAT) HgTe-CdTe photoconductive detector sensitive between 8 μm and 12 μm with a bandwidth of more than 50 MHz. To reduce thermal excitations of carriers the detector is cooled to 77 K with liquid nitrogen. The HgCdTe diode is biased of the order of half a volt, to increase the sensitivity and bandwidth, and a signal is easily detected for laser power of the order of a milliwatt

Schottky barrier diode detector

The Schottky barrier diode detector is used to measure the radiation of the ammonia laser (1.96 THz). There is an array of photolithographically produced gallium arsenide (GaAs) diodes in small wells of size 2 μm (Farran Technology model SD020). Radiation is coupled to one of the diodes via a tungsten antenna of length 5 mm and diameter 30 μm where the tip has been sharpened to a size of about 2 μm, which was performed by electrolytic etching in a sodium hydroxide solution. The antenna is brought into contact with a particular diode by moving the array towards the antenna using a translation stage, and is held in place by the tension created in the antenna due to the final position of the translation stage. The resultant configuration is shown in figure 4.3. To enhance the signal generated from the laser radiation, which is focussed to a beam around 1 mm in diameter, a highly polished corner cube reflector is used to concentrate the radiation onto the antenna. The diode is forward biased to increase the sensitivity. There is an XYZ translation stage to find the optimum position of the corner cube with respect to the antenna.

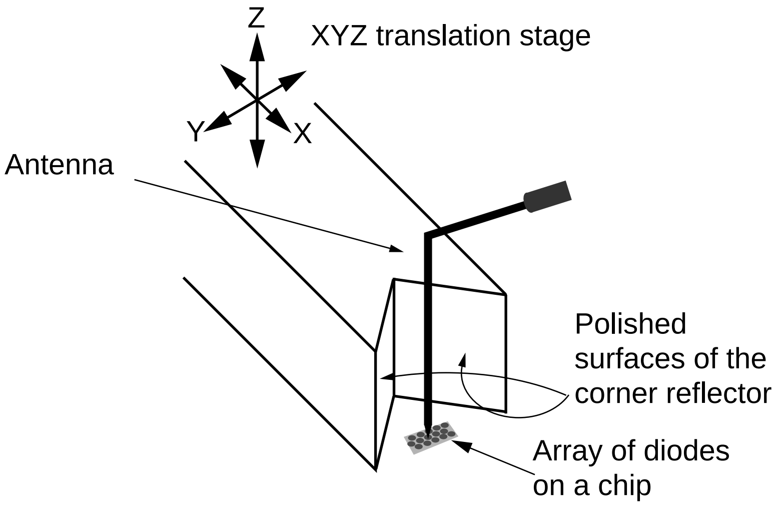

FIGURE 4.3: The arrangement of the Schottky detector.

The laser radiation is half wave rectified by the Schottky diode. The lasing frequency (1.96 THz) is much higher than the bandwidth of the measuring equipment so is filtered out leaving behind the slower laser intensity fluctuations (0-6 MHz) which correspond to the chaotic dynamics.

4.3 The acousto optic modulator

The pump laser can be electronically attenuated and modulated by using an acousto optic modulator. In the experiment a germanium crystal modulator (Isomet 1207B-6) was used which has a spectal range 2–11 μm, with a maximum aperture of 6 mm. Taking into account the velocity of sound in germanium such an aperture implies a rise time of 700 ns. The crystal requires a 30–50 MHz signal with up to 35 W of electrical power to get a diffraction efficiency of 75 % [82]. This was achieved using a signal generator followed by a pre-amplifier, a filter, and a power amplifier as shown in figure 4.4.

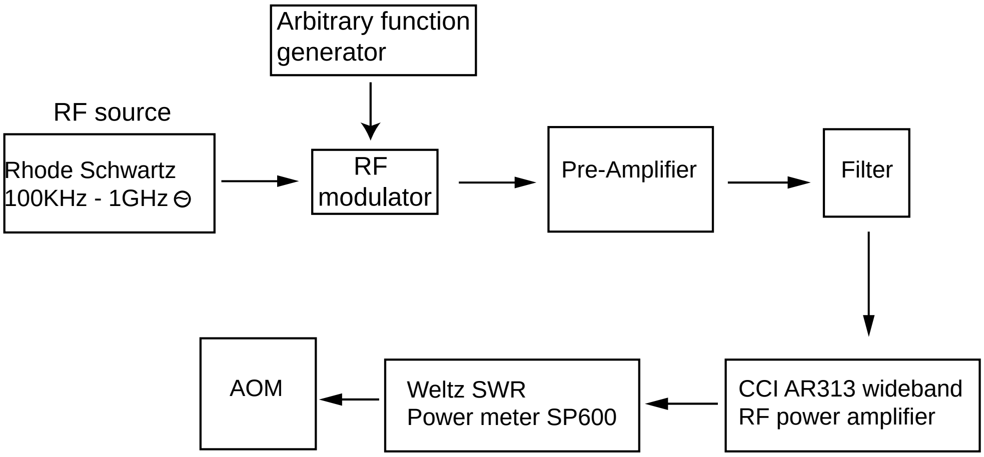

Figure 4.4: The schematic layout for operation of the AOM.

Varying the output power changes the diffraction efficiency of the AOM hence varying the amount of effective attenuation of the laser beam as it passes through the crystal. The diffraction efficiency can be modulated if a time varying signal modulated the carrier signal. Such variations must be slower than the rise time of the AOM so that modulation can take full effect. The carrier signal is modulated by using a series of mixers and power splitters as shown in figure 4.5.

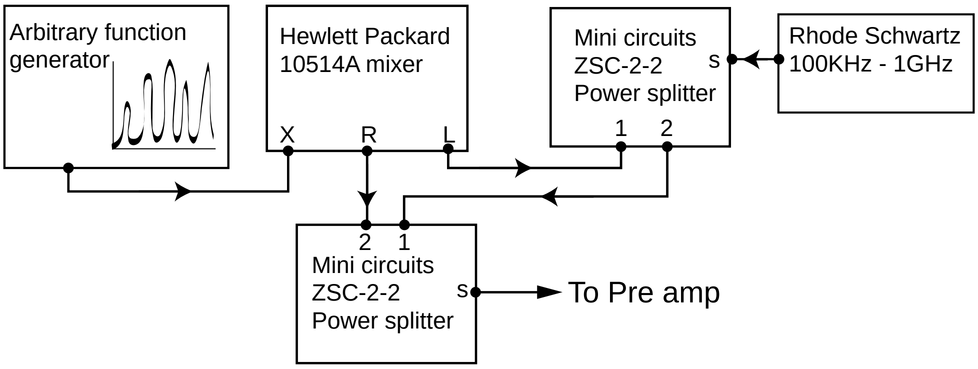

FIGURE 4.5: The schematic details for the modulator in figure 4.4.

4.4 Monitoring frequency drift of the pump laser

The $^{15}NH_3$ pump transition is Doppler broadened allowing velocity selected optical pumping using a $^{13}CO_2$ laser. To select a specific velocity group of $^{15}NH_3$ molecules requires a shift in the pump laser frequency which can be achieved by changing its cavity length. Changing the velocity of the pumped molecules translates into an effective change in the "atomic" resonance frequency, and hence detuning δ, so a controlled change in pump cavity length allows access to different types of dynamics in the FIR laser such as period doubling and spiral chaos. Problems can occur if the pump cavity length varies in an uncontrolled way through temperature drift which causes the length of the invar rod in the cavity to drift. This has the effect of drifting the detuning in the FIR laser and can change the dynamics to a different regime. The experiments thus required the detuning of the FIR laser to be fixed during the course of a particular experiment. This is achieved by making the duration of an experiment short with respect to the drift rate. After a particular run the results are digitally recorded onto a floppy disk which takes orders of magnitude more time to perform than the actual experiment, allowing the pump cavity to drift significantly from the position during the last experimental run. This problem can be reduced if the drift rate of the pump laser is known so that an appropriate voltage can be applied to the piezo attached to the output coupler of the pump laser, allowing the cavity length of the pump to be corrected. Ideally, one would like to continuously measure the value of the pump frequency with respect to the peak absorption frequency as this would allow the detuning δ to be estimated.

To estimate the frequency and drift of the pump laser with respect to the $^{15}NH_3$ line center, the Lamb dip effect was used [83, 84]. The Lamb dip is seen by retro-reflecting part of the pump laser beam through a cell filled with the $^{15}NH_3$ gas at low pressure and measuring the intensity after this double pass of the cell. This cell was used to lock the frequency of a second $^{13}CO_2$ laser using a lock-in amplifier as shown in figure 4.6. This was achieved by applying a small dither voltage (10 V) to the piezo electric transducer holding one of the mirrors on the cavity of the second $^{13}CO_2$ laser, and fixing the laser frequency to the absorption peak in piezo voltage–absorption phase space using the lock–in amplifier.

The pressure in the Lamb dip cell had to be very low to reduce homogeneous broadening and the optimum pressure was found to be approximately 10 mTorr. It required very little laser power to saturate the transition, so a weak reflection off a ZnSe slide placed after the the second $^{13}CO_2$ laser was used in the Lamb dip cell. The zero order reflections off the diffraction gratings from the Fabry-Perot cavity of both the primary and secondary $^{13}CO_2$ lasers were mixed onto a beam splitter, and detected using a HgCdTe photodetector. The beat signal was monitored using a spectrum analyser which gave a direct measure of the pump frequency with respect to

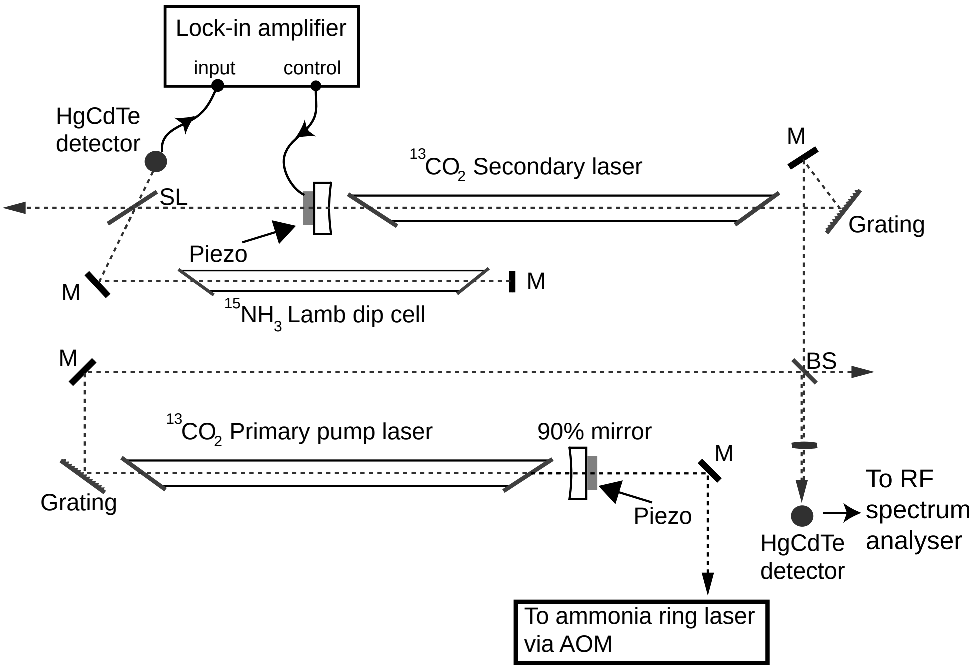

FIGURE 4.6: The schematic layout for the pump frequency monitor. Mirrors labelled M, beam splitter is BS and ZnSe slide is SL. The lock–in amplifier applies a 10 V dither voltage to the piezeo of the second carbon dioxide laser recording the variation in absorption through the Lamp dip cell and locking the laser to the absorption peak using an appropriate feedback control.

the line centre of the $^{15}NH_3$ transition, since the second laser was locked to this. The frequency drift was measured by fixing the primary pump laser to a particular value near the ammonia pump transition, and timing how long it took for the frequency to drift. It was found to be typically 1 MHz/min. There were not enough fast detectors available to simultaneously measure the pump frequency with respect to the isotopic ammonia transition while monitoring the pump dynamics (which was always necessary to ensure the pump remained single transverse mode). However, it was useful experimentally to check how fast the primary pump laser drifted so that the relevant parameters could be appropriately varied during the course of an experiment during a short enough time that the detuning was effectively fixed.

4.5 Dynamics of the ammonia laser

The Lorenz–Haken laser equations are a simplification of a laser system with many assumptions such as a single mode, travelling plane wave, incoherently pumped homogeneously broadened two–level laser in the rotating wave, and slowly varying envelope approximations. The initial work of Weiss *et al.* [63, 85, 86] where an optically pumped ammonia ring laser was used, had the feature of a unidirectional travelling plane wave, and the bad cavity condition was satisfied. Despite the fact that laser transitions at the FIR wavelength are typically Doppler broadened, velocity selected optical pumping excites the molecules with velocities within the range of the homogeneous linewidth of the pump transition. Since the Doppler effect is proportional to the frequency, this affect will be much less on the FIR transition so that the homogeneous broadening will dominate in spite of the low pressure. This satisfies the assumption of a homogeneously broadened laser to a good approximation. The use of optical pumping introduces three–level effects such as dynamic Stark splitting of the upper laser level, which is not present in the Lorenz–Haken laser model. More complex models have been developed to take into account the three–level effects, and Doppler broadening [87]. These higher order effects can be made to be small so that the type of dynamics observed in the ammonia laser matches the type of dynamics in the Lorenz–Haken equations if the laser is operating in a specific parameter range [88]. A review of the characterisation of the chaotic time series and comparison with different models is presented in [71]. In chapter 3 a bifurcation diagram was calculated as a function of two bifurcation parameters, λ the pump strength, and δ the detuning. It is not possible to create a bifurcation diagram with two bifurcation parameters experimentally due to drift issues as discussed earlier. Instead one bifurcation parameter is held fixed and the other parameter is ramped much more slowly than the average pulsation period of the chaotic pulsations. Figure 4.7 is a bifurcation diagram

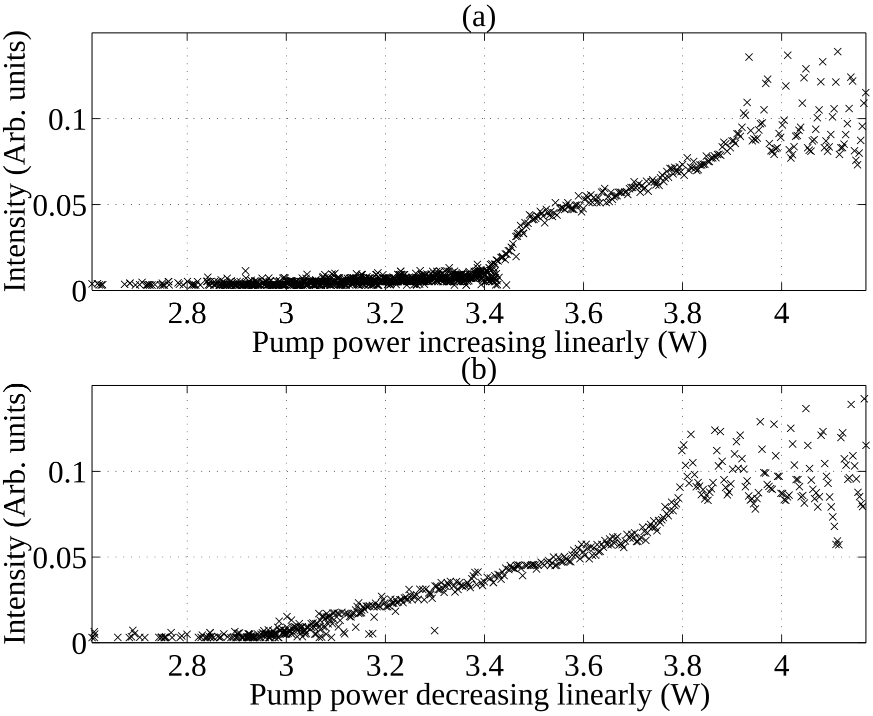

FIGURE 4.7: A bifurcation diagram constructed using the peak intensity pulsations as a function of the pump laser power which is linearly ramped.

created using the peak intensity of pulsations as a function of the pump power which is positively, and negatively ramped in 4.7a, and 4.7b respectively. There are two bifurcations present in 4.7a at 3.4 W, and 3.92 W which correspond to the lasing threshold and chaos threshold respectively. When the pump power is decreasing the above two bifurcation points have changed to 2.7 W, and 3.8 W respectively. The bifurcation points are not at the same location because the pump power has been dynamically varied which causes a delayed bifurcation as discussed in the introduction. The diagram shows there are abrupt changes in dynamics, in particular the irregular intensity peaks following the second bifurcation are a good indication of chaos. 4.4), while recording data during the bifurcation experiment. The pump power is now held fixed and the cavity detuning is swept slowly and again only the peak pulsations

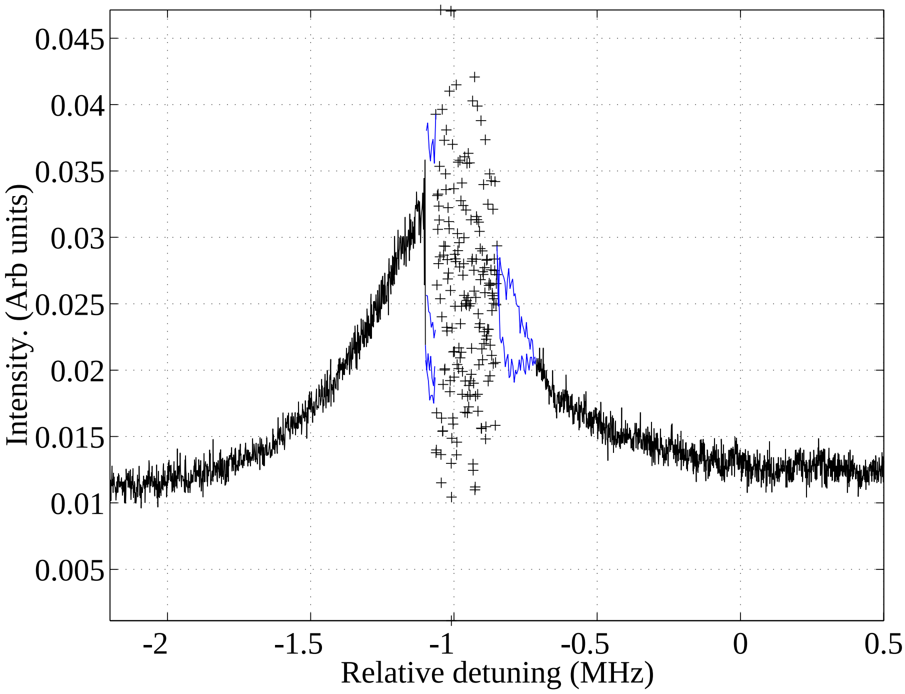

Figure 4.8: Bifurcation diagram as a function of detuning which is linearly ramped at fixed pump power.

are recorded resulting in figure 4.8. It is not possible to independently locate zero detuning as there were not enough detectors to measure the pump laser frequency with respect to the peak absorption frequency of the ammonia transition (see section 4.4). As the cavity detuning is swept the period one intensity pulsations increases. Note that one must view the time series to distinguish period 1 from period 0 in the bifurcation diagram since only the peak intensity pulsations are recorded. At a relative detuning of -1.1 MHz period 1 abruptly changes to period 4 as there are now four lines in figure 4.9 between -1.1 MHz and -1.05 MHz. The time series within that detuning window is shown in figure 4.9a. Chaos emerges between a relative detuning of -1.05 MHz and -0.85 MHz where the laser output now abruptly changes to period 2 pulsations lasting until the relative detuning reaches -0.7 MHz. The time series within the period 2 window is shown in figure 4.9b where the period 2 pulsations are decaying towards period 1 because the detuning is continuously ramped.

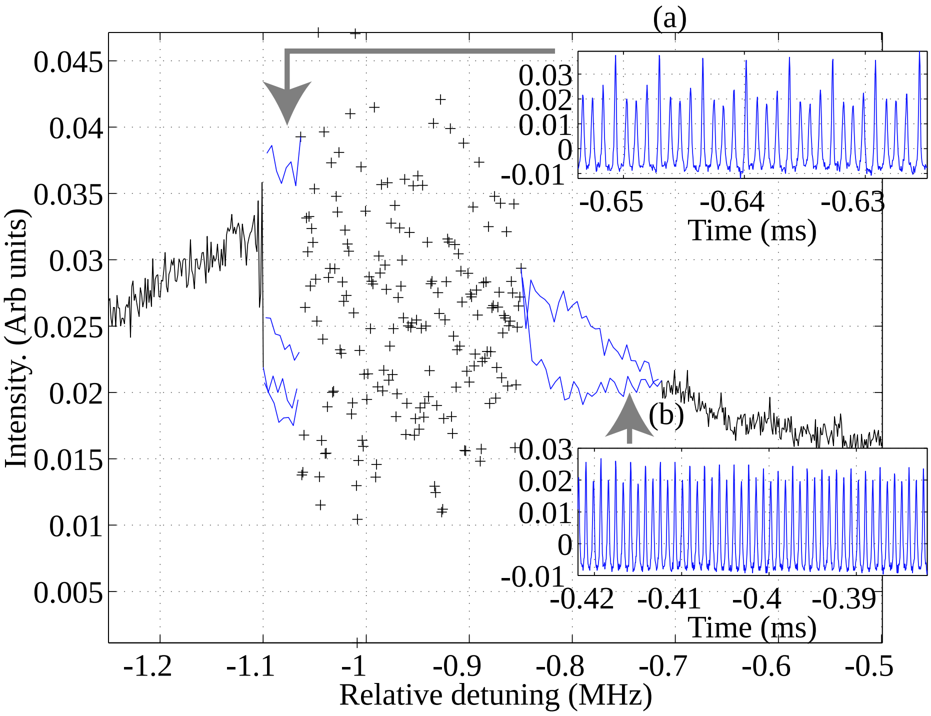

FIGURE 4.9: A close up of the bifurcation diagram 4.8 as a function of detuning which is linearly ramped. The inset plots (a) and (b) show the time traces corresponding to the detuning parameter indicated by the arrows.
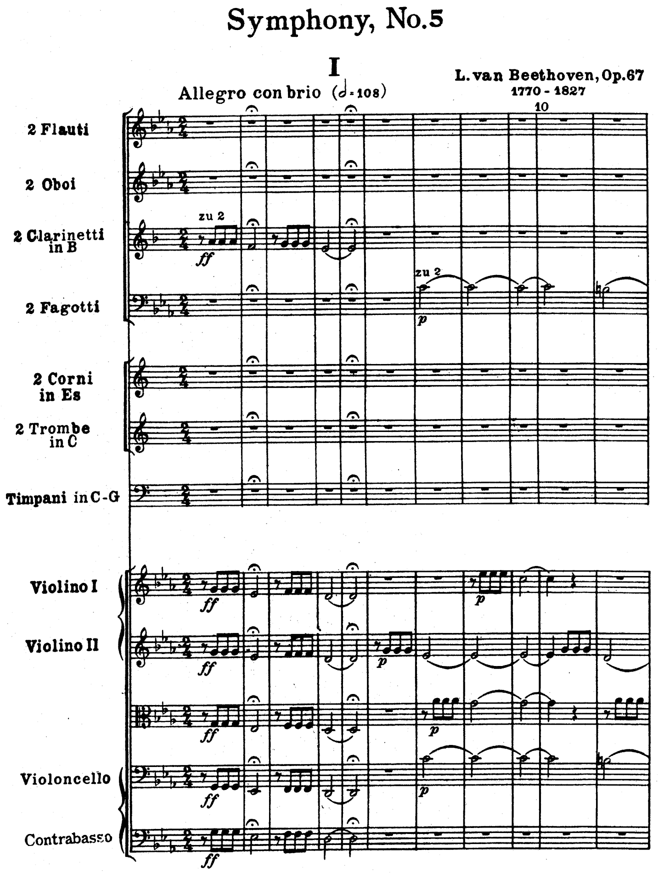
5

Experimentally controlling chaos by periodically modulating the pump

5.1 Introduction

A system must have at least three degrees of freedom for chaos to emerge. In a system with two degrees of freedom chaos can be generated by modulation, and many laser chaos experiments are performed this way [89], with class A and B lasers. System with at least three degrees of freedom can generate chaos without modulation and are therefore known as autonomous. Such systems have been studied both theoretically

[65, 90, 91], and experimentally [25, 92]. However, relatively little work has been done in investigating the properties of an autonomous chaotic system where one of the parameters is made time dependent [93]. This can increase the complexity of the dynamics or simplify it. One mechanism for controlling autonomous chaos is to periodically cross the chaos threshold by varying the pump power [25, 65]. However this mechanism obviously cannot be used to control chaos if the system is permanently above the chaotic threshold as discussed in the introduction. It is well known that a chaotic attractor is wound around a set of unstable periodic orbits [51]. This has led to the development of algorithms such as the OGY method [34] to select these orbits and control them. This requires detailed knowledge of the dynamical system, for example, an accurate estimate of the directions of the unstable and stable manifolds, in order to estimate how much change should be applied to a parameter in order to gain control (see appendix A for further details). Thus the OGY algorithm is suitable for slowly oscillating systems, but the required computation rapidly becomes intractable for fast oscillating systems.

Other feedback methods require no detailed knowledge of the system. Reported examples include occasional proportional feedback in a Nd:YAG pumped KTP crystal forming a multimode autonomous laser [37]; in a diode pumped Nd-doped silica fibre multimode autonomous laser [94]. Control by subtractive feedback has been demonstrated in a non-autonomous CO_2 laser [95] and an autonomous NH_3 laser [96]. These systems require *a priori* knowledge of the average period of the chaotic pulsations, and a subtraction of the measured time series from its value at an earlier time. Such feedback control is explored further in Chapter 7

Since these methods may not always be appropriate, in this section we experimentally explore an alternative approach, which consists of applying a modulation to one of the parameters of the dynamical system. This changes the original system, but for a sufficiently small modulation, the unstable periodic orbits are similar to the corresponding orbits in the unmodulated system. Stabilising one of these orbits should give control as predicted by theoretical studies [51, 91, 97, 98].

To date, only class A and class B lasers have been used in optical studies of control of chaos by modulation. For example, a non-autonomous class B laser was controlled by a small modulation of the losses to a periodic state [99]. Subharmonics of the pump modulation frequency were observed and three different locking ratios were found. Control of a class B multimode autonomous neodymium-doped yttrium aluminium garnet (Nd:YAG) laser to stable periodic orbits was achieved by modulating the laser diode current [100]. In all cases the controlled output contained higher harmonics of the pump modulation frequency. A large range of locking ratios was found and chaos was almost suppressed to a dc level when the modulation frequency was above 25% of the fundamental pulsation frequency. It is interesting that a larger modulation of the pump power was required to control the dynamics compared to modulation of the loss in the case of a multimode Nd:YAG laser with an intracavity frequency doubling titanyl phosphate (KTP) crystal [101]. The corresponding range of modulation amplitudes to stabilize the chaotic laser for the pump, and loss modulation were $16-60\%$, and $0.5-2\%$ respectively. A chaotic non autonomous CO_2 laser was controlled by modulating the intracavity losses where the periodic modulation amplitude was also only a few percent [102]. It seems that control is more difficult to achieve when the pump is modulated rather than a loss.

Here, we use a chaotic class C laser, which, as was explained in Chapter 3, is well-described by the complex Lorenz equations [71]. Previous numerical studies of these equations include modulation of the inversion across the bifurcation point [103], replacing the Rayleigh parameter with a time dependent term [97], and modulation of the inversion above the bifurcation point for the real Lorenz equations (corresponds to a non-detuned laser in Chapter 3) [90]. The real Lorenz equations was extend to include detuning [104], and it is this system which is explore here.

We find that there are many regions in modulation amplitude and modulation frequency parameter space, where the dynamics of the chaotic laser frequency lock to the external periodic modulation. These regions in modulation amplitude–modulation frequency parameter space, which show the regions where the locking ratio is rational, have a definite structure to the shape and are known as Arnold tongues. We show that a chaotic laser can be controlled to period q when modulated at period p, and the fractions $\frac{p}{q}$ belong to the Farey sequence as was found in a non-chaotic laser [105] and in a bimode laser with a saturable absorber [106]. We find that these Arnold tongues are very narrow.

5.2 Experimental

As described in detail in Chapter 4, our system consists of an $^{15}NH_3$ ring laser which is optically pumped by a $^{13}CO_2$ laser through a vibrational transition at 10.78 μm. The lasing occurs through a rotational transition at a wavelength 0.153 mm. We use a semi-confocal ring cavity as shown in Figure 7.23, to achieve uni-directional lasing, where the backward travelling wave is chosen in preference to the forward wave because the A.C. Stark effect splits the gain line in the forward direction [107].

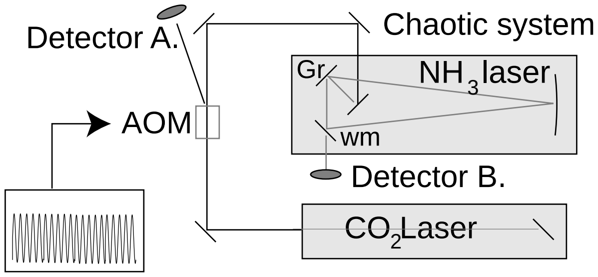

FIGURE 5.1: Experimental schematic: CO_2 laser is the pump; NH_3 ring laser is the chaotic system; Gr is a blazed grating at the pump wavelength ($10.78\mu m$) which doubles as a mirror for the lasing wavelength ($153\mu m$); wm is a wire mesh used as an output coupler; AOM is an acousto–optic modulator; detector A monitors the pump dynamics; detector B monitors the FIR dynamics.

Dynamics are optionally imposed on the pump by passing the pump laser beam though an acousto–optic modulator, AOM. The signal applied to the AOM is programmed using an arbitrary function generator. We monitor the pump intensity via the first diffracted order from the AOM. This is detected by a HgCdTe photodetector A. The dynamics of the far infrared laser are observed by detecting the intensity of the output field with a fast Schottky barrier diode detector, B, see Figure 7.23. The signals from both detectors are recorded simultaneously onto a digital storage oscilloscope.

5.3 Experimental results

5.3.1 Harmonic pump modulation, harmonic generation - control to period 1

In general, modulation of the pump leads to no noticeable simplification in the dynamics. However, we have been able to identify a number of cases where, for specific ranges of modulation frequency and amplitude, periodic pulsations replace the chaotic spiking. Four cases are presented here as examples. Because the parameter ranges where periodic behaviour can be observed are narrow, special care had to be taken to overcome the effects of unavoidable drifts during the experiment. Only then was it possible to distinguish consistent and reproducible patterns of behaviour.

We apply a modulation to the pump of the form $f(t) = A(1 + sin(\omega t))$ rather than $f(t) = A\sin(\omega t)$, so that we can be sure that the system always remains above the chaos threshold. This waveform is programmed into an arbitrary function generator which in turn modulates the amplitude of the RF signal driving the AOM. The modulation frequency was chosen to be near the average pulsation frequency of the free running chaos, f_0. The lower trace of Figure 5.2 indicates the periods where pump modulation was applied. The modulation depth was 20% (peak-to-peak) as shown on the right hand y-axis scale. The upper trace shows the response of the FIR laser to this modulation. In order to display a time period much longer than the time between individual pulses, only the maximum pulse height is displayed which is calculated from the digitised time trace having 8 bit resolution, so that a horizontal line represents periodic pulses and each spike represents a Lorenz ‘spiral’ of several successive pulses of increasing amplitude. It is clear that when modulation is applied, the dynamics of the FIR laser has been transformed and is no longer chaotic. Figure 5.3a is an expanded view of one of the segments from Figure 5.2. This shows that Lorenz-like chaotic pulsations exist before modulation is applied to the system, and a period one signal develops as modulation is applied. The Fourier transform is calculated for the unmodulated laser output, and modulated output from Figure 5.3a, and shown as the upper trace, and lower trace respectively of 5.3b. The initially chaotic system possesses a broad spectrum (grey), with three broadened harmonics

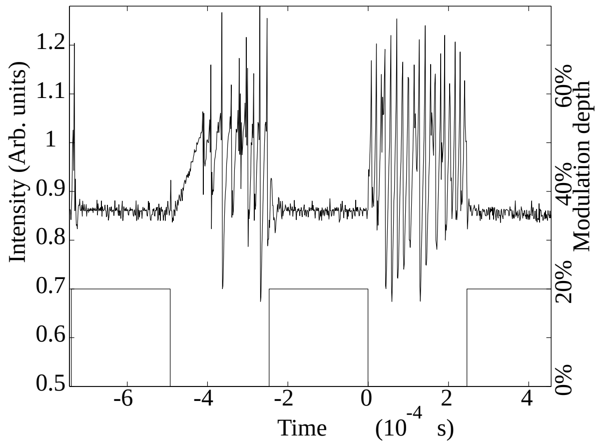

Figure 5.2: Control to period 1. The lower trace is a schematic of the dynamics applied to the pump. The blocks of height 20% represent the period where pump modulation is applied (the modulation depth is shown on the right hand y-axis). The upper trace is the *peak* output intensity of the pumped laser (intensity is shown on the left hand axis). As this is peak intensity, the flat regions represent period 1 pulsations.

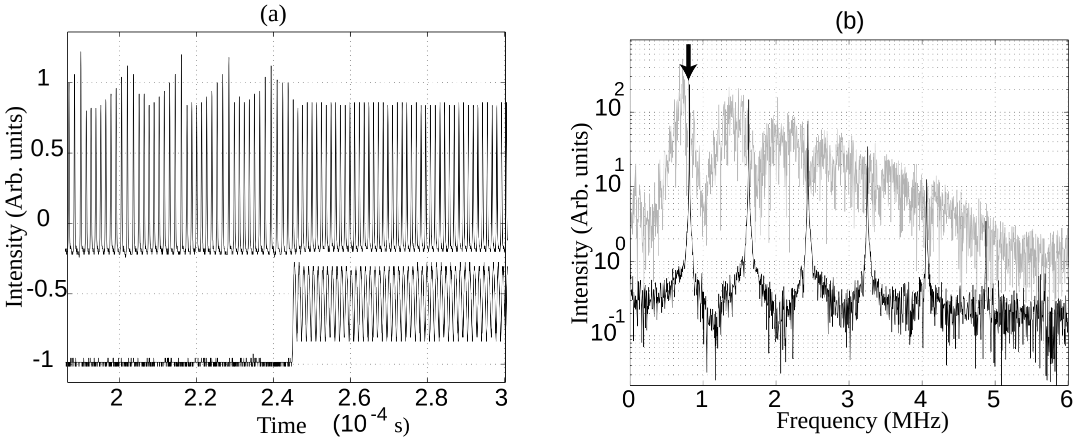

Figure 5.3: Expanded view from -0.23 ms to 0 ms of figure 5.2. (a) Top trace is the intensity of the NH_3 laser output, lower trace is the pump intensity, (the modulation depth between 0.25 ms and 0.3 ms is 20%). The modulation frequency is 17.5% of the average pulsation frequency of the FIR chaos free from modulation, (b) Frequency spectra of the left (right) hand side of the NH_3 intensity trace from (a) are shown as the grey (black) trace. Note that the broad spectrum of the unmodulated case is transformed into a harmonic spectrum in the modulated case. The arrow indicates the position of the fundamental pump modulation frequency.

of the fundamental pulsation frequency. This collapses to a set of sharp well defined harmonics with the fundamental located at the position of the pump modulation frequency. This shows the transformation from chaos to period 1 pulsations. In Figure 5.4 we examine these spectra more closely. Figure 5.4a is the spectrum of the FIR laser under modulation, and Figure 5.4b that of the pump. Higher harmonics of the fundamental are present even though there are only three evident harmonics associated with the pump. This may be that the laser is amplifying the pump harmonics, or that output harmonics are generated from a single pump modulation frequency, of some combination of both.

To analyse the effect of pump modulation on the FIR laser, we take the ratio of the spectrum during modulation, to the spectrum without, as shown in Figure 5.4c. A dashed line is added at the 0 dB level to differentiate attenuation and enhancement. It is clear that most frequencies have been attenuated whilst only the harmonics of

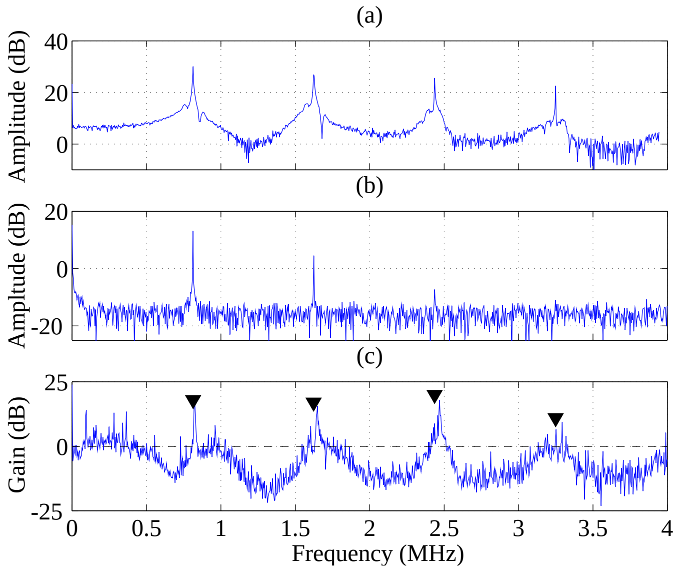

Figure 5.4: Fourier spectra for (a) the pump modulated FIR laser output, (b) the pump modulation and (c) the ratio of the pump modulated FIR laser output to the unmodulated laser output. Triangles indicate the position of the integer harmonics. the dashed line indicates the position of zero gain, note that only the harmonics of the pump are amplified, all other frequencies are suppressed.

the pump modulation frequency have been enhanced.

As the laser is initially chaotic before control was applied, we expect that the dynamics of the system does not immediately change from a chaotic state to a periodic state at the turn-on of the modulation, but does so after a few cycles of irregular behaviour. This is most clearly seen from the results of the following experiment. The laser was modulated at f_0 to give period 1 oscillations, then allowed to return

Figure 5.5: Schematic of modulation applied to the pump. The pump is modulated at f_0, the fundamental pulsation frequency, for 100 cycles between a and b, followed by a period of no modulation between b and c, followed by 100 cycles at f_0 between c and d.

to its chaotic state (by removing the modulation). Finally the same modulation was applied to the laser, thus resulting in a return to period 1 oscillations. Figure

5.5 shows this sequence of events, which allows the laser to develop different initial conditions between the first and second modulation period of control. Figure 5.6 shows the intensity outputs from both periods. The thin black line is the response to the first modulation, while the thick grey line is the response to the second. These lines are different between time zero and 0.014ms, since in this interval the dynamics are not phased locked to the pump modulation. After 0.014ms, both these intensities are phased locked, so that the two curves in the graph of Figure 5.6 collapse onto the phase locked curve.

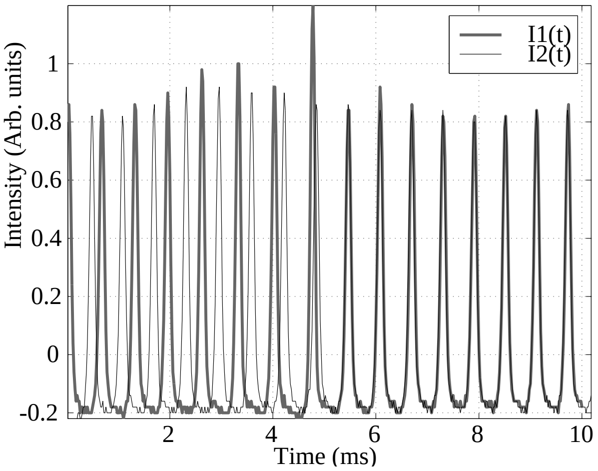

Figure 5.6: Two intensity outputs of the laser corresponding to modulation of the pump to give period 1oscillations. The thin black line is the response to modulation at f_0, while the thick grey line also is a response to the same modulation, but applied after the system was allowed to return to its chaotic state. Therefore the difference between the two traces is the result of the initial conditions.

In order to investigate the affect of control on gain of the harmonics, a modulation at the fundamental pulsation frequency was performed on the chaotic laser operating in four experiments corresponding to slightly different pressure conditions. In each particular experiment two periods of modulation were separated by periods of no modulation as shown in figure 5.5, except experiments two and four had an additional period of modulation followed by a region of no modulation. Only experiment number one gave control to period 1 during the times where the modulation was applied. The other three experiments did not give control as the modulation frequency was shifted slightly from f_0. The gain of the harmonics of the modulation frequency was calculated by taking the ratio of the value of the amplitude of the frequency component at the modulation frequency during modulation, to the amplitude of the same frequency component when the modulation was turned off. The gain of the harmonics for the four experiments is labelled Exp1, Exp2, Exp3, and Exp4 in figure 5.7, where experiment one has been explicitly decomposed into two parts (a), and (b) which corresponds to the first, and second part of the modulation sequence from figure 5.5. In both cases control to period 1 was obtained. The four sets of

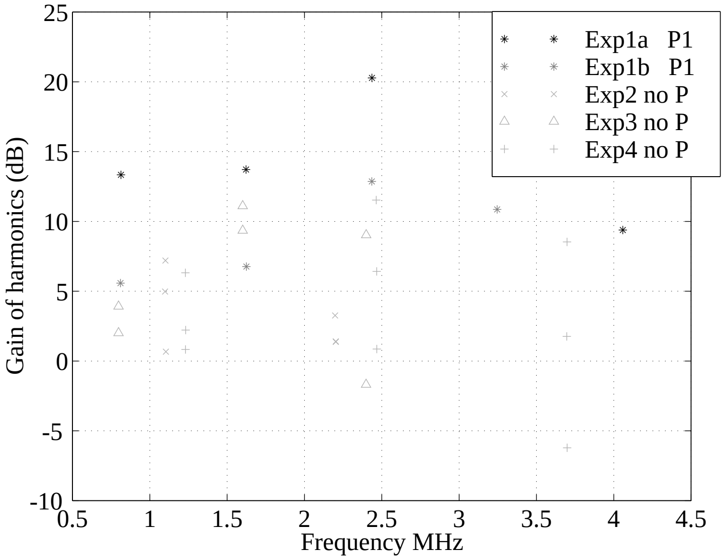

FIGURE 5.7: In four experimentControl to period 1 in slightly different conditions. 'P1' represent period 1 behaviour, and 'no P' means the dynamics was not periodic.

experiments were performed under slightly different pressure conditions, which has altered the value of the average pulsation frequency f_0, that ranges from 0.8 MHz to 1.23 MHz, and the corresponding modulation frequencies were altered appropriately.

Experiment one gave control to period one because the modulation frequency was chosen correctly. However the remaining three experiments did not give control to period 1 since the modulation frequency was chosen to be displaced slightly from the correct frequency. Even though the last three experiments did not give control, there is a significant gain of the harmonics of the pump modulation frequency which is due to the fact that the applied modulation is very close to resonance. The gain results of Exp1a, and Exp1b are significantly higher than the remaining three experiments other than the second harmonic of experiment three as is evident in figure 5.7. The first and third harmonics of experiment three are significantly lower than the corresponding harmonics of Exp1b. These results show that the gain of the harmonics of the modulation frequency near resonance is higher when the system is controlled to period 1.

Generalised synchronisation to period 1

To obtain more information about the period 1 orbit, the pump modulation frequency was shifted from the value yielding control in five discrete steps. This allowed a search for different stages of generalised synchronisation. Five different modulation frequencies of fixed duration were separated equally by a regions of no modulation. This is shown in figure 5.8 where the time trace is divided into five contiguous segments (a–e). The duration of the experiment is 1.55ms which is small enough that drift in the FIR laser, which is of the order 1MHz/min, can be neglected. The constant pump regions were inserted so that the dynamics could return to the original chaotic state before the next modulation frequency was applied. Period 1 emerges after a number of transient pulses as shown in figure 5.8c at the modulation frequency $f = 643.6$ KHz at an amplitude between 0.05 and 0.1. Control is lost at the other four values of modulation frequency, although phase locking occurs at $f = 630.5$, 637.1, and 656.8 KHz where there are no phase slips between the FIR intensity pulsations and the driving modulation, and the average frequency is the same. This is evidence of the second strongest generalised synchronisation, phase synchronisation, where the first refers to perfect phase locking and high amplitude correlation, i.e. control. At $f = 650.2$ KHz there are two phase slips, and the average frequencies of the pump and the intensity output are different, hence unsynchronised.

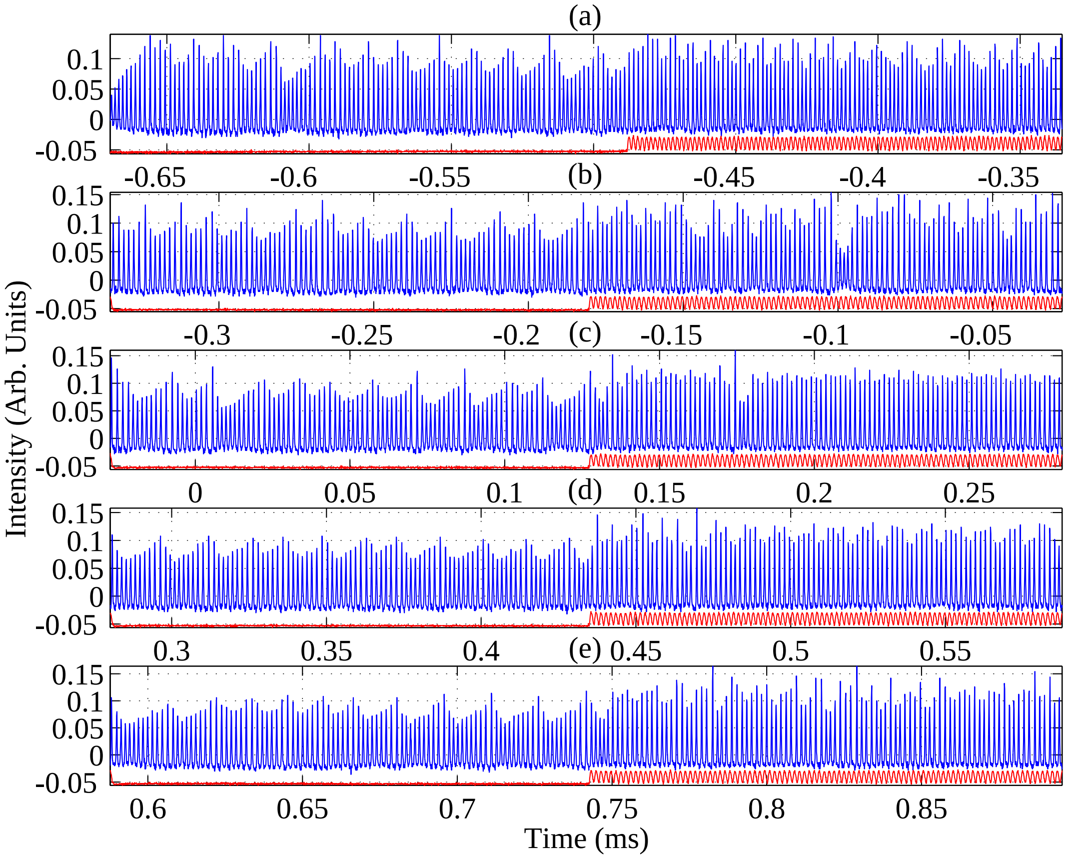

FIGURE 5.8: Synchronisation and control to period 1. The laser is modulated at five frequencies 656.8, 650.2, 643.6, 637.1, and 630.5 KHz as shown in the lower trace of (a), (b), (c), (d), and (e) respectively. No synchronisation occurs at (b) where there are two phase slips while synchronisation occurs (no phase slips) at (a), (c), (d), and (e). Synchronisation is strongest at (c) where period 1 develops after some initial transients.

The dynamics during each stage of modulation can be analysed in terms of return map plots, and the fast Fourier transform (fft) and are shown in figure 5.9(a–e) which corresponds to figure 5.8(a–e). At control to period 1, as shown in (c), there is one distinct point which has some spread due to detector noise, and limited amplitude resolution of 8 bits. The associated fft shows sharp well-defined peaks, and lack of broad band structure. The remaining return maps show a lack of regular structure, and the associated fft spectra show broadened peaks superimposed on a period 1 spectrum.

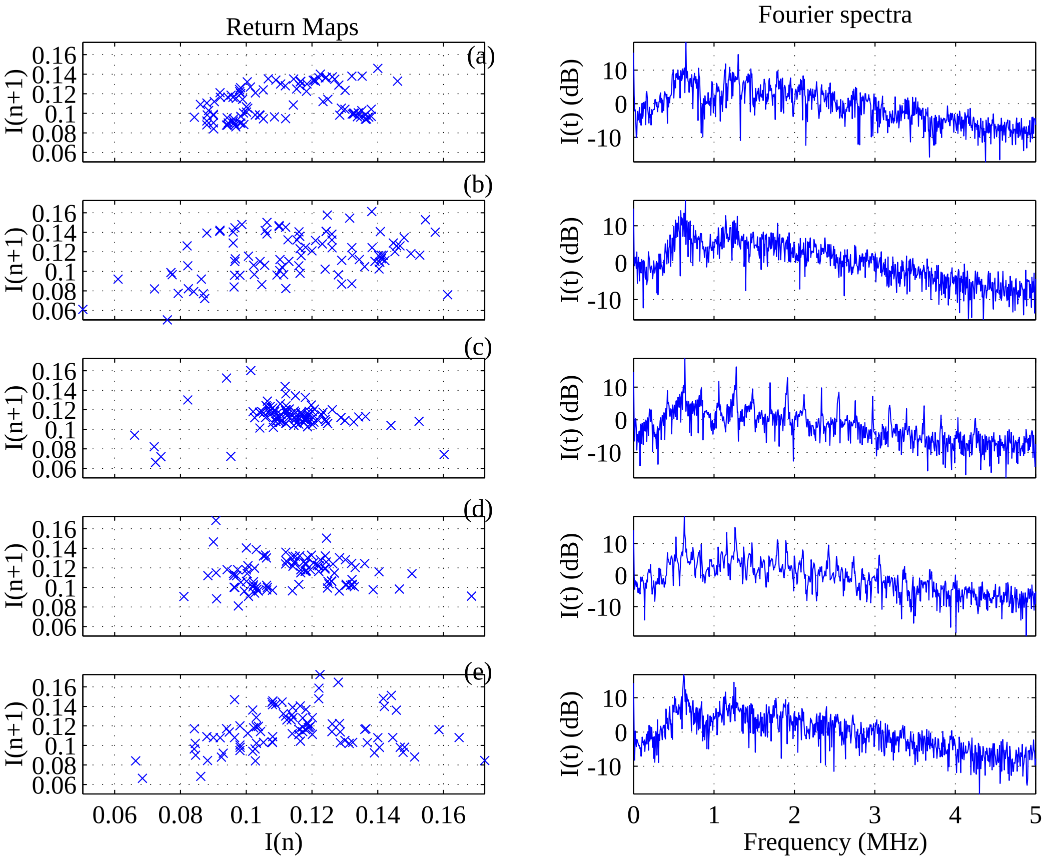

Figure 5.9: The return maps, and fft are calculated for the associated time series in figure 5.8 during the period of modulation. Control to period 1 is clearly visible as a smeared point in (c), and sharp well-defined peaks in the associated fft.

Experimentally, control to period 1 could be observed over a narrow range of pump modulation frequency and amplitude. Changing any one of the parameters by 1% is enough to destroy control. Clearly, experimental drift issues would need to be addressed before undertaking a full map of the parameter space, but these results are enough to show that control is possible, but it is not easy to achieve.

5.3.2 Harmonic pump modulation, subharmonic generation - control to period 3

We also found that it is possible to control states to higher integer periods (e.g. pattern repeats every 3 pulses). Figure 5.10 is similar to figure 5.3a except now the pump modulation frequency is only 4% higher than the average pulsation frequency of the unmodulated chaos f_0 which was 0.96 MHz, rather than 82.5% of f_0 which was 0.69MHz for the experimental conditions used in figure 5.3a. It shows that the laser takes many cycles before it settles down to period 3 pulsations, and that the period 3 behaviour is not perfectly regular.

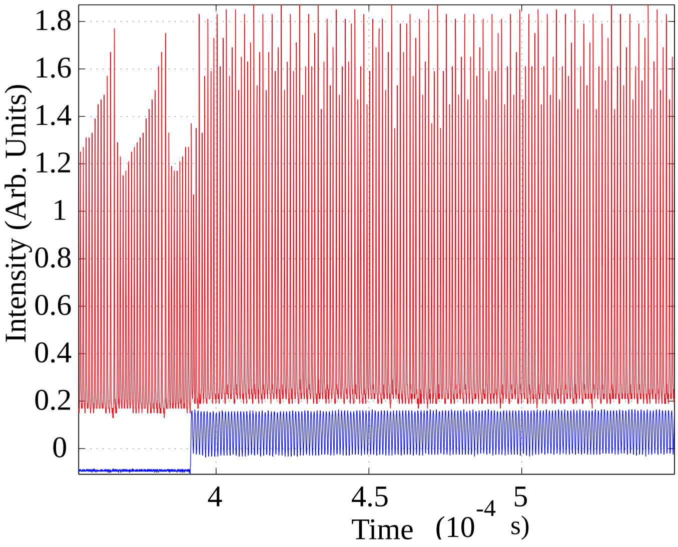

Figure 5.10: Control to period 3 after many pulses of instability. Same conditions as Figure 5.3a except that the modulation frequency is now 4% higher than f_0 of the unmodulated chaos.

We believe this is due to the sensitive dependence on modulation frequency relative to the natural pulsation frequency of the ammonia laser which in turn depends on the frequency and power of the pump laser, both which are subject to jitter and drift. In the frequency domain it is clear that the dynamics of the laser has been simplified, as is evident in Figure 5.11. The frequency spectrum for the FIR laser output is shown on the upper trace, and the pump spectrum on the lower trace. Note that we are pumping near the fundamental frequency f_0, and we generate rational subharmonics at $\frac{1}{3}$ f_0 and $\frac{2}{3}$ f_0, indicated by f_1 and f_2 in figure 5.11, which are not present in the pump. Higher harmonics such as $\frac{4}{3}$ f_0 and $\frac{5}{3}$ f_0 are present as well as integer multiples of all rational harmonics.

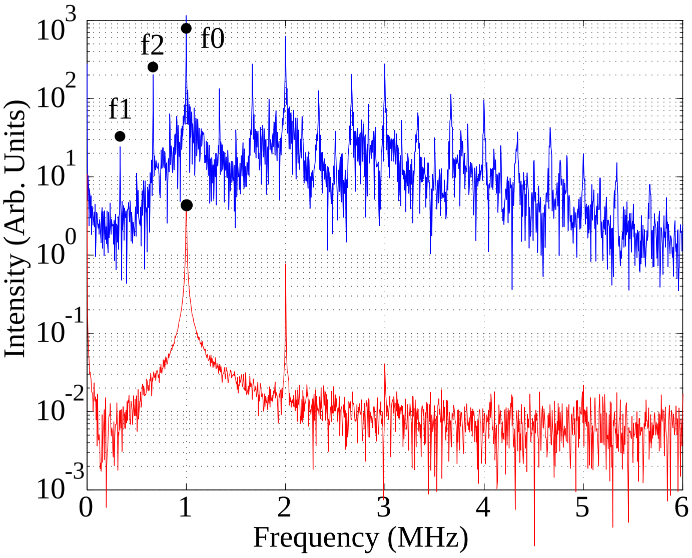

FIGURE 5.11: Control to period 3. Lower trace is the frequency spectra of the pump where the modulation frequency is indicated by a dot. The upper trace is the frequency of the FIR laser during modulation. f0,f2,f1 indicate the fundamental pulsation frequency f_0, and the rational subharmonics $\frac{2}{3}f_0$, and $\frac{1}{3}f_0$ respectively. Note the presence of higher harmonics of these frequencies.

Generalised synchronisation for period 3

As shown in figure 5.12a five regions of different modulation frequencies were separated equally by regions of no modulation as shown in the lower traces starting at

1.45ms in figure 5.12a, and ending at 3ms in 5.12e. Control to period 3 is shown in figure 5.12(e), and (d) which correspond to a modulation frequency of 620.2KHz, and 643.3KHz respectively, and amplitude of approximately 0.05. Control is lost outside these values but at $f = 643.3$KHz, and 650.0 there is phase synchronisation in both cases since there are no phase slips, and the average frequencies of the pump modulation and the FIR intensity pulsations are the same. Increasing the modulation frequency further breaks the synchronisation since now there are two phase slips, and the average frequencies of the pump and FIR laser are no longer equal.

The dynamics can be analysed using return map analysis, and calculating the (fft), and is shown in figure 5.13(a–e), which corresponds to figure 5.12(a–e) during the modulation region. The return map of the period 3 orbit has three distinct points which have some spread due to noise, and limited amplitude resolution of 8 bits. The associated fft shows well-defined sharp peaks as shown in figure 5.13 (e), and (d). The remaining plots lack a regular structure in the return maps, and sharp well-defined peaks in the fft spectra, although there are hints of period 3 in the spectra of the synchronised regions in (b), and (c).

The time differences between adjacent pulse peaks were calculated by fitting a quadratic curve to each pulsation peak in the time series, and obtained an improved estimate of the true peak by extracting the maximum value of the analytic curve, which also gave the associated time for that peak. This procedure was applied to the FIR intensity time trace during the modulation regions, and the variance was calculated using a time difference vector, and the period of the pump modulation as the mean. The controlled state from figure 5.12e gives the lowest variance as shown in figure 5.14.

We found that the laser output contains harmonics of the pump modulation frequency when it was chosen to be about 10% higher than f_0. However, if we bring the modulation frequency to within a few percent of f_0, we find that subharmonics

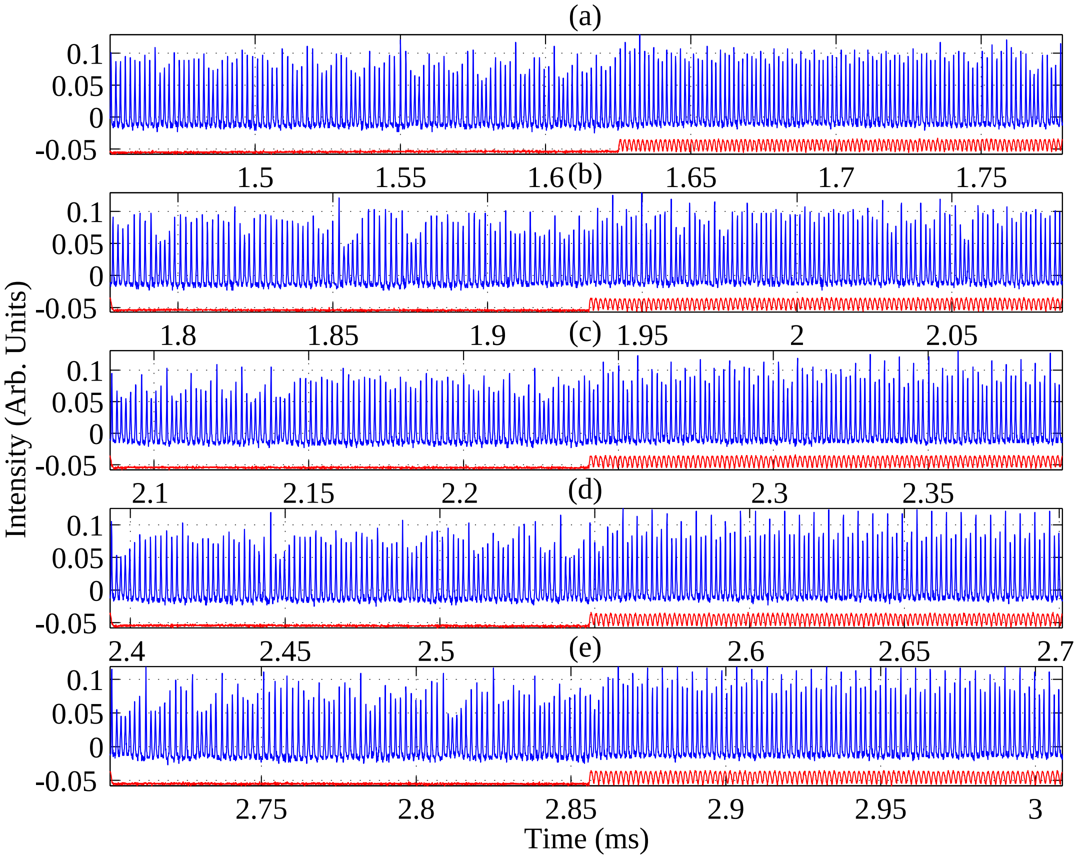

Figure 5.12: Synchronisation and control to period 3. Five different modulation frequencies are applied to (a), (b), (c), (d), and (e) corresponding to 656.5, 650.0, 643.3, 636.8, and 630.2 KHz respectively. The intensity dynamics is uncontrolled in (a) both in amplitude and phase. Synchronisation occurs at (b), and (c) where there are no phase slips, but the intensity is not controlled. The intensity dynamics is controlled to period 3 at modulation (d), and (e) where both phase, and amplitudes are locked.

emerge in addition to the pump harmonics. The frequency width of the control window was calculated to have a lower bound of 1% at an amplitude of about 0.05 which is preceded by synchronisation of frequency width 1%. Once the system lies within the synchronised region then control can be easily found from this position since it lies within the synchronised region.

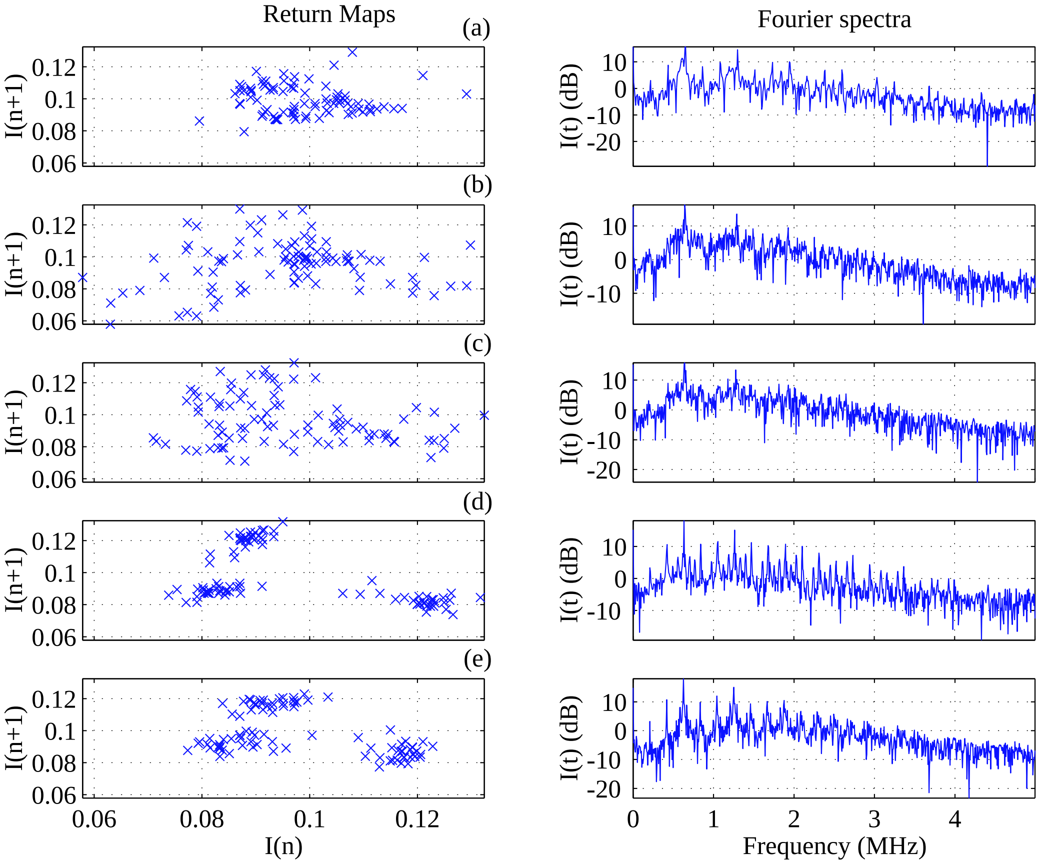

Figure 5.13: The return maps and fft of the associated intensity time traces from figure 5.12 are calculated. Control emerges as distinct point (with some spread) in the return map, and distinct sharp peaks in the fft.

5.3.3 Subharmonic pump modulation, subharmonic generation - control to period 1

Consider the chaotic spectrum of Figure 5.3. The results of the last two sections were obtained by modulating at a frequency near to the first peak of the chaotic spectrum, f_0. If we instead modulate at half this frequency, Figure 5.15 shows the result. There is transient behaviour for approximately 20 cycles before the FIR laser output is controlled to period 1 at f_0. This is clearer in the associated frequency spectrum shown in Figure 5.16 (a) and (b). As previously, there are sharp well defined harmonic peaks

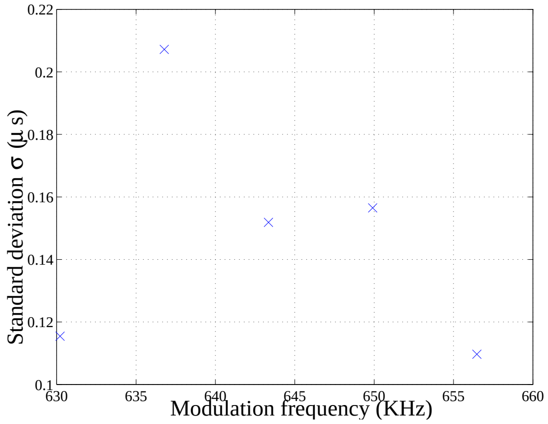

Figure 5.14: The standard deviation of the FIR orbit periods to the period of pump modulation. The deviation is lowest at the controlled state (e) from figure 5.13,

in the FIR laser output spectrum which shows periodic behaviour. However, now the main pulsation frequency of the laser is at twice the pump modulation frequency. Figure 5.16 (c), the ratio of the modulated to the unmodulated spectra, shows that the enhancement of $\frac{1}{2}f_0$ (located at 0.4 MHz) is slightly larger than at f_0. However the time trace in Figure 5.15 clearly shows the main pulsation frequency to be at f_0, not at $\frac{1}{2}f_0$. This is evident in the FIR output spectrum in Figure 5.16a since the signal at f_0 is larger than at $\frac{1}{2}f_0$ due to the fact that the baseline at f_0 is higher than at $\frac{1}{2}f_0$. This suggests that the mechanism for control could be that the unstable periodic orbit at $\frac{1}{2}f_0$ has been stabilised, or that the second harmonic of the pump, is stabilising the unstable periodic orbit f_0 of the FIR laser. The presence of these two harmonics in the pump dynamics makes this distinction ambiguous.

5.3.4 Subharmonic pump modulation and subharmonic generation - control to other periods

We now look for locking ratios other than 1/1, which is the ration of the pump modulation frequency to the FIR pulsation frequency, with the aim of stabilising

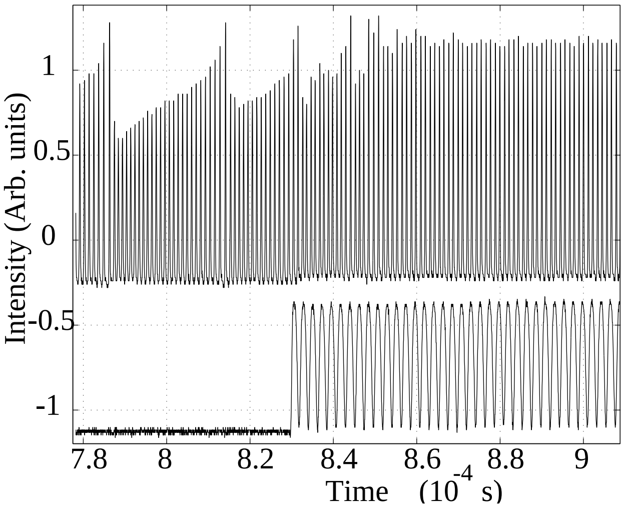

Figure 5.15: Control to period 1 from an initially chaotic state. Upper trace is the FIR laser intensity output, lower trace is the modulation applied to the pump at $\frac{1}{2}f_0$.

other unstable periodic orbits that may exist. We do this by systematically stepping the modulation frequency with a fixed amplitude to search for periodic outcomes. Figure 5.17 is a graphical description of this experiment. The lower trace shows the variations in pump power imposed by the AOM. We fix the amplitude and reduce the frequency of modulation in five discrete steps each of which lasts about 100 cycles. These are separated by unmodulated periods lasting the same amount of time. This is schematically (the actual frequency is too high to represent) shown as sine waves separated by horizontal lines in Figure 5.17. This sequence is sandwiched between two ramp functions.

The purpose of the ramp is to locate the chaos threshold for the laser system. This was used to check that the modulation sequence remained above the chaos threshold in spite of any parameter drift. The upper trace shows the FIR laser response to these events. For display purposes, only the maximum pulse height is shown.

The first modulation applied in the sequence is labelled "100". The dynamics shown in the upper trace is no longer Lorenz-like but more complicated. (This is

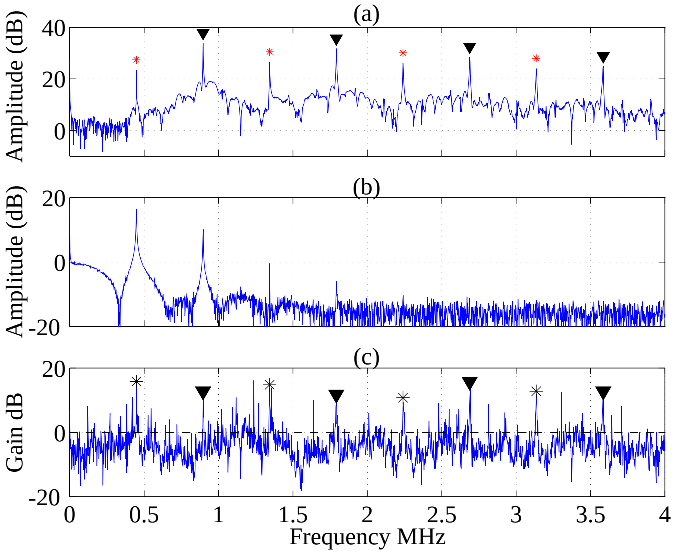

Figure 5.16: Fourier spectra for (a) the pump modulated FIR laser output, (b) the pump modulation and (c) the ratio of the pump modulated FIR laser output to the unmodulated laser output. Triangles indicate the position of the integer harmonics, and the stars indicate multiple of the half integer harmonics. The dashed line indicates the position of zero gain, note that the harmonics and subharmonics of the pump are amplified, all other frequencies are suppressed.

not apparent in Figure 5.17 because of aliasing in the printing). As the frequency is reduced (99) the dynamics is still not simplified. However there is a small section in the time series where the signal is period 4 before complicated dynamics takes over. When the frequency is reduced further (98) there is a small period of transient behaviour at the start of the modulation but the intensity quickly settles down to period 4 pulsations and remains there until the modulation is turned off. This is shown in more detail in Figure 5.18. Decreasing the modulation frequency further (97) destroys any period 4 behaviour in favour of complicated dynamics, although there now is a small section in the time series where period 7 emerges as can be seen at approximately 2.82ms in figure 5.19, but doesn't persist for the modulation duration. Finally, decreasing the frequency by one more step (96) results in the intensity following a period 7 orbit after a relatively short initial irregular behaviour

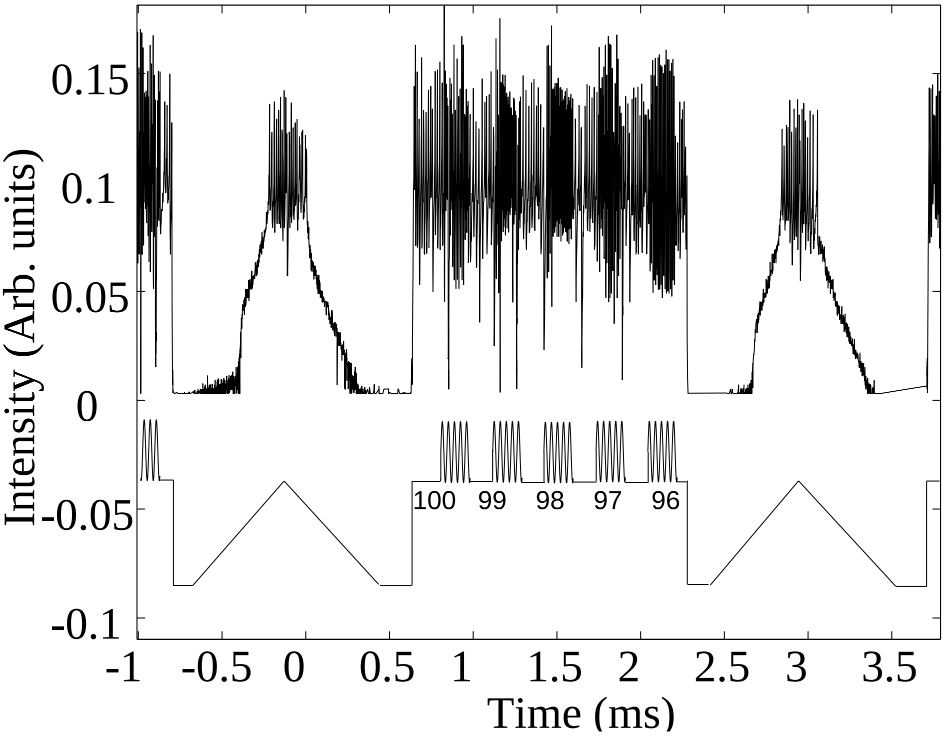

FIGURE 5.17: The lower trace represents the dynamics applied to the pump. This consists of a triangle waveform of low frequency, followed by five sinusoidal waveforms labelled 100,..,96 (with relative frequency 100,..,96 respectively), and are 656.7KHz, 650.1KHz, 643.6KHz, 637.0 KHz, and 630.4KHz respectively, followed by another slow triangle waveform. The triangle waveform is used as a diagnostic to locate the chaos threshold. The five sine waves represent a systematic stepping through the frequency parameter at fixed amplitude. This gives us information on how close controlled orbits are in frequency, and the width of control. The upper trace is FIR laser output where only the intensity pulse peaks are displayed.

as shown in figure 5.20. These results are typical. It is instructive to analyse the dynamics of the system by constructing a Lorenz Map from the intensity data. This is a plot of the peak intensity of a pulse against the peak intensity of the previous pulse [61]. For a Lorenz-like chaotic system a cusp shaped curve is traced out [108]. Figure 5.21 shows the Lorenz Maps of the chaotic system (a) without modulation and (b) with modulation for the period 4 case. Without modulation there is the characteristic cusp shape indicative of chaos. With modulation four definite regions

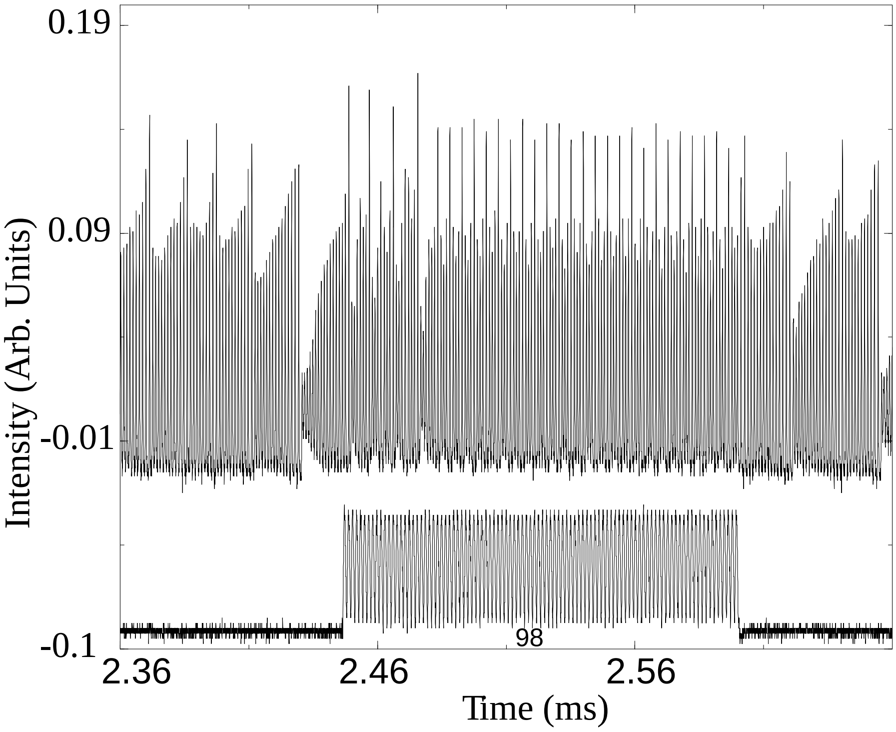

Figure 5.18: Expanded view of the third modulation segment labelled “98” in figure 5.17. This shows period 4 pulsations exist after 32 irregular pulses after the application of modulation.

become apparent. A return map is also shown during control to period 7 in figure 5.22 where there are four distinct regions, and the remaining three are all approximately located at (0.1, 0.1) and cannot be distinguished. All points are connected by lines to give time ordering information, so that periodic behaviour can be easily distinguished from a non-periodic signal or chaos, since a period n signal will appear as an n-sided polygon. The lines outside this polygon are due to the transient behaviour before control. This behaviour is due to the non-perfect intersection of the attractor corresponding to the unmodulated chaotic laser, with the attractor of the modulated laser, and the weak stability of the new attractor as discussed earlier. Sampling error and detector noise cause the four points of the polygon to have some spread from an ideal polygon generated from noise-less points. Figure 5.23 (a1) and (b1) are the

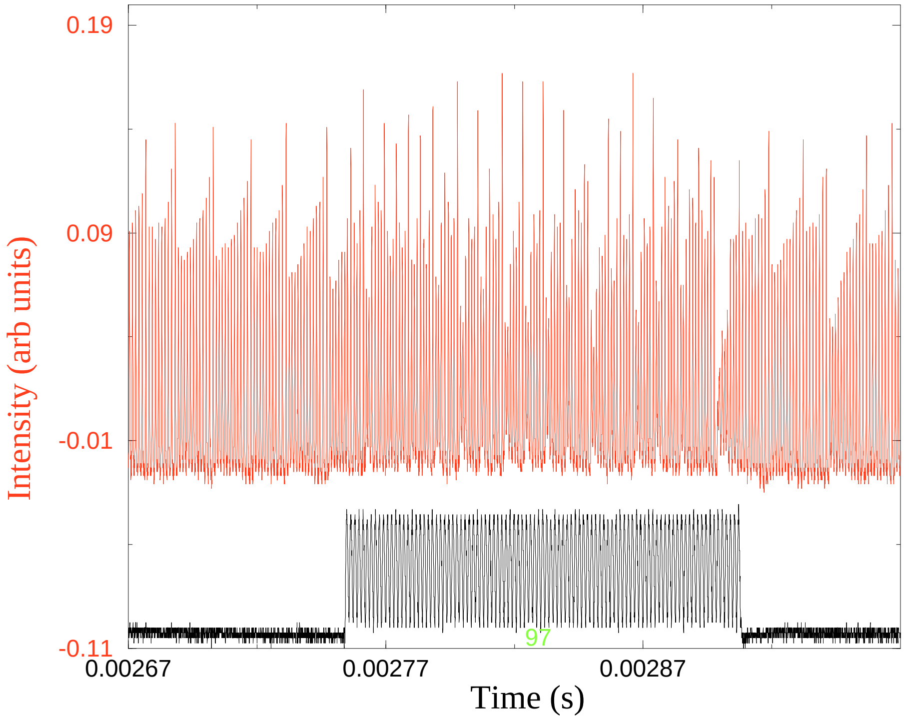

Figure 5.19: Expanded view of the third modulation segment labelled “97” in figure 5.17. This shows a window of period 7 pulsations before chaotic pulsations dominates.

spectra of the modulated FIR laser for period 4 and 7 respectively. The associated pump spectra are shown on plots (a2) and (b2). The stars in the figure indicate the positions of the rational harmonics of the fundamental pulsation frequency f_0 (largest peak) of the FIR output. The modulation frequency of the pump for the period 4 and period 7 case are coincident with $\frac{3}{4}f_0$, and $\frac{5}{7}f_0$ respectively.

To observe the effect of a weakly stable attractor, a modulation is applied which is just outside the edge of an Arnold tongue. The intensity time trace is displayed in figure 5.24 where the laser is initially chaotic for half the time, and modulated for the remainder. There appear bursts of period 4 behaviour at $-0.36 < t < -0.3$ms, and at $-0.27 < t < -0.25$ms which becomes more obvious as these period 4 temporary

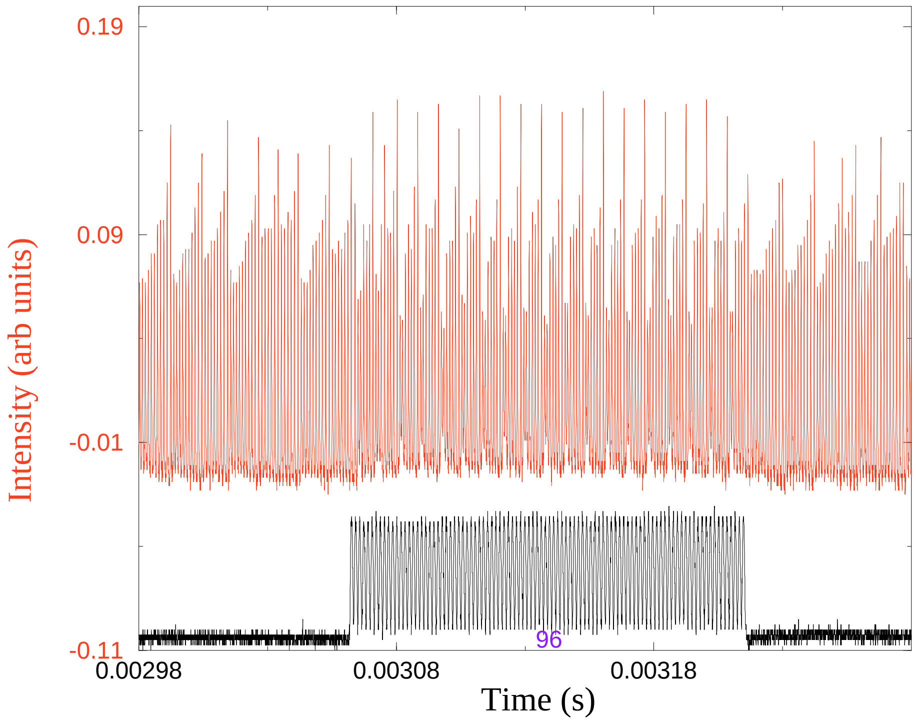

Figure 5.20: Expanded view of the third modulation segment labelled "96" in figure 5.17. This shows control to period 7 pulsations after the application of modulation.

windows are highlighted in the return map of figure 5.25 (lower plot).

The upper return map is calculated from the laser intensity before the modulation was applied. These results indicate there is a weakly unstable period 4 saddle orbit which is capable of controlling the system if the trajectory in phase space is sufficiently "close" to the weakly unstable periodic orbit. Shifting the modulation frequency can cause this effect to either vanish or lock the system onto a period 4 orbit. This effect was observed in figure 5.17 where control to period 4 occurred at $f = 643.6$KHz, and at $f = 637.0$KHz period 4 emerged for a few cycles then was extinguished in favour of non periodic dynamics.

The gain of all the harmonics is calculated for period 4 and period 7 which is

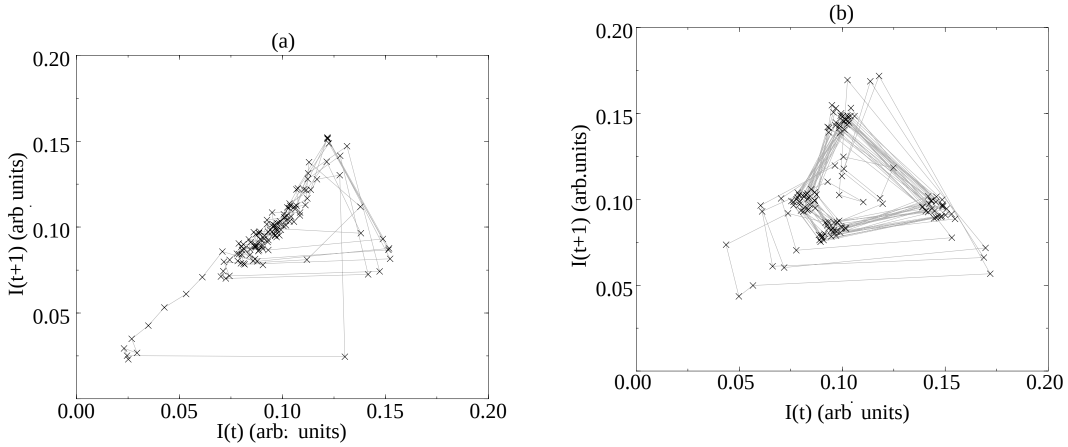

Figure 5.21: Lorenz Maps of the FIR laser output are constructed from Figure 5.18. (a) without modulation and (b) with modulation. The cusp shape in (a) is characteristic of Lorenz-like chaos. The polygon shape of (b) when the points are joined shows period 4 pulsations.

shown in figure 5.26. The first black triangle in the figure with the lowest frequency corresponds to the gain at this modulation frequency f_0. Integer multiples of this frequency are not present in the pump modulation frequency, but are FIR harmonics of f_0. The fundamental pulsation frequency does not correspond to the harmonic with the maximum gain because the FIR frequency components at the rational harmonics are very small when no modulation is present, while there is a significant f_0 component. The initially smaller signal is further from the saturation level than the F_0 component so it will have a higher gain when modulation is applied. The fundamental pulsation frequency f_0 dominates the spectra as seen in figure 5.23 despite having a lower gain since it initially had a significant component before modulation was applied.

A similar sequence of modulation was applied to the pump which resulted in the generation of a period 6 orbit shown in Figure 5.27. The frequency spectra of the modulated pump and laser output are shown on Figure 5.28. It is clear that the pump modulation frequency is not on the fundamental pulsation frequency of the

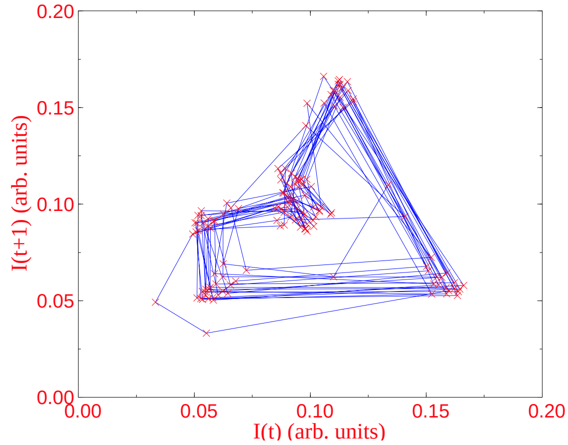

Figure 5.22: Lorenz Map of the FIR laser output is constructed from Figure 5.20 during the modulation cycle. A seven sided polygon is traced out where four points are distinct, while the remaining three points are all located at approximately (0.1, 0.1).

laser output f_0, but at $\frac{5}{6}f_0$.

These results show that the fundamental pulsation frequency of the FIR laser f_0 does not coincide with any of the harmonics of the pump, since control to period 4, 6, and 7 required a modulation frequency of $\frac{3}{4}\mathrm{f}_0$,$\frac{5}{6}\mathrm{f}_0$, and $\frac{5}{7}\mathrm{f}_0$ respectively. From the time domain we know that the pump modulation and the FIR laser output are phase locked. This shows that there are three Arnold tongues with locking ratios 3:4, 5:6, and 5:7 respectively. For the real Lorenz equations, locking ratios of the form $(l-1):l$ and $(l-2):l$ were predicted for $l > 10$ [90]. In our case l was 3, 4, and 5 respectively.

It has been found that the dependence of the locking ratios on a control parameter forms a devil's staircase in the circle map [109] and in the Bonhoeffer Van der Pol model [110], and is considered to be a universal phenomenon. The devil's staircase is made up of rational numbers belonging to the Farey sequence. That is, given two locking ratios $\frac{p}{q}$ and $\frac{r}{s}$ there can be another locking ratio of $\frac{p+r}{q+s}$ restricted to $|ps - qr| = 1$. We have found six of these locking ratios; 1:1, 1:2, 1:3, 3:4, 5:6,

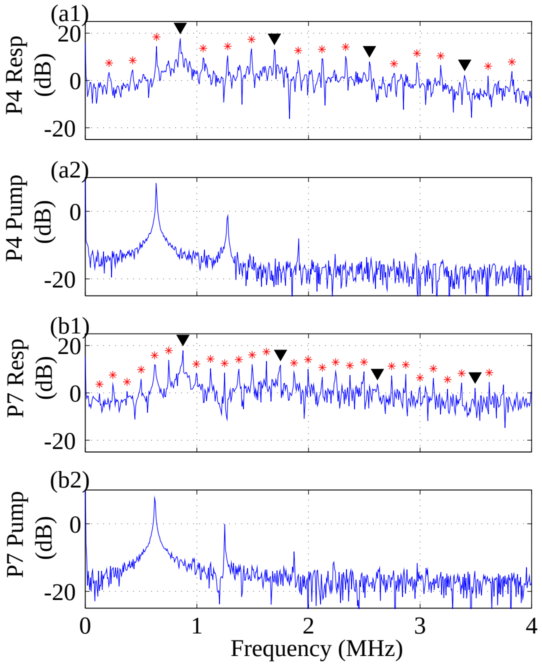

Figure 5.23: Fourier spectra for two different harmonic generation experiments: a1, and b1 are the spectra of the FIR laser during modulation to give periods 4, and 7 respectively. The corresponding dynamics applied to the pump are shown in a2 and b2 respectively. The triangles indicate the position of the integer harmonics, while the stars indicate rational harmonics. In both cases the maximum peak in the FIR spectra correspond to the fundamental pulsation frequency of the unmodulated chaos.

and 5:7. These lie on six stairs of the devil's staircase on a graph of locking ratio against modulation frequency. We cannot explicitly assign lengths to each of these stairs as the modulation frequency could only be altered in discrete steps (1%). To get an estimate of the lengths of each of the stairs we return to the experimental data summarised in Figure 5.17. The segments labelled (99) and (97) show windows of period 4, and period 7 respectively, before complicated dynamics takes over as mentioned earlier. This is not a simple phase slip of the period 4 and period 7 orbits, as can occur at the boundary of an Arnold tongue [111]. Therefore these two segments lie outside the Arnold tongues, and hence we can be sure that the width of these tongues is less than 1% for a modulation depth of 20%. The period

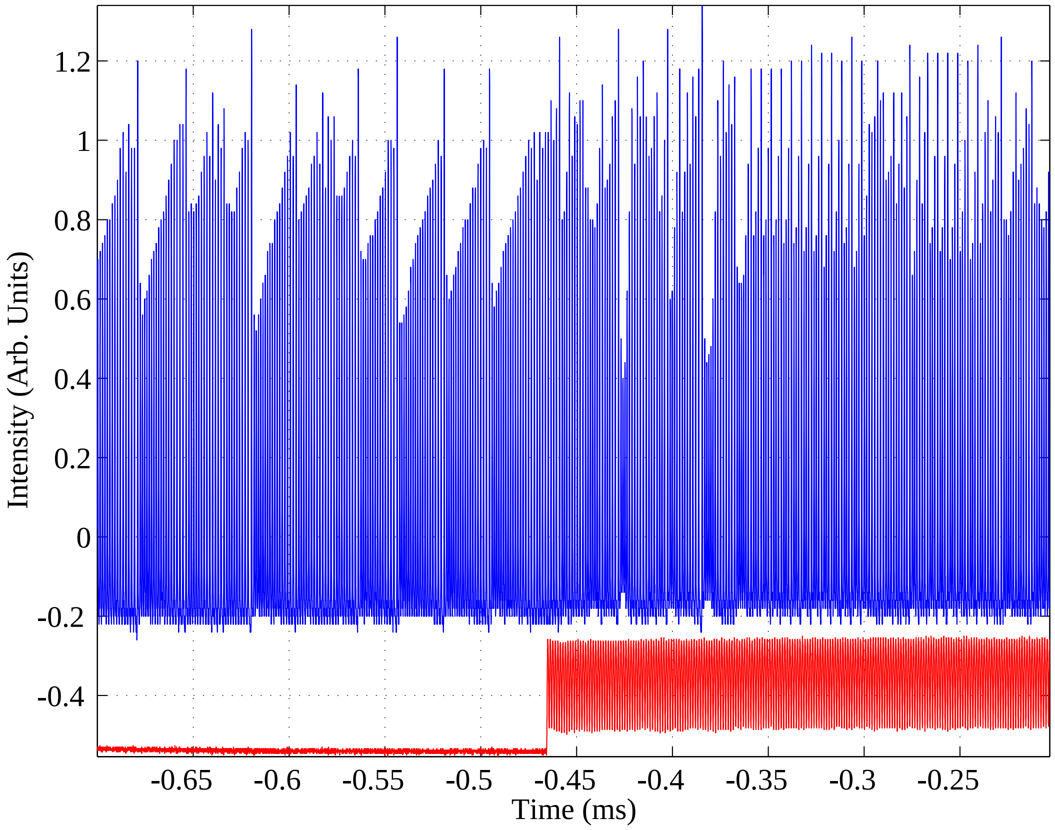

Figure 5.24: Almost control to period 4 where bursts of period 4 occur at $-0.36 < t < -0.3$, and $-0.27 < t < -0.25$ (in milliseconds), but are uncontrolled outside these time windows.

4 and period 7 orbits which briefly appear are the result of the trajectories in phase space finding a weak period 4 and period 7 saddle orbit. The trajectories follow the stable manifold for a few periodic cycles before the unstable manifold of the saddle orbit takes effect and repels it to another torus. Therefore we know the lengths of the stairs in the devil's staircase of our data would have an upper bound of 1% of the modulation frequency, and a non-zero lower bound since these experiments were repeatable. Thus the narrow width of modulation frequency required to give control strongly suggests that resonance is taking place, that is the mechanism for control

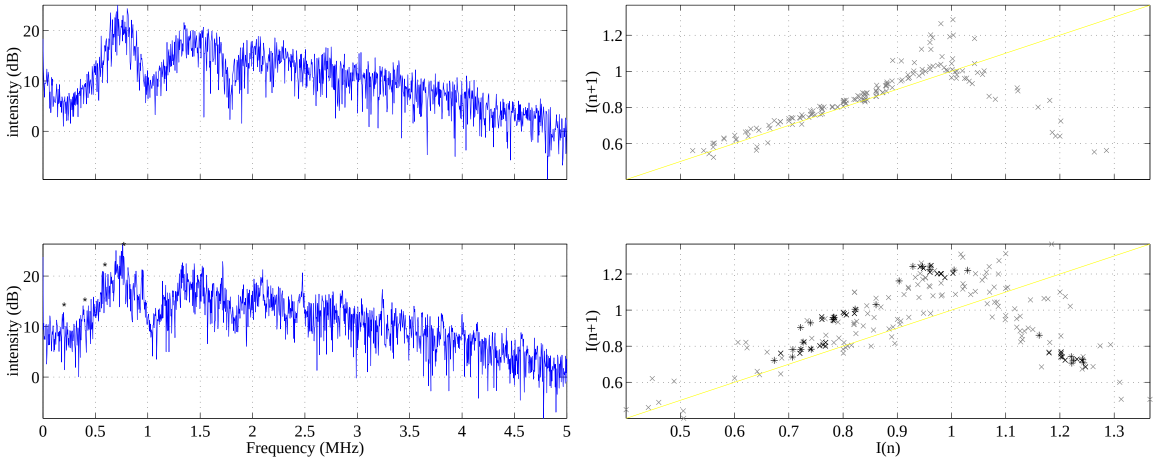

Figure 5.25: The associated fft, and return map for the intensity time trace of figure 5.24 are shown on the left, and right respectively. The upper plots are calculated from the intensity time trace before modulation ($t < -0.47$ms in figure 5.24), and the lower plots during modulation ($t \geq -0.47$ms). The dots are at multiples of $f_0/4$ where $f_0 = 0.76$ MHz.

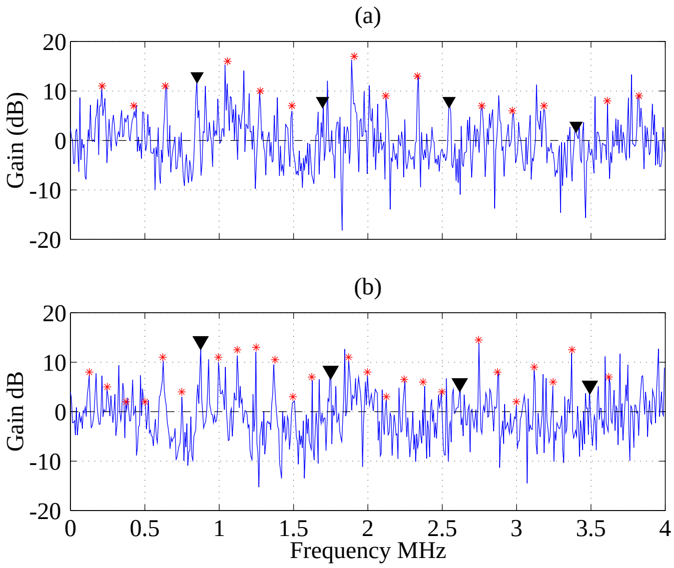

Figure 5.26: Gain is calculated by taking the ratio of the FIR Fourier spectra during modulation to without modulation for the period 4 case (a), and the period 7 case (b). The black triangles indicate integer multiples of the modulation frequency f_0. The asterisks indicate rational harmonics of f_0.

is likely to be stabilisation of the unstable periodic orbit in the modulated system. Measuring different stages of synchronisation has led to measuring a control width of about 2% for period 3, and an additional phase synchronised region of similar width in modulation frequency, which is at least twice the width of the control region for period 3 and period 1.

Experimental difficulties such as drift of the laser parameters and discreteness of modulation frequency make it difficult to locate the position of each stable island in the parameter space. In the next chapter a theoretical treatment is presented that enables a more systematic exploration of the number and structure of these islands in control parameter space [104].

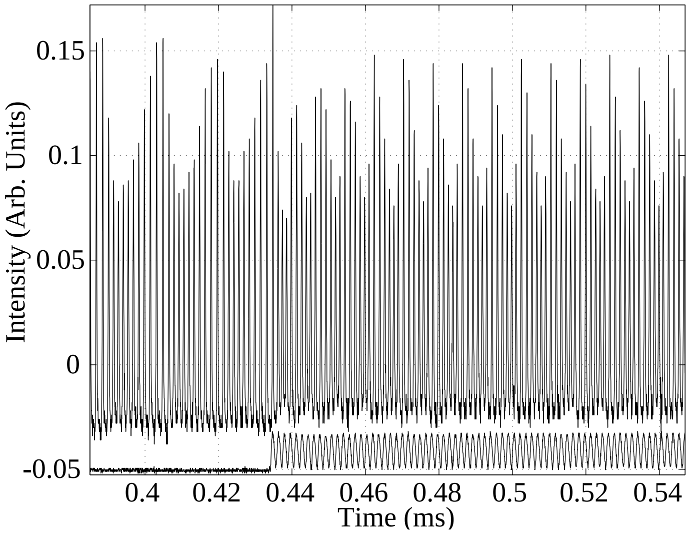

Figure 5.27: Control to period 6. Lower trace is the pump, upper trace is the FIR laser output

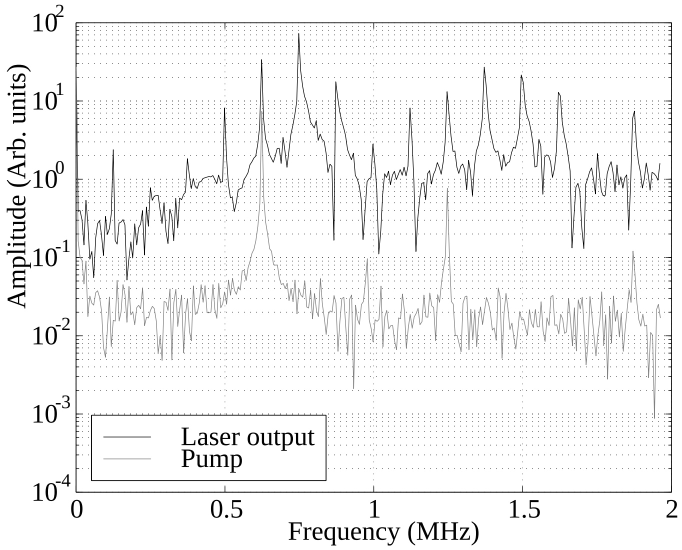

Figure 5.28: Control to period 6. Lower trace is the frequency spectra of the pump during modulation, The upper trace is the frequency of the FIR laser during modulation.

5.4 Conclusion

We have demonstrated experimentally for the first time that a single mode class C laser can be controlled to a periodic state even though it is driven above the chaos threshold, by applying an appropriate modulation frequency to the pump. It is also possible to modulate the pump at the fundamental pulsation frequency of the chaotic laser to generate not only integer harmonics of the pump, but also rational harmonics that are not present in the pump modulation frequency. We have also shown that control is not restricted to modulating at the harmonics of the fundamental pulsation frequency, as pumping at rational values of the harmonic, according to specific values of the Farey sequence, also gave control. We therefore expect there are other locking ratios which could give control. We found that the Arnold tongues were close together but they did not overlap thus allowing control to a unique period for particular parameter values. The width of the tongues in frequency space is very narrow, since changing any parameter of the order of 1% destroyed control. It is likely that the mechanism for control is stabilisation of one of the existing closely spaced unstable periodic orbits in the modulated system.
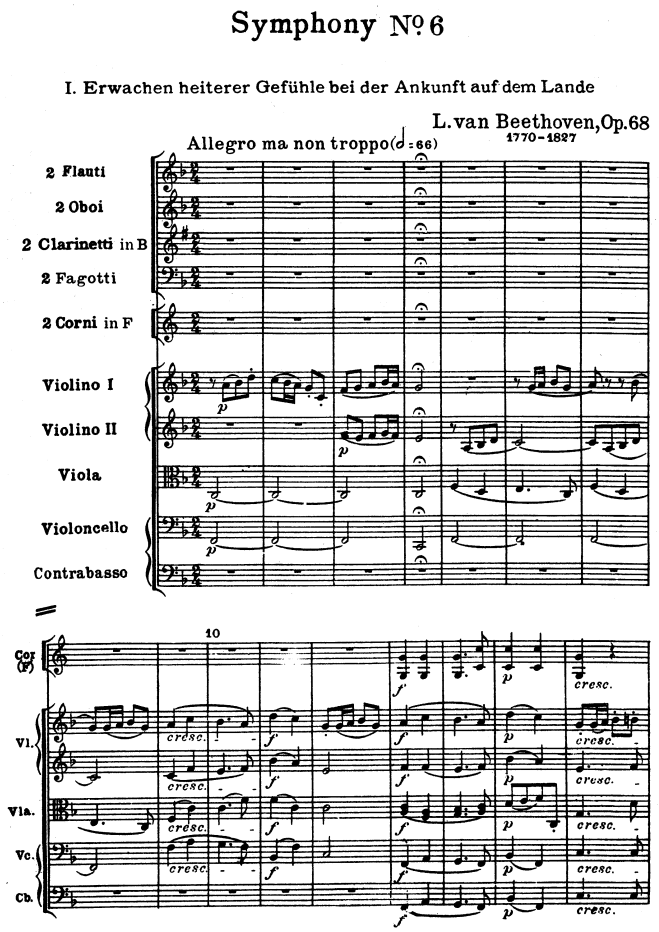
6

Numerical investigation of controlling chaos by periodic modulation

6.1 Introduction

Experimental results presented in the previous chapter show that control of Lorenz-like chaos is possible, so now a numerical investigation of periodically modulating the pump power is made in the chaotic regime using the complex Lorenz equations. The model of the equation 3.1 used is discussed in detail in Chapter 3 and the results can be compared with the experiments. Control of the standard Lorenz equations by modulation has previously been demonstrated by replacing the Rayleigh parameter, R, by $R(1+\sin(\omega t))$ [97, 98, 112]. Since we wish to model an autonomous laser with a modulated pump, we cannot use these results as the transformation from the laser equations to the Lorenz equations assumes the pump is constant. Different transformations must be made which do not involve R (see Appendix B). We show here that when the pump is modulated in our laser model, control to periodic behaviour can be achieved. The total pump power is made to remain above the chaos threshold at all times as in the experiments of Chapter 5, thus excluding a simple delayed bifurcation [65] as the control mechanism.

6.2 The complex Lorenz equations

We investigate numerically the effect of modulating an optically pumped autonomous ring laser above the chaos threshold. We use the Lorenz equations to model the system, which is accurate for a two energy level system, or even a three level system in certain parameter regimes [87]. Previous experiments have shown that an ammonia laser, which is an autonomous system, reproduces the same dynamics as the complex Lorenz equations [71]. The complex equations take into account the possibility that the cavity resonant frequency is detuned from the atomic resonance in general. Using this model we search for control to periodic pulsations which could be seen in autonomous lasers, and investigate different locking ratios between the pump and laser output modulation that may occur. The complex Lorenz equations are:

$$\begin{aligned}
\dot{E} &= -((1+i\delta)E-\lambda P) \qquad (6.1)\\
\dot{P} &= -1/\sigma((1-i\delta)P-ED)\\
\dot{D} &= \beta/\sigma(1-D+f(t)-1/2(E^{\star}P+P^{\star}E)),
\end{aligned}$$

$$\sigma = \kappa/\gamma_\perp \quad \beta = \gamma_\parallel/\gamma_\perp$$

where E, P, and D are the electric field, polarisation and inversion respectively; δ is the detuning of the cavity resonance relative to the atomic line center; κ, $\gamma_\perp$, and $\gamma_\parallel$ are the electric field, polarisation and inversion decay rates respectively; λ is the average pump, and $f(t)$ is the modulation applied to the pump. The parameters in the computations performed here are $\sigma = 1.5$, $\beta = 0.25$, $\delta = 0.2$, and $\lambda = 46$ and are not changed. In our case $f(t) = A\sin(\omega t)$, and for chaos to occur $\kappa > \gamma_\parallel + \gamma_\perp$. This is known as the bad cavity condition since a lossy cavity is required. The pump parameter is written in the form;

$$I_p(t) \quad = \quad \lambda(1 + A\sin(\omega t)) \tag{6.2}$$

where λ is chosen such that $\lambda - A > \lambda_{ch}$ where λ_{ch} is the chaos threshold. Thus the pump parameter I_p is always above the chaos threshold. Since the energy into the laser is varying, this directly effects the population inversion. Previous work has been done using the standard Lorenz equations where the pump parameter λ was replaced by $\lambda(1+A\sin(\omega t))$ [112]. Unfortunately we cannot use this as a correct description of modulation applied to a laser, as the inversion is not directly modulated in that case. Other authors have theoretically found control [97, 103] using the appropriate form of the modulation for our laser, however the total pump power was below the chaos threshold at certain times, i.e. there is a t_1 and t_2 such that $\lambda(1+A\sin(\omega t)) < \lambda_{ch}$ for $2n\pi t_1 < t < 2n\pi t_2$ and n is any integer. This means there is a periodic crossing of the bifurcation point. It has been shown that such a crossing can result in stabilization [65]. Here we ensure that $\lambda(1 + A\sin(\omega t)) > \lambda_{ch}$ for all t so that this mechanism is not the cause of control.

To ensure that the modulated system was initially chaotic, we integrated equation 7.3 in the deep chaotic regime where $\lambda = 46$ and $A = 0$ (no modulation). Periodic behaviour was found for certain values of modulation frequency and amplitude. A simple algorithm was used to identify periodic behaviour in the intensity time series. This involved comparing the size of the last intensity peak with multiples of n previous peaks to give period n, if all the sizes of the peaks were within a prescribed tolerance.

Figure 6.1 shows the Arnold tongues for each period of the signal for pairs of ω and A. An integration mesh of 1200 points on the ω axis and 12 points on the A axis was used, since the sensitivity of the system to ω was much greater than to A. Figure 6.1 shows there are islands of periodic response to modulation at various frequencies and amplitudes of modulation.

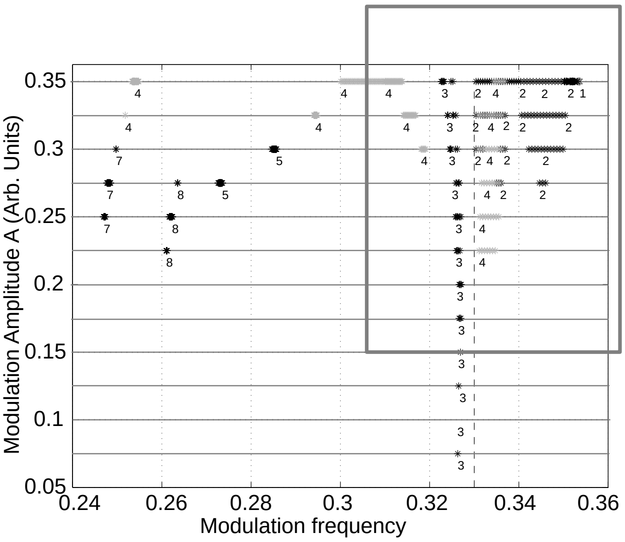

FIGURE 6.1: Control to different periods with various combinations of ω and A. Dark points represent control to the period shown by the number near the points. The light grey band indicates the numerical grid, 1200 × 12. The vertical dashed line represents the average frequency (of 0.33 units corresponding to the scaled time κt as shown at the end of the appendix) of the un-modulated chaos where A=0 along this whole line. The grey box indicates the region where higher resolution calculations were performed shown in figure 6.3

Period 3 dominates the graph near the average pulsation frequency of the un-modulated system shown as a vertical dashed line. The locking ratio, that is the ratio of the pump modulation frequency (ω) to the average pulsation frequency of the intensity, is 1/1 around this line, and p/q further away from this line where p and q

are integers. The island of period 4 centered around the frequency 0.30has a locking ratio $\frac{3}{4}$. On the far left of the graph there is an island of control to period 7, which has a locking ratio $\frac{5}{7}$. Both of these states of control were found in our experiments [113]. The two corresponding (numeric) time traces show control to period 4 and period 7 in Figure 6.2 using typical initial conditions. The lower trace in both plots is the term $A\sin(\omega t)$. The graph shows that the phase between the pump modulation and the output intensity is fixed and commensurate, since every 3 and 5 cycles of the pump for the upper and lower trace respectively, brings the output intensity back to the start of period 4 and 7 respectively. Further analysis of Figure 6.1 shows that

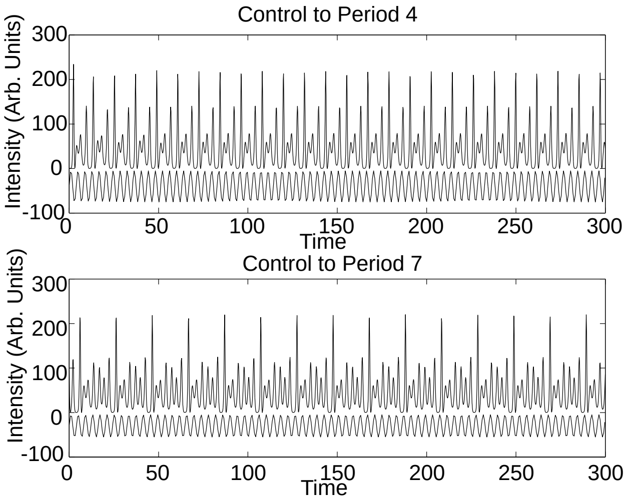

Figure 6.2: Two numeric intensity time traces of control to period 4 and 7 respectively with locking ratios 3/4 and 5/7 respectively using typical initial conditions. The lower trace in both cases is the modulation, the top trace is the intensity $E^*(t).E(t)$. The time units are scaled to the cavity decay rate κ as shown at the end of the appendix. To check for stability we integrated both time traces up to a time of 1500 and found the solution remained periodic.

the modulation frequency affects the average pulsation frequency, even though the average pump power remains fixed at the value λ. For example, period 1 shown in the top far right of figure 6.1 is locked in a 1/1 ratio with the pump, yet the locked frequency is higher than the un-modulated chaos frequency by about 10 %. Figure

6.1 spans a large range of parameter space, so we calculated the periodicity for a particular initial condition over a narrower parameter range indicated by the grey box in figure 6.1, at a much higher resolution. Figure 6.3 shows the result. Increasing the density of the integration mesh has revealed dynamics not seen in the previous calculation. For example, a modulation amplitude of 0.25 in figure 6.1 only shows control to period 3, however in addition to period 3 figure 6.3 shows period 4, 5, 6, and 7 with a significantly narrower window of control in modulation frequency space than for period 3. All the periods in this figure have a locking ratio of $\frac{1}{1}$. This result shows there are even more closely spaced unstable periodic orbits that have been controlled to a periodic state. The shape of the Arnold tongues in figures 6.1 and 6.3 is similar to the triangular shapes obtained in modulated periodic oscillators, except that at higher modulation amplitudes the Arnold tongues become bent due to an increase in nonlinearity.

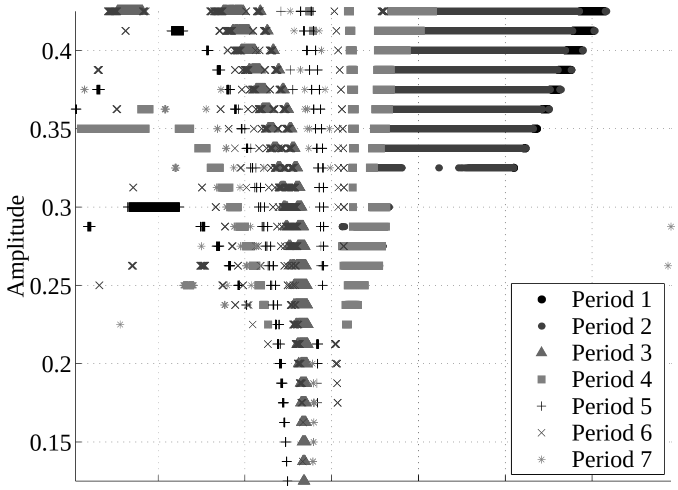

Figure 6.3: Control to different periods with various combinations of ω and A. The frequency corrensponds to the scaled time κt.

Experimentally we found control to periods 1,3,4, and 7 with a locking ratio of $\frac{1}{1}$,$\frac{1}{1}$,$\frac{3}{4}$, and $\frac{5}{7}$ respectively [113]. The amplitude of modulation in all cases was 20% (peak-to-peak). The numerical model agrees well with control to period 3 but the amplitude of modulation required for control is higher for period 4, 7, and 1 where it is 60%, 50% and 70% respectively. Since we use only 2000 initial conditions, it is possible that there are other initial conditions lying on the chaotic attractor which would lead to periodic behaviour at a lower modulation amplitude.

We now investigate the Lyapunov dimension calculated using the Lyapunov exponents [55] of the stabilised system caused by the modulation of the pump. The dimension of the complex Lorenz system was calculated as explained in section 2.2.3, and is approximately 3.1. If the modulation frequency is not a harmonic of the pulsation frequency of the unmodulated laser, or the modulation amplitude is too low, the dimension remains at about 3.1 as can be seen by the grey lines in figure 6.4 and in figure 6.5. When a periodic state is found, the dominant Lyapunov exponent changes from a positive value to zero. All other eigenvalues are negative. If the limit

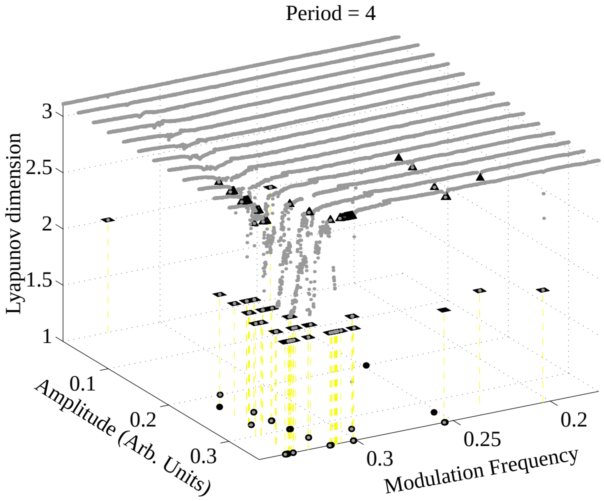

Figure 6.4: This is a plot of the Lyapunov dimension of the modulated system, for different pairs of modulation frequency and amplitude. The chaotic regions are of dimension 3.1 indicated by the grey lines, and the controlled system to period 4 has integer dimension indicated by the black triangles, squares and circles, which represent dimension 3, 2 and 1 respectively. The frequency cornensponds to the scaled time κt.

cycle is one dimensional, then there will be only one zero Lyapunov exponent, and the others will be negative. For a two dimensional limit cycle (two–torus) there will be two zero Lyapunov exponents, and for a three dimensional limit cycle there will be three zero Lyapunov exponents. We find these types of limit cycle occur in our numerical results. Figure 6.4 shows control to period 4, and where chaos remains as a function of modulation amplitude and frequency. The modulation has a much larger impact on the dynamics of the system at the fundamental pulsation frequency (0.33) than at the rational harmonic $\frac{3}{4}f_0$ (at approximately 0.25). This is most clearly seen by observing how the dimension of the chaos changes with amplitude and frequency in both cases. At the fundamental, the dimension of the chaos, even at small modulation amplitudes, drops slightly below 3.1 at the fundamental pulsation frequency.

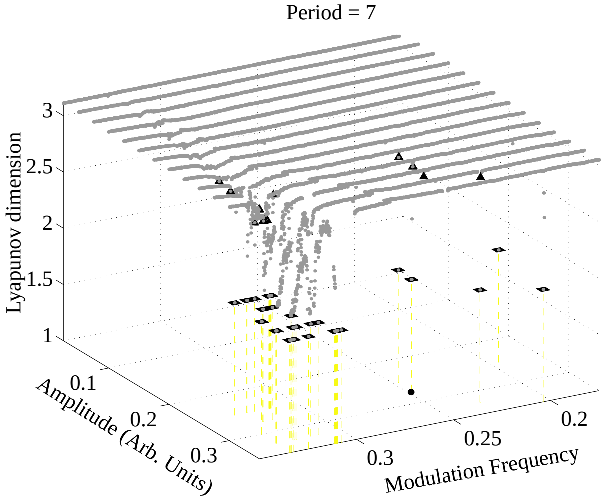

Figure 6.5: This is a plot of the Lyapunov dimension of the modulated system, for different pairs of modulation frequency and amplitude, as in figure 6.4 but for period 7. The frequency corrensponds to the scaled time κt.

This slight drop in dimension becomes progressively deeper approaching 3.0. Once it reaches 3.0 then the system is controlled to a periodic state indicated by the triangles in the figure. At the modulation frequency of 0.25, no such behaviour in the chaos occurs. It remains basically unchanged until the appropriate amplitude is reached, then the dimension drops suddenly to 3.0 and the system is controlled. Notice that the dimension of the stabilised system can change to 3, 2 or 1. Dimension 3 appears first, followed by 2 and 1 confined within a narrow parameter space. At fixed amplitude, the dimension of the controlled system depends on the modulation frequency. There is some maximum width of modulation frequency around 0.33 which gives control; outside this range the system is chaotic. Figure 6.5 shows similar behaviour except that control to period 7 with a dimension of 1 is very rare, but dimension 2 is most common. This is in contrast to figure 6.4 where there were comparable amounts of control to dimension 1, 2, and 3.

We now investigate the dependence of control on initial conditions. We calculated a numerical solution to equation 7.3 without modulation ($A = 0$), and took 2000 (sequential) points lying on the chaotic attractor as the initial conditions for the system under modulation ($A \neq 0$). We do this as we assume the modulated system is initially free from modulation for a period of time such that the points in phase space lie on the attractor of this unmodulated system. The modulated system was integrated using the 2000 initial conditions, and for each initial condition we integrated the equations for different pairs of parameters ω (the modulation frequency), and A (the amplitude). For these pairs of parameters and initial conditions, the periodicity of $E^*(t) \cdot E(t)$, the intensity, was calculated. The solution was defined as periodic if a particular initial condition $\mathbf{x}_i$ and its neighbour $\mathbf{x}_{i+1}$ or $\mathbf{x}_{i-1}$ also gave a periodic solution. We found that if this didn't hold then the solution is not really periodic, as these points do not give periodic solutions when slight modifications are made to the integration routine. In the former case the solutions remain periodic. The periodicity of the signal was then calculated using the last half of the intensity time trace, thus ignoring any transient behaviour that may have occurred.

Not all the points lying on the initially chaotic attractor ended up on the limit cycle generated by the application of the modulation. Of the 2000 initial conditions used, only a small subset of these points (< 5%) lead to control for a particular modulation frequency and amplitude. One should note that these initial conditions cover only a very small part of the five dimensional chaotic attractor, so a more exhaustive coverage is required to make strong claims about basins of attraction, but is computationally intractable as many billions of initial conditions would be required.

Figure 6.6 is a plot of the locking ratio as a function of the applied modulation

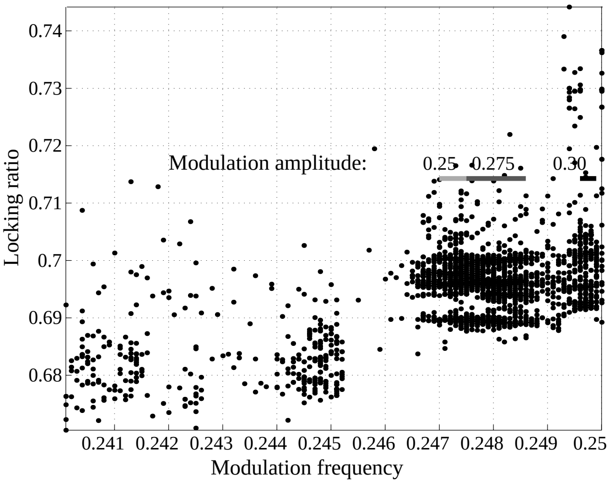

Figure 6.6: Projection of the four variables: locking ratio, modulation frequency, amplitude, and initial conditions to locking ratio Vs modulation frequency. Only the amplitudes A=0.25, 0.275, and 0.30 during control to period 7 are labeled. Other points are a mixture of these three amplitudes and different initial conditions. Scattered points show uncontrolled behaviour while a solid line represents control to period 7. Notice the scattered points below the dark lines showing that modulation frequency and amplitude is not enough to control the system, since the only difference between the line and points here is the initial conditions. The frequency corresponds to the scaled time κt.

frequency. Each point on the graph corresponds to one of three amplitude values, A=0.25, 0.275 and 0.3 which are not distinguished in the figure. The scattered points represent uncontrolled states as the locking ratio is not rational. The grey lines represent control to period 7 at amplitudes A=0.25, 0.275 and 0.3 which is marked on the figure. These lines correspond to a locking ratio of $\frac{5}{7}$. All points on the graph correspond to particular initial conditions which in general are different from each other, but some are the same. Note that this information cannot be extracted from the figure. Control is not uniquely determined by modulation frequency and amplitude alone. This is evident in figure 6.6 by considering the modulation frequency 0.248 and amplitude marked 0.275. This grey band corresponds to control as mentioned above, however some of the scattered points below this line also correspond to an amplitude of 0.275 (not evident in the figure). These points don't correspond to control as the locking ratio is not rational. Thus only some of the initial conditions lead to control. The grey lines of control have a length which is determined by the combination of the maximum allowed frequency deviation from the center for fixed initial conditions, and the maximum frequency deviation for a range of adjacent initial conditions. Now if the frequency is shifted further, control to period 7 is lost for all initial conditions and amplitudes tested. The resulting locking ratio for each initial condition in this case will vary from 0.67 to 0.7 as can be seen at frequency 0.241.

Generalised synchronisation

The dynamics near a periodic state is now analysed by searching for generalised states of synchronisation as was done experimentally in the previous chapter. Figure 6.7a indicates the regions where control to period 5, 3, and 7 occur as a function of modulation frequency, which was calculated in intervals $\Delta f = 0.00001$. At all other values of frequency non-periodic solutions were found. The relationship between the phase slips occurring between the pump modulation frequency, and the intensity pulsation frequency as a function of modulation frequency is shown in figure 6.7b. The total phase slips were calculated during the modulation segment which corresponds to about 4000 intensity pulses, and is labelled "Total". At the state of control, a low number of phase slips appears which is either due to transient irregular behaviour lasting some tens of cycles before the dynamics becomes regular, or a periodic state which occasionally phase slips without the presence of irregular behaviour during the modulation period. To distinguish between these two scenarios, the number of phase slips were calculated after the end of the transient behaviour before control emerged if it existed, and is labelled "Non-transient" in figure 6.7b. On closer inspection the number of non-transient phase slips is zero for the corresponding periodic states in figure 6.7a. The phase dynamics of the intensity solution is synchronised to the pump between 0.3227, and 0.3305 for $A = 0.175$ which is significantly larger than the regions of control indicated in figure 6.7a. This window of synchronised behaviour reduces with amplitude as can be seen by the grey curve in figure 6.7b which corresponds to $A = 0.15$. The largest Lyapunov exponent calculated using the Wolf method [114] discussed in section 2.2.3, is shown in figure 6.7c, and the remaining exponents were calculated, but are not displayed since they were found to be less than or equal to

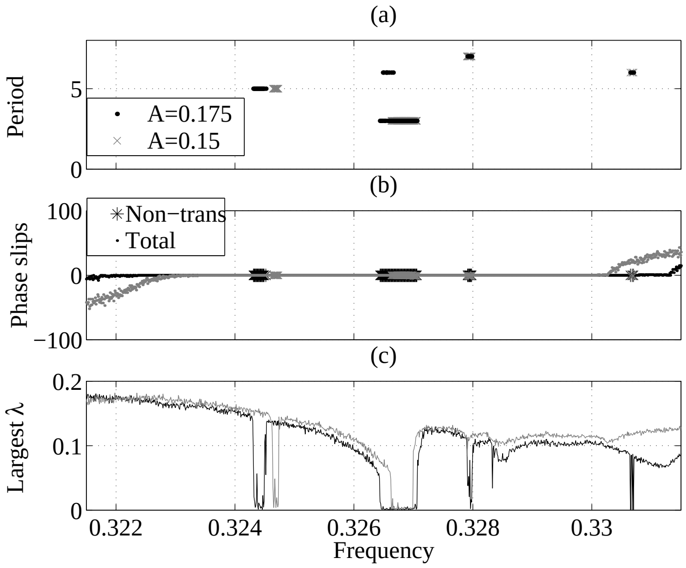

Figure 6.7: The regions of control to a periodic state as a function of modulation frequency is shown in (a). The horizontal frequency axis was divided up into 1000 points where the periodicity of the intensity was determined. No other periodic state were found at this frequency resolution $\Delta f = 0.00001$, and corresponds to the white region of the graph. The phase slips between the pump modulation and intensity is shown in (b) and is labelled "Total", and "Non-transient". See text for explanation. The corresponding largest Lyapunov exponent is shown in the bottom figure indicating a zero exponent during the regions of control, and positive outside this region.

zero, so does not contribute to any instability. Hence the exponent in figure 6.7c can be considered an upper bound to the entropy of the system by using equation 2.29. During the regions of control indicated in figure 6.7a, the Lyapunov exponent has dropped rapidly to zero, therefore the entropy is also zero for the system. The Lyapunov exponent is positive within the synchronisation region, and begins to decrease slowly as the modulation frequency approaches the control region. On closer inspection, there is a significant jump appearing at $f = 0.3305$ corresponding to the point of loss of synchronisation. The loss of synchronisation at $f = 0.3227$ corresponds to a small but sharp bend in the eigenvalue as the frequency decreases. The width of the control window is less than one tenth of the width of the window of synchronisation for period 3, and even narrower for period 5.

The phase difference between the pulse peaks of the intensity, and the applied periodic modulation is averaged over the duration of the modulation to give an average phase difference as a function of modulation frequency. This is then normalised to the modulation period, and the result is shown as a continuous curve in figure 6.8. For comparison, the period is displayed on the right hand axis as short line segments. The average phase difference is approximately constant during the regions of control, and steadily increases with increasing modulation frequency. Synchronisation is destroyed at an average phase difference of 0.45 which is less than half the pulsation period of the applied modulation. No synchronisation would be expected at values greater than 1/2 since the next pump pulse will be too close and cause instability. This is clearly explained in modulated periodic oscillators if we let the phase difference θ in equation 1.1 become slightly larger than half a pulse period so that $\theta = \pi + \epsilon$ for small ϵ, then equation 1.1 approximates to

$$\dot{\theta} = \Delta\omega + C\epsilon \tag{6.3}$$

hence the phase becomes unstable.

These results show that the window of synchronisation is relatively large compared to the windows of control, and finding the synchronisation region is a useful for locating the windows of control. Phase control can still be achieved at modulation frequencies outside the control range.

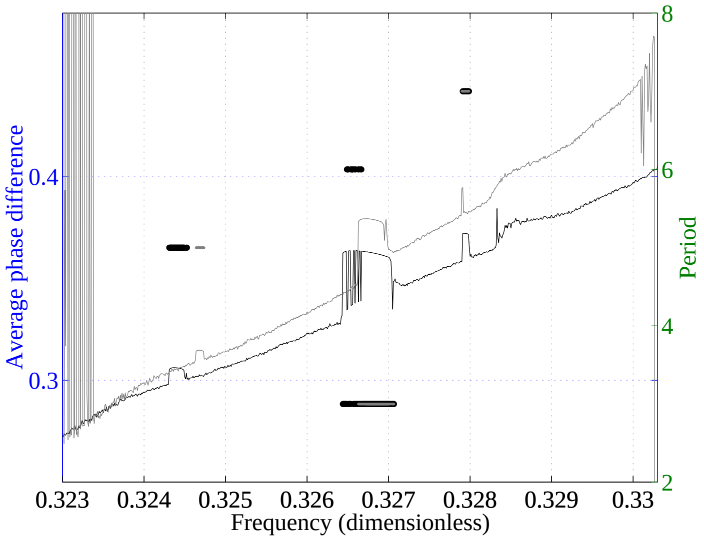

Figure 6.8: The average phase difference between the pulse peaks of the driving periodic modulation, and the pulse peaks of the intensity normalised to the average driving period as a function of modulation frequency is shown on the left hand axes as a continuous line. The period of the intensity pulsations is calculated, and the integer values are plotted as segments which correspond to the period values corresponding to the right hand axis. Non periodic regions are the regions in between the segments of control. During control the average phase difference is constant but varies otherwise.

Scaling of phase slips with modulation frequency

Now that the region of synchronisation has been established, and that phase slips occur outside the synchronised region, the question of how the phase slips scale with modulation frequency is addressed. Two types of scaling behaviour are discussed in section 1.2. The first is super long laminar behaviour where the phase slips become exponentially rarer as the frequency approaches the value corresponding to the synchronised state, ν_c. The average time between phase slips is given by equation 1.2 which is,

$$\ln\frac{1}{\tau} \approx |\nu - \nu_c|^{-1/2}. \tag{6.4}$$

In the second case the phase slips follow a type 1 intermittency, where the average time between phase slips is given by equation 1.3 and is,

$$\tau \approx |\nu - \nu_c|^{-1/2}. \tag{6.5}$$

To investigate whether the phase slips here follow the appropriate scaling laws, equation 6.4 is rearranged,

$$\frac{\gamma}{(\ln(n/T))^2} = |\nu - \nu_c|, \tag{6.6}$$

where γ is an arbitrary constant, and equation 6.5 can be rearranged to give,

$$\gamma(\frac{n}{T})^2 = |\nu - \nu_c|, \tag{6.7}$$

again, γ is an arbitrary constant, T is a time interval taken as 12000 time units, and n is the number of phase slips which occur in the time interval T. If the phase slips data from figure 6.7b (grey curve) follow the two scaling laws, then a linear relationship should be expected between $(\ln(n/T))^{-2}$ and ν for super long laminar behaviour, and $(\frac{n}{T})^2$ should be linear with ν during intermittency. These plots are shown in figure 6.9(a), 6.9(b), and 6.9(c), 6.9(d) respectively. The plots (a), (c), and (b), (d) correspond to analysing the phase slips on the left, and right edge of the Arnold tongue respectively, which are located at $\nu = 0.3234$, and $\nu = 0.3301$ for a modulation amplitude of $A = 0.15$. The left edge of the Arnold tongue is now considered ($\nu = 0.3234$). As ν is decreased from the synchronised state, plot(a) shows a linear relationship for $0.322 < \nu < 0.3234$ before the slope decreases. This suggests

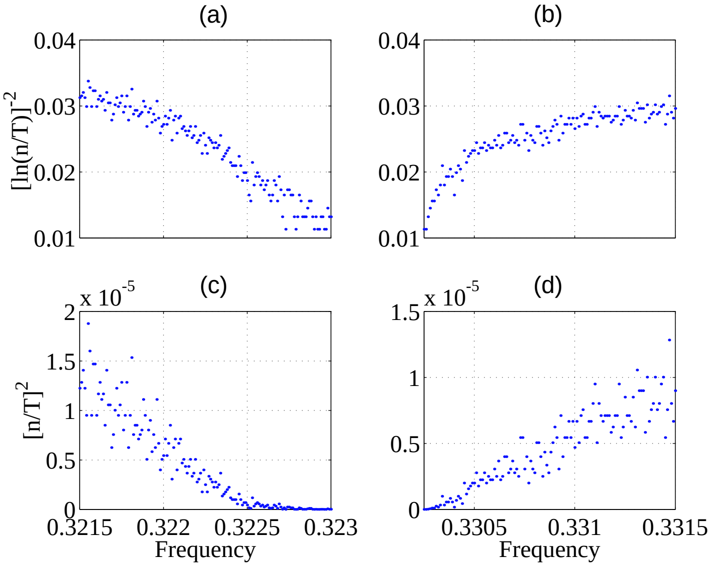

Figure 6.9: This shows the existence of two scaling laws for phase slips beyond the synchronised state, corresponding to the grey line in figure 6.7b with modulation amplitude $A = 0.15$. The edges of the Arnold tongues are located at $f = 0.3234$ and $f = 0.3301$. See text for details.

that super long laminar behaviour occurs within $0.322 < \nu < 0.3234$. The smaller slope at $\nu < 0.322$ indicates that the phase slips occur more often than super long laminar behaviour. The intermittency scaling rule applies after the region of super long laminar behaviour occurs. A linear general trend can be seen in figure 6.9(c) for $0.3215 < \nu < 0.3225$. This is followed by a smaller slope near the edge of the Arnold tongue which in means the phase slips are less regular than intermittency. The combination of figure 6.9(a), and 6.9(c) suggests that there is superlong laminar behaviour close to ν_c, followed by intermittency as the modulation frequency ν is shifted decreased from the synchronised state. The boundary between the two scaling laws occurs for $\nu = 0.322 < \nu < 0.3225$, which may be the region where periodic phase slips occur, as is explained in section 1.2. For the right side of the Arnold tongue, figures 6.9(b), and (d) show a similar effect to (a), and (c) respectively. The region of super long laminar behaviour appears much smaller, $0.3301 < \nu < 0.3303$, then this is followed by intermittency behaviour.

The amplitude of modulation was now reduced so that $A = 0.0375$ where there are no islands of control to a periodic state. The resultant scaling plots are shown in figure 6.10. The width of the Arnold tongue is less than in the previous case due to the lower modulation amplitude. The edges of the tongue are located at $f = 0.3237$ and $f = 0.3255$. Following the same line of argument used to analyse figure 6.9, plots 6.10(a) and (c) show a linear relationship for ν close to the Arnold tongue which indicates the presence of super long laminar behaviour. The remaining plots 6.10(c) and (d) show a linear relationship for $\nu < 0.3225$, and $\nu > 0.327$ respectively indicating the presence of intermittency.

Analysing the two types of scaling laws for phase slips has revealed the presence of super long laminar behaviour for modulation frequency near the Arnold tongue, and the presence of intermittency. The boundary between the two is not clear and may be due to periodic phase slips.

Local stability of the period 1 orbit

The global Lyapunov exponents calculated can show when a system is globally stable. These exponents however do not give information about localised areas of instability which may occur within a globally stable system. In particular there may be coexisting stable and unstable segments of a stable orbit, which corresponds to attractive, and repulsive phases respectively [67]. The local stability of the controlled period 1 orbit is now briefly discussed. A period 1 orbit was obtained by applying a modulation frequency $f = 0.35571$ and amplitude $A = 0.375$, that was chosen on the basis of figure 6.3. A small amount of noise was added to the modulation, but not enough to destroy the controlled period 1 orbit. This can be compared with the noise-free period 1 orbit, to obtain information about local stability and instability of the orbit [115].

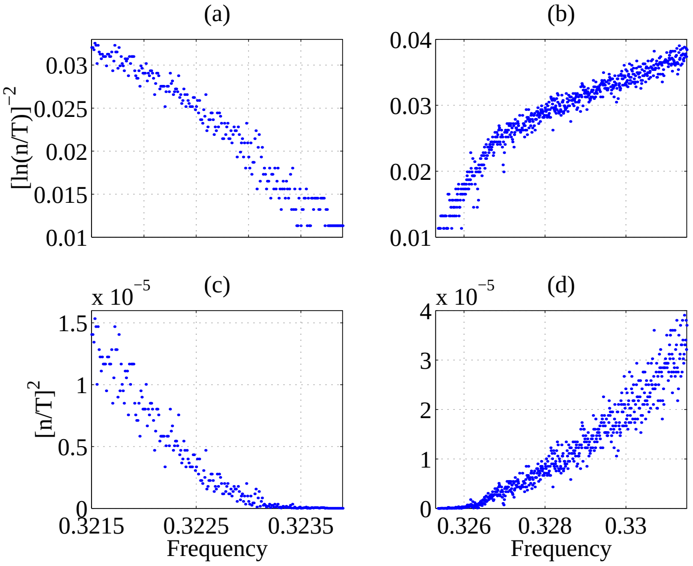

Figure 6.10: This shows the existence of two scaling laws for phase slips beyond the synchronised state, where no control is present, with modulation amplitude $A = 0.0375$. The edges of the Arnold tongues are located at $f = 0.3237$ and $f = 0.3255$. See text for details.

Noise was applied so the resultant modulation was $f(t) = Asin(2\pi ft)+N_A(noise(t)-1/2)$ where the time average of the noise term is 1/2, and the noise amplitude is N_A. The distance in phase space is calculated between the period 1 noise-free orbit at time t, and the modified period 1 orbit at t due to the addition of noise. Both orbits had the same initial conditions. This distance is plotted against the time over one orbit cycle, which is related to the phase of the orbit, and the noise amplitude. At time $t = 0$ the phase of the orbit can be defined as zero, so then at $t = 2.81$ the phase becomes 2π. The value of the phase at other times along the orbit depends on the specific definition of phase, which is not unique as discussed in section 3.3. Hence time is used here to refer to the position along the orbit rather than the phase. The noise has least impact on the distance at phases corresponding to the times 0 and at 2.5, and the most impact between 1 and 1.5 depending on the noise strength. There is a rapid increase in distance at a noise level of 0.008 corresponding to 0.8 %. At

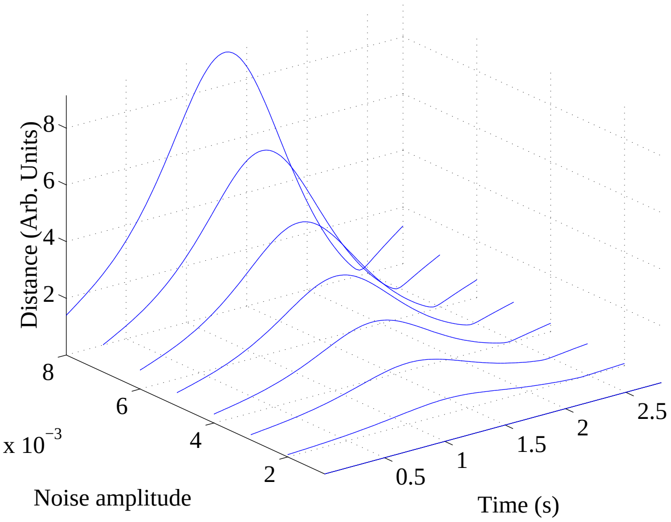

Figure 6.11: The relationship of the distance in phase space between a noise-free period 1 orbit, and a period 1 orbit with noise applied to the pump, is shown as a function of noise level, and time during one orbit cycle.

larger values the distance curves do not follow a uniform monotonic pattern for each successive increase in noise strength, and the value becomes comparable to the radius of the attractor and too large to conveniently show on the graph. Noise generated from different seeds was used to test if this result was sensitive to the details of the noise, and it was found that in all cases the distance curves for noise amplitudes less than 0.006 gave very similar results to figure 6.11. This indicates that the phase of the orbit corresponding to the smallest distance in figure 6.11 corresponds to a strongly attracting region of the periodic orbit. The phase of the orbit corresponding to the peak distance indicates the corresponding region in phase space is less stable, and may contribute to longer than average number of transient pulses before settling to period 1.

Stages of synchronisation are now searched near the controlled period 1 orbit. At the controlled state the Lyapuonv exponent is zero (and hence entropy is also zero) as shown in figure 6.12a. During control there are only a few phase slips as seen in figure

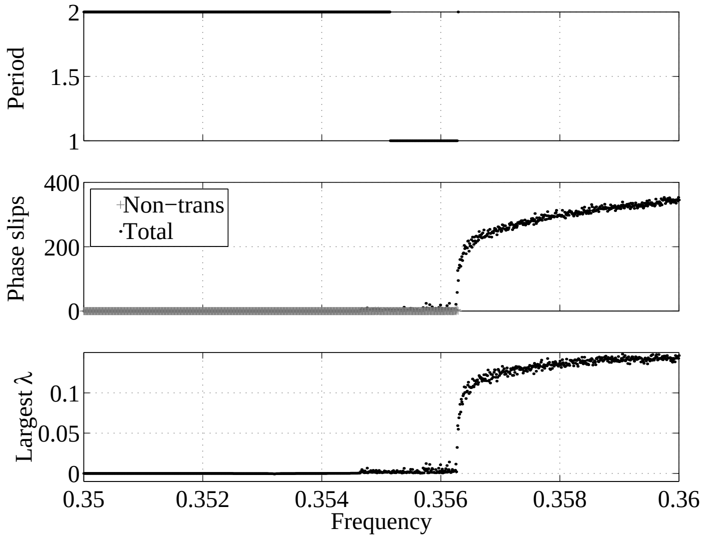

FIGURE 6.12: The period, number of phase slips, and the largest Lyapunov exponent are shown as a function of driving frequency is shown for an amplitude $A = 0.375$. Controlled states are shown in (a), number of phase slips for global (which includes all transient behaviour), and local (only during the controlled regions) in (b), and the largest Lyapunov exponent in (c).

6.12b, but the number increases as rapidly as the Lyapunov exponent outside the control region in figure 6.12c, so there is almost no region of synchronisation outside the control window. This is unlike the case in figure 6.7 where synchronisation can occur where the Lyapunov exponent is positive. A possible explanation for this is that the modulation amplitude for period 1 is much larger than was used in figure 6.7. This causes significant distortions in the attractor of the original system to the point where the attractor itself is a function of the applied modulation frequency.

6.3 Conclusion

We have shown that the complex Lorenz equations describing an autonomous chaotic laser, can be controlled to a periodic state by modulating the pump parameter appropriately. We find there exist islands of control to various periods in modulation amplitude–frequency parameter space. These islands are accessed only for a subset of the initial conditions that were used. The width of control in frequency space is quite narrow, but increases with increasing modulation amplitude. Control is not as sensitive to the modulation amplitude, although increasing the amplitude sufficiently can change the period of control. Regions of synchronisation orders of magnitude wider than the control window were found, and could be used for phase control alone as an alternative to phase and amplitude control. The nonlinearity of the system has been successfully exploited since rational locking ratios of the pump to intensity output gave control. The results are in good agreement with the experimental results in the previous chapter and show the Arnold tongues have very fine structure which appears fractal.
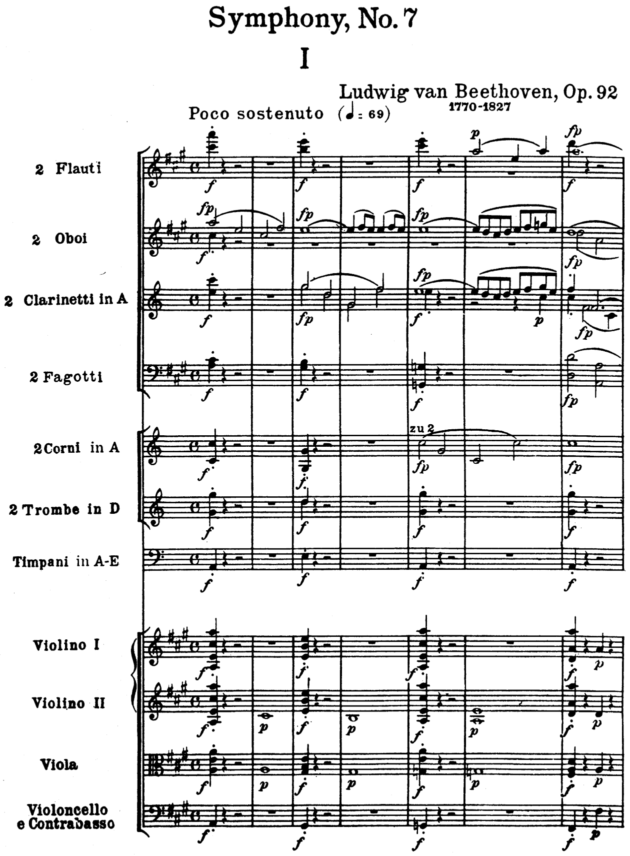
7

Controlling chaos in a Lorenz-like system using feedback

7.1 Introduction

Control by periodic modulation falls into the category of non–feedback control, and has been successful in simplifying the chaotic dynamics of the ammonia laser both experimentally, and numerically as discussed in the previous two chapters. Control by feedback is an alternative approach which may be simpler to implement than the non–feedback method. This requires extracting a system variable and feeding that back into another variable or parameter. In general the extracted signal can be modified before feeding it back into the system.

The term "feedback control" is often understood in the chaos literature to mean subtractive feedback. That is, the control signal is expressed in the form $F(t) = G(x(t) - x(t - \tau))$, where τ is the delay time, and G is some function with the condition that $G(0) = 0$. One example is control of a chaotic CO_2 laser by feedback of a variable which has been subtracted from its value at an earlier time [95]. $F(t)$ can be thought of as an error signal which tends to zero as the system approaches control, control meaning a periodic state where $x(t) = x(t-\tau)$. The advantage of this type of scheme is that no knowledge of the system other than the average pulsation period is required (control is achieved only for certain values of τ in the vicinity of the average pulsation period). Experiments with subtractive feedback on the Lorenz-like ammonia laser showed that control to periodic and even steady state is possible [96]. The feedback error signal was generated by analogue subtraction using a coaxial delay line. When the laser was controlled to a periodic state, the feedback signal was itself periodic, so we can think of this as self-synchronisation. It has also been shown that this type of laser operating above the chaos threshold could be synchronised to another chaotic system via feedback to the pump [92]. Here we make a detailed theoretical analysis of the subtractive feedback system to elucidate the range of conditions under which control is possible. In an attempt to further simplify the control of chaos we have examined the possibility of avoiding the subtraction process in the generation of the feedback error signal. Now if $F(t) = G(x(t))$ then $F(t)$ is non-zero in general. This type of feedback has been investigated and is known to destabilize a system in general [116]. The advantage would be that no subtraction of delayed signals would be required. We investigate this possibility, which we call here "non-subtractive feedback", numerically and experimentally and find that control is in fact possible.

Necessary condition for control by delayed feedback

A chaotic system with feedback can be described by $\dot{x} = F[x(t), K(x(t) - x(t-\tau))]$ where the feedback term is represented as $K(x(t) - x(t-\tau))$. This can be used to stabilise an unstable periodic orbit $\xi(t)$ with period τ so that $\xi(t) = \xi(t+\tau)$. The stability of the orbit can be investigated by applying a perturbation to the orbit to observe whether the solution diverges, or converges to the orbit. Linearisation of the nonlinear equations of motion about the periodic orbit $\xi(t)$ gives

$$\delta\dot{x} = D_1F(\xi(t), 0)\delta x(t) + D_2F(\xi(t), 0)K[\delta x(t) - \delta x(t-\tau)] \tag{7.1}$$

where D_iF denotes the Jacobian for the ith argument. According to Floquet theory, the perturbation also satisfies $\delta x(t) = \exp[(\lambda + i\omega)t]\mathbf{u}(t)$where $\mathbf{u}(t)$ is a periodic eigenvector, so that equation 7.1 can be written as [117]

$$[\Lambda + i\Omega] = \Gamma[K(1 - \exp(-\Lambda\tau - i\Omega\tau))] \tag{7.2}$$

where Γ is some function, with the boundary condition $\Gamma[0] = \lambda + i\omega$ which is the unperturbed eigenvalue. The point here is that Ω must be finite (*finite torsion*) for the control method to work at all. If Ω is zero then the right hand side of equation 7.2 cannot change from positive to negative, which is required for stabilisation, hence control will not work. Pyragas found that the standard Lorenz equations 3.1 with $\sigma = 10$, $r = 28$, and $b = 8/3$, had zero torsion and hence could not be controlled by perturbative delayed feedback [118].

The parameters used here in the complex Lorenz equations (see next section for values) are different to the standard Lorenz parameters. In order that the complex Lorenz equations can be controlled by the usual delayed feedback (Pyragas) method, the unstable periodic orbits must have finite torsion. This can be calculated by first locating a particular orbit to be controlled, then the stability can be calculated using Floquet theory as discussed above. Finding the unstable periodic orbit is not always trivial, and there are a number of methods which have been used to do this. The Newton-Raphson method [119] was attempted here to locate the period 1 orbit, but that was unsuccessful. The algorithm was written in FORTRAN and tested on the standard Lorenz equations (3.1) where the correct value for the Floquet exponent was found. The robustness of convergence to the unstable orbit using the standard Lorenz equations, was tested by adding ϵ to the initial condition lying on the period 1 orbit, and found that changing the initial condition less than 2% was enough to prevent it from converging to the orbit. The initial period of the orbit had to be even closer to the true value for convergence to occur. Hence there is only a small window of convergence surrounding points lying on the unstable periodic orbit using the Newton-Raphson method. In the complex Lorenz equations, the system has five dimensions, plus time. This means that a search in 6 dimensions is required to locate the position and period of the periodic orbit, which proved to be difficult. The author is aware there are less "brute force" methods available such as the SD method [120], and others are mentioned in the article by Pingel *et al.*[121] describing the theory of detecting unstable periodic orbits. Time did not permit these other avenues to be explored, hence the question of the existence of torsion for the parameters used here remains unknown. A lack of torsion may not necessarily prevent delayed feedback methods from controlling a chaotic system to regular behaviour if the applied feedback is not a small perturbation. This was tested on the standard Lorenz equations where the periodic orbit is known to have zero torsion [118], and it was found that control to periodic behaviour was possible, as will be shown in section 7.2.1.

7.2 Numerical

We use the complex Lorenz equations in our simulations of delayed feedback on a chaotic system. The complex Lorenz equations are:

$$\dot{E} = -((1 + i\delta)E - \lambda P) \tag{7.3}$$

$$\dot{P} = -1/\sigma((1 - i\delta)P - ED) \tag{7.4}$$

$$\dot{D} = \beta/\sigma(1 - D + f(t) - 1/2(E^\star P + P^\star E)) \tag{7.5}$$

where

$$\sigma = \kappa/\gamma_\perp \quad \beta = \gamma_\parallel/\gamma_\perp$$

E, P, and D are the electric field, polarisation and inversion respectively. λ is the average pump level, f(t) is the modulation applied to the pump, δ is the detuning of the cavity resonance relative to the atomic line center; $\kappa, \gamma_\parallel$ and $\gamma_\perp$ are the cavity, polarisation and inversion decay rates respectively. In all our simulations the parameters are $\sigma = 1.5$, $\beta = 0.25$, $\delta = 0.2$, and $\lambda = 46$. As introduced in Chapter 3, for chaos to occur the relation between the decay rates must be $\kappa > \gamma_\parallel + \gamma_\perp$ this is known as the bad cavity condition since a lossy cavity is required.

Variations in the pump power directly affect the population inversion so the feedback term appears as $f(t)$. We investigate two cases of feedback, the first being the form of subtractive feedback [41] $f(t) = A(I(t) - I(t - \tau))$ where $I(t) = E(t) \cdot E^*(t)$ represents the laser intensity, and A is the feedback amplitude. This type of feedback was experimentally implemented by driving an acousto-optic modulator (AOM) with a signal generated using a coaxial cable delay line to perform the subtraction [96]. To compare these results with our numerical results, we introduce an additional delay in the feedback loop of our model to account for the propagation delay T within the

AOM used to convert the error signal into a modulation of the pump power. For the second case of non subtractive feedback, we dispense with the subtraction step and set the feedback to be $f(t) = AI(t - T)$ and investigate the amplitude–feedback delay parameter space. In both these feedback cases the system is operating well above the chaos threshold λ_{th} so that the average pump level λ is chosen such that $\inf(\lambda + f(t)) > \lambda_{th}$. In all our calculations time is scaled [104] as κt which is dimensionless since κ represents the cavity decay rate. Hence the feedback variables T and τ are also dimensionless.

7.2.1 Control by subtractive feedback

As explained above in all our experiments there was an additional delay T within the AOM, so we define the feedback term to be

$$f(t) = A(I(t - T) - I(t - (T + \tau))) \tag{7.6}$$

The difference delay τ is the time between the two measurements of output intensity, the difference between which constitutes the error signal. The feedback delay is defined as the time T for the feedback signal to enter back into the system. We integrate the complex Lorenz equations using this feedback term, and for different pairs of parameters τ, T and amplitude A, construct the time series $I(t)$. The periodicity of I(t) was calculated for the long term dynamics by waiting until transient behaviour had passed. The period of the time trace was plotted on the difference delay–feedback delay parameter space, for periods up to 6. The first result was calculated using a very weak feedback amplitude 0.0004 and the plot is shown in figure 7.1. Since the intensity pulsations range between 80 and 120 units, this sets the maximum feedback amplitude to be about 4% of the average pump power. The average pulsation period is 3.08 dimensionless time units. Only periods greater than 3 exist for very weak feedback as is evident in figure 7.1. If the feedback amplitude is increased to 0.001,

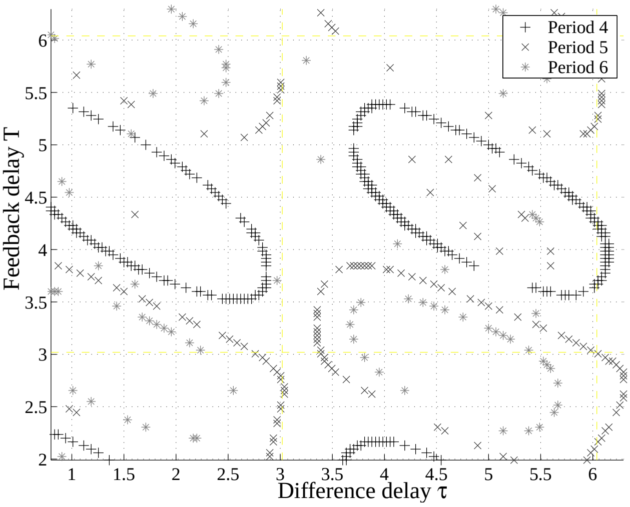

Figure 7.1: Control to various periods by subtractive feedback of maximum amplitude of 0.04% of the pump. The difference delay τ, and the feedback delay T are both dimensionless, see text for details.

equivalent to 10% of the average pump power, we find this increases the number of periodic states and leads to the existence of period 0 – the steady state. This is shown in figure 7.2, and the dashed line indicates the average pulsation period for the chaotic sytem without feedback (3.08). Many of the features in the weak feedback case in figure 7.1 are evident in figure 7.2, such as the rings of period 4 in parameter space. In the stronger feedback case, these rings have been distorted and the positions shifted slightly. These rings contain regions of control to less than period 4 where period 0 dominates. As might be expected, islands of control exist at multiples of the average pulsation period along the feedback delay axis. The same applies for the difference delay axis. If we leave the feedback amplitude at 0.001 but change the sign of the feedback to negative, the result is shown in figure 7.3. There are similar structures here as in the previous figure except that the islands are displaced half an average pulsation period upwards. This can be understood by considering the change of sign of the feedback term to be equivalent to a phase shift of half a period. These well defined islands of stability are destroyed if the feedback amplitude is too large. We

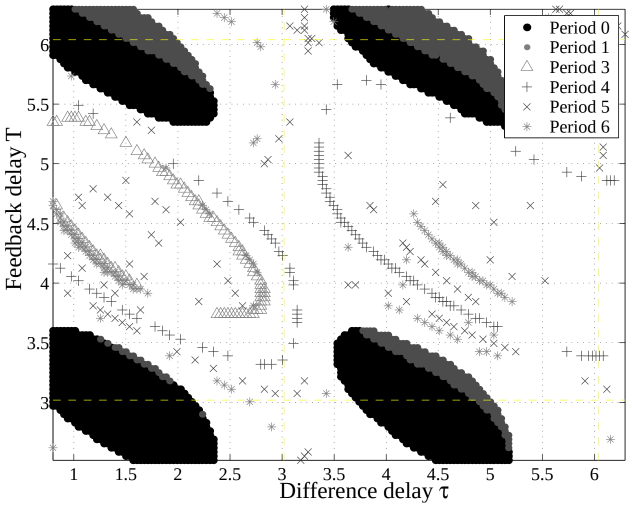

FIGURE 7.2: Control to various periods by subtractive feedback of maximum amplitude 10% of the pump. The difference delay is τ, and the feedback delay is T.

increased the feedback amplitude to 0.006 which would correspond to an average of 60% of the average pump power. The result is shown in figure 7.4. Since the feedback amplitude modulation is so large it is no longer perturbative and the system is no longer Lorenz like. Figure 7.4 shows there are now islands of control which are not at multiples of the average pulsation period of the unperturbed system in either the difference delay axis or the feedback delay axis. The size of the period 0 islands are significantly smaller in the strong feedback case compared to the moderate feedback case as in figure 7.2. One would expect the islands to be smaller since if the system isn't very close to the periodic state, then the large feedback amplitude drives the system quickly away from the periodic state. Previous experiments [96] showed that the laser was controlled to period 0 when the feedback amplitude was 3% and 7%. The difference delay τ used was about one laser pulse period. Control to period 1, 2, 4, 6 was observed at 5% modulation depth. Numerically, we found control to period 0, 1, 3, 4, 5, 6 with a modulation depth of 10% for the second multiple of the average pulsation period as well as the first multiple. We did not find any period 2 at this

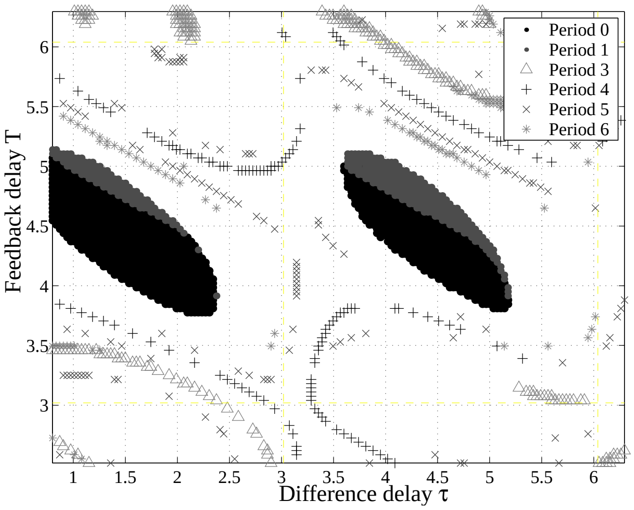

Figure 7.3: Control to various periods by subtractive feedback of maximum amplitude 10% of the pump. The difference delay is τ, and the feedback delay is T. The error signal has been inverted with respect to figure 7.2.

amplitude. This could be due to the fact that numerically we calculated the periodicity of intensity traces that contained about 1000 pulsations. The experiments have the limitation that during control only about 70 pulses could be recorded. Thus it is possible that what appeared to be period 2 was actually a long transient which eventually approaches period 1. This is always a problem with any finite time series since one cannot be sure whether the dynamics in a finite time series is permanent or transient.

Control to period 1 was not found around $\tau = 3$, and $T = 0$, for $A \leq 0.001$ which corresponds to the region where the original Pyragas method [40] is expected to work subject to the torsion condition. When the feedback amplitude was increased, period 2 emerged that wasn't present in the lower modulation cases, and period 1 was found at $\tau = 3$, and $T = 0$ as shown in figure 7.5.

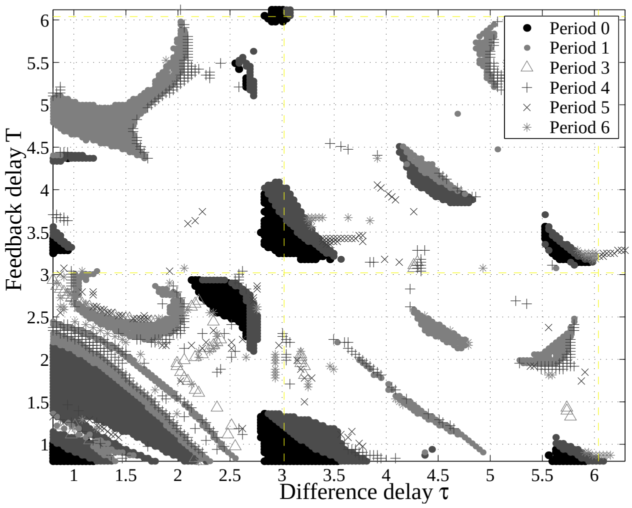

FIGURE 7.4: Control to various periods by subtractive feedback of maximum amplitude of 60% of the pump. The difference delay is τ, and the feedback delay is T.

Effective modulation depth

The feedback may not be perturbative so the size of the modulation depth is calculated for period 1 from figure 7.5. This was achieved by recording the maximum peak of the feedback signal during control to period 1, and multiplying it by the feedback amplitude A. The resultant value is divided by the steady state pump power, which appears as '1' in equation 7.5 due to normalisation. The modulation depth as a function of τ and T is shown in figure 7.6. The maximum modulation depth of about 15% occurs approximately in the centre of the period 1 islands for $T = 3$ and $T = 6$, which correspond to the feedback delay values $\tau = 1.5$ (equivalent to $\frac{1}{2}T_1$) and $\tau = 4.5$ (equivalent to $\frac{3}{2}T_1$) respectively, where T_1 is the pulsation period for period 1. Shifting in either direction in (τ, T) lowers the effective modulation depth, as one would expect since $x(t) - x(t - \tau)$ is largest at half integer multiples of T_1. This phenomenon occurs for the four period 1 islands located at $T = 3$ and $T = 6$. The situation is different for $T = 0$ since the modulation depth is minimum at $\tau = 3$ ($< 5\%$), and very large (30%) at other values of (τ, T) within the period 1 island.

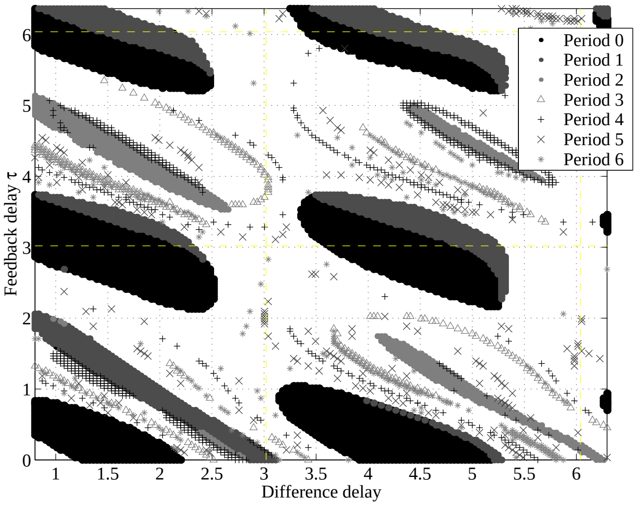

Figure 7.5: Control to various periods by subtractive feedback of maximum amplitude of 14% of the pump. The difference delay is τ, and the feedback delay is T.

These results show that the modulation depth quickly increases as a small loop delay is introduced to the original Pyragas method, but for delays T that are multiples of period 1, the modulation depth can be reduced to reasonable values.

The standard Lorenz equations 3.1 are torsion free, so it is useful to investigate if periodic dynamics can be achieved using moderate amplitudes, so that modulation depths can be compared with the complex Lorenz equations. Applying feedback to the standard Lorenz equations generates periodic orbits as shown in figure 7.7. There is no period 1 orbit stabilised with a period of 1.5586, corresponding to the unstable periodic orbit [118], as forbidden by this system. However, there are many islands of control at other delays and feedback amplitudes. As the amplitude increases, one would expect control to become more likely since the dynamics of the system becomes slaved to the drive. It appears that the modulation amplitude is not large in figure 7.7. This can be confirmed by similar analysis to figure 7.6 where the modulation depth now is a function of only one delay (difference delay), and the feedback amplitude. The result is shown in figure 7.8, where the effective amplitude can be as low as 0.2%,

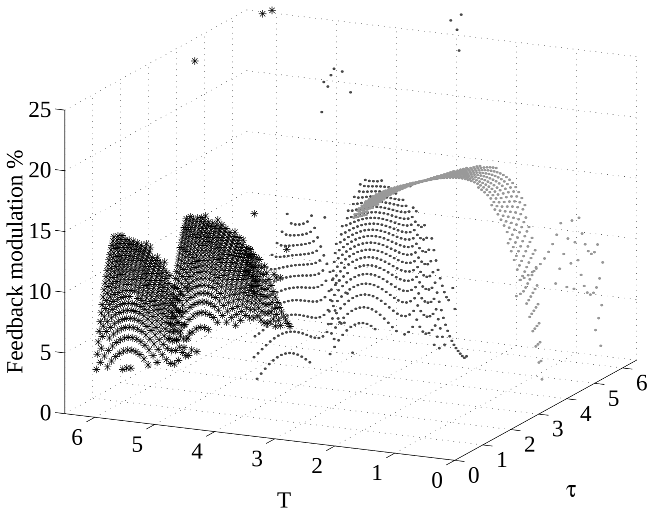

FIGURE 7.6: Effective feedback modulation strength during control to period 1, as a function of the difference delay τ, feedback delay is T. The feedback amplitude is $A = 0.0014$.

and over 30% depending on τ and A for the period 1 islands. These results show that the effective modulation depth for the complex Lorenz system with a feedback delay is comparable to the standard Lorenz equations without a feedback delay (or loop delay), and only a difference delay. One would expect that the additional loop delay would increase the error signal, since the correlation of the current signal to the delayed value is finite, and typically not very large.

All the previous results were obtained using Lorenz–like chaos where the detuning $\delta = 0.2$. The complex Lorenz system can generate chaos which evolved from a period doubling bifurcation, so for completeness, control was implemented for this type of chaos. The detuning was chosen on the basis of figure 3.3 where a period doubling route to chaos was obtained without additional windows of stability appearing, as can occur for other values of detuning (e.g. $\delta = 0.375$ has only a small band of chaos), hence the detuning was set to $\delta = 0.42$. The result is shown in figure 7.9. There are four large islands of period 2 surrounded by 4 windows located at $(1.5, 1.5)$, $(1.5, 4.5)$, $(4.5, 1.5)$, and $(4.5, 4.5)$. The period 0 islands are significantly smaller than occurs

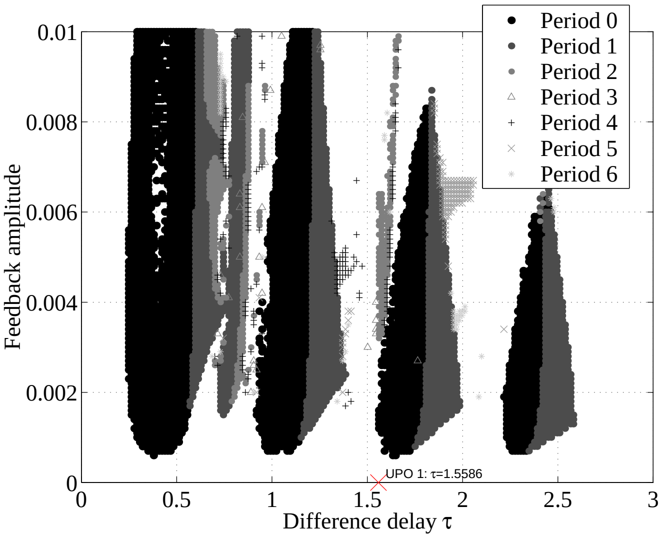

FIGURE 7.7: Control to various periods by subtractive feedback using the Pyragas method, for various feedback amplitudes and difference delays, τ Parameters are $\sigma = 10$, $\beta = 8/3$, $r = 28$. The intensity is fed back the $\dot{z}$ equation.

in figure 7.2. Period 3 also appears to be more extensive for the controlled period doubled chaos, rather than the observed in figure 7.2.

A simple way to see how an unstable orbit can be stabilised by subtractive feedback is to consider an unstable oscillator of the form $\ddot{x} - \alpha\dot{x} + kx = 0$ which is oscillatory unstable for $\alpha > 0$ and $k > \frac{\alpha^2}{4}$. A subtractive feedback signal can be applied to the system to give $\ddot{x} - \alpha\dot{x} + kx = -A(x(t) - x(t - (T + \epsilon)))$, where $x(t) = x(t + T)$ at control. The feedback expression can be expanded using perturbation theory and it is easy to show that both the initially positive eigenvalues of the linearised system become negative for $A > \frac{\alpha}{T}$ assuming small ϵ.

Returning to the numerical results in the figures, The islands of stability have a definite preferred orientation, in particular the period 0 islands all have a slope of $-\frac{1}{2}$. This can be understood the following way. Period 0 occurs after the oscillation is completely damped so just before it is extinguished it is a sinusoid to a good approximation. So we can write the signal as $f(t) = a\sin(\omega t)$ and the delayed signal

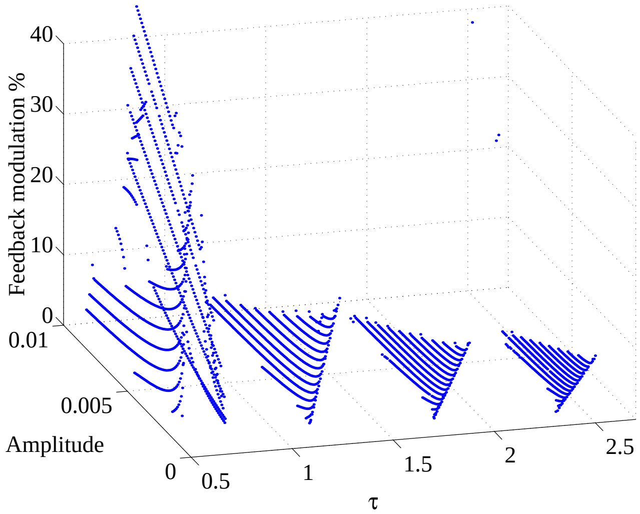

Figure 7.8: Effective modulation depth as a function of the difference delay (τ), and feedback amplitude for the standard Lorenz equations.

will be $f(t+\tau) = a\sin(\omega t + \phi))$, where $\phi = \omega\tau$ is the phase difference between the two signals due to the subtraction time τ. Since

$$f(t) - f(t+\tau) = -2a\sin(\frac{\phi}{2})\cos(\omega t + \frac{\phi}{2}) \qquad (7.7)$$

the generated difference signal has an effective delay equal to half the delay τ within the control island. This can be compensated by an equal but opposite change in the feedback delay T.

Linear stability analysis

We now look at the stability of the fixed points of the nonlinear system to gain some insight into the mechanism of control. The eigenvalues of the feedback system cannot be obtained analytically since the determinant of the Jacobian is a transcendental function, so this can only be solved numerically. There are an infinite number of complex solutions to this type of equation in general, and the system will be stable if all the eigenvalues are negative. We search the same parameter space as in figure

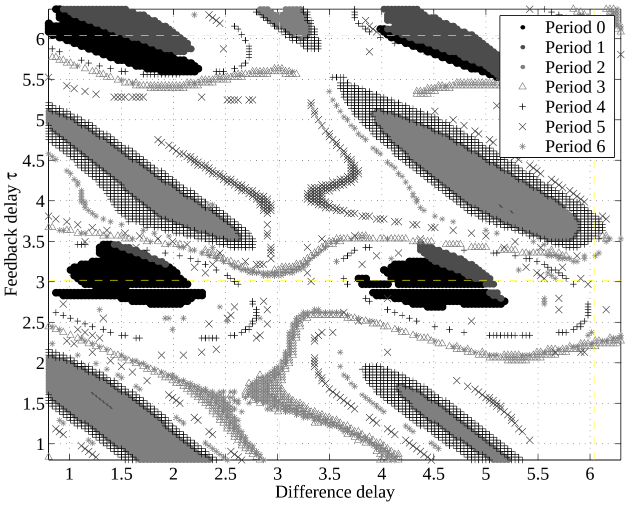

FIGURE 7.9: Control to various periods by subtractive feedback for period doubling chaos. The detuning is $\delta = 0.42$, $A = 0.001$, the difference delay is τ, and the feedback delay is T.

7.2 and set $A = 0.001$ and plot (figure 7.10) whenever all the eigenvalues of the determinant of the Jacobian are less than or equal to zero. Without the feedback ($f(t) = 0$ in equation 7.3) the eigenvalues of these fixed points are positive. It is clear that the position of the islands of control to period 0 and period 1 are contained within the islands in figure 7.10. This shows that the eigenvalues of the fixed points of the system are all negative during control to period 0 and period 1. Control to a periodic state by stabilising an existing unstable periodic orbit of a chaotic attractor has previously been demonstrated experimentally and theoretically as discussed in the introduction. These methods of control rely on the system having a reasonable probability of visiting the desired unstable periodic orbit where a control mechanism can take full effect. This is not the case for period 0 since the system never visits the unstable fixed point [122]. We overcome this by applying the feedback. This changes the stability of the unstable fixed points, allowing an initially inaccessible region of phase space to be visited for certain values of feedback parameters such as shown in figure 7.10.

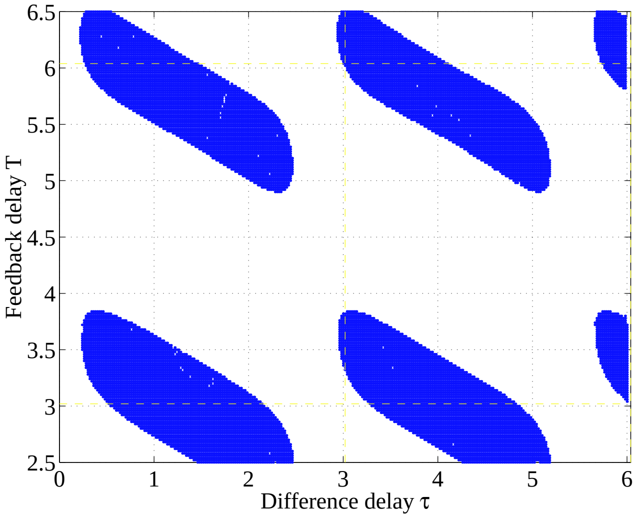

FIGURE 7.10: Islands represent the non positive Lyapunov spectrum of equation 7.3 for the feedback parameter $A = 0.001$ The difference delay is τ, and the feedback delay is T.

In previous feedback experiments [96] and in our experimental results following this section, the feedback signal to the laser system is a.c. coupled. This will only give a non zero final error signal if the unfiltered error signal is varying with time, and a constant unfiltered signal will appear as zero final error signal. To check what effect this might have, we include this effect in our model by applying a high pass and a low pass filter to $f(t)$, based on RC circuit theory, and using this modified $f(t)$ as the feedback signal in the differential equations. These are

$$\dot{f_1} = \frac{-f_1(2 + \frac{R1.C1}{R2.C2}) - \frac{f_2}{R2C2} + 2\dot{I}(t)}{R1.C1} \quad (7.8)$$

$$\dot{f_2} = f_1 \quad (7.9)$$

where the low pass cut off frequency is $\omega_{max} = \frac{1}{R1.C1}$, and the high pass cut off is $\omega_{min} = \frac{1}{R2.C2}$. The signal to be filtered enters the equation as $\dot{I}(t)$, and the filtered output is f_2. The high pass filter models the a.c. coupling while we also include a low pass filter to model the finite bandwidth of the AOM. We apply this procedure to the subtractive feedback case and the results are shown in figure 7.11. In all cases the high pass cut off is set to 0.01 and the low pass cut off is 6, 2, 1, 0.85, 0.75, and 0.5 in (a), (b), (c), (d), (e), and (f) respectively. The characteristic pulsation period is 3.08, where time has been scaled to the parameter κ. The cut off frequency in 7.11(a) is three times the average pulsation frequency which results in only a slight decrease of the fundamental frequency, allowing control to proceed. As the cut off frequency decreases, there is a greater attenuation of the fundamental frequency which gets fed back into the equations. This results in an effectively lower modulation amplitude at the fundamental frequency and therefore the range of control becomes narrower. This is evident in the figure 7.11(a-f) where the islands of control retain their orientation but decrease in size. These results with the inclusion of a.c. coupling and bandwidth limitation to the feedback system are essentially the same as for the unfiltered case. There is only a significant difference when the bandwidth of the feedback signal is equal or less than the characteristic frequency of the system, and this just causes the control islands to shrink and become destroyed if the bandwidth is much less than the characteristic frequency.

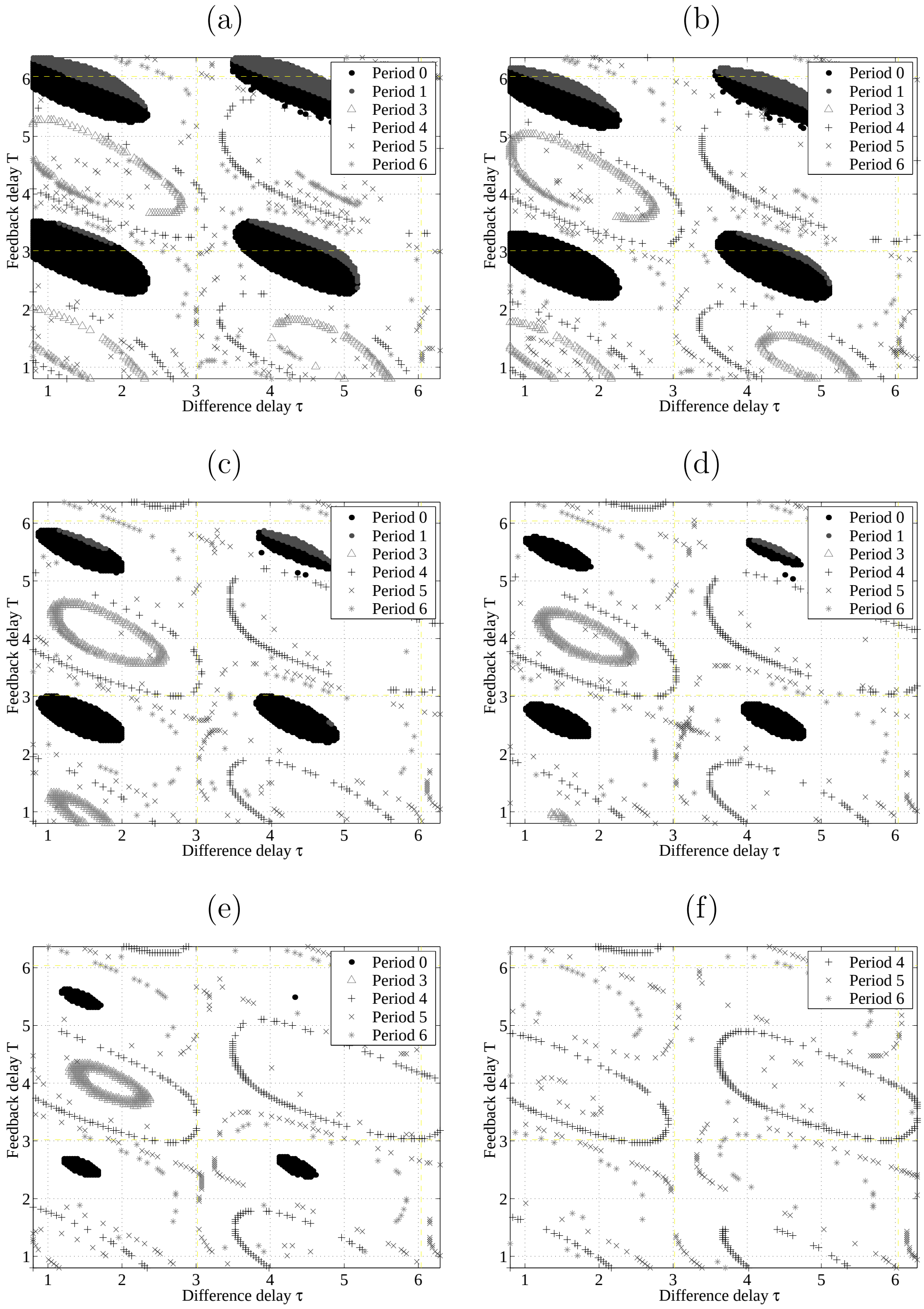

FIGURE 7.11: Control to various periods by subtractive feedback for different high pass cut off values ω_{max}. In (a), (b), (c), (d), (e), and (f) the high pass cut off frequencies are 6, 2, 1, 0.85, 0.75, and 0.5 respectively. The low pass cut off in each case is 0.01.

7.2.2 Stability of control and generalised synchronisation

The windows of control in parameter space were found in the previous section, and they show the final dynamical states of the intensity solution for a range of feedback amplitudes. As discussed earlier the periodic states were calculated ignoring initial transient behaviour that may have occurred before control emerged, and non periodic states were discarded. To gain more information about the dynamical states near control the behaviour of the system must be considered over the entire range of the feedback parameters, and less strict measures are needed that quantify dynamical states other than periodic.

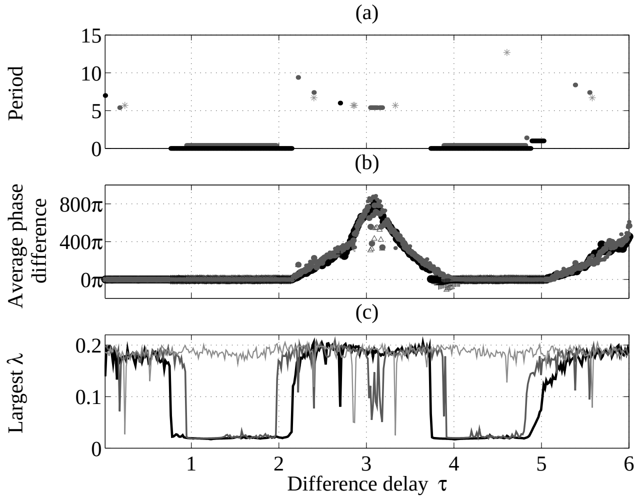

FIGURE 7.12: The period as a function of the difference delay τ for a fixed feedback delay $T = 3$ is shown in (a) for feedback amplitudes $A = 0.001$ (black), $A = 0.00075$ (dark grey), and $A = 0.0005$ (light grey), and white regions represent a non periodic solution. The average phase difference between the intensity solution, and the feedback signal is shown in (b), and the symbols indicate the average phase slips during a particular controlled state. The largest Lyapunov exponent is shown in (c).

The results from figure 7.2 are recalculated for three values of feedback amplitude $A = 0.001$, $A = 0.00075$, and $A = 0.0005$ for a fixed feedback delay $T = 3$, and a number of measures were calculated as a function of the difference delay τ which ranged from 0.15 to 6. A coarse measure is to compare the average frequencies of the intensity solution, and the applied feedback solution. The difference between the number of cycles of the intensity, and feedback solutions were used instead of average frequency, then this difference is accumulated over the duration of the feedback, and converted to phase which is labelled "average phase difference" in figure 7.12b. For comparison the periodic states are displayed in figure 7.12a which corresponds to the strongest form of synchronisation–perfect synchronisation. The black line ($A = 0.001$) is a horizontal slice through $T = 3$ in figure 7.2, and the resolution has been increased by an order of magnitude along the τ axis. The frequency difference between the intensity, and feedback solutions is zero during the regions of control to a periodic state, and for $\tau < 0.76$. The amplitudes and phases of the two solutions are uncorrelated or highly complex so this is the weakest stage of generalised synchronisation. The Lyapunov exponents were calculated using the Wolf algorithm [114], where the feedback term $f(t)$ was taken as constant at each integration step, since the past solution is necessarily stored as a discrete vector. This may lead to some inaccuracies but is much computationally faster to calculate than solving the infinite dimensional problem with a finite number of ordinary differential equations. Hence the Lyapunov exponents shown here are only used as a guide, and an approximate estimate of the entropy of the system using equation 2.29.

Only the largest exponent as a function of τ is displayed in figure 7.12 since the remaining exponents were either zero or negative. The exponent drops to zero during the regions of control, and approximately a constant positive value otherwise. This measure is almost as strict as the calculation of the periodicity. However it shows how quickly control is extinguished at the end points of the control window for $0.76 < \tau < 2.15$, and $3.73 < \tau < 4.88$. The above analysis is repeated for amplitudes $A = 0.00075$, and $A = 0.0005$ and is shown as dark grey, and light grey lines respectively in the three graphs of figure 7.12. At $A = 0.0005$ there is no control to a periodic state other than a few isolated points which appear in figure

7.12a, and the Lyapunov exponent is roughly constant ($e = 0.19$). The average frequency difference is zero for $\tau < 2.15$ and for almost the width of the second period 0 window for $A = 0.001$. This indicates that even though control has not been achieved, synchronisation is still possible over a similar range in τ compared to the other cases of higher amplitude where control was found. At the intermediate amplitude $A = 0.00075$ there is control to periodic states but with a narrower window in τ compared to $A = 0.001$ as to be expected. The Lyapunov exponent drops to zero at the appropriate τ location. The average phase difference is very similar to the other two amplitudes. The symbols in figure 7.12b represent the average number of phase slips which occur during a controlled state which is zero for period 0, and period 1. In between the period 0 islands there is no generalised synchronisation.

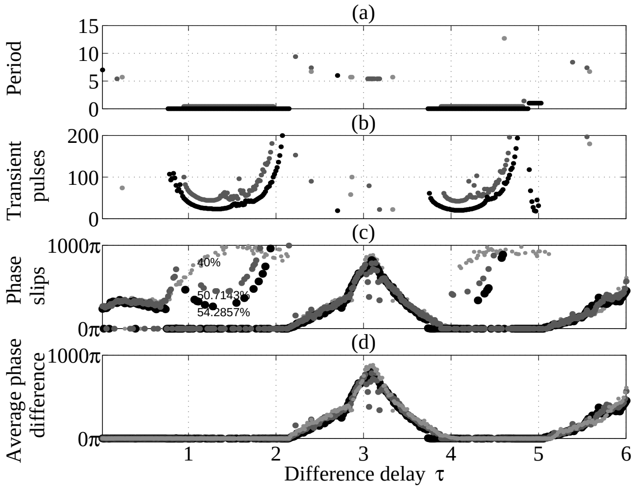

FIGURE 7.13: This shows the regions of control as a function of the difference delay τ with a fixed feedback delay $T = 3$ for subtractive feedback. The period is shown in (a) for feedback amplitudes $A = 0.001$ (black), $A = 0.00075$ (dark grey), and $A = 0.0005$ (light grey), and white regions represent a non periodic solution. The number of transient pulses before control develops is shown in (b), the net phase slips accumulated during feedback (c), where zero implies phase synchronisation, and a positive value indicates the accumulated absolute value of the phase slips. The percentage synchronisation for $\tau \leq 2$ is given for the three feedback amplitudes. The frequency difference between the intensity solution, and the feedback signal is represented as the average phase difference during feedback in (d).

A controlled state may have emerged from many cycles of instabilities before finally reaching equilibrium. The number of pulses before a periodic state emerges is shown in figure 7.13b, and again for comparison the periodic state is shown in 7.13a. The minimum number of transient pulses before control emerges is not in the center of the control window but shifted to the left indicating that the fastest convergence to control is not in the center of the control window. The average phase difference is a useful coarse measure which ignores the details of the behaviour of the relative phase. In particular, the weak synchronised state (corresponding to a zero average phase difference) may or may not have phase jumps occurring such that the average frequency remains zero. This information can be extracted if the magnitude of the phase jumps are extracted by comparing each successive intensity peak time, and feedback peak time keeping track of their relative orientation, and counting the number of times the sign of the difference between these peak times changes. The result is shown in figure 7.13c. At the highest amplitude there are few phase slips during the large control window of period 1 and 0. As soon as control is extinguished then there are many phase slips for $\tau < 0.76$ but they average out to give a zero average frequency as seen in figure 7.13d. As the feedback amplitude is decreased more phase slips appear in the controlled region. The calculation of the phase slips was applied to the regions where there is a zero average phase difference. Outside this region the count of phase slips was set to the average phase difference since, since these regions are not even weakly synchronised. In figure 7.13c three values of percentage phase synchronisation for $\tau \leq 2$ are displayed. This is the fraction of calculated points free from phase slips relative to the total number of points in that region. For amplitudes 0.001, 0.00075, and 0.0005 the synchronisation ratio is 54.3%, 50.7%, and 40% respectively. This shows that a larger amplitude decreases the number of phase slips during control, and even if control is not achieved a reasonable amount of synchronisation can be achieved which is free from phase slips.

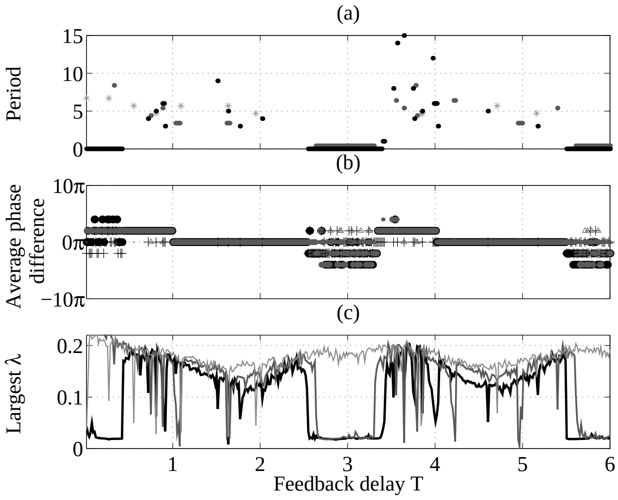

Figure 7.14: Same as figure 7.12 except that the difference delay is fixed at $\tau = 1.5$, and the feedback delay is swept from 0.15 to 6.

The difference delay was fixed at $\tau = 1.5$, and the effect of varying the feedback delay T is calculated from 0.15 to 6.0 in 1000 intervals. This value of τ corresponds to the centre of the period 0 island in figure 7.2. The periodicity, average phase difference, and largest Lyapunov exponent are shown in figure 7.14(a), (b), and (c) respectively at amplitudes $A = 0.001$ (black), $A = 0.00075$ (dark grey), and $A = 0.0005$ (light grey) respectively. In between the period 0 control islands the average frequency difference between the intensity and the feedback signal is zero, and there are also no phase slips in this region other than just before the second, and third period 0 island as shown in figure 7.15c. This is unlike figure 7.13c where there is no generalised synchronisation in between the period 0 islands. The approximate Lyapunov exponent drops towards 0 at the appropriate location, and the number of transient pulses for control obtained is shown in figure 7.15b which is minimum slightly left of the centre of the island.

A simple explanation as to why there is no synchronisation in between the period 0 islands in figure 7.13c is the following. If the value of τ at the centre of the two period

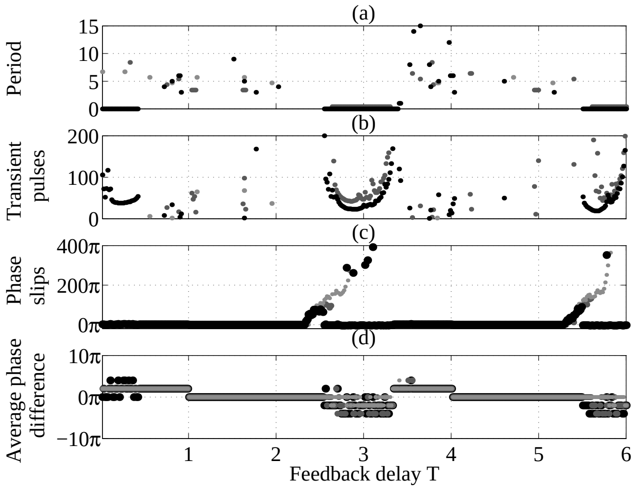

FIGURE 7.15: Same as figure 7.13 except that the difference delay is fixed at $\tau = 1.5$, and the feedback delay T ranges from 0.15 to 6.

0 islands is substituted into equation 7.7 (which assumes that period zero emerges from a decaying oscillation which becomes more sinusoidal as the amplitude decays due to the decreasing nonlinearity), for the first island, $\tau = 1.5$. This corresponds to $\phi = \pi$ so that $\sin(\omega t) - \sin(\omega t + \pi) = 2\sin(\omega t)$. For the second island $\tau = 4.5$ which corresponds to $\phi = 3\pi$ so $\sin(\omega t) - \sin(\omega t + \pi) = 2\sin(\omega t)$ as well. However in between the period 0 islands $\tau = 3$ but consider ϕ to be only slightly larger than π so that $\phi = 2\pi + \epsilon$. Then $\sin(\omega t) - \sin(\omega t + 2\pi + \epsilon) = -2\sin(\pi + \epsilon/2)\cos(\omega t + \epsilon/2)$, which tends zero as $\epsilon \longrightarrow 0$ resulting in a minimum correlation between the intensity and feedback signal. This means a maximum average phase difference. At non zero values of ϵ the feedback term is opposite to the expression calculated at the centre of the control islands and hence leads to instability rather than control. It is interesting that phase slips occurs to the left hand side of the period 0 control islands, and not on the right hand side.

Previous experimental results show control of amplitude and phase was possible [49] therefore can be considered the first stage of synchronisation. An experimental example of the second stage of synchronisation, phase synchronisation, is shown in

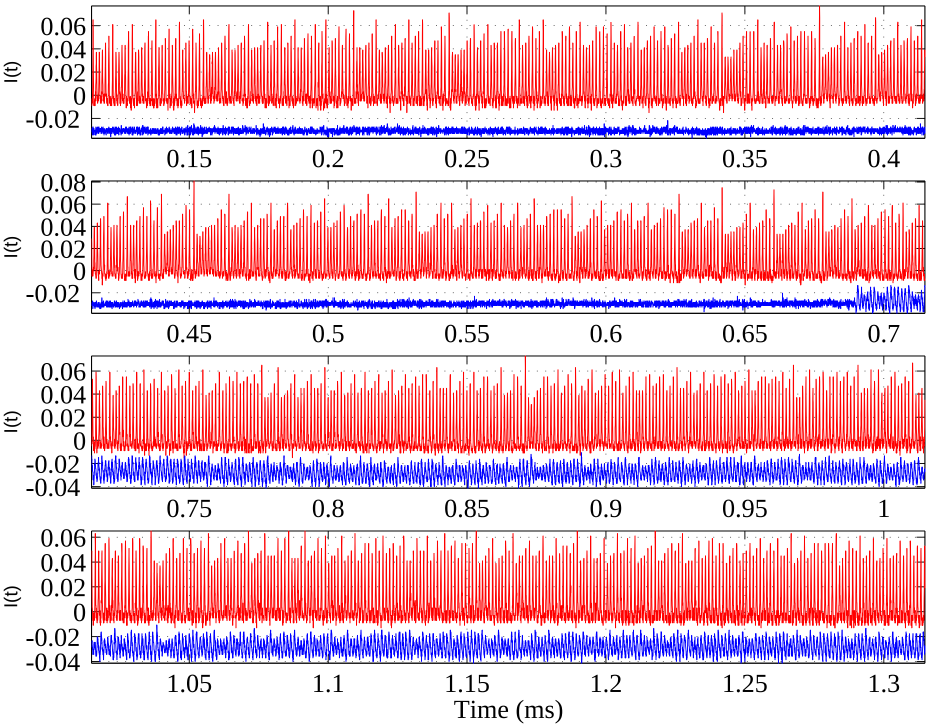

FIGURE 7.16: Subtractive feedback of the FIR laser with A approximately 0.1. No control is achieved but the laser intensity is synchronised to the feedback signal which has an average pulsation frequency of 817 KHz. There is only one phase slip out of 500 pulsation peaks.

figure 7.16. The initially chaotic time series is frequency locked to the feedback signal apart from one isolated phase slip. The intensity during feedback is not regular but has a lower depth of modulation compared to the initially chaotic time series. A histogram of the time difference between the peaks of the laser intensity, and feedback signal is calculated and shown in figure 7.17. The feedback signal was relatively weak so there was an error of approximately 0.1μs in calculating the value of the peak times. The negative time differences of the histogram were manually checked by observing the corresponding peaks in the time series directly, and there was found to be only one phase slip which corresponds to the bin at -0.2μs in figure 7.17. The third stage of synchronisation has been found where only the average frequencies of the intensity

and feedback are the same.

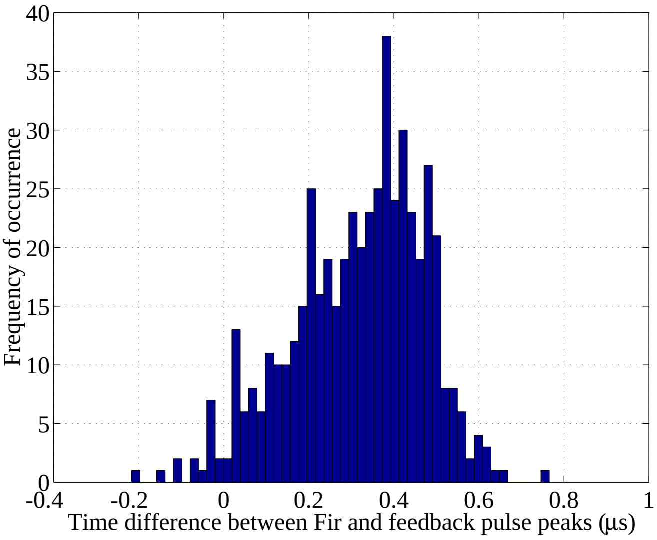

Figure 7.17: A histogram is calculated for the time difference between the peaks of the laser intensity, and the feedback signal. The average pulsation period is $1.223 \mu s$.

Calculating coarser measures other than determining whether a state is periodic has given information about the fastest region of convergence within a control window, and the quality of control by measuring the number of phase slips collected during the duration of control. The region of generalised synchronisation may be used to control only phase as an alternative to full control.

7.2.3 Control by non–subtractive feedback

We now simplify the feedback term so that there is no subtraction and simply take $f(t) = AI(t-T)$. As before we integrate the complex Lorenz equations using this feedback term, and for different pairs of parameters T and amplitude A, construct the time series $I(t)$ associated with each of the parameters. The periodicity of I(t) was calculated the same way and a map of the results as a function of delay and feedback amplitude was constructed as shown in figure 7.18. Again the average pulsation period of the unperturbed system is 3.08 as indicated by the dashed line. Period 0 dominates the regions near multiples of the average pulsation period, 3.08 and 6.16, which first appear at a feedback amplitude of 1.1×10^{-3} corresponding to about 11% modulation depth. As this amplitude increases, more different period numbers emerge. The numerical results in figure 7.18 show that control to period 1 occurs only on the right hand side of the large period 0 block. This segment of period 0 begins at slightly more than the average pulsation period of the unperturbed system. This is the only region we can explore experimentally since there are delays in the acousto–optic modulator which cannot be removed.

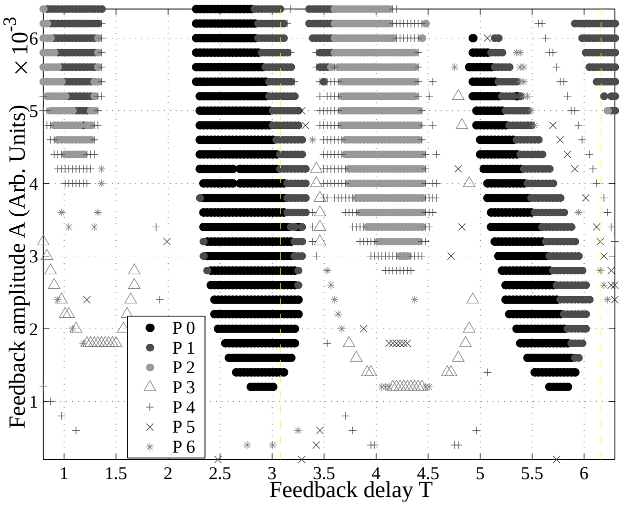

FIGURE 7.18: Control to various periods by non-subtractive feedback as a function of the difference delay τ and amplitude A.

As before we can use the unstable oscillator model of the form $\ddot{x} - \alpha\dot{x} + kx = 0$ to show that it can be stabilised by applying a nonsubtractive feedback signal to give $\ddot{x} - \alpha\dot{x} + kx = Ax(t - (T + \epsilon))$. Expanding this using perturbation theory and using linear stability theory shows that this system is stabilised for $\frac{\alpha}{T} < A$ for small ϵ. The eigenvalues of the Jacobian of equation 7.3 were calculated and only non-positive eigenvalues are plotted in figure 7.19. The period 0 and period 1 islands from figure

7.18 appear in a similar position to the islands in figure 7.19. They demonstrate the stabilisation of the fixed points during control to period 0 and period 1 thus allowing an initially inaccessible region of phases space to be reached.

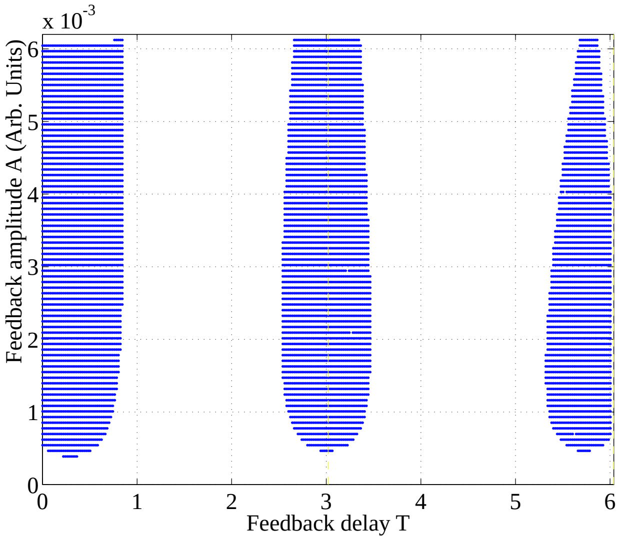

Figure 7.19: Islands represent an all non positive Lyapunov spectrum of equation 7.3. The the feedback delay is T and amplitude is A.

The measures discussed in section 7.2.2 were now applied to the non subtractive feedback case. Here the only delay parameter is the feedback delay which is fixed to $T = 3$. The average phase difference, largest Lyapunov exponent, transient number of pulses before control emerges, and the number of phase slips were calculated as a function of feedback amplitude. The period shown in figure 7.20a (and in figure 7.21a) corresponds to the vertical line at $T = 3$ in figure 7.18, and the number of amplitude points has been increased by an order of magnitude to increase the resolution in this calculation. The average phase difference which is related to the average frequency is displayed in 7.20b, and the difference is less than 4π where the number of cycles is approximately 1000. This shows that the weakest form of generalised synchronisation occurs for the whole amplitude range calculated for the fixed feedback delay of $T = 3$. The largest Lyapunov exponent is shown in 7.20c which shows global stability is not

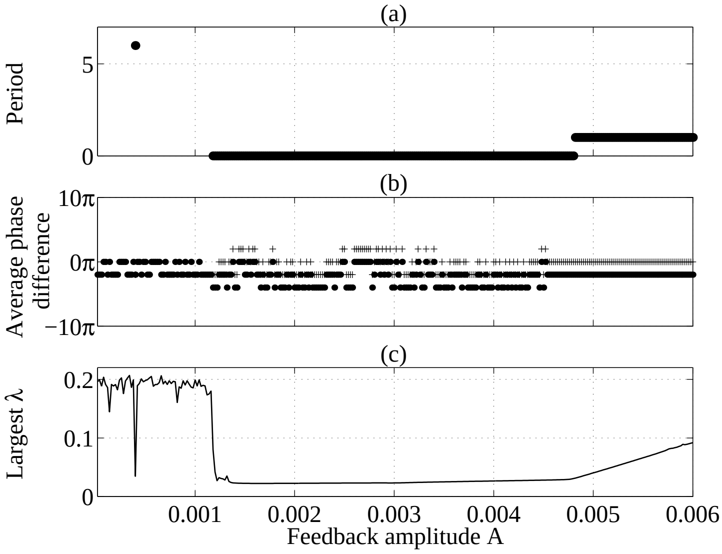

FIGURE 7.20: The period, average phase difference, and largest Lyapunov exponent as a function of feedback amplitude is shown in (a), (b), and (c) respectively where the feedback delay is fixed at 3 time units.

achieved until the feedback amplitude is greater than 0.0013. The number of transient pulses before control emerged is shown in 7.21b indicating that the fastest rate of convergence to the periodic state is approximately in the center of the amplitude control window. There is a period 6 orbit at $A = 0.0004$ which has a corresponding low number of transient pulses, and the associated largest Lyapunov exponent also drops in figure 7.20c. The number of phase slips was calculated and is shown in figure 7.21c. There are generally few phase slips during the controlled state other than at $A = 0.003$, and $A = 0.0015$ which correspond to the edges of the Arnold tongue in figure 7.18. There are some phase slips for $A < 0.0011$ but this amounts to only 18% of the data points in this region giving a high synchronisation ratio of 82%.

The measures used in this analysis show that generalised synchronisation occurs for a wide range of feedback parameters, and perfect synchronisation occurs before control emerges for $0.0011 < A < 0.0013$. The phase slips measure can show when a dynamical state is approaching the edge of an Arnold tongue, and quantifies the

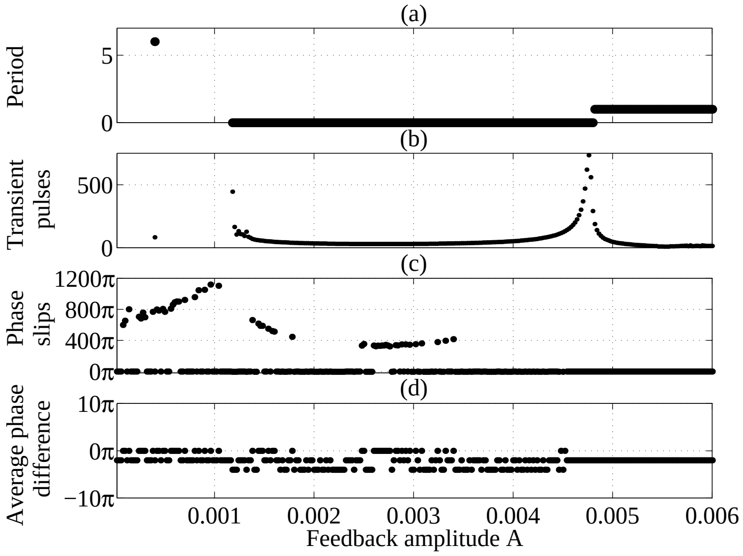

FIGURE 7.21: The period, number of transient pulses before control emerges, phase slips, and average phase difference as a function of feedback amplitude is shown in (a), (b), (c), and (d) respectively.

quality of the synchronised state.

We now modified the model of the non subtractive feedback system by including filtering and the results are shown in figure 7.22. Again as the low pass cut off is decreased there is less modulation at the fundamental frequency so a greater feedback amplitude is required to compensate. This is evident in the figure as the islands of control move towards a higher amplitude of feedback as the cut off is decreased. The islands also move towards a slightly smaller period and this is due to the fact that there is a non zero average feedback signal which increases the effective "pump" λ in the equations. These results show that limiting the bandwidth of the error signal has the effect of raising the threshold for control and for a sufficiently large bandwidth the results are essentially the same as the unfiltered case.

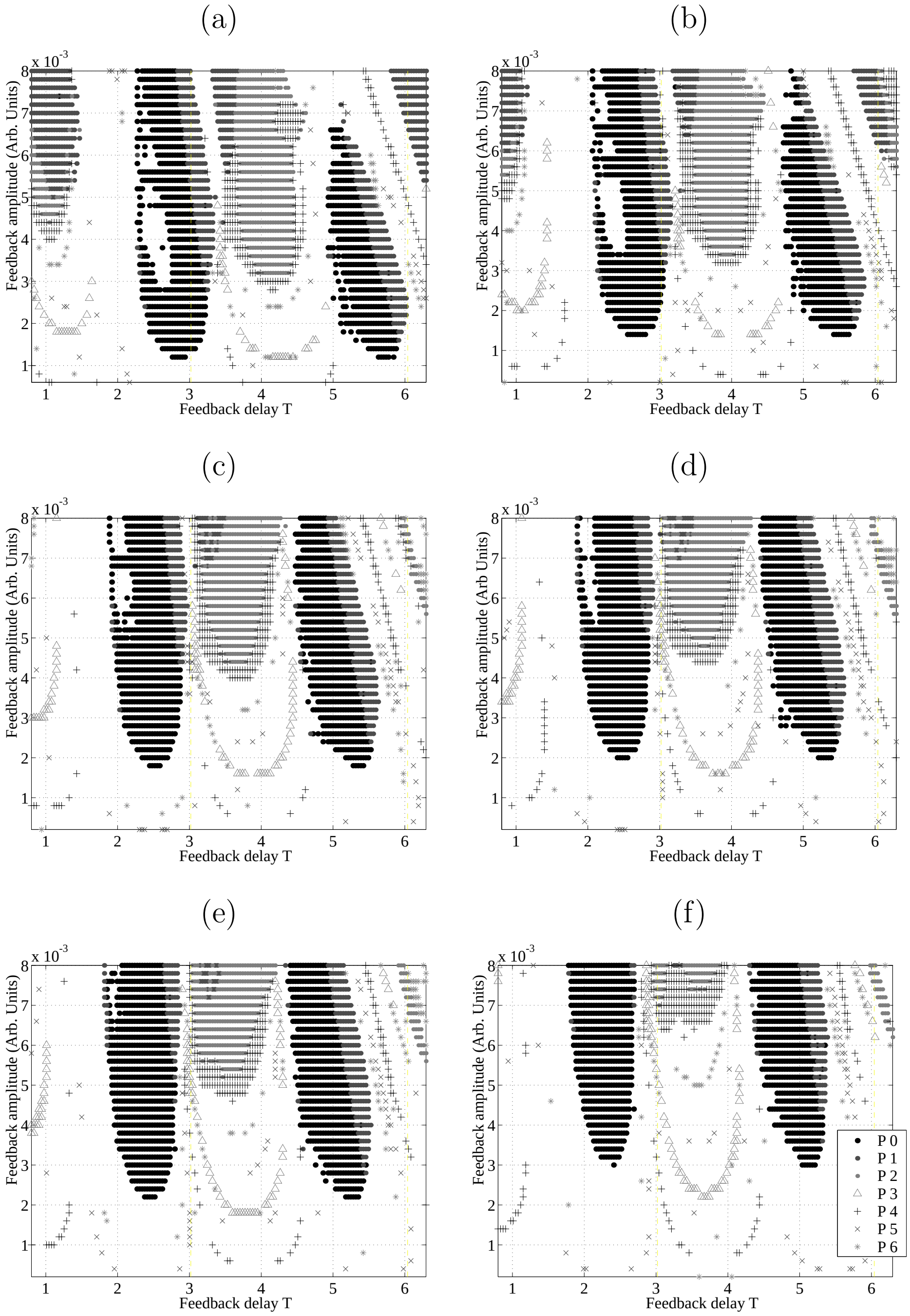

FIGURE 7.22: Control to various periods by non-subtractive feedback for different high pass cut off values ω_{max}. In (a), (b), (c), (d), (e), and (f) the high pass cut off frequencies are 8, 2, 1, 0.85, 0.75, and 0.5 respectively. The low pass cutt off in each case is 0.01.

7.3 Experimental

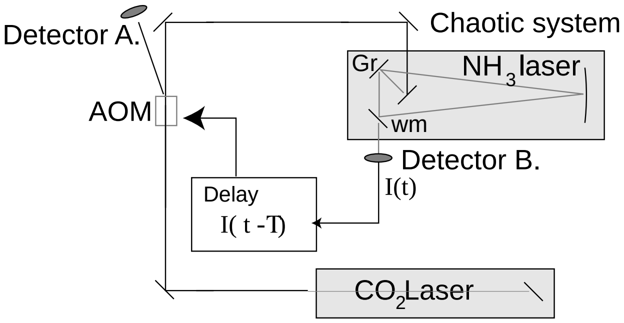

FIGURE 7.23: Experimental schematic. Gr is a blazed grating at the pump wavelength which doubles as a mirror for the lasing wavelength. wm is a wire mesh used as an output coupler. The FIR intensity output is measured, delayed, and applied to the AOM

Figure 7.23 is a diagram of the experimental system used for the non subtractive feedback experiments. The intensity of the backward wave in the ring $^{15}NH_3$ laser is measured with a Schottky barrier diode B. This signal is monitored by a spectrum analyser and recorded by a digital storage oscilloscope. The signal $I(t)$ is also fed into a buffering amplifier, rescaled, amplified, then applied to the acousto-optic modulator. The finite acoustic velocity in the AOM crystal creates a small delay (of order 1μs) between the modulation of the RF drive signal and the action of the CO_2 laser pump beam. This time delay could be varied by approximately 20% of the fundamental pulsation period by adjusting the AOM's position transverse to the CO_2 pump beam. There is a second detector A which is used to monitor the pump dynamics. This signal is simultaneously recorded with the signal measured in detector B onto a digital storage oscilloscope.

7.4 Experimental results

The delay time T was adjusted so that this corresponded to the average pulsation period of the laser. Control to period one was observed as shown in figure 7.24. Here the average feedback amplitude was 5%. Before the feedback control was turned on (at $t = 1.2$ms) the laser produced Lorenz–like chaos. Initially the control signal caused the Lorenz–like pulsations to break into transient pulses before the system settled to period 1 pulsations, and the feedback signal was also periodic. The phase difference between the feedback signal and the intensity output was locked only during the controlled state as expected. The smallest feedback delay which could be achieved in the experiment was about twice the average pulsation period of the unperturbed system so that we could not explore $\tau < 6.0$ in figure 7.18.

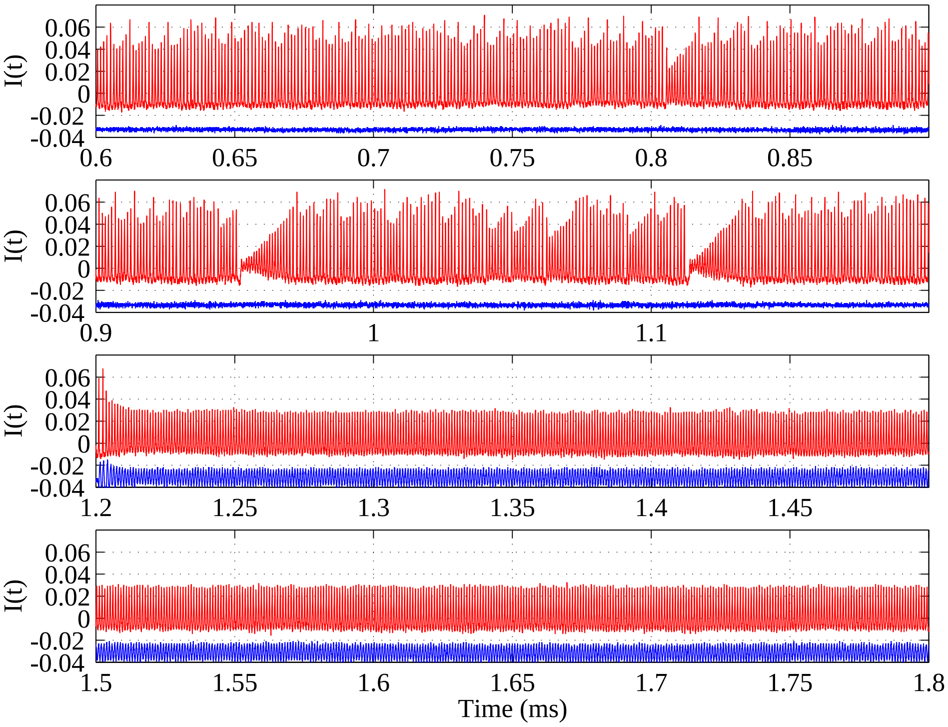

Figure 7.24: Control to period 1 using non subtractive feedback of the FIR laser with A approximately 0.05. The average pulsation period before and during control is 1.179μs, and 0.9747μs respectively.

We also find that when the sign of the feedback is reversed, control can still be achieved by adjusting the delay of the feedback (not shown since it looks the same as non-reversed feedback).

We also found that outside the range where control was achieved, the initially chaotic intensity can be synchronised so that the output and feedback is fully phase locked, and the time series is shown in figure 7.25. It appears that a different type of chaos is produced during feedback. This resembles Lorenz–like chaos operating closer to the chaos threshold (from above) compared to the unperturbed system due to the lengthening of the spirals. To check for phase slips a histogram is calculated for the time difference between the FIR intensity peaks, and the feedback signal, and the result is shown in figure 7.26. The synchronisation has a significant lag between the FIR intensity, and the feedback signal, and all peaks are within the average pulsation period $T = 1.068$. The histogram contains two peaks where the larger peak corresponds to the start of the spiral, and the smaller to the end of the spiral which is preceded by approximately ten cycles with a significantly larger period than the average. The average pulsation period decreases with increasing pump strength when no feedback is applied, so the feedback has increased the period during the last few cycles of the spiral despite the fact that the average energy of the pump during that region is slightly higher than at the start of the FIR spiral.

These results show that control to period 1 can be achieved by choosing an appropriate delay time. Synchronisation can be achieved which can be used to create a modified chaos which has a higher bandwidth than the unperturbed system.

7.5 Conclusion

We numerically investigated control of Lorenz-like chaos to various periodic states, including period 0, using two feedback control methods. The first case was subtractive feedback of intensity including loop delay. We found that for a small amplitude control to periods greater than three existed. At moderate feedback amplitude, control to

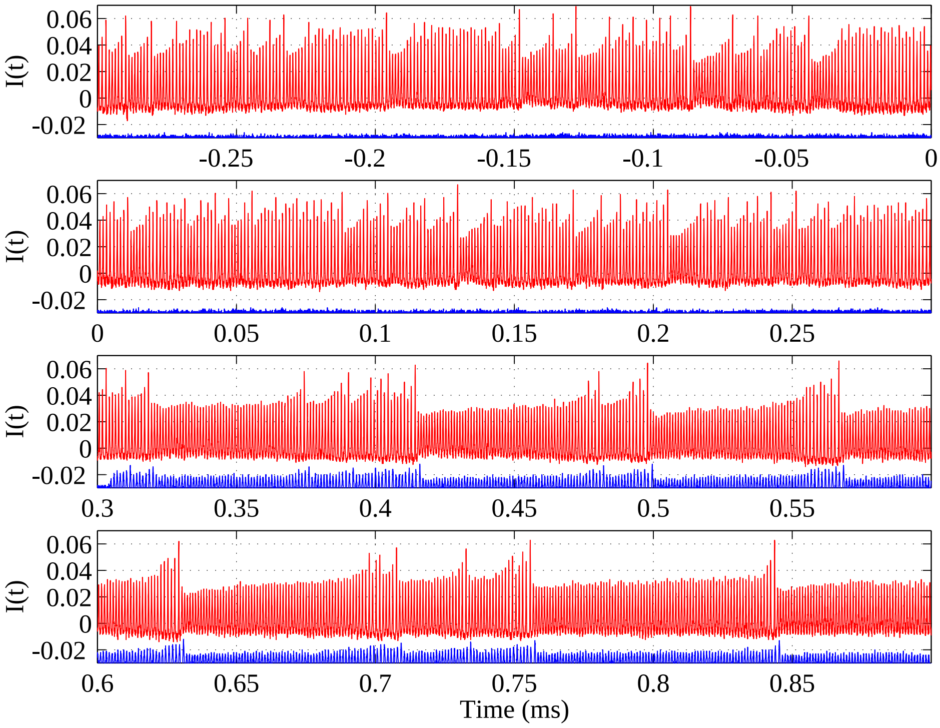

FIGURE 7.25: Synchronisation by non subtractive feedback. Average pulsation period before feedback, and during feedback are 1.1933μs, and 1.068μs respectively. There are no phase slips when the non subtractive feedback is turned on.

period 0, 1, 3, 4, 5, and 6 emerged where large islands of period 0 dominate the difference delay–feedback delay parameter space. These islands are separated by the average pulsation period of the system. They can be shifted half a period by inverting the feedback signal. We showed that islands of period 0 and period 1 correspond to a non positive set of eigenvalues of the chaotic system with feedback. Further analysis revealed that all three stages of synchronisation were present in both the subtractive and the non subtractive case. Results were shown for two of the stages. Perfect synchronisation was observed, where both the amplitude and phase were controlled where there were no phase slips. Also the presence of phase synchronisation occurred in the laser where there were no phase slips, and the amplitudes remained

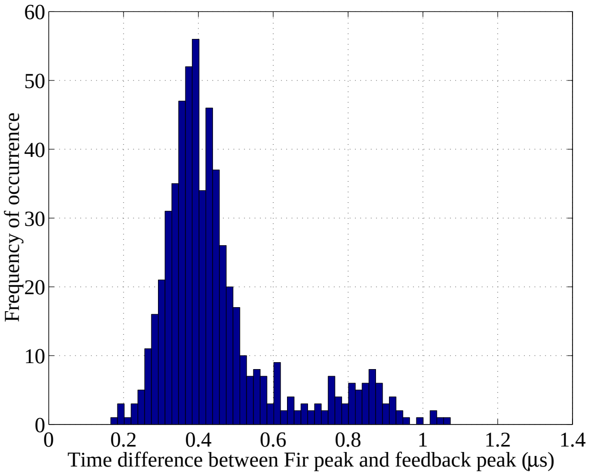

FIGURE 7.26: This shows the frequency of occurrence for the time difference between the FIR intensity peaks, and the associated pump fluctuation peaks, corresponding to figure 7.25. The average pulsation period is 1.068μs. Peak detection error ranges from 0.05–0.1μs.

uncontrolled. We then examined the effect of applying an a.c. filter to the feedback signal and varied the bandwidth before feeding it into the chaotic equations. Control is still possible even if the high pass cut off frequency was less than the characteristic frequency of the system. The second feedback case examined consisted of a simpler subtraction free feedback with only a loop delay. We found control to the same periodic cycle numbers as in the subtractive case at the same feedback amplitude, and with the addition of period 2. The period 0 and period 1 islands dominate the feedback delay–amplitude parameter space. These islands corresponds to the fixed points of the feedback system containing no positive eigenvalues. Modifying the feedback signal by applying the same a.c. filtering and finite bandwidth as in the subtractive feedback case, we find that this has the effect of raising the threshold amplitude for control as the bandwidth approaches the characteristic frequency of the system.

Experimentally we were able to control a chaotic Lorenz-like laser to period 1 by this non subtractive method but were prevented from demonstrating period 0 by time delays in the AOM. Synchronisation was also obtained which controls the phase of the chaotic laser, and numerically a larger region of parameter space is available to achieve the result. Overall, the concordance of experimental and theoretical results confirms that control of a strongly chaotic system can be achieved by controlling a single parameter using an error signal based on a single variable, without any computations. Further the system can be controlled not only to periodic states but also to the technically more useful steady state even though this region of phase space is inaccessible in the original system.
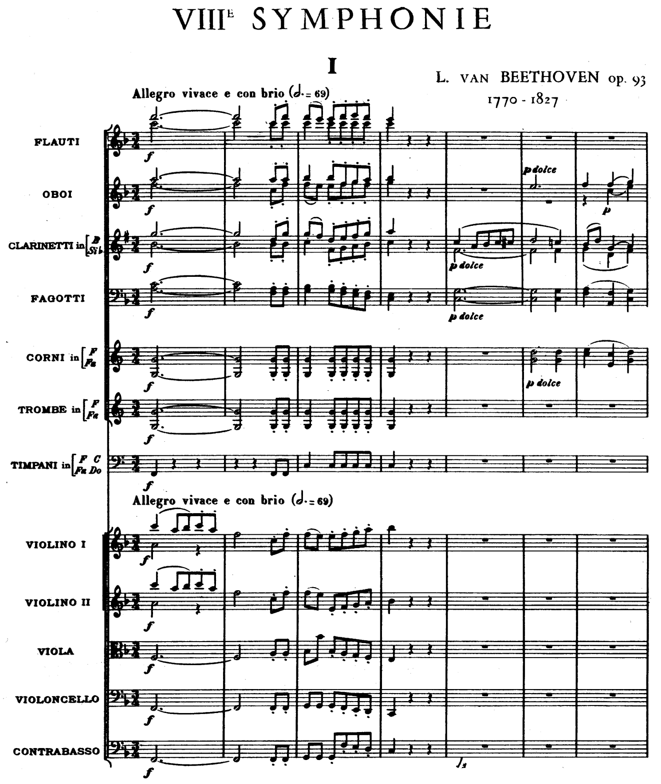
8

Chaotic synchronisation

The previous results in this thesis have dealt with controlling chaos to periodic behaviour using various modulations applied to the chaotic system. Synchronisation, as discussed in Chapter 1 was also investigated and its relation to control was explored. During phase synchronisation high correlations were found between the phases of the drive and the response. Even though full control was not exerted, the system was collapsed to a subset of the attractor so it can be thought of as a form of control. In this final chapter the aim is to determine whether a chaotic system can be controlled in some more general sense to applied modulation. In particular the modulation used in this chapter is chaotic, and the question is whether the dynamics of the laser can either be simplified, or be controlled by generalised synchronisation.

Pecora and Carroll [123] showed that two identical chaotic systems $\dot{x}_1(t)$, and $\dot{x}_2(t)$ can achieve synchronisation so that both systems evolve with the same orbit $x_1(t) = x_2(t)$, despite the fact that both systems have exponential instabilities. This result has created extensive interest and has led to the study of coupled chaotic systems. Different degrees of synchronisation were discovered, such as *complete synchonisation* [123], which appears only between identical chaotic systems. *Generalised synchronisation* (GS) [1] is defined as the emergence of a functional relation between the state of the response and drive so that $\mathbf{y}(t) = F(\mathbf{x}(t))$, that is, all the variables in system $\mathbf{x}(t)$ are functionally related to the variables in system $\mathbf{y}(t)$. *Phase synchronisation* (PS) [11] occurs when the phases of two chaotic systems, $\phi_1(t)$ and ϕ_2 are entrained. As discussed in the introduction the strict definition of PS is that the phases $\phi_1(t)$ and $\phi_2(t)$ with a locking ratio $n : m$ obey the condition $|n\phi_1(t) - m\phi_2(t)| = const.$ This condition can be relaxed in the presence of noise [11] so that the phase difference is bounded $|n\phi_1(t) - m\phi_2(t)| < const.$ There are other forms of synchronisation which include *lag synchronisation* [124], and *measure synchronisation* [125]. Each type of synchronisation has been extensively studied, but the transition from one type to another is not well understood. PS is usually considered a weaker form than GS since Parlitz *et al.* [126] claimed that GS leads always to PS, and PS can occur between two systems where no GS can be observed, implying that GS is stronger than PS. There were two examples presented by Zheng *et al.*[127], which included the standard Lorenz system, contradict the previous claim in that GS has been found to occur before PS between two chaotic systems with mismatched parameters. Zheng *et al.* found that the threshold for phase synchronisation for the standard Lorenz equations was significantly higher than the threshold for generalised synchronisation.

The experimental system used here can be described by the complex Lorenz equations, and an investigation is made to determine what type of synchronisation can be achieved, if GS implies PS for this system, and if the chaotic intensity fluctuations of the laser can be minimised by synchronising to a chaotic pump. To observe possible PS or GS in the laser, a variation of the *auxiliary-system method* [1] is used. The original method requires an exact replica of the response system so that generalised synchronisation occurs if the pump dynamics induces the same fluctuations in both the response, and auxiliary systems. In other words, the response is predictably dependent on the pump and is (relatively) insensitive to the initial conditions. Here, instead of using a replica of the laser as an auxiliary system, the laser itself is used both as the response, and as the auxiliary system. To implement this, the drive dynamics was applied twice to the laser, where the laser was allowed to return to its original chaotic state before the second drive dynamics was applied. The high dissipation in the chaotic laser allowed the dynamics to return to the original chaotic attractor relatively quickly, hence by the time the second drive dynamics was applied to the laser, the initial conditions of the laser are sufficiently different from that at the start of the first modulation period.

The definition of generalised synchronisation presented earlier, is that the *all* the variables in the response system are functionally related to drive system $\mathbf{y}(t) = F(\mathbf{x}(t))$ [1]. The variables $\mathbf{x}(t)$ and $\mathbf{y}(t)$ satisfy

$$\dot{\mathbf{x}}(t) = F(\mathbf{x}(t)) \tag{8.1}$$

$$\dot{\mathbf{y}}(t) = F(\mathbf{y}(t)). \tag{8.2}$$

Coupling can be introduced in the response system so that

$$\dot{\mathbf{y}}(t) = F(\mathbf{y}(t)) - \mathbf{G} \cdot [\mathbf{y}(t) - \mathbf{x}(t)]. \tag{8.3}$$

Then synchronised motion is bounded on the manifold $\mathbf{y}(t) = \mathbf{x}(t)$. Since the response system used here, the laser, is coupled through a parameter rather than a variable, it is difficult to find a mathematical expression for the synchronisation manifold. The aim here is not to find the functional relationship between the drive and response, but to observe whether there is a relationship, by using the auxiliary-system method. Generalised synchronisation was found by Tang *et al.* [29] in a similar system using the auxiliary method, where the laser intensity dynamics was determined by the pump dynamics. It appears that that the phase dynamics of the intensity was also determined by the phase dynamics of the pump, hence generalised synchronisation occurred. I now introduce the idea of a partial generalised synchronisation. There may be a subsystem of $\mathbf{x}(t)$, and $\mathbf{y}(t)$ which obeys generalised synchronisation, but the remaining variables remain uncorrelated. That is, there may be an $x_1(t)$, and $y_1(t)$, which are components of $\mathbf{x}(t)$, and $\mathbf{y}(t)$ respectively, that satisfy

$$y_1(t) = F(x_1(t)). \tag{8.4}$$

In particular the variable of interest here is phase. There may be a situation where the phases of the two chaotic systems are functionally related, but the remaining variables may not be coupled. This would mean that the response and auxiliary system are both split into two subsystems. One part of each subsystem will be functionally related, and the other parts will be uncorrelated. This phenomenon can be observed by using the auxiliary-system method. If phase dynamics of the response system is the same as the auxiliary system, then there must be a functional relationship between the phases of the pump and response dynamics. In other words, there is phase synchronisation between the response and auxiliary system, which may, or may not imply the existence of phase synchronisation between the pump and response dynamics. This phenomenon is explored here. I will define such phase synchronisation between the response and auxiliary system to be *generalised phase synchronisation* GPS. (This is not to be confused with a very recent article that discussed a phenomenon also called *generalised phase synchronisation* [128], but that involved two non-identical driving systems.)

The response of a chaotic laser to a chaotic modulation of the pump is now studied to observe possible stages of generalised synchronisation. The chaotic modulation is obtained by generating an intensity time series, from integrating the standard Lorenz equations, and applying this to the pump dynamics through the AOM. The experimental setup is the same as in figure 4.1 except that the arbitrary function generator is programmed with the calculated intensity time trace to be used as the chaotic modulation.

8.1 Chaotic modulation of the pump

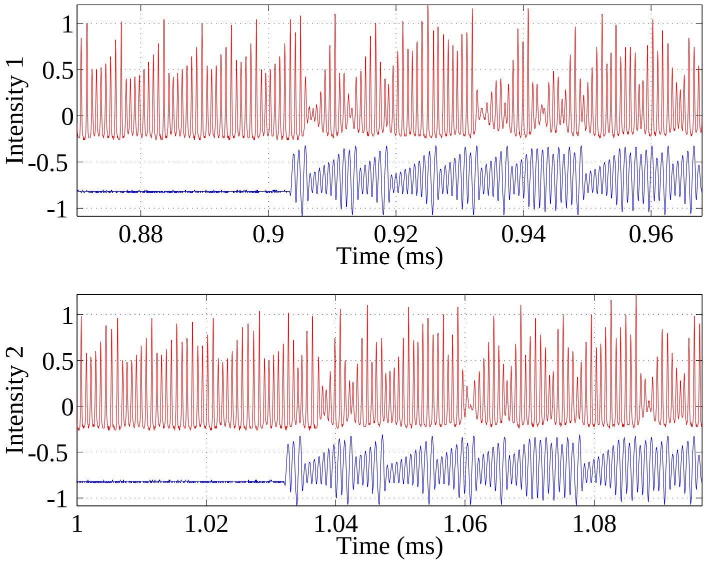

Figure 8.1: A Lorenz–like modulation is applied where $\Delta f = 0.3\%$ of f_0, and amplitude is approximately 5%. Top trace is laser output, lower trace is the pump. Intensity 1, and Intensity 2 are defined in the text and are represented as $I1(t)$, and $I2(t)$ respectively.

A chaotic modulation was pre-calculated using the standard Lorenz equations and applied to the laser at a weak modulation strength of approximately 5%, and the result is shown in figure 8.1. The average modulation frequency was 0.3% higher than f_0, the average pulsation frequency of the FIR laser. One may notice that the pump dynamics shown in figure 8.1 doesn't quite look Lorenz–like. This is due to bandwidth limitations in the AOM which is of the order of $2f_0p$ where f_0p is the average pump pulsation frequency. The dynamics of the laser during modulation in the upper, and lower trace are labelled $I1(t)$, and $I2(t)$ respectively. It is clear that from observing these time traces that there is no generalised synchronisation between the pump dynamics and FIR laser intensity dynamics, since $I1(t) \neq I2(t)$. There does appear to be a weak relation between the two intensities, so there may be some information in their phase dynamics. This is examined by constructing an auxiliary plot which is constructed as follows. The time difference between the laser pulsation peaks, and the modulation peaks will be defined as $dt_{Ii(t),f(t)}$ for the ith intensity time trace. The auxiliary plot is a graph of $dt_{I2(t),f(t)}$, against $dt_{I1(t),f(t)}$, and results corresponding to weak modulation are shown in figure 8.2. If a $y = x$ type relationship is observed, then generalised synchronisation is present. From the figure it appears that there is generalised phase synchronisation. Closer examination

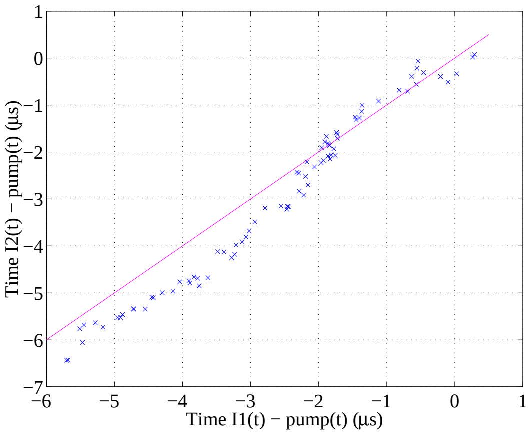

FIGURE 8.2: A time auxiliary plot is calculated using the results from figure 8.1. This shows the relationship between $dt_{I2(t),f(t)}$ and $dt_{I1(t),f(t)}$ where $dt_{Ii(t),f(t)}$ is the time difference between the FIR and pump pulsation peaks. The pump modulation frequency offset was $\Delta f = 0.3\%$ of f_0. This shows there is GPS.

of the time traces in figure 8.1 shows that there is no phase synchronisation between the pump dynamics, and the FIR laser dynamics since there are approximately 8 more intensity pulsation peaks than the number of modulation peaks in the same time interval. A plot of the evolution of $dt_{I1(t),f(t)}$, and $dt_{I2(t),f(t)}$ is shown in figure 8.3, where time increases monotonically with the number of pulse peaks. Despite

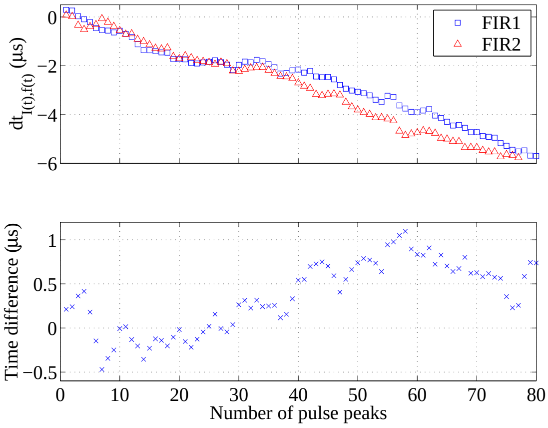

FIGURE 8.3: The time evolution of the time difference between the FIR laser and pump pulsation peaks is shown using the results from 8.1. The upper plot shows the evolution of $dt_{I1(t),f(t)}$, and $dt_{I2(t),f(t)}$ labelled "FIR1" and "FIR2". The lower figure is the difference FIR2-FIR1. Time increases monotonically with the number of pulse peaks. The frequency mismatch between the pump and laser pulsation frequency at zero coupling is $\Delta f = 0.3\%$ of f_0. This plot confirms the presence of GPS, and lack of PS.

there being a frequency mismatch, between the applied modulation frequency, and the FIR pulsation frequency before modulation was applied, this mismatch is almost the same for both the FIR traces. There is a hint of the two curves in the top plot diverging from each other, but they seem to converge again. For weak modulation very close to the average pulsation frequency of the laser, generalised synchronisation of the phases seems to occurring, despite the fact that the frequencies of the pump and laser dynamics are not locked. These results are analogous to the results of Zheng *et al.* [127] where they found the threshold of *generalised synchronisation* to be lower than phase synchronisation between coupled standard Lorenz systems.

The modulation amplitude was then increased to approximately 10%, and the frequency difference increased to 6% of f_0. The result is displayed in figure 8.4 which shows the response of the FIR laser to a chaotic modulation which was pre-calculated using the standard Lorenz equations. There is no obvious amplitude synchronisation between either the FIR intensity time traces with the corresponding modulation, or between the two responses $I1(t)$ and $I2(t)$. Hence there is no generalised synchronisation between the amplitudes of the pump and laser dynamics, although the average frequencies of the FIR dynamics, and the corresponding pump dynamics are the same. There are also very few phase slips other than at the start of the modulation, which is seen as negative values within the first few pulse peaks in figure 8.5(a). The time difference between the FIR and the corresponding pump dynamics is less than the average period and approximately constant, making them phase synchronised. There is an average lag between the laser and pump pulsation peaks of 0.4μs

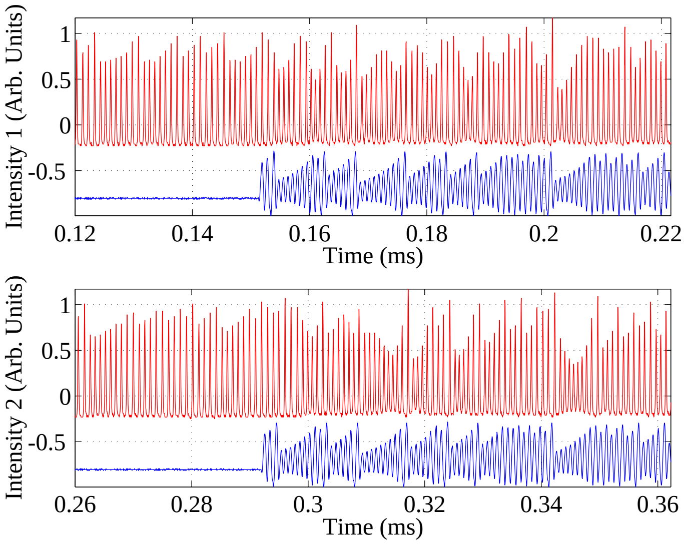

FIGURE 8.4: A chaotic intensity chaotic intensity is applied to the laser twice, where the dynamics is allowed to return to chaos before the second modulation is applied. The modulation is higher than f_0 so that $\Delta f = 6\%$ of f_0. This figure indicates the presence of PS

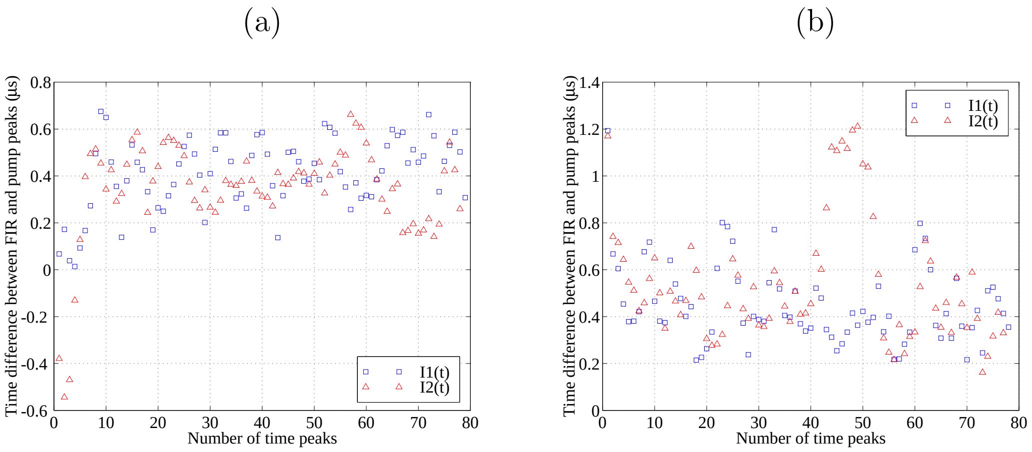
(a) (b)

Figure 8.5: This shows how the time between the FIR, and pump pulsation peaks varies with the number of pulse peaks during modulation, for the two plots in figure 8.4. The amplitudes of $I1(t)$ and $I2(t)$ are uncorrelated, but there is phase synchronisation between the FIR output, and the pump. $\Delta f = 6\%$ of f_0 in (a), $\Delta f = 9\%$ of f_0 in (b).

which implies that lag synchronisation is occurring. To determine whether there is generalised phase synchronisation present between the phases of the laser and pump dynamics, an auxiliary plot in time is made, i.e., $dt_{I2(t),f(t)}$, against $dt_{I1(t),f(t)}$, which is shown in figure 8.6. The identity line is included in the figure for comparison, which clearly shows that the data points do not follow this line, hence there is no generalised synchronisation between the phases of the pump and laser dynamics.

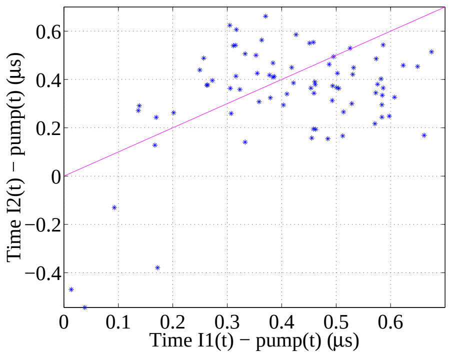

Figure 8.6: A time auxiliary plot is generated from the results of figure 8.4. The frequency mismatch is $\Delta f = 6\%$. This spread of points indicates that there is no GPS.

In figure 8.7 the average pump pulsation difference frequency was set to be 9% higher than f_0. Again, $I1(t)$ and $I2(t)$ are not correlated with each other, or the pump dynamics. There appears to be some phase synchronisation since the phase difference between the FIR output and the corresponding pump dynamics is bounded, as shown in figure 8.5(b). The second FIR time trace, $I2(t)$, shows phase slips occurs between pulses 40 and 50, otherwise phase synchronisation is present. It is clear from the FIR dynamics during modulation in figure 8.7, that the intensity dynamics has actually fluctuated more than the initial chaotic pulsations prior to modulation. The fact that there are now bursts of phase slips occurring, and the average lag time $dt_{I(t),f(t)}$ has increased to about 0.5μs shows that lag synchronisation is being destroyed. This is not particularly useful in terms of control, or at least minimising fluctuations. If a system cannot be easily controlled then an attempt could be made to at least stabilise a particular unstable aspect of chaotic system. At higher modulation amplitudes it has

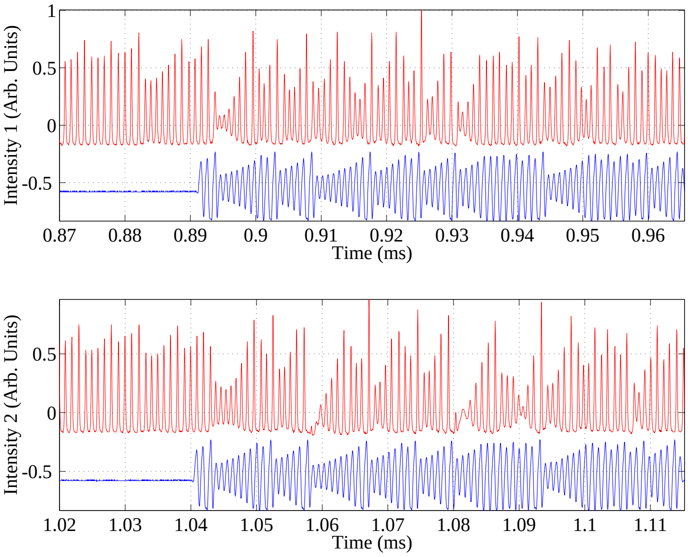

FIGURE 8.7: A chaotic intensity is pre-calculated and is applied to the laser twice, where the dynamics is allowed to return to chaos before the second modulation is applied. $\Delta f = 9\%$ of f_0. Only PS is present.

been shown that the amplitude dynamics of a chaotic laser can be correlated with the pump dynamics under appropriate condition [29]. The modulation amplitude used there was about 20%. Here, because the pump laser was failing, there was not enough laser pump power to explore the dynamics in that region.

These results show that generalised phase synchronisation can occur without requiring phase synchronisation when the average modulation frequency was near resonance, and lag synchronisation appeared without generalised phase synchronisation when the average modulation frequency was shifted by about 5%.

8.2 Chaotic phase modulation

An alternative approach was investigated. Instead of applying a Lorenz–like chaotic signal to the pump laser, which is chaotic in both the amplitude and phase, a constant amplitude modulation with chaotic phase was applied. This signal was generated by taking the Hilbert transform of a Lorenz–like chaotic intensity time series, to separate the amplitude dynamics from the phase dynamics, as discussed in section 3.3. It is only the phase dynamics which is used as the modulation here. It is well known that synchronisation between identical systems can occur [123], so applying a chaotic Lorenz–like signal to the pump dynamics is expected to work due to the similarities between the dynamics of the pump and response, and the previous results in the last section are consistent with this. It is worth reviewing how the dynamics of the laser responds to a chaotic modulation of the pump when it is in the the CW or periodic state. The results are summarised in figure 8.8. The laser was operating in the CW regime before modulation was applied in the left hand plots in the figure. The laser was then set to period 1 pulsations before modulation was applied which correspond to the right hand plots in the figure. When the laser was operating in CW mode, the dynamics of both chaotic phase modulation, and chaotic phase and amplitude

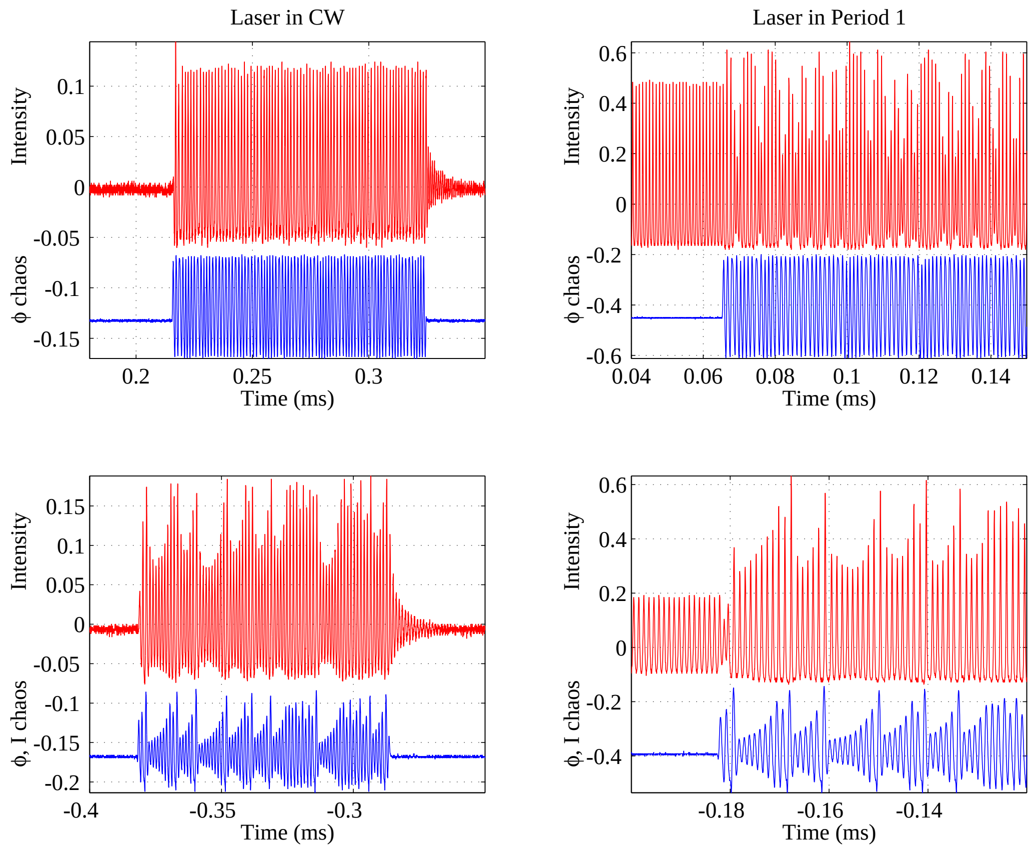

Figure 8.8: This shows the response of the FIR laser which is operating in CW mode, to a modulation containing a constant amplitude with chaotic phase, and chaotic amplitude and chaotic phase respectively, in the two left plots. The same two types of modulation signals are applied to the laser on the right hand plots, except that the laser is operating in a stable period 1 oscillation rather than CW.

applied to the pump appeared in the laser intensity almost exactly, shown in the top left, and bottom left plots respectively, in figure 8.8. This is to be expected since the laser is globally stable, and is behaving like a linear amplifier. The dynamics of the laser is still globally stable when it is operating in period 1 mode, except that the nonlinearities have been increased so that the laser may no longer behave as a linear amplifier. This is shown to be the case in the top right plot of figure 8.8 where a chaotic phase modulation was applied to the laser. The behaviour is different between the laser and pump dynamics. When Lorenz–like chaos was used to modulate the laser operating at period 1, the laser dynamics followed the chaotic pump well as shown in figure 8.8.

The relationship between the amplitude of the laser intensity and the phase of the dynamics is not a simple one, since the phase and amplitude are nonlinearly coupled to each other in the laser system. The laser may respond in a certain way during a particular time interval $dt_p(t)$ of the pump, which is the time difference between adjacent pump peaks. This response may depend on the location of the state of the system in phase space. Since only an intensity time trace is available, no complete relationship between the response of the laser to the pump can be obtained. An attempt is made however to show that there is a relationship which appears complex. This is likely to involve the time difference between adjacent pump peaks, and the corresponding difference in FIR intensity peaks. This clearly is not going to be unique as it may (at least) depend on the instantaneous value of intensity. These three quantities are plotted in figure 8.9. Data from the top right plot of figure 8.8 is plotted where the points are connected with grey lines to include information about time ordering. The two plots in the figure are just different projection angles of the same graph. The figure indicates that there is not a simple relationship between the three parameters. In the case of Lorenz–like chaotic modulation of the laser operating in the periodic regime, the amplitudes of the pump and laser output appears to have a very simple relationship as was shown in figure 8.8. The result from figure 8.9 indicates that synchronisation between the laser dynamics and chaotic phase modulation may be difficult to do. The chaotic laser intensity pulsations also have chaotic phase dynamics. If this phase dynamics is similar to the chaotic phase dynamics of the pump, then this could open up the possibility of synchronisation between the laser output, and the modulation. It could also allow for a wider range of synchronised states, or generalised synchronisation states to be accessed, since there is no restriction of the nonlinear dependence of phase and amplitude dynamics which is present in a

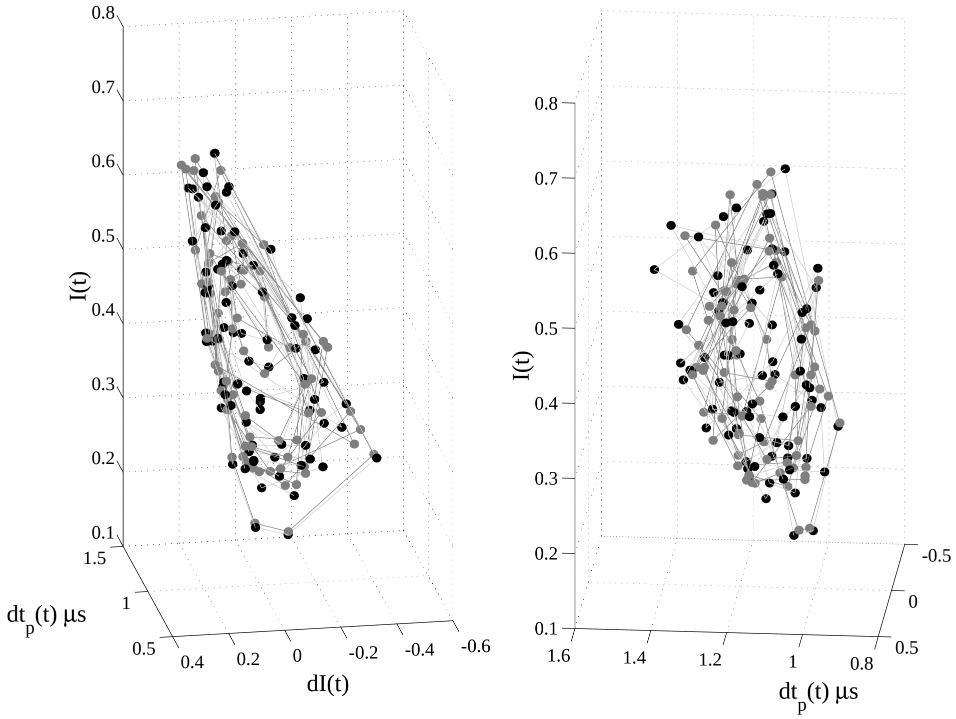

FIGURE 8.9: The ammonia laser was initially set to operate in the period 1 regime. The instantaneous intensity and the difference between adjacent intensity pulsations is shown as a function of the time difference between adjacent pump pulsation peaks.

chaotic (amplitude and phase) modulation.

A near resonance weak chaotic phase modulation of average difference frequency was -0.3% of f_0 (i.e. 3% lower) was applied to the chaotic laser, where the amplitude was about 5%. The result is shown in figure 8.10 and indicates the average frequency of the laser and pump dynamics are the same during the modulation period, and that there is phase synchronisation. This is unlike the chaotic modulation observed in figure 8.1 where the average frequencies did not lock together. To test for generalised synchronisation, a time auxiliary plot ($dt_{I2(t),f(t)}$ against $dt_{I1(t),f(t)}$) is constructed and displayed in figure 8.11. There are a number of data points which appear scattered and are far from the identity line indicating that generalised synchronisation for phase is not occurring. There are a significant number of points

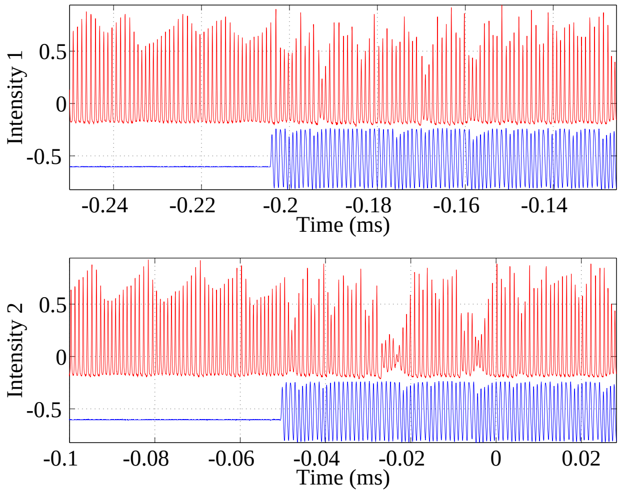

FIGURE 8.10: Response of the laser to a weak ($A = 5\%$) chaotic phase modulation near resonance where $\Delta f = -0.3\%$ of f_0. The figure indicate that PS is present.

lying near the identity line, but it is not clear from the figure which points are due to transient behaviour, as time ordering information is lost in the construction of the time auxiliary plot. Figure 8.12 shows the evolution of the time difference $dt_{I1(t),f(t)})$ and $dt_{I2(t),f(t)})$ against the number of pulse peaks which increases monotonically with time. This figure shows that there are 50 transient pulses, then the time differences converge to approximately 0.1μs, and clearly shows that generalised synchronisation is occurring between the phases of the pump and laser dynamics. So applying a near resonance weak perturbation using chaotic modulation has generated phase and generalised phase synchronisation.

Chaotic phase modulation was applied to the laser where the frequency was shifted to $\Delta f = -3\%$ of f_0 with amplitude approximately 10%. The result is shown in figure 8.13 which indicates a simplification of chaotic amplitude dynamics, and the existence of a phase relationship between the pump dynamics and the FIR output. The phase difference is examined further by plotting the time difference $dt_{I2(t),f(t)}$, against $dt_{I1(t),f(t)}$ The result is shown in figure 8.14(a), where a 45 degree line is added

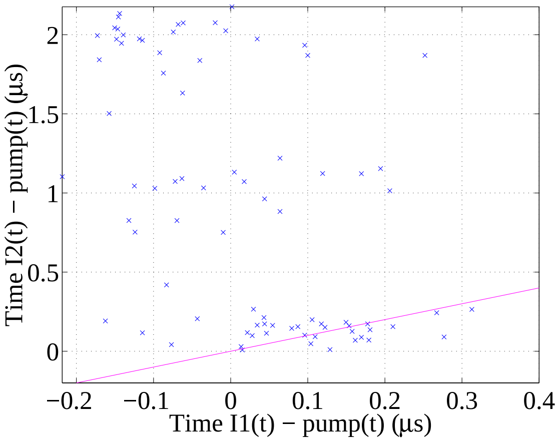

FIGURE 8.11: This is a time auxiliary plot ($dt_{I2(t),f(t)}$ against $dt_{I1(t),f(t)}$) calculated from 8.10, and an identity line is added. There is an indication of GPS since there are a significant number of points lying near the identity line. The average pump modulation frequency is $\Delta f = -0.3\%$ of f_0.

to indicate the location of perfect synchronisation. The appears to be some scattered points in the figure, so to check to see if these were due to transient behaviour, the first 14 data points were labelled which correspond to the first 14 pulsations in both the laser and the modulation. The scattered points clearly correspond to initial transient behaviour at the start of the modulation. Each data point has an associated error due to 8 bit sampling and the presence of detector noise so the error ranges from 0.05–0.1μs. The figure 8.14(a) shows that there is a strong correlation between $dt_{I1(t),f(t)}$, and $dt_{I2(t),f(t)}$, hence the phases of $I1(t)$ and $I2(t)$ are also related which indicates the presence of generalised synchronisation. The correlation is reasonable in figure 8.14 but not perfect since the data was sampled at only 8 bits, and there were errors in estimating the pulse peaks due to the presence of noise in the detector. The phases between the two intensity outputs are not only correlated with each other, but also with their respective pump dynamics. This can be seen in figure 8.15(a) where the evolution of the time differences $dt_{I1(t),f(t)}$ and $dt_{I2(t),f(t)}$, follow one another. They are also bounded within the average pulsation period of the pump which is about

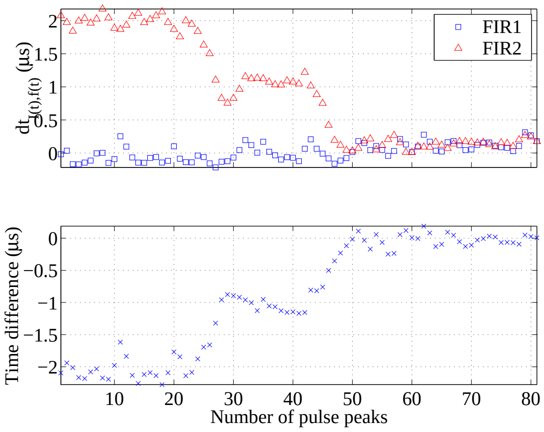

FIGURE 8.12: This shows the evolution of the time differences $dt_{I1(t),f(t)}$) and $dt_{I2(t),f(t)}$ where the number of pulse peaks increases monotonically with time. A weak modulation frequency $\Delta f = -0.3\%$ of f_0 is applied with amplitude approximately 5%. This figure confirms the presence of GPS and PS.

1μs. This boundedness is apparent in figure 8.16, which is a histogram of $dt_{I1(t),f(t)}$. The histogram also shows there are no phase slips larger than the average pulsation period, but the sign of the relative phases between the laser intensity and the pump pulsations is equally positive and negative. Combining this information with the time series shows that there are positive and negative oscillations of the relative phases between $I(t)$ and $f(t)$. This may be a significant contributing factor in lowering the depth of intensity fluctuation, as compared to the initially chaotic laser dynamics. If a functional relationship can be calculated which describes how a chaotic system will respond to one modulation cycle of a given period, then a modulation with appropriate phase dynamics could perhaps be used to control, or simplify a chaotic system as was observed here as an alternative to existing control methods.

Figure 8.17 shows the response of the FIR laser to chaotic phase modulation of average difference frequency 5% of f_0. The laser is now operating in a slightly different chaotic regime than was observed in figure 8.13. The fluctuations of the intensity are not reduced in figure 8.17 to the extent as observed in figure 8.13, but there still

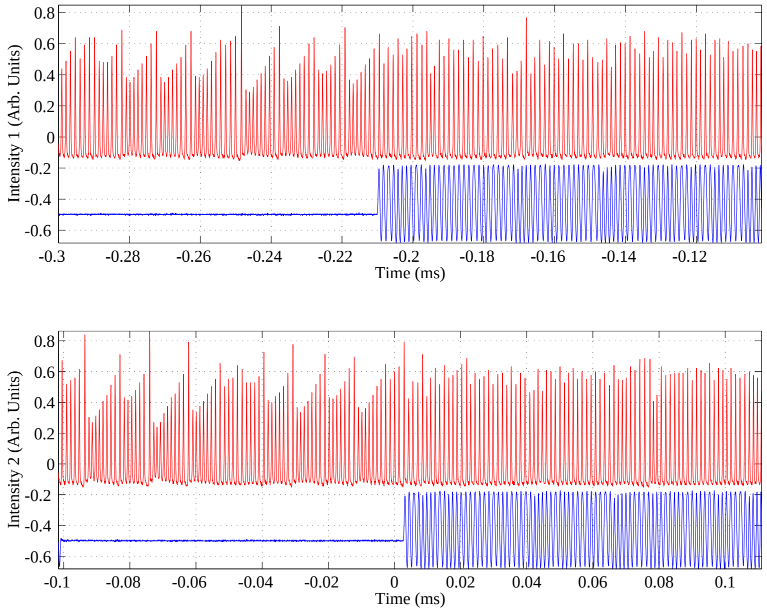

FIGURE 8.13: A pre-calculated signal with constant amplitude and chaotic phase, is applied to the laser twice. The average frequency between the FIR output, and the corresponding modulation are the same. There is a high correlation between the phases of $I1(t)$, and $I2(t)$ indicating the presence of GPS. $\Delta f = -3\%$ of f_0.

is generalised synchronisation between the phases of the two time traces $I1(t)$, and $I2(t)$. This is evident in figure 8.15(b) which shows the time evolution of $dt_{I1(t),f(t)}$, and $dt_{I2(t),f(t)}$. The maximum time difference of $dt_{I2(t),f(t)} - dt_{I1(t),f(t)}$ is 0.4μs, which is less than half the average pulsation period. So a frequency difference of 5% of f_0 is not enough to destroy phase synchronisation, but it is enough to destroy generalised synchronisation between the phases of the pump and laser dynamics as is shown by the time auxiliary plot in figure 8.14(b). There is a much larger spread of points as compared with 8.14(a) which corresponds to a modulation difference frequency -3% of f_0. Hence there is no generalised synchronisation at a frequency difference of 5%, but there is synchronisation. It was found that increasing the frequency difference to 6% of f_0 was enough to completely destroy phase synchronisation.

To obtain generalised synchronisation it is usually considered that the average

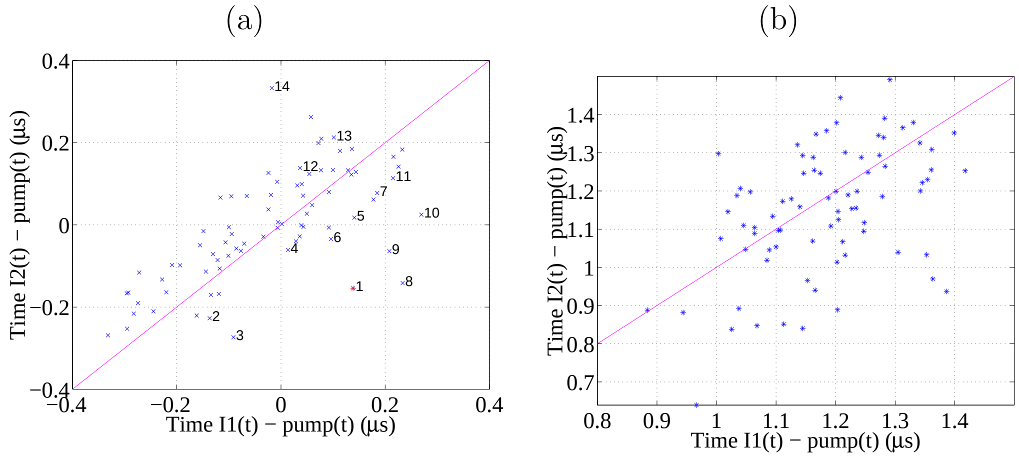

FIGURE 8.14: This shows how the time between the FIR, and pump peak pulsations varies with the number of pulse peaks during modulation. The plots (a) and (b) correspond to figures 8.13 and figure 8.17. The amplitude between $I1(t)$ and $I2(t)$ are uncorrelated, but there is phase synchronisation between the FIR output, and the pump. $\Delta f = -3\%$ of f_0 in (a), $\Delta f = 5\%$ of f_0 in (b).

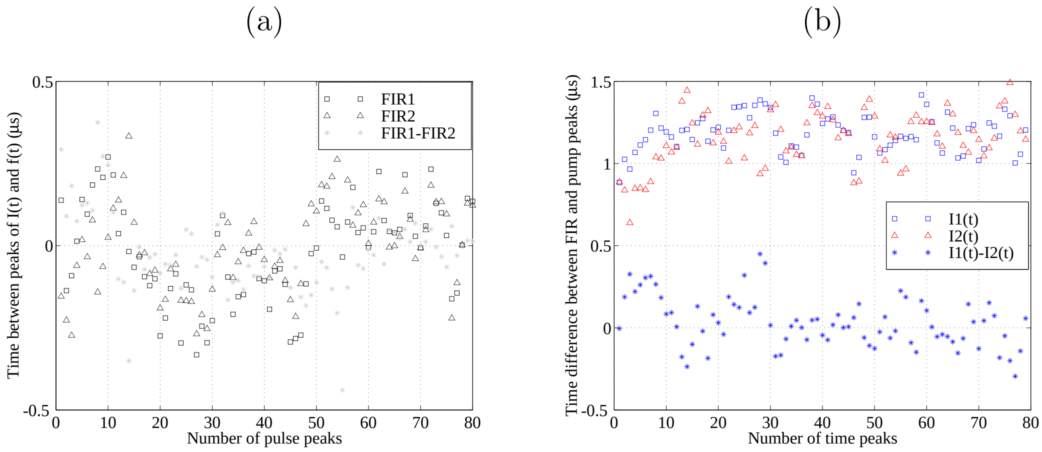

FIGURE 8.15: The evolution of the phase difference between $I1(t)$ and $f(t)$, and the phase difference between $I2(t)$ and $f(t)$ is plotted, and shows a relatively high correlation. The figure implies there is PS, and confirms GPS, where $\Delta f = -3\%$ of f_0 for (a) and the figure shows there is PS where $\Delta f = 5\%$ of f_0 for (b).

pump modulation frequency should be almost equal to the average pulsation frequency of the system [126] Increasing the amplitude of the modulation allows generalised synchronisation to occur between two quantities i.e. the existence of a functional relationship. An investigation is now made to determine whether it is possible

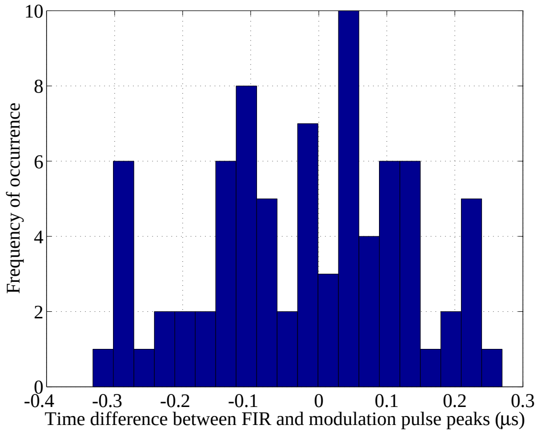

FIGURE 8.16: This is a histogram of the time difference between the peaks of $I1(t)$ and the pump $f(t)$. This figure shows that the time differences between $I1(t)$ and $f(t)$ are bounded. $\Delta f = -3\%$ of f_0. This confirms the presence of PS.

to have generalised synchronisation occurring where the average frequencies of the FIR output and the pump dynamics are far from equal. Generalised synchronisation was found to occur between the phases of the pump and laser dynamics in figure 8.10 where there was a small frequency mismatch between the pump and laser pulsation frequency. It is found here that generalised synchronisation is possible even though the average pump modulation frequency is far from the average FIR pulsation frequency as shown in figure 8.18. The average modulation frequency is slightly larger than $\frac{1}{3}f_0$, (38% of f_0). From this time trace it is clear that generalised synchronisation has occurred between the amplitudes of $I1(t)$), and $I2(t)$. This is explicitly shown in figure 8.19(a) which is a plot of the peak pulsation intensities of $I2(t)$, against $I1(t)$. Equality of the two intensity dynamics is represented as the function $I1(t) = I2(t)$, and this is clearly visible in the figure hence generalised synchronisation is occurring between the pump and laser intensity dynamics.

It is now interesting to investigate the dynamics of the phase difference between the FIR output and the pump dynamics, since the average modulation frequencies between the two are different by almost a factor of three. A time auxiliary plot

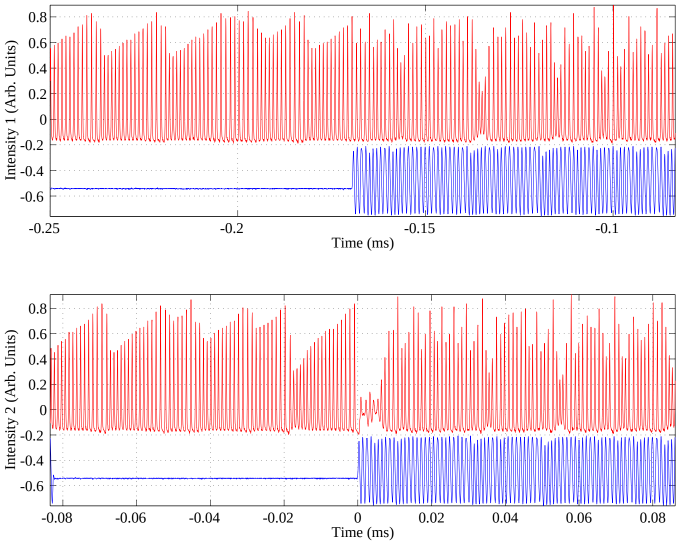

FIGURE 8.17: Chaotic phase modulation was applied to the FIR laser where the average frequencies between the FIR output was shifted so that $\Delta f = 5\%$ of f_0. The figure indicates the presence of PS.

is shown in figure 8.19(b) where the data again follows an identity plot. This shows that generalised synchronisation was also occurring between the modulation and laser phase dynamics. Another way to analyse the phases of the dynamics is to take the time for each third FIR pulsation peak and subtract it from each successive pump peak, and the result is shown in figure 8.20 for both $I1(t)$, and $I2(t)$. This time difference grows for both the intensities since the modulation frequency is not exactly at $\frac{1}{3}f_0$. The appearance of a strong relationship between $dt_{I1(t),f(t)}$ and $dt_{I2(t),f(t)}$, and the number of pulsation peaks (which is related to time) is in agreement with the time auxiliary plot 8.19(b). One final way to analyse the phase dynamics is to apply the analytic signal approach using the Hilbert transform as discussed in section 3.3. This procedure can be performed on the intensity time traces so that the amplitude and phase fluctuations are separated. The evolution of the phases of the FIR intensity ($I1(t)$) and pump pulsations, are shown in figure 8.21(a). The phases of both quantities have been unwrapped, and the phase calculated for the pump

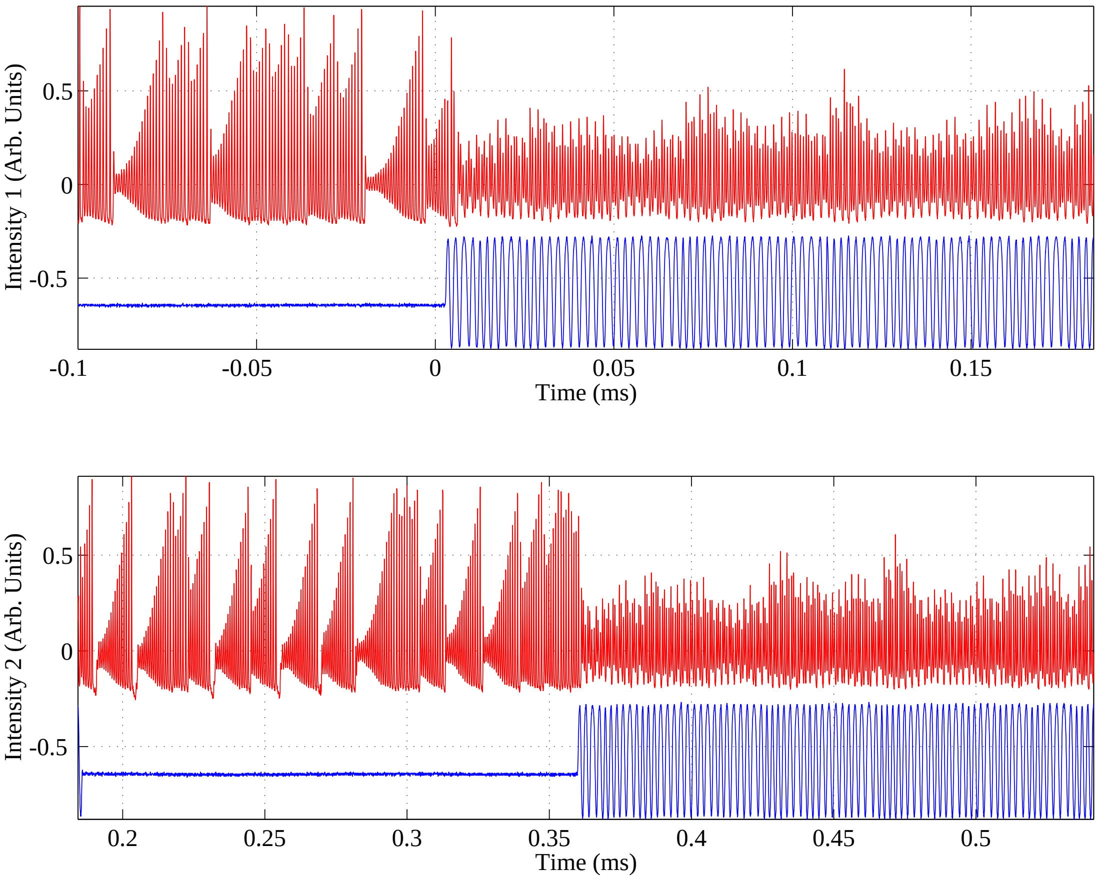

FIGURE 8.18: A chaotic modulation is applied the laser where $\Delta f = 38\%$ of f_0. The equal laser responses shows there is GS.

was multiplied by three for display convenience, since the pulsation frequency of the pump is almost $\frac{1}{3}f_0$. The phase difference $\phi_{I(t)} - 3\phi_{pump}$ is shown for $I1(t)$ (black line), and $I2(t)$ (grey line) in figure 8.21(b). This gives more detailed information about the phases than figure 8.20 since the whole intensity waveform was used to calculated the phase using the Hilbert transform, rather than just using the pulse peak times. These results show that generalised synchronisation is possible without phase synchronisation which is in agreement with Zheng *et al.* [127]. Not only can generalised synchronisation be obtained without phase synchronisation, but the

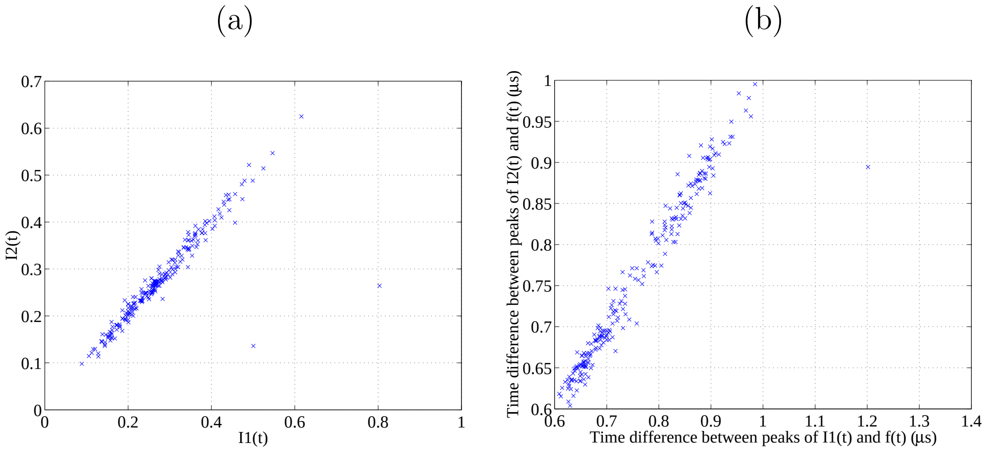

Figure 8.19: An auxiliary plot is generated from figure 8.18 where $\Delta f = 38\%$ of f_0. (a) is an auxiliary plot in I, (b) is an auxiliary plot in dt. Both plots confirm generalised synchronisation is occurring, as defined by [1]

frequency mismatch between the pump and laser intensity pulsation frequencies has shown to be large.

The arbitrary function generator available had a limited number of points so that only one value of modulation amplitude could be explored at a time. If the modulation could be varied in small discrete stages, then observing the evolution of the phase corresponding to each modulation amplitude could provide an insight to how this type of behaviour can emerge, and how phase synchronisation, generalised phase synchronisation, and generalised synchronisation are related.

All the experimental results are summarised on the diagram in figure 8.22.

8.3 Conclusion

Generalised synchronisation of intensity, and phase, was investigated between a chaotic laser and two types of pump dynamics. A Lorenz–like modulation was considered first, which has chaotic amplitude and chaotic phase dynamics which resembles a second chaotic system. Lag synchronisation was observed between the laser, and

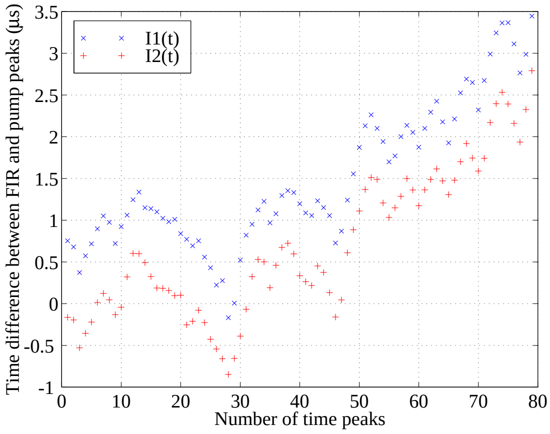

FIGURE 8.20: The evolution of the time difference between the peaks of the intensity and the corresponding pump is shown for the two intensities $I1(t)$, and $I2(t)$. The phase of each intensity is correlated with the corresponding pump, and with each other. $\Delta f = 38\%$ of f_0.

the Lorenz–like pump dynamics for a moderate modulation amplitude which existed up to a frequency mismatch of 9% between the laser and the modulation with zero coupling. No generalised synchronisation was found during the lag synchronisation regime. When a weaker modulation was applied very close to resonance, generalised phase synchronisation was found between the pump and laser dynamics even though there was a frequency mismatch greater than at zero coupling. Generalised phase synchronisation had a lower threshold than phase synchronisation which is analogous with Zheng *et al.* [127].

Another modulation signal was used which had a constant amplitude and chaotic phase dynamics. At near resonance with low modulation amplitude, generalised phase synchronisation, and phase synchronisation was observed between the pump and laser dynamics. Comparing this result with Lorenz–like modulation at near resonance indicates that chaotic phase modulation can have a greater impact on the dynamics of a chaotic system than full Lorenz–like modulation.

When the modulation amplitude was increased and the average frequency was

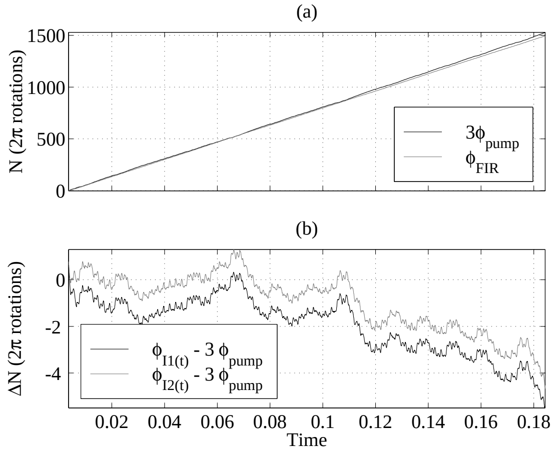

Figure 8.21: This shows the evolution of the phases between the intensities $I1(t)$, and $I2(t)$ with their corresponding pumps $f(t)$. This was calculated using the Hilbert transform on the time series of figure 8.18. $\Delta f = 38\%$ of f_0.

shifted away from resonance by about 3% generalised synchronisation persisted which dissolved at a frequency difference of 5%. At both these frequencies, phase synchronisation remained until the difference was 6%. Generalised synchronisation was investigated where the modulation frequency was far from resonance. A striking result was observed where both phase and amplitude generalised synchronisation was found, despite a frequency mismatch between the pump and laser pulsation frequency at zero coupling.

These results shown that the laser dynamics could be decomposed into two subsystems where the dynamics of one system was functionally related to the pump dynamics, while the other appeared uncorrelated. Generalised phases synchronisation could occur without requiring phase synchronisation to occur between the pump and laser dynamics, therefore phase synchronisation is not a necessary condition for generalised phase synchronisation.

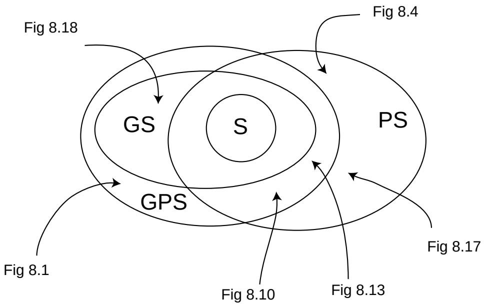

FIGURE 8.22: Summary of results. Labels are: Synchronisation S, Generalised synchronisation GS, Phase synchronisation PS, and Generalised phase synchronisation GPS. The figure number associated with the appropriate time series is shown at the start of the arrows.
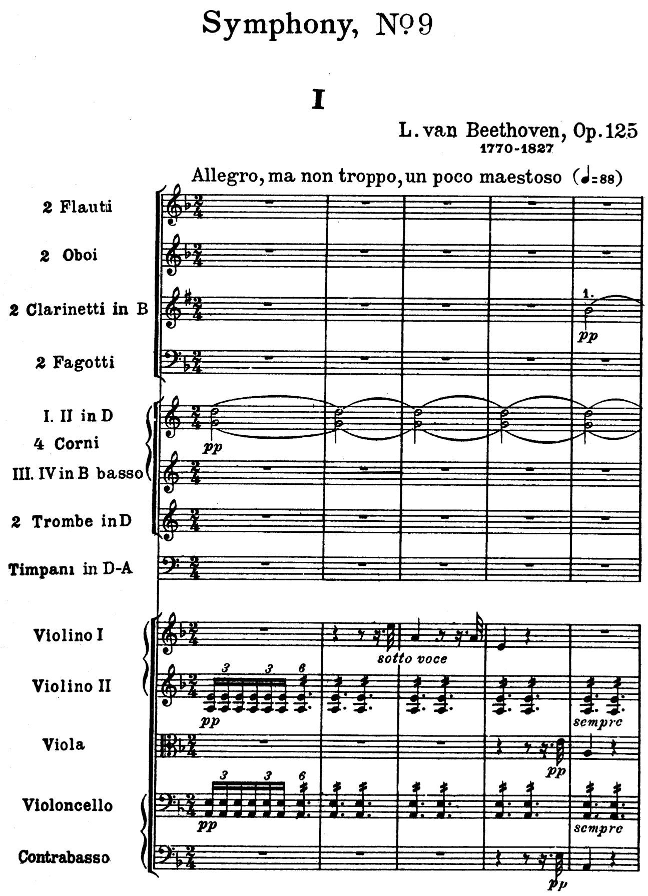
9

Conclusion

Two different chaos control methods were studied. A parametric perturbation method was considered first, that works on the principle that control to a periodic state is possible if an appropriate sinusoidal modulation is applied to a chaotic system. Control well above the chaos threshold had never been observed in the ammonia laser, contrary to expectation. Careful experimental and numerical studies were presented here which showed that such control is possible with modulation at a frequency near the average chaotic pulsation frequency. These results confirmed that not only is control possible in this system, but there is a wide choice of stabilised orbits which lie in a very narrow parameter region. Although difficult to implement, this method did allow access to a number of orbits once one is found.

The second method of control investigated here was based on the delayed feedback method introduced by Pyragas. An error signal was generated from the difference between a signal, and its value delayed in time, and this difference was fed back to modulate a system parameter. This method is based on the idea that a trajectory evolving on the attractor visits the desired orbit with a significant probability, and can become stabilised when sufficiently close to the orbit.

Control to various periodic states, and the steady state, had previously been observed in the ammonia laser, and was confirmed by the author. Detailed numerical studies supported and extended the experimental results, and were used to explore the effects of varying the feedback delay over several pulse periods. An additional loop delay was introduced to allow for the fact that the difference signal took some time to be fed back into the system in the ammonia laser. Control was achieved for delays of several pulsation periods. Perturbative control to steady state using the Pyragas method should not be possible in the Lorenz system since the unstable fixed point and nearby regions in phase space are never visited by a chaotic trajectory. The unexpected result of control to steady state had occurred since the feedback amplitude was not a small perturbation and thus changed the nature of the dynamical system. This was also manifested in the fact that the error signal did not go to zero in the controlled periodic states as expected by the Pyragas method.

The question of difficulty of control was also addressed, and it was shown that in both state independent and feedback methods the controlled periodic states were embedded in a relatively large area of parameter space where synchronisation occured. In the case of feedback methods ‘synchronisation’ refers to the self–synchronisation of the system with its own behaviour at an earlier time. Synchronisation can be thought of as a weaker form of control in the sense that only the phase of the dynamics is entrained to the driving signal, and the amplitude is typically uncorrelated. This extra freedom allows the synchronised region to span a larger parameter space. Since control lied within this region then locating the synchronised region could be used to find the control region, and provide information about the stability of the controlled state.

A simpler feedback method known as non subtractive feedback was also investigated where the error signal was generated without the subtraction of an earlier signal. Control to steady state was found, in which case the feedback signal vanished. At other controlled periodic states the feedback signal was periodic, so that once again the feedback system can be thought of as part of a new more complex dynamical system which can have simpler dynamics. Finally the effect of detector bandwidth on both feedback methods was investigated numerically, and it was found that control continues to work even when the bandwidth of the feedback was somewhat less than the characteristic frequency of the chaotic system.

A more general form of control known as chaotic synchronisation was investigated. Instead of coupling two chaotic systems through their variables, as has been a strong emphasis in the synchronisation literature, coupling was performed here through a system parameter. These results showed that generalised phase synchronisation did not require phase synchronisation to occur. Generalised synchronisation could occur despite a very large frequency mismatch between the two systems at zero coupling.

All these results showed that in a real autonomous chaotic system, a number of periodic states could be controlled by sinusoidal modulation or by feedback to a single parameter, without the necessity for a detailed model or real time computation. Slight modification of the dynamical system by incorporation of a feedback loop could change the overall dynamics to produce periodic states that were similar to the associated unstable periodic orbits in the unmodified system. The inclusion of the filter in the feedback loop forced the feedback signal to have very few harmonics so that the resultant signal was near sinusoidal. Therefore the chaotic system with delayed feedback is rather similar to the chaotic system with periodic modulation during the controlled state.

A more significant result is that control to the unstable fixed point was possible even though regions in the vicinity of the steady state were not part of the the original attractor, so that the feedback therefore allowed a creation of a new dynamical state. The feedback methods used here gave a wider choice of possible dynamics than perturbative feedback methods.

9.1 Future work

Despite the large number of publication on control of chaos, only a few control methods such as the OGY method are well understood. Perturbation theory can be used successfully in estimating appropriate parameters to implement control for situations where the control signal vanishes. These approximations are no longer valid for non vanishing control signal. Since analytical estimates of control parameters are not possible, the suitable control parameters used here were obtained by trial and error within the technical limits in the experiment. Once appropriate numbers were found then these were used in the numerical model. These simulations showed islands of control in parameter space which are predicted using perturbation theory only for period 0. However, a rich structure of islands of control to other periods were found that wasn't predicted using perturbation theory. Further work is required to develop techniques to estimate appropriate control parameters where the feedback signal does not vanish, and to provide an explanation for the location and structure of the islands of control to periodic states. This may lead to a clearer understanding of how control is achieved, which may involve following the structure of the attractor during the process of control. We need answers to questions such as: given an arbitrary system what control method is the most efficient for that particular system ? At the moment this is generally done by trying various methods as was done here. It is hoped, the results in this thesis will stimulate more research into control using non vanishing feedback signals with moderate perturbation, and these results may lead to new insights in the area of chaotic encryption, and in reducing chaotically fluctuating to a technically useful steady state.

A

The OGY method

This method, first proposed by Ott, Grebogi, and Yorke (OGY) [34] in 1990 aims to efficiently convert chaotic motion to regular periodic motion by using only tiny perturbations of the system parameters. It makes use of the property of a chaotic system that all the unstable periodic orbits are accessed within a finite time since the system is ergodic, which also means that there will be trajectories $x(n)$ in phase space that visit a neighbourhood of a particular unstable periodic orbit with significant regularity. In this neighbourhood, the stable and unstable manifold of the unstable periodic orbit are approximately linear and can be approximated by e_s and e_u respectively as shown in figure A.1. When $x(n)$ wanders into this neighbourhood a perturbation

δp is applied to one of the accessible system parameters p which shifts the location of the unstable periodic orbit x_{upo} to $x{*}_{upo}$, and the previous manifolds to $\tilde{e}_s$ and $\tilde{e}_u$ respectively. The state $x(n)$ follows the directions of the new manifolds to the new location $x(n+1)$.

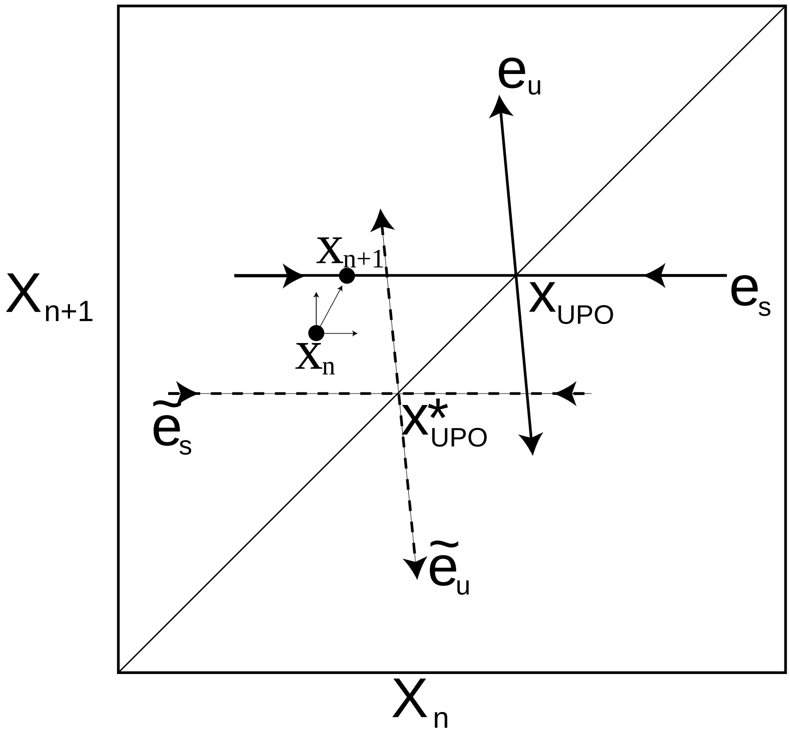

Figure A.1: Geometric interpretation of the OGY method. A return map is used so that the unstable periodic orbit x_{upo} appears as a fixed point. This has an associated stable e_s and unstable e_u manifold. A perturbation is applied when $x(n)$ is sufficiently close to x_{upo}, which shifts the location of the unstable periodic orbit x^*_{upo} and its associated manifolds $\tilde{e}_s$ and $\tilde{e}_u$. This causes the point $x(n)$ to move to $x(n+1)$ due to the attracting and repelling properties of the new manifolds. The perturbation is turned off once the new point lies on the stable manifold prior to perturbation. The point $x(n+1)$ will now move towards x_{upo} along e_s. This process is repeated at each iteration to prevent the unstable manifold e_u from taking the state away from the desired unstable periodic orbit.

The control perturbation is turned off so that the new unstable periodic orbit $x{*}_{upo}$ returns to the previous position x_{upo} as do the manifolds. The control perturbation δp is chosen so that the new iterate $x(n+1)$ lies on the stable manifold e_s and will move in the direction of the desired orbit x_{upo}. This process must be repeated at every iteration since the unstable manifold will eventually repel $x(n)$ away from the desired orbit. This procedure exploits the linearity of the stable manifold in the neighbourhood of the unstable periodic orbit, and the exponential sensitivity thus allowing the perturbation to be small. The directions of the manifolds and the location of the unstable periodic orbit is required to be known, and can in principle be estimated from the past data.

The advantage of this method is that control is perturbative and any unstable periodic orbit can be stabilised. No global model is required as the relevant dynamics can be reconstructed from a time series [76, 129]. This method has been successfully implemented in experiments on a forced magnetoelastic ribbon which showed control to various periodic states [35]. This however poses difficulties since the state must be located at a particular point in phase space. A large amount of data is required so that an accurate estimate of the manifolds can be obtained, but it is difficult to calculate from reconstructed data since the reconstruction is not perfect, and computation time is a major issue for relatively fast oscillating systems like the laser studied in the Author's work. A Poincare section is required so that the desired orbit crosses this surface, and the value/s of the system on this surface are used in the feedback algorithm. Although choosing a Poincare section is not difficult in a non autonomous system as there is a well defined phase based on the driving source, however for autonomous systems the phase is not well defined, so the choice is not obvious. For these reasons the author has sought alternative control schemes.

B

Deriving the Lorenz–Haken equation with arbitrary pump modulation

Starting with the Maxwell–Bloch equations;

$$\begin{aligned}
\dot{E} &= -\kappa(1+i\delta)E - \frac{i\omega_c}{2\epsilon_0}P \qquad \text{(B.1)} \\
\dot{P} &= -\gamma_\perp(1-i\delta)P - \frac{iU^2}{\hbar}ED \\
\dot{D} &= -\gamma_\parallel(D-D_0) - \frac{1}{2i\hbar}(E^\star P - P^\star E),
\end{aligned}$$

we make the transformation;

$$E = \frac{-\hbar}{i\nu_{12}}\sqrt{\gamma_{\|}\gamma_{\perp}}E' \tag{B.2}$$

$$P = -2\sqrt{\gamma_{\|}\gamma_{\perp}}\frac{\epsilon_0\hbar\kappa}{\omega_c\nu_{12}}P' \tag{B.3}$$

$$D = \frac{2\epsilon_0\hbar\kappa\gamma_{\perp}}{\omega_c U^2}D' \tag{B.4}$$

Where $U^2 = \nu_{12}\nu_{12}^{\star}$, and $\delta = \frac{\omega-\omega_c}{\kappa}$. The lasing frequency is pulled to ω, and ω_c is the empty cavity frequency. This gives;

$$\begin{aligned}
\dot{E}' &= -\kappa((1+i\delta)E' - P') && \text{(B.5)}\\
\dot{P}' &= -\gamma_{\perp}(1-i\delta)P' + \gamma_{\perp}E'D' && \text{(B.6)}\\
\dot{D}' &= -\gamma_{\|}(D' - D_0\frac{\omega_c U^2}{2\epsilon_0\hbar\kappa\gamma_{\perp}}) - \gamma_{\|}(E'^{\star}P' + P'^{\star}E') && \text{(B.7)}
\end{aligned}$$

Now the steady state population inversion becomes modulated so $D_0 = D_{ss}(1+f(t))$ and substituting λ as

$$\lambda = \frac{\omega_c U^2}{2\epsilon_0\hbar\kappa\gamma_{\perp}}D_{ss} \tag{B.8}$$

Thus the equation B.7 becomes

$$\dot{D}' = -\gamma_{\|}(D' - \lambda(1+f(t))) - \gamma_{\|}(E'^{\star}P' + P'^{\star}E') \tag{B.9}$$

$$\tag{B.10}$$

Finally transforming only the static part of the pump

$$\begin{aligned}
E' &= E && \text{(B.11)}\\
P' &= \lambda P\\
D' &= \lambda D
\end{aligned}$$

and rescaling time $t = \tau = \kappa t$ transforms the decay rates and the result is equation

$$\begin{aligned} \dot{E} &= -((1+i\delta)E - \lambda P) \\ \dot{P} &= -1/\sigma((1-i\delta)P - ED) \\ \dot{D} &= \beta/\sigma(1 - D + f(t) - 1/2(E^{\star}P + P^{\star}E)), \end{aligned} \tag{B.12}$$

where

$$\sigma = \kappa/\gamma_{\perp} \quad \beta = \gamma_{\|}/\gamma_{\perp}$$

and these equations appear in Chapter 6 as equation 7.3

References

[1] N. F. Rulkov, M. M. Sushchik, L. S. Tsimring, and H. D. I. Abarbanel. *Generalised synchronisation of chaos in directionally coupled chaotic systems.* Phys. Rev. E **51**(2), 980 (1995).

[2] C. Huygenii. *Horologium Oscillatorium* (Apund F. Muguet, Parisiis, 1673).

[3] R. J. Blackwell. *The pendulum clock or geometrical demonstration concerning the motion of pendula as applied to clocks*, chap. 30, p. 30 (The Iowa State University Press, Iowa, 1986), 1 ed.

[4] Y. Kuramoto. *Chemical Oscillations, Waves and Turbulence* (Springer, Berlin, 1984).

[5] N. R. Rulkov. *Images of synchronised chaos: Experiments with circuits.* Chaos **6**(3), 262 (1996).

[6] A. Andronov, A. Vitt, and S. Khaykin. *Theory of oscillations* (Pergamon Press, Oxford, 1966).

[7] A. G. Balanov, N. B. Janson, D. E. Postnov, and P. V. E. McClintock. *Coherent resonance versus synchronisation in a periodically forced self-sustained system.* Phys. Rev. E **65**, 41105 (2002).

[8] S. Boccaletti, J. Kurths, G. Osipov, D. L. Vallandares, and C. Zhou. *The synchronisation of chaotic systems.* Phys. Rep **366**, 1 (2002).

[9] S. Boccaletti, E. Allaria, R. Meucci, and F. T. Arecchi. *Experimental characterisation of the transition to phase synchronisation of chaotic co2 laser systems.* Phys. Rev. Lett. **89**(19), 194101 (2002).

[10] P. Manneville and Y. Pomeau. *Different ways to turbulence in dissipative dynamical systems.* Physica **1D**, 219 (1980).

[11] M. G. Rosenblum, A. S. Pikovsky, and J. Kurths. *Phase synchronisation of chaotic oscillators.* Phys. Rev. Lett. **76**, 1804 (1996).

[12] A. S. Pikovsky, M. Rosenblum, G. V. Osipov, and J. Kurths. *Phase synchronisation of chaotic oscilltors by external driving.* Physica D **104**, 219 (1997).

[13] B. Blasius, A. Huppert, and L. Stone. *Complex dynamics and phase synchronisation in spatially extended ecological systems.* Nature **399**, 354 (1999).

[14] K. Josic and D. J. Mar. *Phase synchronisation of chaotic systems with small phase diffusion.* Phys. Rev. E **64**, 56234 (2001).

[15] C. M. Ticos, E. Rosa, J. W. B. Pardo, J. A. Walkenstein, and M. Monti. *Experimental real-time synchronisation of a paced chaotic plasma discharge.* Phys. Rev. Lett. **85**(14), 2929 (2000).

[16] D. Maza, A. Vallone, H. Mancini, and S. Boccaletti. *Experimental phase synchronisation of a chaotic convection flow.* Phys. Rev. Lett. **85**(26), 5567 (2000).

[17] E. Allaria, F. T. Arecchi, A. D. Garbo, and R. Meucci. *Synchronisation of homoclinic chaos.* Phys. Rev. Lett. **86**(5), 791 (2001).

[18] C. Schafer, M. G. Rosenblum, J. Kurths, and H. H. Abel. *Heartbeat synchronisation with ventilation.* Nature **392**, 239 (1998).

[19] P. Tass, M. G. Rosenblum, J. Weule, J. Kurths, A. Pikovsky, J. Volkmann, A. Schnitzler, and H.-J. Freund. *Detection of n:m phase locking from noisy data: Application to magnetoencephalography.* Phys. Rev. Lett. **81**, 3291 (1998).

[20] E. Rodriguez, N. George, J. Lachaux, J. Martinerie, B. Renault, and F. J. Varela. *Perception's shadow: long-distance synchronisation of human brain activity.* Nature **397**, 430 (1999).

[21] P. Mandel and T. Erneux. *Laser Lorenz equations with a time-dependent parameter.* Phys. Rev. Lett. **53**(19), 1818 (1984).

[22] R. Vilaseca, A. Kulminskii, and R. Corbalan. *Tracking unstable steady states by large periodic modulation of a control parameter in a nonlinear system.* Phys. Rev. E **54**, 82 (1996).

[23] A. Kul'minskii, R. Vilaseca, and R. Corbalan. *Tracking unstable steady states by large-amplitude low-frequency periodic modulation of a control parameter: Phase space analysis.* Phys. Rev. E **61**(3), 2500 (2000).

[24] A. N. Pisarchik, B. F. Kuntsevich, and R. Corbalan. *Stabilizing unstable orbits by slow modulation of a control parameter in a dissipative dynamic system.* Phys. Rev. E **57**(4), 4046 (1998).

[25] R. Dykstra, A. Rayner, D. Y. Tang, and N. R. Heckenberg. *Experimentally tracking unstable steady states by large periodic modulation.* Phys. Rev. E **57**(1), 397 (1998).

[26] R. Lima and M. Pettini. *Suppression of chaos by resonant parametric perturbations.* Phys. Rev. A **41**, 726 (1990).

[27] L. Fronzoni, M. Giocondo, and M. Pettini. *Experimental evidence of suppression of chaos by resonant parametric perturbations.* Phys. Rev. A **43**(12), 6483 (1991).

[28] K. Pyragas. *Predictable chaos in slightly perturbed unpredictable chaotic systems.* Phys. Lett. A **181**, 203 (1993).

[29] D. Y. Tang, R. Dykstra, M. W. Hamilton, and N. R. Heckenberg. *Observation of generalised synchronisation of chaos in a driven chaotic system.* Phys. Rev. E **57**, 5247 (1998).

[30] Yun-Liu, P. Davis, Y. Takiguchi, T. Aida, S. Saito, and Jia-Ming-Liu. *Injection locking and synchronisation of periodic and chaotic signals in semiconductor lasers.* IEEE Journal of quantum electronics **39**(2), 269 (2003).

[31] E. Ott, P. So, E. Barreto, and T. Antonsen. *The onset of synchronisation in systems of globally coupled chaotic and periodic oscillators.* Physica D **173**(1), 29 (2002).

[32] M. Yoshimoto and S. Kurosawa. *Chaos control using noise.* Materials Science and Engineering C **12**, 63 (2000).

[33] J.-Y. Ko, K. Otsuka, and T. Kubota. *Quantum-noise-induced order in lasers placed in chaotic oscillation by frequency-shifted feedback.* Phys. Rev. Lett. **86**(18), 4025 (2001).

[34] E. Ott, C. Greborgi, and J. A. Yorke. *Controlling chaos.* Phys. Rev. Lett. **64**, 1196 (1990).

[35] W. L. Ditto, S. N. Rauseo, and M. L. Spano. *Experimental control of chaos.* Phys. Rev. Lett. **65**, 3211 (1990).

[36] E. R. Hunt. *Stabilising high-period orbits in a chaotic system: The diode resonator.* Phys. Rev. Lett. **67**(15), 1953 (1991).

[37] R. Roy, J. T. W. Murphy, T. D. Maier, and Z. Gills. *Dynamical control of a chaotic laser: Experimental stabilisation of a globally coupled systems.* Phys. Rev. lett. **68**(9), 1259 (1992).

[38] Z. Gills, C. Iwata, R. Roy, I. B. Schwartz, and I. triandaf. *Tracking unstable steady states: extending the stability regime of a multimode laser system.* Phys. Rev. Lett. **69**(22), 3169 (1992).

[39] A. M. Rhode, W. R. Rollins, and D. H. Dewald. *On a simple recursive control algorithm automated and applied to an electrochemical experiment.* Chaos **7**(4), 653 (1997).

[40] K. Pyragas. *Continuous control of chaos by self-controlling feedback.* Phys. Lett. A **170**, 421 (1992).

[41] K. Pyragas and A. Tamasevicius. *Experimental control of chaos by delayed self-controlling feedback.* Phys. Lett. A **180**, 99 (1993).

[42] A. S. zu Schweinsberg and U. Dressler. *Characterisation and stabilisation of the unstable fixed points of a frequency doubled nd:yag laser.* Phys. Rev. E **63**(5), 56210 (2001).

[43] N. F. Rulkov, L. S. Tsimring, and H. D. I. Abarbanel. *Tracking unstable orbits in chaos using dissipative feedback control.* Phys. Rev. E **50**(1), 314 (1994).

[44] A. Namajunas, K. Pyragas, and A. Tamasevicius. *Stabilisation of an unstable steady state in a Mackey–Glass system.* Phys. Lett. A **204**, 255 (1995).

[45] M. Ciofini, A. Labate, and R. Meucci. *Stabilisation of unstable fixed points in the dynamics of a laser with feedback.* Phys. Rev. E **60**(1), 398 (1999).

[46] A. Schenck, zu Schweinsberg, and U. Dressler. *Characterisation and stabilisation of the unstable fixed points of a frequency doubled Nd:YAG laser.* Phys. Rev. E **63**, 56210 (2001).

[47] W. Just, E. Reibold, H. Benner, K. Kacperski, P. Fronczak, and J. Holyst. *Limits of time-delayed feedback control.* Phys. Lett. A **254**, 158 (1999).

[48] K. Pyragas. *Control of chaos via extended delay feedback.* Phys. Lett. A **206**(5), 323 (1995).

[49] R. Dykstra. *Control of chaos is the* $^{15}NH_3$ *laser: A single mode, homogeneously broadened laser.* Ph.D. thesis, The University of Queensland, Queensland, Australia (1998).

[50] S. Newhouse, D. Ruelle, and F. Takens. *Occurrence of strange axiom a attractors near quasiperiodic flows on* t^m, $m \geq 3$. Commun. Math. Phys. **64**, 35 (1978).

[51] J. P. Eckmann and D. Ruelle. *Ergodic theory of chaos and strange attractors.* Rev. Mod. Phys. **57**(3), 617 (1985).

[52] M. Dhamala, Y.-C. Lai, and E. J. Kostelich. *Detecting unstable periodic orbits from transient chaotic time series.* Phys. Rev. E **61**(6), 6485 (2000).

[53] V. I. Oseledec. *A multiplicative ergodic theorem. lyapunov characteristic numbers for dynamical systems.* Moscow Math. Soc. **19**, 197 (1968).

[54] G. Benettin, L. Galgani, A. Giorgilli, and J. M. Strelcyn. *Lyapunov characteristic exponents for smooth dynamical systems and for hamiltonian systems; a method for computing all of them.* Meccanica **15**, 9 (1980).

[55] J. L. Kaplan and J. A. Yorke. *Functional differential equations and approximation of fixed points* (Springer, Berlin, 1979).

[56] P. Grassberger and I. Procaccia. *Characterisation of strange attractors.* Phys. Rev. Lett. **50**, 346 (1983).

[57] A. Renyi. *Probability theory* (North-Holland, Amsterdam, 1970).

[58] C. Grebogi, E. Ott, and J. A. Yorke. *Unstable periodic orbits and the dimensions of multifractal chaotic attractors.* Phys. Rev. A **37**(5), 1711 (1988).

[59] D. Ruelle. *Chaotic evolution and strange attractors* (Cambridge University Press, New York, 1989).

[60] J. B. Pesin. *Lyapunov characteristic exponents and ergodic properties of smooth dynamical systems with an invariant measure.* Sov Math. Doklady **17**, 196 (1976).

[61] E. N. Lorenz. *Deterministic nonperiodic flow.* J. Atmos. Sc **20**, 130 (1963).

[62] A. Z. Grasiuk and A. N. Oraevkij. *Quantum electronics and coherent light* (Academic Press, New York, 1964).

[63] C. Weiss and W. Klische. *On observability of Lorenz instabilities in lasers.* Optics Comm. **51**(1), 47 (1984).

[64] P. Mandel and Zeghlache. *Stability of a detuned single mode homogeneously broadened ring laser.* Opt. Commun. **47**, 146 (1983).

[65] H. Zeghlache and P. Mandel. *Influence of detuning on the properties of laser equations.* J. Opt. Soc. Am. B **2**(1), 18 (1985).

[66] N. B. Abraham, U. A. Allen, E. Peterson, A. Vicens, R. Vilaseca, V. Espinosa, and G. L. Lippi. *Structural similarities and differences amoung attractors and their intensity maps in the laser-Lorenz model.* Optics Commun. **117**, 367 (1995).

[67] F. Ali and M. Menzinger. *On the stability of limit cycles.* Chaos **9**(2), 348 (1999).

[68] C. Sparrow. *The Lorenz equations: bifurcations, chaos, and strange attractors*, vol. 41 (Springer-Verlag, New York, 1982).

[69] J. T. Malos. *Transitions between laser states.* Ph.D. thesis, The University of Queensland, Queensland, Australia (1998).

[70] L. Minying. *Single and multimode chaos in a laser.* Ph.D. thesis, The University of Queensland, Queensland, Australia (1995).

[71] C. Weiss, R. Vilaseca, N. Abraham, R. Corbalan, E. Roldan, and G. de Valcarcel. *Models, predictions, and experimental measurements of far-infrared* nh_3 *-laser dynamics and comparisons with the Lorenz-Haken model.* Appl. Phys. B **61**, 223 (1995).

[72] C. O. Weiss, N. B. Abraham, and U. Hubner. *Homoclinic and heteroclinic chaos in a single-mode laser.* Phys. Rev. Lett. **61**, 1587 (1988).

[73] R. Dykstra, J. Malos, N. R. Heckenberg, and R. G. McDuff. *Metastable chaos in the ammonia ring laser.* Phys. Rev. A **56**(4), 3180 (1997).

[74] C. O. Weiss, W. Klische, N. B. Abraham, and U. Hubner. *Comparisons of* nh_3 *laser dynamics with the extended Lorenz model.* Appl. Phys. B **49**, 211 (1989).

[75] D. Gabor. *Theory of communication.* J. Inst. Elect. Engng. **93**, 429 (1946).

[76] F. Takens. *Detecting strange attractors in turbulence* (Springer, Berlin, 1981).

[77] R. Marx, U. Hübner, I. Abdul-Halim, J. Heppner, Y. C. Ni, G. D. Willenberg, and C. O. Weiss. *Far-infrared CW Raman and laser gain of* 14^nh_3. IEEE J. Quant. Elect. **QE-17**, 1123 (1981).

[78] G. D. Willenberg, J. Heppner, and F. B. Foote. *Interaction of three coherent fields with Doppler broadened serial four-level systems: Applications to four-level FIR lasers.* IEEE J. Quant. Elect. **QE-18**, 2060 (1982).

[79] E. M. Frank, C. O. Weiss, K. Seimsen, M. Grinda, and G. D. Willenberg. *Predictions of far-infrared laser lines from* $^{14}nh_3$ *and* $^{15}nh_3$. Opt. Lett. **7**, 96 (1982).

[80] D. Y. Tang, R. Dykstra, and N. R. Heckenberg. *Antiphase dynamics in an optically pumped bidirectional ring laser.* Opt. Commun. **126**, 318 (1996).

[81] S. T. Shanahan and N. R. Heckenberg. *A simple method for frequency controlling* co_2 *pump lasers for submillimeter lasers.* J. Phys. E:Sci. Instrum **17**, 640 (1984).

[82] U. T. Win. *Non-linear dynamics of a laser system:* $153\mu m$ $^{15}NH_3$ *far infrared laser.* Ph.D. thesis, The University of Queensland, Queensland, Australia (1992).

[83] W. E. Lamb. *Theory of an optical maser.* Phys. Rev. E **134**, 1429 (1964).

[84] R. A. McFarlane, J. W. R. Bennett, and W. E. Lamb. *Single mode tuning dip in the power output of a hene optical laser.* Appl. Phys. Lett. **2**, 189 (1963).

[85] C. O. Weiss, W. Klische, P. S. Ering, and M. Cooper. *Instabilities and chaos of a single mode* nh_3 *laser.* Opt. Commun. **52**, 405 (1985).

[86] C. O. Weiss and J. Brock. *Evidence for Lorenz-type chaos in a laser.* Phys. Rev. Lett. **57**, 2804 (1986).

[87] R. Gilmore, R. Vilaseca, R. Corbalan, and E. Roldan. *Topological analysis of chaos in the optically pumped laser.* Phys. Rev. E **55**(3), 2479 (1997).

[88] C. O. Weiss, U. Hübner, N. B. Abraham, and D. Y. Tang. *Lorenz-like chaos in* nh_3 *FIR lasers.* Infrared Phys. Technol. **36**, 489 (1995).

[89] R. Roy and K. S. T. Jr. *Experimental synchronisation of chaotic lasers.* Phys. Rev. Lett **72**(13), 2009 (1994).

[90] E.-H. Park, M. A. Zaks, and J. Kurths. *Phase synchronisation in the forced Lorenz system.* Phys. Rev. E **60**(6), 6627 (1999).

[91] Y. Braiman and I. Goldhirsch. *Taming chaotic dynamics with weak periodic perturbations.* Phys. Rev. Lett. **66**(20), 2545 (1991).

[92] D. Y. Tang, R. Dykstra, M. Hamilton, and N. R. Heckenberg. *Experimental evidence of frequency entrainment between coupled chaotic oscillations.* Phys. Rev. E **57**(3), 3649 (1998).

[93] W. X. Ding, H. Q. She, W. Huang, and C. X. Yu. *Controling chaos in a discharge plasma.* Phys. Rev. Lett. **72**(1), 96 (1994).

[94] S. Bielawski, D. Derozier, and P. Glorieux. *Experimental characterization of unstable periodic orbits by controlling chaos.* Phys. Rev. A **47**(4), R2492 (1993).

[95] S. Bielawski, D. Derozier, and P. Glorieux. *Controlling unstable periodic orbits by a delayed continuous feedback.* Phys. Rev. E **49**(2), R971 (1994).

[96] R. Dykstra, D. Y. Tang, and N. R. Heckenberg. *Experimental control of single-mode laser chaos by using continuous, time-delayed feedback.* Phys. Rev. E **57**(6), 6596 (1998).

[97] J. Bhattacharjee, K. Banerjee, D. Chowdhury, and R. Saravanan. *Limit cycles in a forced Lorenz system.* Phys. Lett. **104A**(1), 33 (1984).

[98] K. A. Mirus and J. C. Sprott. *Controlling chaos in low- and high-dimensional systems with periodic parameter perturbations.* Phys. Rev. E **59**(5), 5313 (1999).

[99] M. Ciofini, R. Meucci, and F. T. Arecchi. *Experimental control of chaos in a laser.* Phys. Rev. E **52**(1), 94 (1995).

[100] M. Kang, K. Cho, C. Kim, S. Gil, and J. Lee. *Taming chaos of a laser diode pumped multimode Nd:YAG laser by small periodic modulation.* J. Opt. Soc. Am. B **15**(9), 2410 (1998).

[101] P. Colet and Y. Braiman. *Control of chaos in multimode solid state lasers by the use of small periodic perturbations.* Phys. Rev. E **53**(1), 200 (1996).

[102] R. Meucci, W. Gadomski, M. Ciofini, and F. T. Arecchi. *Experimental control of chaos by means of weak parametric perturbations.* Phys. Rev. E **49**, R2528 (1994).

[103] T. Ogawa and E. Hanamura. *Numerical analysis of multi-mode laser with modulated inversion.* Appl. Phys. B **43**, 139 (1987).

[104] G. Kociuba and N. R. Heckenberg. *Controlling the complex Lorenz equations by modulation.* Phys. Rev. E p. 26205 (2002).

[105] D. Baums, W. Elsasser, and E. Gobel. *Farey tree and devil's staircase of a modulated external cavity semiconductor laser.* Phys. Rev. Lett. **63**(2), 155 (1989).

[106] D. Hennequin, D. Dangoisse, and P. Glorieux. *Farey hierarchy in a bimode co2 laser with a saturable absorber.* Phys. Rev. A **42**(11), 6966 (1990).

[107] G. Willenberg, J. Heppner, and G. Schinn. *A.c. stark effect.* IEEE J. Quant. Electron. **QE-18**, 2060 (1982).

[108] M. Y. Li and N. R. Heckenberg. *Maps and distributions for the* $^{15}nh_3$ *FIR laser Lorenz chaos.* Opt. Comm. **108**, 104 (1994).

[109] M. Jensen, P. Bak, and T. Bohr. *Complete devil's staircase, fractal dimension, and universality of mode-locking structure in the circle map.* Phys. Rev. Lett **50**(21), 1637 (1983).

[110] S. Yasin, M. friedman, S. Goshen, A. Rabinovitch, and R. Thieberger. *Intermittency and phase locking of the bonhoeffer van der pol model.* J. theor. Biol. **160**, 179 (1993).

[111] A. Pikovsky, G. Osipov, M. Rosenblum, M. Zaks, and J. Kurths. *Attractor-repeller collision and eyelet intermittency at the transition to phase synchronisation.* Phys. Rev. Lett. **79**(1), 47 (1997).

[112] Y. Liu and J. R. R. Leite. *Control of Lorenz chaos.* Phys. Lett. A **185**, 35 (1991).

[113] G. Kociuba, N. R. Heckenberg, and A. G. White. *Transforming chaos to periodic oscillations.* Phys. Rev. E **64**, 56220 (2001).

[114] A. Wolf, J. B. Swift, H. L. Swinney, and J. A. Vastano. *Determining lyapunov exponents from a time series.* Physica D **16**(3), 285 (1985).

[115] J. N. Blakely, D. J. Gauthier, G. Johnson, T. L. Carroll, and L. M. Pecora. *Experimental investigation of high-quality synchronisation of coupled oscillators.* Chaos **10**(3), 738 (2000).

[116] G. Huyet, J. K. White, A. J. Kent, S. P. Hegarty, J. V. Moloney, and J. G. McInerney. *Dynamics of a semiconductor laser with optical feedback.* Phys. Rev. A **60**(2), 1534 (1999).

[117] W. Just, T. Bernard, M. Ostheimer, E. Reibold, and H. Benner. *Mechanism of time-delayed feedback control.* Phys. Rev. Lett. **78**(2), 203 (1997).

[118] K. Pyragas. *Control of chaos via an unstable delayed feedback controller.* Phys. Rev. Lett. **86**(11), 2265 (2001).

[119] T. S. Parker and L. O. Chua. *Practical numerical algorithms for chaotic systems* (Springer-Verlag, New York, 1989).

[120] P. Schmelcher and F. K. Diakonos. *Detecting unstable periodic orbits of chaotic dynamical systems.* Phys. Rev. Lett. **78**, 4733 (1997).

[121] D. Pingel and P. Schmelcher. *Theory and applications of the systematic detection of unstable periodic orbits in dynamical systems.* Phys. Rev. E **62**(2), 2119 (2000).

[122] R. Dykstra, J. T. Malos, N. R. Heckenberg, and R. G. McDuff. *Metastable chaos in the ammonia ring laser.* Phys. Rev. A **56**(4), 3180 (1997).

[123] L. M. Pecora and T. L. Carroll. *Synchronisation in chaotic systems.* Phys. Rev. Lett. **64**, 821 (1990).

[124] M. G. Rosenblum, A. S. Pikovsky, and J. Kurths. *From phase to lag synchronisation in coupled chaotic oscillators.* Phys. Rev. Lett. **78**(22), 4193 (1997).

[125] A. Hampton and D. H. Zanette. *Measure synchronisation in coupled Hamiltonian systems.* Phys. Rev. Lett. **83**(11), 2179 (1999).

[126] U. Parlitz, L. Junge, W. Lauterborn, and L. Kocarev. *Experimental observation of phase synchronisation.* Phys. Rev. E **54**(2), 2115 (1996).

[127] Z. Zheng and G. Hu. *Generalised synchronisation versus phase synchronisation.* Phys. Rev. E **62**(6), 7882 (2000).

[128] D.-S. Lee, W.-H. Kye, S. Rim, T.-Y. Kwon, and C.-M. Lim. *Generalised phase synchronisation in unidirectionally coupled chaotic oscillators.* Phys. Rev. E **67**, 45201 (2003).

[129] R. Mane. *Dynamical system and turbulence, Warwick 1980 page 230* (Springer, Berlin, 1981).